EPFL

Three-dimensional hydraulic fracture propagation in homogeneous and heterogeneous media

Carlo PERUZZO

École
polytechnique
fédérale
de Lausanne

2023

Abstract

Hydraulic fractures are tensile fractures that occur in solid materials due to the natural intrusion or anthropogenic injection of a viscous fluid into a fracture channel. The deliberate creation of hydraulic fractures is part of an industrial technology having various applications. For example, it is used for: the stimulation of hydrocarbon wells, the development of deep geothermal systems, and for measuring the in situ stress in rock formations. Additionally, hydraulic fractures may result from industrial processes such as geological carbon sequestration or wastewater injection.

Hydraulic fractures propagate in a plane perpendicular to the minimum in situ compressive stress. In most sedimentary basins, the direction of this stress is horizontal, hence hydraulic fractures propagate in a vertical plane. Their vertical growth, often referred to as height growth, can be detrimental to the effectiveness of their application. For instance, in the stimulation of hydrocarbon wells, excessive height growth above the targeted layer will result in the delivery of fluid and proppant to unproductive zones and possibly the stimulation of water-bearing layers. Concerns have been raised about the migration of fluids into strata containing potable groundwater caused by hydraulic fracturing treatments. Another example is the case of in-situ stress estimation where an excessive height growth can compromise the measurement by connecting the pressurized interval to the rest of the wellbore. It is known that height growth can be hindered or arrested by the presence of different rock layers or in situ stress inhomogeneity. However, a complete understanding of the relative importance of the different types of heterogeneities on hydraulic fracture propagation is still lacking. Significant progress has been made over the last two decades thanks to the understanding of the multi-scale nature of the problem. This progress has led to the development of the Implicit Level Set Algorithm (ILSA). This numerical tool has been verified as capable of efficiently and accurately reproducing the planar propagation of hydraulic fractures, as observed in experiments carried out in both homogeneous and heterogeneous media.

In this thesis work, we extend the scope of the ILSA algorithm to cases of large fracture front deformations. These cases are typically encountered when the front is locally pinned by tough and localized heterogeneities. We then further validate the ILSA algorithm by comparing it with new and recent analytical and experimental results. In particular, we highlight the comparison with the co-planar coalescence experiment of two hydraulic fractures. Based on the results obtained during these comparisons, we use the ILSA algorithm to study the effect of heterogeneities on fracture propagation. We determine the conditions under which the fracture front is arrested by a region of material characterized by a higher fracture energy. We

Abstract

determine how long two layers of material characterized by higher fracture energy can contain the hydraulic fracture propagation. We demonstrate a new hydraulic fracture containment mechanism in the case that propagation occurs in a material composed of a succession of layers.

Keywords: Hydraulic fracture mechanics, fracture coalescence, fracture toughness, heterogeneities, height growth, fracture containment, upscaling.

Sommario

Le fratture idrauliche sono così chiamate perché la loro propagazione viene causata dalla penetrazione di un fluido viscoso nel canale della frattura. Questo fenomeno fisico può essere sia il risultato di un processo naturale che di un processo antropico nel quale il fluido viene forzato all'interno della frattura (ad es. tramite pompaggio). Le fratture idrauliche infatti sono parte di una vera e propria tecnologia industriale. Essa è utilizzata, ad esempio, per incrementare la produzione di idrocarburi dai pozzi di estrazione, per lo sviluppo di formazioni geologiche profonde per usi geotermali, nonché come tecnica di misurazione dello lo stress in-situ nelle formazioni rocciose. D'altra parte, in certe attività industriali, la creazione di fratture idrauliche può costituire un rischio risultante dallo svolgimento dell'attività stessa. Ne sono esempi il sequestro geologico dell'anidride carbonica o l'iniezione di acque di scarto industriale nel sottosuolo.

La propagazione delle fratture idrauliche avviene in un piano ortogonale alla direzione del minimo stress in situ chiamato anche "confining stress". Nella maggior parte dei bacini sedimentari questo stress ha una direzione orizzontale implicando che le fratture idrauliche siano orientate verticalmente. La propagazione in questa direzione, definita anche come "height growth" nella letteratura scientifica, può andare a scapito dei vantaggi apportati dall'uso della fratturazione idraulica. Infatti, nel caso dei pozzi di estrazione degli idrocarburi, un'eccessiva propagazione della frattura fuori della zona di interesse rappresenta sia uno spreco del fluido utilizzato per la fratturazione che del "proppant" (particelle in esso sospese con lo scopo di mantenere aperta la frattura). Uno scenario peggiore si avrebbe nel caso in cui gli strati di roccia adiacenti contengano acqua e siano raggiunti dalla frattura. Infatti, ciò provocherebbe un incremento indesiderato del quantitativo di acqua in ingresso al pozzo di estrazione. Oltre a queste problematiche, sono state sollevate alcune preoccupazioni riguardanti la possibilità che la fratturazione idraulica faciliti la migrazione di fluidi verso strati contenenti acqua potabile. Un eccessiva propagazione verticale delle fratture idrauliche è indesiderata anche in altre applicazioni industriali. Ne è un esempio l'uso delle fratture idrauliche per la misurazione degli stress in situ. In tale applicazione un tratto del pozzo viene inizialmente isolato idraulicamente. Successivamente questo tratto è pressurizzato al fine di indurre la propagazione di una frattura. Nel caso in cui questa riesca a creare una connessione idraulica tra l'intervallo pressurizzato del pozzo e la rimanente parte di esso, la misurazione può essere anche totalmente compromessa. È noto che la crescita verticale della frattura possa essere limitata o addirittura arrestata dalla presenza di strati di roccia di natura differente. Lo stesso può accadere anche a causa della disomogeneità dello stress tra gli strati. Tuttavia

Sommario

l'importanza relativa che le diverse eterogeneità rivestono nella propagazione della frattura idraulica non è ancora stata quantificata. Ciononostante, grazie alla comprensione della natura multi-scala del problema, negli ultimi vent'anni sono stati fatti progressi significativi. Questi progressi hanno portato allo sviluppo dell'algoritmo noto come "Implicit Level Set Algorithm (ILSA)". Questo strumento di calcolo ha dimostrato di essere sufficientemente rapido ed accurato per la simulazione della propagazione della frattura idraulica osservata in esperimenti condotti sia in materiali omogenei che eterogenei.

In questo lavoro di tesi estendiamo il campo di applicazione dell'algoritmo ILSA ai casi di grandi deformazioni del fronte di frattura. Questi casi sono tipicamente incontrati quando esso risulta localmente bloccato o "impigliato" da eterogeneità localizzate. Successivamente validiamo ulteriormente l'algoritmo ILSA grazie al confronto con nuovi e recenti risultati analitici e sperimentali. In particolare, tra questi evidenziamo il confronto con l'esperimento di coalescenza co-planare di due fratture idrauliche. Forti dei risultati ottenuti durante questi confronti, utilizziamo l'algoritmo ILSA per lo studio delle eterogeneità sulla propagazione della frattura. Nello specifico, determiniamo le condizioni nelle quali il fronte di frattura viene arrestato da una regione di materiale caratterizzata da una più elevata energia di frattura. Stabiliamo per quanto tempo due strati di materiale caratterizzati da una più elevata energia di frattura possono contenere la propagazione della frattura idraulica. Dimostriamo un nuovo meccanismo di contenimento della frattura idraulica nel caso la propagazione avvenga in un materiale composto da una successione di strati.

Keywords: meccanica della frattura idraulica, coalescenza di fratture, energia di frattura, eterogeneità, contenimento della frattura, adeguamento alla scala superiore.

Contents

Contents

1 **Introduction**

1.1   Motivations and Background

1.1.1   Hydraulic fracturing

Hydraulic fracturing is a physical process that consists of the propagation of tensile (mode I) fractures driven by either the pressurization or the injection of a viscous fluid into a solid (Detournay, 2016).

Natural hydraulic fractures. Hydraulic fracturing is not only an engineering technology used in industrial applications, but also a natural phenomenon. It is the case of the formation of breccias (Phillips, 1972; Jébrak, 1997), and it can explain the morphology of particular rock veins observed on Mars (Caswell and Milliken, 2017). On Earth, the kilometers-scale intrusions of magma in the upper part of the lithosphere forming volcanic dikes and sills are one of the most striking examples of natural hydraulic fractures (Rivalta et al., 2015; Spence et al., 1987; Lister and Kerr, 1991). Another type of natural hydraulic fracture is the drainage of a glacial lake that separates a glacier from its bed (Das et al., 2008; Tsai and Rice, 2010, 2012).

Hydraulic fracturing as an industrial technology. Since the 1950s, hydraulic fracturing has become a widespread practice for enhancing the production of hydrocarbons from low permeability rocks (Economides and Nolte, 2000). Examples of these rocks include mudstones, coal, tight sandstones, and shales. To describe the typical hydraulic fracturing process, we can begin by examining a single well drilled to the target formation at a few km of depth in the subsurface. The initial step involves perforating a target interval of the well (via shaped explosive charges) to promote a flaw in the formation, then hydraulically isolating this perforated interval from the rest of the wellbore using specific completion hardware (e.g. packers, bridge plugs). The fracturing fluid is then injected into the interval until the pressure is sufficient to generate one or more hydraulic fractures beyond the region of near wellbore damage. Subsequently, solid particles referred to as proppant are added to the fluid. The proppant, which can be sand or

specially designed solid particles, prevents the fracture from closing in the long term. The newly established fracture remains open, providing a highly permeable connection between the reservoir and the well. This process is typically performed multiple times for each well, and multiple wells are drilled to exploit the reservoir. Today up to thousands of cubic meters of fluid and hundreds of tonnes of proppant can be injected during hydraulic fracturing treatments (Montgomery and Smith, 2010).

Other uses of hydraulic fracturing technology. Over time, hydraulic fracturing technology has been applied in various industrial settings. It is notably used to determine the minimum in-situ principal stress in rock formations at depth (Desroches and Thiercelin, 1993), and to create chemically reactive barriers in remediation projects for contaminated soils (Murdoch, 2002). It is also employed to precondition ore (Chacon et al., 2004) and to cause cave-ins in mining operations (Van As and Jeffrey, 2000). Furthermore, hydraulic fracturing is being utilized in applications that could aid the shift towards a renewable energy supply, replacing the reliance on fossil fuels. For example, hydraulic fracturing is used to create underground water storage lenses, where pumping water enables the storage of excess renewable energy through both elastic deformation of rock layers (elastic energy) and lifting of the overburden (potential energy) (Schmidt, 2010; Schmidt et al., 2023). Hydraulic fracturing has also been used in Enhanced Geothermal Systems (Moska et al., 2021). In this context, creating a network of fractures in impermeable hot rock at depth allows the flow of technological fluid to be forced in a loop between at least two wells. The fluid is heated as it passes through the hot rock and is then pumped to the surface, utilizing the thermal energy to drive turbines for electricity generation.

Concerns related to anthropogenic hydraulic fracture propagation. There are two primary concerns about hydraulic fracture propagation. First, hydraulic fracturing can trigger significant seismicity if the created fractures interact with an existing fault, then further re-activating possibly leading to the nucleation of frictional rupture. Only some examples have been recorded in the past decade (Holland, 2013; Clarke et al., 2014; Schultz et al., 2015; Eyre et al., 2019). The absence of nearby seismogenic faults is a pre-requisite for any hydraulic fracturing campaign Schultz et al. (2020). Note that seismicity associated with wastewater injection (which intrinsically perturbed a larger volume of rock) has been responsible for a much larger number of induced earthquakes (Council, 2013).

A second paramount concern is the vertical expansion of hydraulic fractures, known as height growth or fracture containment. Sufficient height growth is essential for optimal stimulation of the target reservoir, however, excessive height growth can result in the delivery of fluid and proppant to unproductive zones and even activate water-bearing strata, causing increased water inflow into the well (Economides and Nolte, 2000). The containment of fluid migration to strata containing potable groundwater is a matter of concern, particularly in shallow wells that are close to such resources (EPA., 2016). This issue is particularly relevant for shallow

reservoirs such as coal seam methane wells in the United States and Australia. What controls the vertical propagation of hydraulic fractures is the central theme of this thesis and our sole focus hereafter.

1.1.2 Heterogeneities and hydraulic fracture propagation

Most of the applications of hydraulic fracturing technology relate to geological formations. The presence of heterogeneities (strata, bedding planes, joints) and discontinuities (faults, fractures, microcracks) at a several different length scales can have substantial effects on fracture propagation (Bunger and Lecampion, 2017). Predicting and controlling the shape of the growing fracture have essential economic and potential environmental implications. A characteristic length-scale can be associated with each type of heterogeneity and/or discontinuity. The layer thickness, the microcrack size, and the distance between bedding planes are just a few examples. The direction and velocity of the hydraulic fracture propagation are affected by heterogeneities characterized by a length scale similar to the one of the fracture. A heterogeneous and anisotropic in-situ stress over this length scale can also perturb the propagation. This can result in multiple and non-planar crack paths. On the other hand, the presence of a principal direction of minimum in-situ stress (*confining stress*), together with its spatial uniformity, promote the planarity of the propagating fracture (Hubbert and Willis, 1957). Additionally, if heterogeneities are distributed, and their associated length scale is much smaller than any other, a representative element volume can be identified. Hence, at larger scales, the solid material can be modeled as homogeneous and characterized by equivalent properties (equivalent fracture toughness, equivalent elastic constants). This interplay between heterogeneities and hydraulic fracture growth at different length scales has been documented by several hydraulic fracture field experiments (see Jeffrey et al. (2009) and references therein). In particular, as reported in Jeffrey et al. (2009), the path followed by the hydraulic fracture can be tortuous at the meter scale while, at the decameter scale, the fracture appears quasi-planar. In situations where the stress regimes are either normal or strike-slip, the plane of propagation is vertical, and the hydraulic fracture interacts with sub-horizontal sedimentary rock layers of dissimilar materials with a length-scale comparable to the hydraulic fracture's one. The strata in sedimentary rock formations can differ in elastic properties, fracture toughness and/or permeability. Their in-situ confining stress also often differs. The variation of one or more of these parameters between the layer in which the fracture initiates and the bounding ones, can accelerate, hinder, or even arrest the growth of the planar fracture. The fractures can deviate into a weak bedding plane or a weak layer's interface, when the in-situ stresses are sufficiently low and transform into T-shape like fractures (Bunger and Lecampion, 2017; Xing, 2018; Chen et al., 2015). In these situations homogenizing the material properties is impossible, and the heterogeneity must be explicitly accounted for in physical models. This has been the case since the earliest hydraulic fracturing models. The PKN (Perkins, Kern, and Nordgren's) model (Perkins and Kern, 1961; Nordgren, 1972) assumes a hydraulic fracture lying on a vertical plane and characterized by a constant vertical extent (constant height), and extending only in the horizontal direction. The works of Simonson

et al. (1978), Cleary (1978) and Daneshy (1978) are among the first to address the main factors, currently considered to promote or impede hydraulic fracture containment. Namely, the stress contrast between layers, the variation of elastic properties and the density contrast between the fluid and the rock that can lead to buoyant fractures. Many other works shortly followed and investigated those factors theoretically and/or experimentally, see, for example Hanson et al. (1981); van Eekelen (1982); Warpinski et al. (1982) and the review of Mendelsohn (1984).
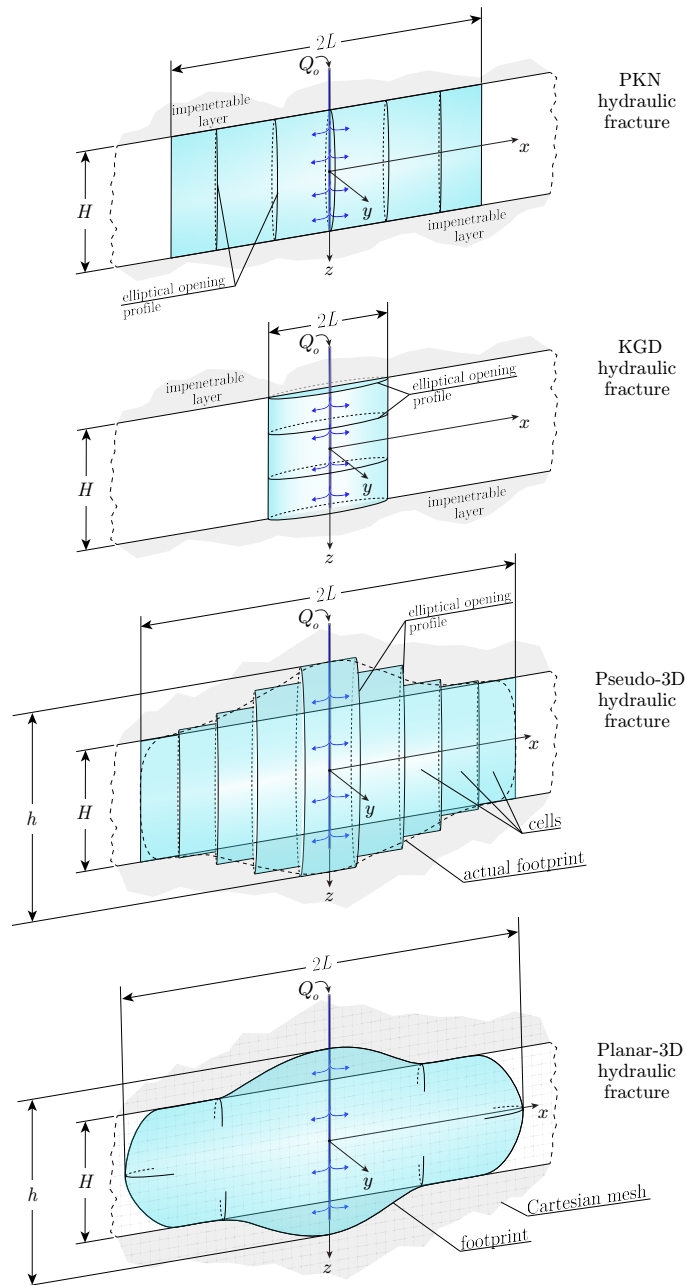

Figure 1.1 – Evolution of hydraulic fracture models, from simple 1D fixed-height approximation to full planar-3D geometries. .

1.1.3   Effect of fracture toughness variation on the height growth

Variation of fracture toughness between different layers is another mechanism that can promote fracture containment. However, it has received less attention than the other types of heterogeneities. This is explained because, as argued in van Eekelen (1982); Gu and Siebrits (2008), it appears that the toughness of rocks varies only "over a limited range." A decade after the work of Simonson et al. (1978), Thiercelin et al. (1989) demonstrated, employing a few 3D numerical simulations, that a "sufficiently" higher fracture toughness in the bounding layers (while keeping all the other properties constant) can stop the height growth of a 3D planar hydraulic fracture (and vice versa). Later Li and Keer (1992) confirmed these results but only considered the injection of an inviscid fluid for larger fracture toughness in the bounding layers. Ho and Suo (1993) studied the propagation of a radial defect into a contained fracture. This last study was conducted in the context of dry cracks and layered materials, but it paved the way for the recent derivation of the PKN-K solution in the context of hydraulic fracturing by Sarvaramini and Garagash (2015). We will recall the meaning of "-K" (related to the dominance of fracture energy) shortly as this notation was introduced in a more recent body of literature. After these early works, no further significant investigations have been made on this topic. In the meantime, during the last twenty years, significant progress has been made in understanding hydraulic fracture propagation in a homogeneous medium. It became clear that, during propagation, two energy dissipation mechanisms are competing: the energy dissipated in the creation of new fractures and the one dissipated in the flow of a viscous fluid (see Detournay (2016) for a review). In the limit of a low-permeability medium (little to no fluid leak-off in the surrounding media), the ratio between these two dissipations (namely the dimensionless toughness) is the only dimensionless number governing the spatiotemporal evolution of fracture opening, fluid pressure, and fracture velocity. Two different limiting propagation regimes correspond to the extreme values of this ratio. In the so-called viscosity dominated regime ("-M" regime), the work required by the flow of a viscous fluid is much greater than the one spent in the fracturing process. The opposite holds in the toughness dominated regime ("-K" regime). To appreciate the difference between these regimes, it is worth recalling the case of a penny-shaped hydraulic fracture driven by constant injection. The fracture radius L_R evolves from $L_{R,M} \propto t^{4/9}$ in the viscosity dominated regime, to $L_{R,K} \propto t^{2/5}$ at late time, in the toughness dominated regime (see Savitski and Detournay (2002) for more details). Conversely, as recently shown by Dontsov (2021) and Garagash (2023), for a blade-like (also referred to as PKN) fracture geometry, the fracture half-length evolves from $L_{PKN,K} \propto t$ in the toughness dominated regime to $L_{PKN,M} \propto t^{2/5}$ at late time when the viscosity dominated regime has established.

1.2   Research questions addressed in this thesis

In summary, the research questions addressed in this thesis are:

- Can current hydraulic fracture models reproduce quantitatively complex coplanar prop-

agations, such as the coalescence of two hydraulic fractures?

- What are the conditions for arresting a hydraulic fracture by a region of larger fracture toughness?

- For how long can two layers of fracture toughness can confine the propagation of a hydraulic fracture?

- Can a hydraulic fracture be ultimately contained when propagating in a material with a layered distribution of fracture toughness?

1.3   Outline of the different chapters

The thesis is organized as follows.

In Chapter 2, we present the mathematical formulation used to model hydraulic fracture propagation. We describe the numerical implementation and examine the fracture front reconstruction algorithm that has been presented in the existing literature. We then introduce a novel fracture front reconstruction algorithm and compare its results against the analytical solution of a semi-infinite fracture encountering a zone of higher fracture toughness.

In Chapter 3, we compare the predictions generated by the numerical model to laboratory experiments conducted in both homogeneous and heterogeneous media. Emphasis is placed on the comparison with an experiment that involves the interaction and coalescence of two hydraulic fractures propagating in the same plane.

In Chapter 4, we derive the energy balance for a 3D planar hydraulic fracture of general shape, and we make some considerations about the relative importance of the different physical processes at play.

In Chapter 5, we determine the minimum contrast in fracture toughness necessary for a region with an arbitrary shape to arrest the propagation of a finite hydraulic fracture, locally. This is accomplished by combining the energy balance for a semi-infinite hydraulic fracture and a local propagation condition.

In Chapter 6, we analyze a three-layer scenario where the fracture toughness varies between the layers (but elastic properties remain uniform), with higher values in the bounding layers than the central layer. We evaluate the duration of containment for an initially radial fracture, confined within the bounding layers in this scenario.

In Chapter 7, we study the propagation of a hydraulic fracture through a repetitive sequence of layers having similar elastic properties but varying fracture toughness. We analyze the long-term evolution of the fracture footprint and distinguish two possible outcomes, depending on

both the ratio of fracture toughness between the layers and the relative height of the layers. In the first outcome, the fracture will be effectively contained at late times, while in the second outcome, the fracture will propagate with a nearly constant aspect ratio.

The conclusions of this work and the perspectives for the future are reported in Chapter 8.

2 Simulating 3D planar HF

Disclaimer and acknowledgements: My contributions to this chapter are: *i)* the development and implementation of a new front reconstruction algorithm in the original numerical code (PyFrac) *ii)* the idea and the comparison to the solution of a semi infinite fracture penetrating a layer of higher fracture toughness *iii)* the formulation and implementation of a technique to reduce the memory requirement of the elastic kernels (taking advantage of their block Toeplitz structure). *iv)* the integration of an iterative solver in PyFrac and the implementation of the preconditioner described in Peirce (2006). *v)* The written exposition of this chapter and the numerical results presented. Dr. H. Zia. has first found why the front reconstruction proposed in Peirce and Detournay (2008) breaks down for large front deformations. Prof. B. Lecampion, had the idea to use a bilinear interpolation of the discrete level set function to develop a new front reconstruction algorithm. Both Dr. H. Zia and Prof. B. Lecampion developed the original version of the numerical code (PyFrac) to which I contributed.

2.1   Mathematical model

The mathematical model adopted in this thesis to study hydraulic fracture propagation belongs to Linear Hydraulic Fracture Mechanics (Detournay, 2016; Lecampion et al., 2018). It combines the use of Linear Elastic Fracture Mechanics describing the fracture propagation and the lubrication approximation for the fluid flow inside the fracture. The other usual assumptions are that:

- the dimension of the injection source (the wellbore diameter) is much smaller than the fracture length such that the injection can be considered to take place at a point

- the fracture propagation plane is perpendicular to the in-situ minimum confining stress σ_o, such that zeros shear tractions act on the fracture

- the fluid lag is assumed to remain negligible during the entire process. This condition is

ensured when $\mu V E'^2/\sigma_o^3 \ll 1$ where V is the fracture front velocity, μ is the fracturing fluid viscosity, E' is the rock plane-strain elastic modulus and σ_o the in-situ confining stress normal to the fracture plane (Garagash and Detournay, 1998). This is typically the case of deep fractures in rocks for which σ_o is sufficiently large (Lecampion and Detournay, 2007)

- the inertial effects are considered to be negligible as hydraulic fractures propagate at the very most of a few meters per second

- the solid medium is consider as a homogeneous linearly elastic isotropic medium, and we restrict to the case of an infinite medium

- the fluid rheology is assumed to be Newtonian.

Elastic deformations. For one or more coplanar tensile fractures, loaded by an internal fluid pressure, the momentum balance written for the solid medium reduces to a single hyper singular boundary integral equation that relates the fracture width w and the normal component of the traction vector (Hills et al., 2013; Crouch S.L., 1983):

$$T_{x,y,t}(x,y) - \sigma_o(x,y) = -\frac{E'}{8\pi} \int_{\Sigma(t)} \frac{w(x',y',t)}{\left[(x'-x)^2 + (y'-y)^2\right]^{3/2}} \mathrm{d}x' \mathrm{d}y', \qquad (2.1)$$

where the Σ represents the fractures' trace on the middle fracture plane. The symbols T and σ_o are the normal components of the tractions on the fracture surfaces and the far-field in-situ compressive stress (the confining stress). Rough surfaces are formed during hydraulic fracture propagation in rocks. For this reason when the fracture closes it never does completely. We assume the fracture does not close back below a residual opening w_a. We define this residual opening as the minimum between the maximum opening ever achieved at a given location and a minimum value $w_{\min}$, which can be considered as an empirical 'fracture' material property. This can be expressed by the contact conditions:

$$(w - w_a) \geq 0, \qquad (T - p_f)(w - w_a) = 0. \qquad (2.2)$$

In particular, if the fracture is mechanically open at a given position, the fluid pressure $p_f(x,y)$ is equal to the normal traction $T(x,y)$ on the faces of the fracture.

Fluid flow and mass balance Thin-film lubrication flow occurs inside the deformable fracture. The local fluid volume conservation for a slightly compressible liquid (of compressibility c_f) can thus be expressed as follows (Batchelor, 1967):

$$\frac{\partial w(\boldsymbol{x},t)}{\partial t} + c_f w(\boldsymbol{x},t)\frac{\partial p_f(\boldsymbol{x},t)}{\partial t} + \nabla \cdot \mathbf{q} + v_L - Q_o(\boldsymbol{x},t)\delta(\boldsymbol{x}) = 0, \qquad (2.3)$$

where the fluid flux in the fracture is expressed by (the vector) $\mathbf{q} = w\mathbf{v}^f$ (width times averaged fluid velocity) generally as

$$\mathbf{q} = \mathbf{q}\left(Re(\boldsymbol{x}, t), w(\boldsymbol{x}, t), p(\boldsymbol{x}, t)\right),$$

where Re is the fluid Reynolds number to possibly account for turbulent flow in the fracture (Lecampion and Zia, 2019). The vector $\boldsymbol{x}$ indicates the dependence on the coordinates x and y. Under most practical conditions, fluid flow is laminar in the fracture, such that the width-averaged balance of momentum for the fluid gives the well-known Poiseuille relation

$$\mathbf{q} = -\frac{w(\boldsymbol{x}, t)^3}{\mu'}\left(\boldsymbol{\nabla}p_f(\boldsymbol{x}, t) - \rho_f \boldsymbol{g}\right), \tag{2.4}$$

where $\mu' = 12\mu$, μ is the fluid viscosity, ρ_f is the fluid density and $\boldsymbol{g}$ is the gravitational vector. The fluid volume conservation 2.3 also accounts for the potential leak-off of the fracturing fluid in the surrounding medium. The leak off velocity v_L is

$$v_L = v_L\left(\boldsymbol{x}, t, p(\boldsymbol{x}, t)\right) \tag{2.5}$$

In its simplest form, at early time for normally pressurized porous formation, it can be evaluated using the Carter's leak off approximation:

$$v_L = \frac{2C_L(\boldsymbol{x})}{\sqrt{t - t_0(\boldsymbol{x})}} \tag{2.6}$$

where C_L is the leak-off coefficient and t_0 is the time at which the fracture front reaches the position $\boldsymbol{x}$ (see Lecampion et al. (2018) for a discussion).

Propagation conditions The quasi-static fracture propagation conditions apply at each coordinate γ along the fracture front Γ

$$\begin{cases} V(\gamma)\, G_c(\gamma) \geq 0 \\ \left(G - G_c(\gamma)\right) V(\gamma) = 0 \end{cases} \qquad \forall \gamma \in \Gamma \tag{2.7}$$

where G is the energy release rate, $V(\gamma) = \mathbf{v}(\boldsymbol{x}) \cdot \mathbf{n}(\gamma)$ is the magnitude of the local fracture front velocity and $\mathbf{n}(\gamma)$ is the normal to the front. In the absence of a fluid lag, both the width and the fluid flux normal to the front vanish at the crack front (see Detournay and Peirce (2014) for discussion).

2.2   The algorithm for simulating hydraulic fracture propagation

The efficient and accurate numerical modelling of hydraulic fractures is a challenging task. The reasons can be found in the moving boundary nature of the fracture problem, the non locality of elasticity and the central role played by the coupling between fluid flow in the fracture and elastic deformation in the material. Assuming a "simple" linear elastic brittle

solid and a lubrication-like fluid flow leads to an extremely non-linear coupling between the solid deformation and the fluid flow. The root of this extremely non-linear coupling is the dependence of the hydraulic transmissivity with the cube of the local fracture width (w^3). This strong coupling is also responsible for the multiscale structure of the solution near the fracture front. The classic linear elastic fracture mechanics asymptote describes the solution near the fracture front well, where energy is mainly dissipated in creating new fracture surfaces. On the other hand, a viscous asymptote controls the far field behaviour where the energy entering the system is mainly dissipated in the viscous fluid flow (Desroches et al., 1994). Such a transition from a linear elastic asymptote to a viscous asymptote has been observed experimentally (Bunger and Detournay, 2008). The structure of the solution becomes even more complex if we consider the transient phenomenon of the fluid leaking off from the fracture in the surrounding medium. In this case, an intermediate asymptote can appear as analytically demonstrated by Garagash et al. (2011). To address the final level of added complexity in this discussion, let us consider the case where there is no fluid leak-off. Even for this simpler case, the size of the near tip region where the solution can be described by the classic linear elastic fracture mechanics asymptote evolves in time as the fracture propagates. This region can reduce to a small boundary layer in the case where the energy flux entering the system via the injection is mainly dissipated in the flow of the viscous fluid in the newly created fracture. This represents a real challenge for a numerical model as it implies that the discretization of the near tip region needs to be adapted during the simulation to properly capture the solution to the problem near the fracture front. Because of the moving boundary nature of the fracture problem, capturing the solution near the fracture front is needed to guarantee the overall accuracy of the results.

2.2.1 The Implicit Level Set Algorithm

The Implicit Level Set Algorithm (ILSA) is an efficient and accurate numerical scheme for hydraulic fracture propagation originally developed by Peirce and Detournay (2008) (see also Dontsov and Peirce (2017)). The main idea behind the algorithm is to avoid resolving the multiscale structure of the solution near the fracture front by taking advantage of the known asymptotic solution of a steadily moving hydraulic fracture (Garagash et al., 2011).

In the following, we limit the description of the algorithm to its initial version where the fracture is growing over a fixed Cartesian mesh. The cells that discretize the fracture footprint are divided in three groups: "the survey elements", "tip elements", and the "channel elements" (see Fig. 2.3). The tip elements are the ones partially traversed by the fracture front. The survey elements are located immediately behind the tip elements and are inside the footprint. The channel elements consist of all the cells that discretize the fracture except the tip cells.

The unknowns in the problem are: the fluid pressure, the fracture opening, the fracture front position and the fracture velocity. The fluid pressure and the fracture opening are defined in the fracture footprint for each cell. The fracture velocity is defined locally along the front. The

different fracture front position between two successive time steps characterize it. While going from the time step n to $n+1$, the focus of the algorithm is to converge on the new fracture front position together with the increments of fracture opening and fluid pressure in the fracture domain. The fracture front position is tracked by its closest distances to the centres of the survey elements.

The solution for a time-step is articulated in two distinct steps.

- In the first step, the fracture is supposed to be non propagating and the footprint at the previous time step is considered. The non-linear system of equations is solved for the fluid pressure increment and the fracture opening increment in all of the cells.

- The second step involves the iteration on the front position, and the asymptotic solution of a steadily moving hydraulic fracture (Garagash et al., 2011) comes into play. This solution is used as a relationship between the fracture opening and the distance to the front. For clarity, we divide this step in few substeps.

  - At the beginning of the second step, the asymptotic solution is used along with the new fracture opening at the survey cells to compute the distance to the new trial front position.

  - The distance to the front at the survey cells is then used as initial condition to solve for the (signed) distances in the rest of the grid. The signed distances in the rest of the grid are the values of a level set function. These values are obtained by solving the Eikonal equation (2.39) via a fast marching method.

  - The fracture front is reconstructed using a piece-wise linear approximation within each cell. The new fracture front possibly includes new cells classified as tip cells.

  - Knowing the distance of each tip cell from the new front and integrating the asymptotic solution, it is possible to compute the fluid volume stored in each tip cell. The average fracture opening to be imposed in a given tip cell is then obtained by dividing the fluid volume stored in the tip cell by the cell area.

  - The coupled system of equations (elasticity and lubrication) is then solved again. Unlike in the initial step, the openings at the tip cells are now imposed according to the near-tip asymptote. The new unknowns are the pressure in the tip cells and the opening in the channel elements.

  - A new position of the fracture front can be calculated once the new fracture opening is calculated at the survey elements. Then the procedure repeats until convergence.

- Convergence is reached when subsequent estimates of the level set function at all survey points fall below a given tolerance.
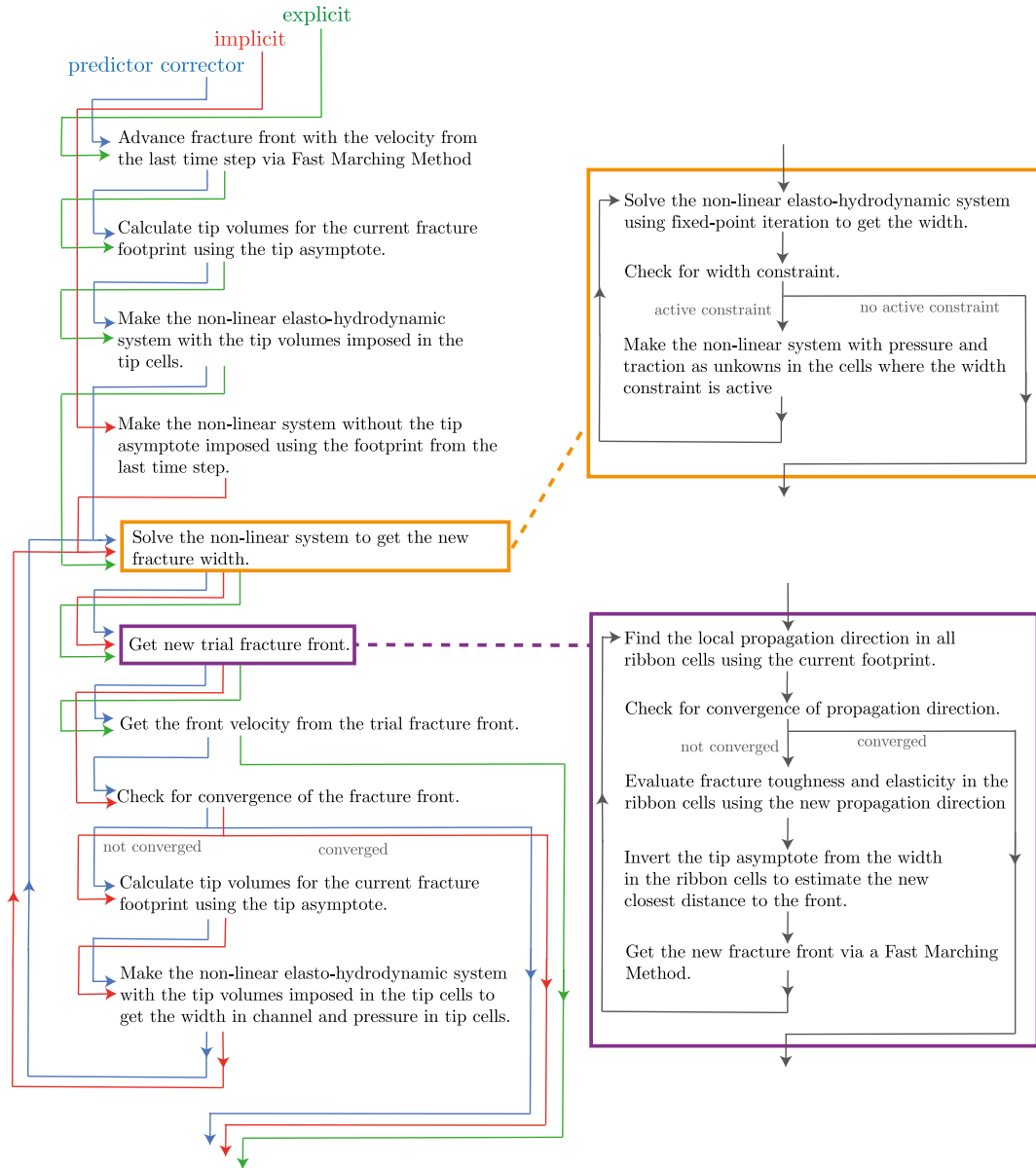
Figure 2.1 – Schematic of the algorithm used by the numerical code PyFrac to advance a time step. Figure reproduced from Zia and Lecampion (2020).

Our implementation of the ILSA algorithm allows for other two strategies to advance the front. These are the "explicit front advancement" and the "predictor-corrector" schemes. The idea behind the explicit front advancement scheme is to avoid the iteration on the front position and use the velocity computed at the end of the previous time-step to advance the fracture. Similarly, the predictor corrector scheme uses the velocity from the previous time step to advance the fracture. However, after the first computation of the front position, this algorithm follows back the implicit scheme. A comparison between the different front advancement

algorithms is shown in Fig. 2.1 - see also Zia and Lecampion (2019).For further details on our numerical solver "PyFrac" the reader is referred to Zia and Lecampion (2020). The code has been released under open source and is available at https:// www.epfl.ch/labs/gel/pyfrac/.

2.3 Numerical discretization of the equations

In this section, we discretize the governing equations in time and space and derive the final system of equations to be solved at each trial position of the fracture front. At each time step t_n, the fracture opening (w) and the net pressure (p) are the main unknowns. In the following, we express a generic quantity ($\cdot$) at time t_n using the following notation $(\cdot)_n \equiv (\cdot)_{t_n}$. Analogously, at time t_{n+1} we assume that $(\cdot)_{n+1} \equiv (\cdot)_{t_{n+1}}$.

Spatial discretization - elasticity

Equation (2.1) is discretized on a Cartesian mesh with rectangular cells of sizes Δx and Δy. Within each cell, the fracture opening is constant.

$$T_{i,j} - \sigma_{0\,i,j} = \sum_{m,n} \mathbf{E}_{i-m,j-n} w_{m,n}(t), \tag{2.8}$$

where

$$\mathbf{E}_{i-l,j-m} = -\frac{E'}{8\pi} \left[\frac{\sqrt{(x_i - x)^2 + (y_j - y)^2}}{(x_i - x)(y_j - y)} \right]_{x=x_l-\Delta x/2,\, y=y_m-\Delta y/2}^{x=x_l+\Delta x/2,\, y=y_m+\Delta y/2}$$

In matrix form, the previous equation writes as:

$$\mathbf{E}\mathbf{w}(\boldsymbol{x}, t) = \mathbf{T}(\boldsymbol{x}, t) - \sigma_0 \tag{2.9}$$

One important property of Eq. (2.1) is that the kernel of the integral equation depends only on the distance between the points (x', y') and (x, y) considered. As a consequence, when this equation is discretized through a Cartesian mesh, the resulting matrix $\mathbf{E}$ is symmetric with a Block Toeplitz structure [1]. Furthermore, the total number of independent matrix entries depends on the *number of unique distances $\mathcal{N}_d$* between the centers of the elements in the Cartesian mesh. An example is presented in Figure 2.2.

---

[1]A Block Toeplitz matrix is made by the repetition of a set of smaller matrices. An example is shown in Fig. 2.2. The letters identify distinct matrix entries while the colours highlight the repeated blocks.
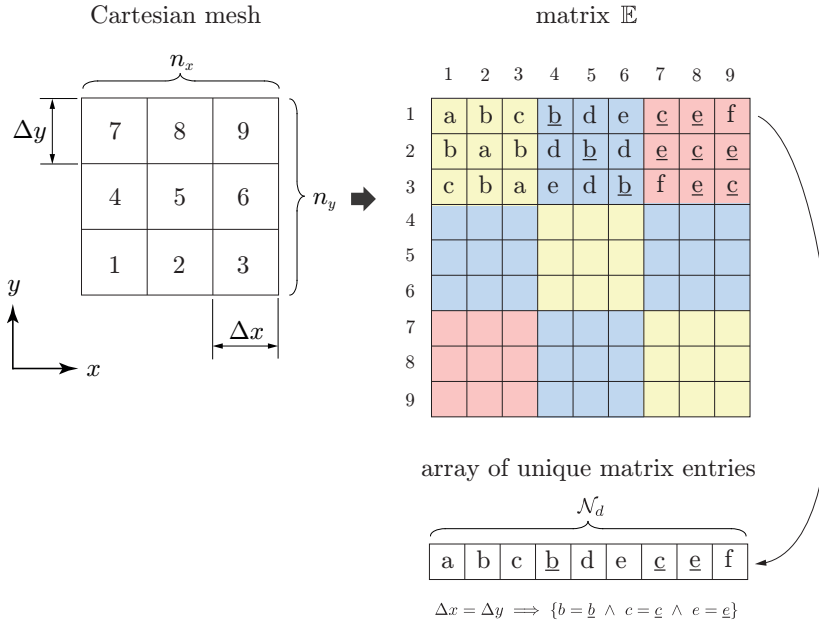
Figure 2.2 – A Cartesian mesh where the elements are numerated form 1 to 9 is shown on the left. On the right, the corresponding matrix $\mathbb{E}$ is displayed.

On the left, a Cartesian mesh discretized with $n_x = n_y = 3$ elements in both the x and y directions is shown. Each element has sizes Δx and Δy and has been numbered from 1 to 9. On the right part of the figure one can see the structure of the corresponding matrix $\mathbb{E}$. Each entry is identified by a letter such that the same numerical value corresponds to the same letter. The empty matrix blocks are supposed to contain the same letters found in the filled block of the corresponding color. The value of $\mathcal{N}_d$ depends both on the choice of n_x, n_y and Δx, Δy as shown in Table 2.1. In general $\mathcal{N}_d = \mathcal{O}\left(n_x n_y\right)$. This represents a particular advantage in case the solution of a system involving Eq. (2.8) is obtained utilizing an iterative scheme where the dot product of $\mathbf{E} \cdot \mathrm{w}$ is necessary for its solution. In fact, instead of memorizing all the $\mathcal{O}\left(n_x^2 n_y^2\right)$ entries it is possible to store only $\mathcal{O}\left(n_x n_y\right)$. Then, when the dot product is needed, it is possible to use a simple mapping to reconstruct one row of $\mathbf{E}$ at a time and compute one vector-vector product. Note that this operation can be executed in parallel. If necessary, a number of copies of the vector of unique entries of $\mathbf{E}$ can be created in the memory of the computer to limit the possibility of simultaneous memory access by different cores.

The elasticity equation (2.9) is valid $\forall t$ such that we can write it at two times t_n and t_{n+1} and subtract the two equations

$$\mathbf{E}\Delta\mathbf{w}(\boldsymbol{x}, t) = \Delta\mathbf{T}(\boldsymbol{x}, t) \tag{2.10}$$

Note that between two time steps the confining stress is assumed to be constant (although it may vary in space).

	$n_x = n_y = n$	$n_x \neq n_y$
$\Delta x = \Delta y$	$\mathcal{N}_d = n^2 - \frac{1}{2} n (n+1)$	$\mathcal{N}_d = n_x n_y - \frac{1}{2} \min(n_x, n_y) \left[\min(n_x, n_y) + 1 \right]$
$\Delta x \neq \Delta y$	$\mathcal{N}_d = n^2$	$\mathcal{N}_d = n_x n_y$

Table 2.1 – *Number of unique distances $\mathcal{N}_d$ between the centers of the elements in a Cartesian mesh as a function of the number of elements in the two directions (n_x and n_y) and the element sizes (Δx and Δy).*

Temporal discretization - fluid flow

We note that in case where the confining stress does not vary in time, we can rewrite Eq. (2.3) in terms of the net pressure p. To avoid confusion, it is sufficient to remember that the fluid pressure is $p_f = p + \sigma_o$. We integrate all the terms in Eq. (2.3) between time t_n and t_{n+1} using a Backward Euler (BE) scheme. Let us recall the application of the BE scheme on a simple ODE like $\frac{df}{dt} = g(t, f(t))$. First we integrate in time, and afterwards we approximate the RHS integral by the right-hand rectangle method as

$$\int_{t_n}^{t_{n+1}} \frac{df}{dt} dt = \int_{t_n}^{t_{n+1}} g(t, f(t)) dt$$

$$f_{n+1} - f_n \approx \left[g(t_{n+1}, f(t_{n+1})) - g(t_n, f(t_n)) \right] (t_{n+1} - t_n)$$

$$f_{n+1} - f_n \approx \left[g(t_{n+1}, f(t_{n+1})) - g(t_n, f(t_n)) \right] \Delta t$$

Now, with regard to equation (2.3) one obtains:

$$(w_{n+1} - w_n) + c_f w_{n+\frac{1}{2}} (p_{n+1} - p_n) - \Delta t \left(\frac{\partial}{\partial x} \left(\frac{w^3}{12\mu} \frac{\partial p_{n+1}}{\partial x} \right) + \frac{\partial}{\partial y} \left(\frac{w^3}{12\mu} \frac{\partial p_{n+1}}{\partial y} \right) \right) +$$

$$+ \Delta t \left(\frac{\partial}{\partial x} \left(\frac{w^3}{12\mu} \rho_f g_x \right) + \frac{\partial}{\partial y} \left(\frac{w^3}{12\mu} \rho_f g_y \right) \right) + \int_{t_n}^{t_{n+1}} \frac{2 C_L(\boldsymbol{x})}{\sqrt{t - t_0(\boldsymbol{x})}} dt - \Delta t Q(\boldsymbol{x}, t) \delta(\boldsymbol{x} - \boldsymbol{x}_i) = 0 \tag{2.11}$$

One can notice that we approximated the integral $\int_{t_n}^{t_{n+1}} c_f w \frac{\partial p}{\partial t} dt \approx c_f w_{n+\frac{1}{2}} (p_{n+1} - p_n)$ where $w_{n+\frac{1}{2}} = \frac{1}{2} (w_{n+1} + w_n)$. The integral left in the equation (2.11) can easily be solved analytically. Finally

$$\Delta w + c_f w_{n+\frac{1}{2}} \Delta p - \Delta t \left(\frac{\partial}{\partial x} \left(\frac{w^3}{12\mu} \frac{\partial p_{n+1}}{\partial x} \right) + \frac{\partial}{\partial y} \left(\frac{w^3}{12\mu} \frac{\partial p_{n+1}}{\partial y} \right) \right) - \Delta t \left(\frac{\partial}{\partial y} \left(\frac{w^3}{12\mu} \rho_f g \right) \right) +$$

$$+ 4 C_L(\boldsymbol{x}) \left(\sqrt{t_{n+1} - t_0(\boldsymbol{x})} - \sqrt{t_n - t_0(\boldsymbol{x})} \right) - \Delta t Q(\boldsymbol{x}, t) \delta(\boldsymbol{x} - \boldsymbol{x}_i) = 0 \tag{2.12}$$

where we expressed $\Delta w = (w_{n+1} - w_n)$, $\Delta p = (p_{n+1} - p_n)$, and we assumed $g_x \equiv 0$ and $g_y \equiv -g$ (gravity acting along the $-y$ direction).

Spatial discretization - fluid flow
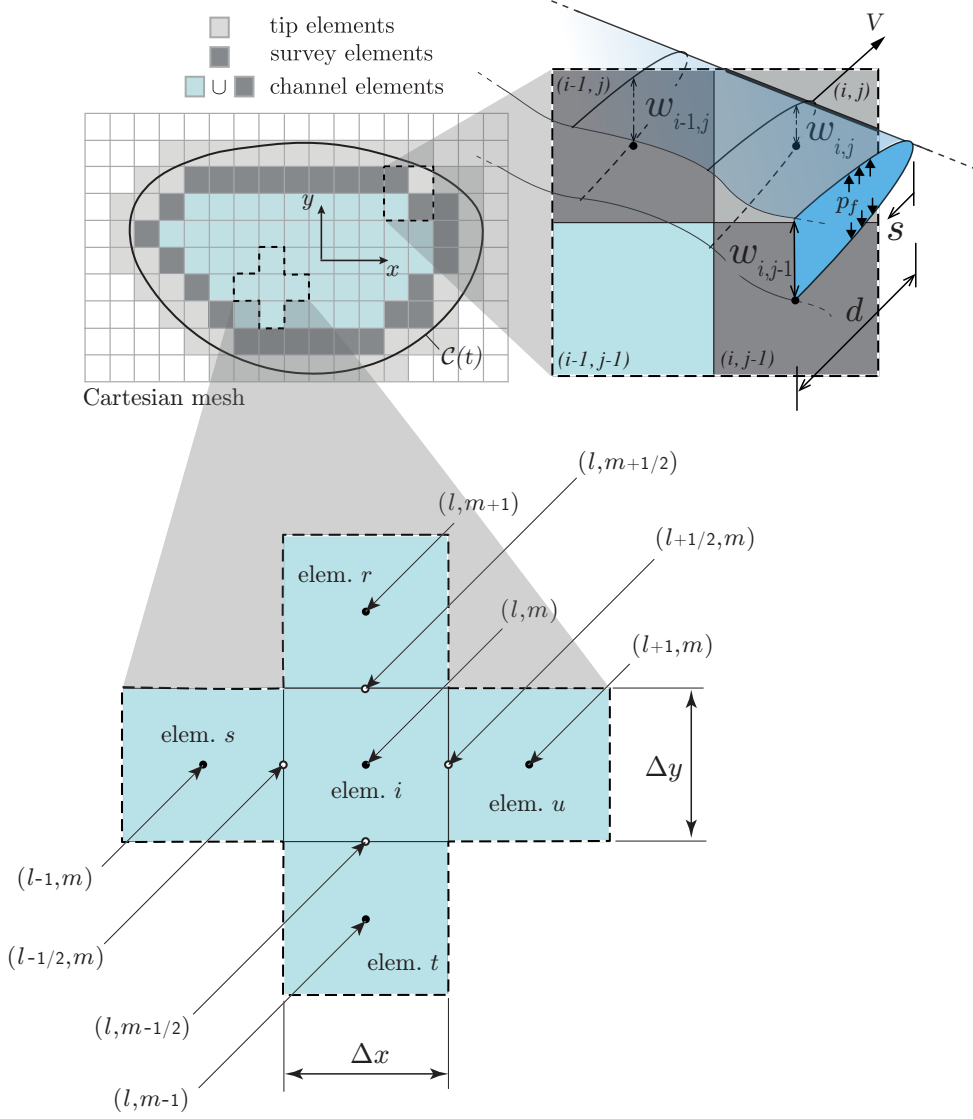
Figure 2.3 – Five point stencil related to the element i located at (l, m) with l and m respectively the column and row numbers in the Cartesian mesh.

We adopt the same spatial discretization for both the equations describing the fluid flow and the elasticity. The fluid pressure p_f is assumed to be constant in each cell (as the fracture opening). The number of cells in the domain at time t_{n+1} is $N_e(t_{n+1})$ and the number of unknowns is $2N_e(t_{n+1})$. The system in equation (2.9) provides a set of $N_e(t_{n+1})$ equations. The remainings are obtained by writing the width averaged mass conservation for each cell in the domain represented by equation (2.12).

The spatial derivatives that are left in equation (2.12) are approximated by a finite difference method. Considering the five point stencil in Fig. 2.3, the term containing the second derivative in space is expressed by

$$
\left(\frac{\partial}{\partial x} \left(\frac{w^3}{12\mu} \frac{\partial p_{n+1}}{\partial x} \right) + \frac{\partial}{\partial y} \left(\frac{w^3}{12\mu} \frac{\partial p_{n+1}}{\partial y} \right) \right) \approx
$$

$$
\approx \frac{1}{12\mu} \frac{1}{\Delta x^2} \left(w^3_{l+1/2,m} p_{l+1,m} - \left(w^3_{l+1/2,m} + w^3_{l-1/2,m} \right) p_{l,m} + w^3_{l-1/2,m} p_{l-1,m} \right)_{t_{n+1}}
$$

$$
+ \frac{1}{12\mu} \frac{1}{\Delta y^2} \left(w^3_{l,m+1/2} p_{l,m+1} - \left(w^3_{l,m+1/2} + w^3_{l,m-1/2} \right) p_{l,m} + w^3_{l,m-1/2} p_{l,m-1} \right)_{t_{n+1}}
$$

and the term containing the first derivative in space results as

$$
\frac{\partial}{\partial y} \left(\frac{w^3}{12\mu} \rho_f g \right) \approx \frac{\rho_f g}{12\mu} \left(w^3_{l,m+1/2} - w^3_{l,m-1/2} \right)_{t_{n+1}}
$$

The final equation, integrated over the cell area $\Delta A_e = \Delta x \Delta y$, is:

$$
\begin{aligned}
&\Delta w + c_f w_{n+\frac{1}{2}} \Delta p + \\
&\frac{-\Delta t}{12\mu\Delta x^2} \left(w^3_{l+1/2,m} p_{l+1,m} - \left(w^3_{l+1/2,m} + w^3_{l-1/2,m} \right) p_{l,m} + w^3_{l-1/2,m} p_{l-1,m} \right)_{t_{n+1}} \\
&\frac{-\Delta t}{12\mu\Delta y^2} \left(w^3_{l,m+1/2} p_{l,m+1} - \left(w^3_{l,m+1/2} + w^3_{l,m-1/2} \right) p_{l,m} + w^3_{l,m-1/2} p_{l,m-1} \right)_{t_{n+1}} + \\
&-\Delta t \frac{\rho_f g}{12\mu} \left(w^3_{l,m+1/2} - w^3_{l,m-1/2} \right)_{t_{n+1}} + 4 C_L(\boldsymbol{x}) \sqrt{t-t_0} \, |^{t_{n+1}}_{t_n} - \Delta t \frac{Q(\boldsymbol{x},t)}{\Delta A_e} \delta(\boldsymbol{x} - \boldsymbol{x}_i) = 0
\end{aligned}
\tag{2.13}
$$

Writing the previous equation for all the cells in the domain leads to the following system:

$$
\begin{aligned}
&\Delta \mathbf{w} + \mathbf{C}_f(\mathbf{w}_{n+1/2}) \Delta \mathbf{p} + \Delta t \, \mathbf{V}(\mathbf{w}_{n+1}) \mathbf{p}_{n+1} + \\
&-\Delta t \, \mathbf{G}(\mathbf{w}_{n+1}) + \mathbf{q}_{\text{out}}(t_{n+1}, t_n) - \Delta t \, \mathbf{q}_{\text{in}}(t_{n+1}) / \Delta A_e = 0
\end{aligned}
\tag{2.14}
$$

where $\mathbf{C}_f$ is the compressibility matrix

$$
\mathbf{C}_{f i,j} = \begin{cases} c_f (w_n + w_{n+1})_i / 2 & \text{if } i = j \\ 0 & \text{if } i \neq j \end{cases} \quad ,
$$

$\mathbf{V}(\mathbf{w}_{n+1})$ is the five point stencil finite difference matrix, where the row associated to element i

in figure 2.3 has been explicitated

$$\mathbf{V} = \begin{bmatrix} \cdots & & & & & & \cdots & & & & \cdots & \\ & & & & & & \vdots & & & & & \\ & & & & & & \vdots & & & & & \\ & & & & & & \vdots & & & & & \\ & & & & & \ddots & \vdots & & & & & \\ 0 & \cdots & 0 & V_{i,t} & 0 & \cdots & 0 & V_{i,s} & V_{i,i} & V_{i,u} & 0 & \cdots & 0 & V_{i,r} & 0 & \cdots & 0 \\ & & & & & & \vdots & \ddots & & & & \\ & & & & & & \vdots & & & & & \\ \cdots & & & & & & \cdots & & & & \cdots & \end{bmatrix}_{t_{n+1}}$$

$$V_{i,i} = \frac{1}{12\mu\Delta x^2}\left(w^3_{l+1/2,m} + w^3_{l-1/2,m}\right)_{t_{n+1}} + \frac{1}{12\mu\Delta y^2}\left(w^3_{l,m+1/2} + w^3_{l,m-1/2}\right)_{t_{n+1}}$$

$$V_{i,r} = -\left(\frac{w^3_{l,m+1/2}}{12\mu\Delta y^2}\right)_{t_{n+1}}$$

$$V_{i,s} = -\left(\frac{w^3_{l-1/2,m}}{12\mu\Delta x^2}\right)_{t_{n+1}}$$

$$V_{i,t} = -\left(\frac{w^3_{l,m-1/2}}{12\mu\Delta y^2}\right)_{t_{n+1}}$$

$$V_{i,u} = -\left(\frac{w^3_{l+1/2,m}}{12\mu\Delta x^2}\right)_{t_{n+1}}$$

Note that the matrix V is symmetric and diagonal. $\mathbf{G}$ is the gravity term vector, and its i-th term is expressed as

$$\mathbf{G}_i = \frac{\rho g}{12\mu\Delta y}(w^3_{l,m+1/2} - w^3_{l,m-1/2})_{t_{n+1}},$$

$\mathbf{q}_{\text{in}}$ and $\mathbf{q}_{\text{out}}$ are vectors containing the injection and leak off terms respectively. It is useful to write the system (2.14) only in terms of increments $\Delta\mathbf{w}$ and $\Delta\mathbf{p}$. The main steps are summarized below.

$$\Delta\mathbf{w} + \mathbf{C}_f\Delta\mathbf{p} + \Delta t\,\mathbf{V}\mathbf{p}_{n+1} - \Delta t\,\mathbf{G} + \mathbf{q}_{\text{out}} - \Delta t\,\mathbf{q}_{\text{in}}/\Delta A_e = 0$$

$$\Delta\mathbf{w} + \mathbf{C}_f\Delta\mathbf{p} + \Delta t\,\mathbf{V}\mathbf{p}_{n+1} - \Delta t\,\mathbf{V}\mathbf{p}_n = -\Delta t\,\mathbf{V}\mathbf{p}_n + \Delta t\,\mathbf{G} - \mathbf{q}_{\text{out}} + \Delta t\,\mathbf{q}_{\text{in}}/\Delta A_e$$

$$\Delta\mathbf{w} + \mathbf{C}_f\Delta\mathbf{p} + \Delta t\,\mathbf{V}\Delta\mathbf{p} = -\Delta t\,\mathbf{V}\mathbf{p}_n + \Delta t\,\mathbf{G} - \mathbf{q}_{\text{out}} + \Delta t\,\mathbf{q}_{\text{in}}/\Delta A_e$$

Finally one obtains:

$$\Delta\mathbf{w} + \left(\Delta t\,\mathbf{V} + \mathbf{C}_f\right)\Delta\mathbf{p} = -\Delta t\,\mathbf{V}\mathbf{p}_n + \Delta t\,\mathbf{G} - \mathbf{q}_{\text{out}} + \Delta t\,\mathbf{q}_{\text{in}}/\Delta A_e \tag{2.15}$$

2.4 Coupling the equations and forming the non-linear system

In the case in which the fracture is open, i.e. there is no contact between the fracture faces, the normal component of the traction vector T on the fracture is assumed to be equal to the fluid pressure p_f. An increment on the fluid pressure Δp_f between two time steps corresponds to an increment on the net pressure Δp, as the confining stress is constant in time. Coupling the elasticity (2.10) and hydrodynamic (2.15) equations results in the following nonlinear system.

$$
\begin{bmatrix} \mathbf{E} & -\mathbf{I} \\ \mathbf{I} & \Delta t\,\mathbf{V} + \mathbf{C}_f \end{bmatrix} \begin{bmatrix} \Delta \mathbf{w} \\ \Delta \mathbf{p} \end{bmatrix} = \begin{bmatrix} 0 \\ \mathbf{f}_L \end{bmatrix} \tag{2.16}
$$

where $\mathbf{L} = \Delta t\,\mathbf{V} + \mathbf{C}_f$ and $\mathbf{f}_L = -\Delta t\,\mathbf{V}\mathbf{p}_n + \Delta t\,\mathbf{G} - \mathbf{q}_{\text{out}} + \Delta t\,\mathbf{q}_{\text{in}}/\Delta A_e$.

The Implicit Level Set Algorithm (Peirce and Detournay, 2008; Dontsov and Peirce, 2017) incorporates near tip asymptote solution in the cells traversed by the fracture front by imposing the average fracture width obtained by integrating the tip asymptote solution. Therefore for this set of cells the unknown is only the fluid pressure. In addition, the scheme implemented in our numerical solver (PyFrac) allows for fracture closure. As previously discussed, we assume that once the fracture opens for the first time, it never closes back below a residual opening w_a. We defined this residual opening as the minimum between the maximum opening ever achieved at a given location and a minimum value $w_{\min}$. Recall that for the cells where this minimum width constraint is active, the traction T and the fluid pressure p_f are not equal, as assumed in Eq. (2.16), and have to be solved separately. To identify the cells where we solve for the fracture opening and the ones where the width has been imposed during the numerical solution, we use:

- the superscript $\mathscr{C}$ to represent the channel cells, i.e. the cells inside the fracture, apart from the tip cells.

- the superscript $\mathscr{A}$ to represents the cells where the width constraint is active.

- the superscript $\mathscr{T}$ represents the tip cells where the fracture opening is imposed.

We can rewrite the system (2.16) making the distinction between these different cell types as:

$$
\begin{bmatrix}
\mathbf{E}^{\mathscr{C}\mathscr{C}} & \mathbf{E}^{\mathscr{C}\mathscr{T}} & \mathbf{E}^{\mathscr{C}\mathscr{A}} & & & \\
\mathbf{E}^{\mathscr{T}\mathscr{C}} & \mathbf{E}^{\mathscr{T}\mathscr{T}} & \mathbf{E}^{\mathscr{T}\mathscr{A}} & & -\mathbf{I} & \\
\mathbf{E}^{\mathscr{A}\mathscr{C}} & \mathbf{E}^{\mathscr{A}\mathscr{T}} & \mathbf{E}^{\mathscr{A}\mathscr{A}} & & & \\
& & & \mathbf{L}^{\mathscr{C}\mathscr{C}} & \mathbf{L}^{\mathscr{C}\mathscr{T}} & \mathbf{L}^{\mathscr{C}\mathscr{A}} \\
& \mathbf{I} & & \mathbf{L}^{\mathscr{T}\mathscr{C}} & \mathbf{L}^{\mathscr{T}\mathscr{T}} & \mathbf{L}^{\mathscr{T}\mathscr{A}} \\
& & & \mathbf{L}^{\mathscr{A}\mathscr{C}} & \mathbf{L}^{\mathscr{A}\mathscr{T}} & \mathbf{L}^{\mathscr{A}\mathscr{A}}
\end{bmatrix}
\begin{bmatrix}
\Delta \mathbf{w}^{\mathscr{C}} \\
\Delta \mathbf{w}^{\mathscr{T}} \\
\Delta \mathbf{w}^{\mathscr{A}} \\
\Delta \mathbf{p}^{\mathscr{C}} \\
\Delta \mathbf{p}^{\mathscr{T}} \\
\Delta \mathbf{p}^{\mathscr{A}}
\end{bmatrix}
=
\begin{bmatrix}
0 \\
0 \\
0 \\
\mathbf{f}_L^{\mathscr{C}} \\
\mathbf{f}_L^{\mathscr{T}} \\
\mathbf{f}_L^{\mathscr{A}}
\end{bmatrix}
\tag{2.17}
$$

where $\Delta \mathbf{w}^{\mathscr{T}} = \mathbf{w}_{n+1}^{\mathscr{T}} - \mathbf{w}_n^{\mathscr{T}}$ and $\mathbf{w}_{n+1}^{\mathscr{T}}$ represents the width in the tip cells evaluated using the tip asymptote. Similarly, $\Delta \mathbf{w}^{\mathscr{A}} = \mathbf{w}_{n+1}^{\mathscr{A}} - \mathbf{w}_n^{\mathscr{A}}$ but $\mathbf{w}_{n+1}^{\mathscr{A}} = \mathbf{w}_n^{\mathscr{A}} \equiv \mathbf{w}_a$ and w_a is the minimum width

corresponding to the asperity of the rock material. Therefore, the value of $\Delta \mathbf{w}^{\mathscr{A}}$ is always zero for an active cell. The system is made of 6 equations and 4 unknowns i.e.: $\Delta \mathbf{w}^{\mathscr{C}}$, $\Delta \mathbf{p}^{\mathscr{T}}$, $\Delta \mathbf{p}^{\mathscr{A}}$ and $\Delta \mathbf{p}^{\mathscr{C}}$. One can express the first row of the matrix as:

$$\mathbf{E}^{\mathscr{C}\mathscr{C}} \Delta \mathbf{w}^{\mathscr{C}} + \mathbf{E}^{\mathscr{C}\mathscr{T}} \Delta \mathbf{w}^{\mathscr{T}} + \mathbf{E}^{\mathscr{C}\mathscr{A}} \Delta \mathbf{w}^{\mathscr{A}} - \Delta \mathbf{p}^{\mathscr{C}} = 0$$

$$\Delta \mathbf{p}^{\mathscr{C}} = \mathbf{E}^{\mathscr{C}\mathscr{C}} \Delta \mathbf{w}^{\mathscr{C}} + \mathbf{E}^{\mathscr{C}\mathscr{T}} \Delta \mathbf{w}^{\mathscr{T}} + \mathbf{E}^{\mathscr{C}\mathscr{A}} \Delta \mathbf{w}^{\mathscr{A}}$$

$$\Delta \mathbf{p}^{\mathscr{C}} = \mathbf{E}^{\mathscr{C}\mathscr{C}} \Delta \mathbf{w}^{\mathscr{C}} + \mathbf{b}^{\mathscr{C}} \tag{2.18}$$

where $\mathbf{b}^{\mathscr{C}} = \mathbf{E}^{\mathscr{C}\mathscr{T}} \Delta \mathbf{w}^{\mathscr{T}} + \mathbf{E}^{\mathscr{C}\mathscr{A}} \Delta \mathbf{w}^{\mathscr{A}}$. One can substitute this equation in the last 3 equations of system (2.17) obtaining:

$$\begin{bmatrix} \mathbf{I} + \mathbf{L}^{\mathscr{C}\mathscr{C}} \mathbf{E}^{\mathscr{C}\mathscr{C}} & \mathbf{L}^{\mathscr{C}\mathscr{T}} & \mathbf{L}^{\mathscr{C}\mathscr{A}} \\ \mathbf{L}^{\mathscr{T}\mathscr{C}} \mathbf{E}^{\mathscr{C}\mathscr{C}} & \mathbf{L}^{\mathscr{T}\mathscr{T}} & \mathbf{L}^{\mathscr{T}\mathscr{A}} \\ \mathbf{L}^{\mathscr{A}\mathscr{C}} \mathbf{E}^{\mathscr{C}\mathscr{C}} & \mathbf{L}^{\mathscr{A}\mathscr{T}} & \mathbf{L}^{\mathscr{A}\mathscr{A}} \end{bmatrix} \begin{bmatrix} \Delta \mathbf{w}^{\mathscr{C}} \\ \Delta \mathbf{p}^{\mathscr{T}} \\ \Delta \mathbf{p}^{\mathscr{A}} \end{bmatrix} = \begin{bmatrix} \mathbf{f}_L^{\mathscr{C}} - \mathbf{L}^{\mathscr{C}\mathscr{C}} \mathbf{b}^{\mathscr{C}} \\ \mathbf{f}_L^{\mathscr{T}} - \mathbf{L}^{\mathscr{T}\mathscr{C}} \mathbf{b}^{\mathscr{C}} \\ \mathbf{f}_L^{\mathscr{A}} - \mathbf{L}^{\mathscr{A}\mathscr{C}} \mathbf{b}^{\mathscr{C}} \end{bmatrix} \tag{2.19}$$

By recalling that $\mathbf{L} = \Delta t \, \mathbf{V} + \mathbf{C}_f$ and that $\mathbf{C}_f$ is strictly diagonal, one can rewrite the previous system as following:

$$\begin{bmatrix} \mathbf{I} + \mathbf{L}^{\mathscr{C}\mathscr{C}} \mathbf{E}^{\mathscr{C}\mathscr{C}} & \Delta t \, \mathbf{V}^{\mathscr{C}\mathscr{T}} & \Delta t \, \mathbf{V}^{\mathscr{C}\mathscr{A}} \\ \Delta t \, \mathbf{V}^{\mathscr{T}\mathscr{C}} \mathbf{E}^{\mathscr{C}\mathscr{C}} & [\Delta t \, \mathbf{V} + \mathbf{C}_f]^{\mathscr{T}\mathscr{T}} & \Delta t \, \mathbf{V}^{\mathscr{T}\mathscr{A}} \\ \Delta t \, \mathbf{V}^{\mathscr{A}\mathscr{C}} \mathbf{E}^{\mathscr{C}\mathscr{C}} & \Delta t \, \mathbf{V}^{\mathscr{A}\mathscr{T}} & [\Delta t \, \mathbf{V} + \mathbf{C}_f]^{\mathscr{A}\mathscr{A}} \end{bmatrix} \begin{bmatrix} \Delta \mathbf{w}^{\mathscr{C}} \\ \Delta \mathbf{p}^{\mathscr{T}} \\ \Delta \mathbf{p}^{\mathscr{A}} \end{bmatrix} =$$
$$= \begin{bmatrix} \mathbf{f}_L^{\mathscr{C}} - \mathbf{L}^{\mathscr{C}\mathscr{C}} \mathbf{b}^{\mathscr{C}} \\ \mathbf{f}_L^{\mathscr{T}} - \Delta \mathbf{w}^{\mathscr{T}} + \Delta t \, \mathbf{V}^{\mathscr{T}\mathscr{C}} \mathbf{b}^{\mathscr{C}} \\ \mathbf{f}_L^{\mathscr{A}} - \Delta \mathbf{w}^{\mathscr{A}} + \Delta t \, \mathbf{V}^{\mathscr{A}\mathscr{C}} \mathbf{b}^{\mathscr{C}} \end{bmatrix} \tag{2.20}$$

$$\begin{bmatrix} \mathbf{I} + \mathbf{L}^{\mathscr{C}\mathscr{C}} \mathbf{E}^{\mathscr{C}\mathscr{C}} & \mathbf{L}^{\mathscr{C}\mathscr{A}} \\ \mathbf{L}^{\mathscr{A}\mathscr{C}} \mathbf{E}^{\mathscr{C}\mathscr{C}} & \mathbf{L}^{\mathscr{A}\mathscr{A}} \end{bmatrix} \begin{bmatrix} \Delta \mathbf{w}^{\mathscr{C}} \\ \Delta \mathbf{p}^{\mathscr{A}} \end{bmatrix} =$$
$$= \begin{bmatrix} \mathbf{f}_L^{\mathscr{C}} - \mathbf{L}^{\mathscr{C}\mathscr{C}} \mathbf{E}^{\mathscr{C}\mathscr{A}} \Delta \mathbf{w}^{\mathscr{A}} \\ \mathbf{f}_L^{\mathscr{A}} - \Delta \mathbf{w}^{\mathscr{A}} + \mathbf{L}^{\mathscr{A}\mathscr{C}} \mathbf{E}^{\mathscr{C}\mathscr{A}} \Delta \mathbf{w}^{\mathscr{A}} \end{bmatrix} \tag{2.21}$$

$$\begin{bmatrix} \mathbf{I} + [\Delta t \, \mathbf{V}(\mathbf{w}_{n+1}) + \mathbf{C}_f]^{\mathscr{C}\mathscr{C}} \mathbf{E}^{\mathscr{C}\mathscr{C}} & \Delta t \, \mathbf{V}(\mathbf{w}_{n+1})^{\mathscr{C}\mathscr{A}} \\ \Delta t \, \mathbf{V}(\mathbf{w}_{n+1})^{\mathscr{A}\mathscr{C}} \mathbf{E}^{\mathscr{C}\mathscr{C}} & [\Delta t \, \mathbf{V}(\mathbf{w}_{n+1}) + \mathbf{C}_f]^{\mathscr{A}\mathscr{A}} \end{bmatrix} \begin{bmatrix} \Delta \mathbf{w}^{\mathscr{C}} \\ \Delta \mathbf{p}^{\mathscr{A}} \end{bmatrix} =$$
$$= \begin{bmatrix} \mathbf{f}_L^{\mathscr{C}} - [\Delta t \, \mathbf{V}(\mathbf{w}_{n+1}) + \mathbf{C}_f]^{\mathscr{C}\mathscr{C}} \mathbf{E}^{\mathscr{C}\mathscr{A}} \Delta \mathbf{w}^{\mathscr{A}} \\ \mathbf{f}_L^{\mathscr{A}} - \Delta \mathbf{w}^{\mathscr{A}} + \Delta t \, \mathbf{V}(\mathbf{w}_{n+1})^{\mathscr{A}\mathscr{C}} \mathbf{E}^{\mathscr{C}\mathscr{A}} \Delta \mathbf{w}^{\mathscr{A}} \end{bmatrix} \tag{2.22}$$

where the right hand side of the system can be explicitly written as:

$$
\begin{bmatrix}
\mathbf{f}_L^{\mathscr{C}} - \mathbf{L}^{\mathscr{CC}}\mathbf{b}^{\mathscr{C}} \\
\mathbf{f}_L^{\mathscr{T}} - \Delta\mathbf{w}^{\mathscr{T}} + \Delta t\, \mathbf{V}^{\mathscr{TC}}\mathbf{b}^{\mathscr{C}} \\
\mathbf{f}_L^{\mathscr{A}} - \Delta\mathbf{w}^{\mathscr{A}} + \Delta t\, \mathbf{V}^{\mathscr{AC}}\mathbf{b}^{\mathscr{C}}
\end{bmatrix}
=
\begin{bmatrix}
+\Delta t\, \mathbf{G}^{\mathscr{C}} - \mathbf{q}_{\text{out}}^{\mathscr{C}} + \Delta t\, \mathbf{q}_{\text{in}}^{\mathscr{C}}/\Delta A_e \\
+\Delta t\, \mathbf{G}^{\mathscr{T}} - \mathbf{q}_{\text{out}}^{\mathscr{T}} + \Delta t\, \mathbf{q}_{\text{in}}^{\mathscr{T}}/\Delta A_e - \Delta\mathbf{w}^{\mathscr{T}} \\
+\Delta t\, \mathbf{G}^{\mathscr{A}} - \mathbf{q}_{\text{out}}^{\mathscr{A}} + \Delta t\, \mathbf{q}_{\text{in}}^{\mathscr{A}}/\Delta A_e - \Delta\mathbf{w}^{\mathscr{A}}
\end{bmatrix}
+
$$

$$
+
\begin{bmatrix}
-\Delta t\, \left[\mathbf{V}\mathbf{p}_n\right]^{\mathscr{C}} - \left[\Delta t\, \mathbf{V} + \mathbf{C}_f\right]^{\mathscr{CC}}\mathbf{b}^{\mathscr{C}} \\
-\Delta t\, \left[\mathbf{V}\mathbf{p}_n\right]^{\mathscr{T}} + \Delta t\, \mathbf{V}^{\mathscr{TC}}\mathbf{E}^{\mathscr{CT}}\Delta\mathbf{w}^{\mathscr{T}} + \Delta t\, \mathbf{V}^{\mathscr{AC}}\mathbf{E}^{\mathscr{CA}}\Delta\mathbf{w}^{\mathscr{A}} \\
-\Delta t\, \left[\mathbf{V}\mathbf{p}_n\right]^{\mathscr{A}} + \Delta t\, \mathbf{V}^{\mathscr{AC}}\mathbf{E}^{\mathscr{CT}}\Delta\mathbf{w}^{\mathscr{T}} + \Delta t\, \mathbf{V}^{\mathscr{AC}}\mathbf{E}^{\mathscr{CA}}\Delta\mathbf{w}^{\mathscr{A}}
\end{bmatrix}
\tag{2.23}
$$

Now we rewrite the last term on the right hand side, in the previous equation in order to express it in function of the pressure at time t_n, rather than the opening increment Δw. The first component can be written as:

$$
-\Delta t\, \left[\mathbf{V}\mathbf{p}_n\right]^{\mathscr{C}} - \left[\Delta t\, \mathbf{V} + \mathbf{C}_f\right]^{\mathscr{CC}} b^{\mathscr{C}} =
$$

$$
-\Delta t\, \mathbf{V}^{\mathscr{CC}}\mathbf{p}_n^{\mathscr{C}} - \Delta t\, \mathbf{V}^{\mathscr{CT}}\mathbf{p}_n^{\mathscr{T}} - \Delta t\, \mathbf{V}^{\mathscr{CA}}\mathbf{p}_n^{\mathscr{A}} +
$$
$$
- \left[\Delta t\, \mathbf{V} + \mathbf{C}_f\right]^{\mathscr{CC}}\mathbf{E}^{\mathscr{CT}}\Delta\mathbf{w}^{\mathscr{T}} - \left[\Delta t\, \mathbf{V} + \mathbf{C}_f\right]^{\mathscr{CC}}\mathbf{E}^{\mathscr{CA}}\Delta\mathbf{w}^{\mathscr{A}} =
$$

$$
-\Delta t\, \mathbf{V}^{\mathscr{CC}}\mathbf{p}_n^{\mathscr{C}} - \Delta t\, \mathbf{V}^{\mathscr{CT}}\mathbf{p}_n^{\mathscr{T}} - \Delta t\, \mathbf{V}^{\mathscr{CA}}\mathbf{p}_n^{\mathscr{A}} +
$$
$$
-\Delta t\, \mathbf{V}^{\mathscr{CC}}\mathbf{E}^{\mathscr{CT}}\Delta\mathbf{w}^{\mathscr{T}} - \mathbf{C}_f^{\mathscr{CC}}\mathbf{E}^{\mathscr{CT}}\Delta\mathbf{w}^{\mathscr{T}} +
$$
$$
-\Delta t\, \mathbf{V}^{\mathscr{CC}}\mathbf{E}^{\mathscr{CA}}\Delta\mathbf{w}^{\mathscr{A}} - \mathbf{C}_f^{\mathscr{CC}}\mathbf{E}^{\mathscr{CA}}\Delta\mathbf{w}^{\mathscr{A}} =
$$

$$
-\Delta t\, \mathbf{V}^{\mathscr{CC}}\mathbf{p}_n^{\mathscr{C}} - \Delta t\, \mathbf{V}^{\mathscr{CT}}\mathbf{p}_n^{\mathscr{T}} - \Delta t\, \mathbf{V}^{\mathscr{CA}}\mathbf{p}_n^{\mathscr{A}} +
$$
$$
-\Delta t\, \mathbf{V}^{\mathscr{CC}}\mathbf{E}^{\mathscr{CT}}\Delta\mathbf{w}^{\mathscr{T}} - \Delta t\, \mathbf{V}^{\mathscr{CC}}\mathbf{E}^{\mathscr{CA}}\Delta\mathbf{w}^{\mathscr{A}} +
$$
$$
-\mathbf{C}_f^{\mathscr{CC}}\left(\mathbf{E}^{\mathscr{CT}}\Delta\mathbf{w}^{\mathscr{T}} + \mathbf{E}^{\mathscr{CA}}\Delta\mathbf{w}^{\mathscr{A}}\right)
$$

we substitute $\mathbf{p}_n^{\mathscr{C}} = \mathbf{E}^{\mathscr{CC}}\mathbf{w}_n^{\mathscr{C}} + \mathbf{E}^{\mathscr{CT}}\mathbf{w}_n^{\mathscr{T}} + \mathbf{E}^{\mathscr{CA}}\mathbf{w}_n^{\mathscr{A}} + \sigma_0^{\mathscr{C}}$ in this last expression, and we obtain:

$$
-\Delta t\, \mathbf{V}^{\mathscr{CC}}\left(\mathbf{E}^{\mathscr{CC}}\mathbf{w}_n^{\mathscr{C}} + \mathbf{E}^{\mathscr{CT}}\mathbf{w}_n^{\mathscr{T}} + \mathbf{E}^{\mathscr{CA}}\mathbf{w}_n^{\mathscr{A}} + \sigma_0^{\mathscr{C}}\right) +
$$
$$
-\Delta t\, \mathbf{V}^{\mathscr{CC}}\mathbf{E}^{\mathscr{CT}}\Delta\mathbf{w}^{\mathscr{T}} - \Delta t\, \mathbf{V}^{\mathscr{CC}}\mathbf{E}^{\mathscr{CA}}\Delta\mathbf{w}^{\mathscr{A}} +
$$
$$
-\Delta t\, \mathbf{V}^{\mathscr{CT}}\mathbf{p}_n^{\mathscr{T}} - \Delta t\, \mathbf{V}^{\mathscr{CA}}\mathbf{p}_n^{\mathscr{A}} +
$$
$$
-\mathbf{C}_f^{\mathscr{CC}}\left(\mathbf{E}^{\mathscr{CT}}\Delta\mathbf{w}^{\mathscr{T}} + \mathbf{E}^{\mathscr{CA}}\Delta\mathbf{w}^{\mathscr{A}}\right).
\tag{2.24}
$$

We can now simplify expression (2.24) by recalling that $\Delta\mathbf{w} = \mathbf{w}_{n+1} - \mathbf{w}_n$:

$$
-\Delta t\, \mathbf{V}^{\mathscr{CC}}\left(\mathbf{E}^{\mathscr{CC}}\mathbf{w}_n^{\mathscr{C}} + \mathbf{E}^{\mathscr{CT}}\mathbf{w}_{n+1}^{\mathscr{T}} + \mathbf{E}^{\mathscr{CA}}\mathbf{w}_{n+1}^{\mathscr{A}} + \sigma_0^{\mathscr{C}}\right) +
$$
$$
-\Delta t\, \mathbf{V}^{\mathscr{CT}}\mathbf{p}_n^{\mathscr{T}} - \Delta t\, \mathbf{V}^{\mathscr{CA}}\mathbf{p}_n^{\mathscr{A}} +
$$
$$
-\mathbf{C}_f^{\mathscr{CC}}\left(\mathbf{E}^{\mathscr{CT}}\Delta\mathbf{w}^{\mathscr{T}} + \mathbf{E}^{\mathscr{CA}}\Delta\mathbf{w}^{\mathscr{A}}\right).
\tag{2.25}
$$

We shorten expression (2.25), by defining $\mathbf{p}'^{\mathcal{C}}_n = \mathbf{E}^{\mathcal{CC}}\mathbf{w}^{\mathcal{C}}_n + \mathbf{E}^{\mathcal{CT}}\mathbf{w}^{\mathcal{T}}_{n+1} + \mathbf{E}^{\mathcal{CA}}\mathbf{w}^{\mathcal{A}}_{n+1} + \sigma^{\mathcal{C}}_0$:

$$
\begin{aligned}
&-\Delta t\, \mathbf{V}^{\mathcal{CC}}\mathbf{p}'^{\mathcal{C}}_n + \\
&-\Delta t\, \mathbf{V}^{\mathcal{CT}}\mathbf{p}^{\mathcal{T}}_n - \Delta t\, \mathbf{V}^{\mathcal{CA}}\mathbf{p}^{\mathcal{A}}_n + \\
&-\boldsymbol{C}^{\mathcal{CC}}_f\left(\mathbf{E}^{\mathcal{CT}}\Delta\mathbf{w}^{\mathcal{T}} + \mathbf{E}^{\mathcal{CA}}\Delta\mathbf{w}^{\mathcal{A}}\right).
\end{aligned}
\tag{2.26}
$$

We note that:

$$
\begin{aligned}
&-\boldsymbol{C}^{\mathcal{CC}}_f\left(\mathbf{E}^{\mathcal{CT}}\Delta\mathbf{w}^{\mathcal{T}} + \mathbf{E}^{\mathcal{CA}}\Delta\mathbf{w}^{\mathcal{A}}\right) = \\
&-\boldsymbol{C}^{\mathcal{CC}}_f\mathbf{p}'^{\mathcal{C}}_n + \boldsymbol{C}^{\mathcal{CC}}_f\left(\mathbf{E}^{\mathcal{CC}}\mathbf{w}^{\mathcal{C}}_n + \mathbf{E}^{\mathcal{CT}}\mathbf{w}^{\mathcal{T}}_n + \mathbf{E}^{\mathcal{CA}}\mathbf{w}^{\mathcal{A}}_n + \sigma^{\mathcal{C}}_0\right),
\end{aligned}
\tag{2.27}
$$

and we substitute this equation in expression (2.26):

$$
\begin{aligned}
&-\Delta t\, \mathbf{V}^{\mathcal{CC}}\mathbf{p}'^{\mathcal{C}}_n - \boldsymbol{C}^{\mathcal{CC}}_f\mathbf{p}'^{\mathcal{C}}_n + \\
&-\Delta t\, \mathbf{V}^{\mathcal{CT}}\mathbf{p}^{\mathcal{T}}_n - \Delta t\, \mathbf{V}^{\mathcal{CA}}\mathbf{p}^{\mathcal{A}}_n + \\
&+\boldsymbol{C}^{\mathcal{CC}}_f\left(\mathbf{E}^{\mathcal{CC}}\mathbf{w}^{\mathcal{C}}_n + \mathbf{E}^{\mathcal{CT}}\mathbf{w}^{\mathcal{T}}_n + \mathbf{E}^{\mathcal{CA}}\mathbf{w}^{\mathcal{A}}_n + \sigma^{\mathcal{C}}_0\right).
\end{aligned}
\tag{2.28}
$$

The expression between brackets in (2.28) coincides with the definition of $\mathbf{p}'^{\mathcal{C}}_n$. After substituting it we obtain the final expression

$$
-\Delta t\left[\Delta t\, \mathbf{V} + \boldsymbol{C}_f\right]^{\mathcal{CC}}\mathbf{p}'^{\mathcal{C}}_n - \Delta t\, \mathbf{V}^{\mathcal{CT}}\mathbf{p}^{\mathcal{T}}_n - \Delta t\, \mathbf{V}^{\mathcal{CA}}\mathbf{p}^{\mathcal{A}}_n + \boldsymbol{C}^{\mathcal{CC}}_f\mathbf{p}^{\mathcal{C}}_n.
\tag{2.29}
$$

The second component of the last term in equation (2.23) can be written as:

$$
-\Delta t\left[\mathbf{V}\mathbf{p}_n\right]^{\mathcal{T}} + \Delta t\, \mathbf{V}^{\mathcal{TC}}\mathbf{E}^{\mathcal{CT}}\Delta\mathbf{w}^{\mathcal{T}} + \Delta t\, \mathbf{V}^{\mathcal{AC}}\mathbf{E}^{\mathcal{CA}}\Delta\mathbf{w}^{\mathcal{A}} =
$$

$$
\begin{aligned}
&-\Delta t\, \mathbf{V}^{\mathcal{TC}}\mathbf{p}^{\mathcal{C}}_n - \Delta t\, \mathbf{V}^{\mathcal{TT}}\mathbf{p}^{\mathcal{T}}_n - \Delta t\, \mathbf{V}^{\mathcal{TA}}\mathbf{p}^{\mathcal{A}}_n + \\
&+\Delta t\, \mathbf{V}^{\mathcal{TC}}\mathbf{E}^{\mathcal{CT}}\Delta\mathbf{w}^{\mathcal{T}} + \Delta t\, \mathbf{V}^{\mathcal{AC}}\mathbf{E}^{\mathcal{CA}}\Delta\mathbf{w}^{\mathcal{A}}.
\end{aligned}
$$

We expand the right hand side of the previous equation by recalling that $\mathbf{p}^{\mathcal{C}}_n = \mathbf{E}^{\mathcal{CC}}\mathbf{w}^{\mathcal{C}}_n + \mathbf{E}^{\mathcal{CT}}\mathbf{w}^{\mathcal{T}}_n + \mathbf{E}^{\mathcal{CA}}\mathbf{w}^{\mathcal{A}}_n + \sigma^{\mathcal{C}}_0$:

$$
\begin{aligned}
&-\Delta t\, \mathbf{V}^{\mathcal{TC}}\left(\mathbf{E}^{\mathcal{CC}}\mathbf{w}^{\mathcal{C}}_n + \mathbf{E}^{\mathcal{CT}}\mathbf{w}^{\mathcal{T}}_n + \mathbf{E}^{\mathcal{CA}}\mathbf{w}^{\mathcal{A}}_n + \sigma^{\mathcal{C}}_0\right) \\
&+\Delta t\, \mathbf{V}^{\mathcal{TC}}\mathbf{E}^{\mathcal{CT}}\Delta\mathbf{w}^{\mathcal{T}} + \Delta t\, \mathbf{V}^{\mathcal{AC}}\mathbf{E}^{\mathcal{CA}}\Delta\mathbf{w}^{\mathcal{A}} + \\
&-\Delta t\, \mathbf{V}^{\mathcal{TT}}\mathbf{p}^{\mathcal{T}}_n - \Delta t\, \mathbf{V}^{\mathcal{TA}}\mathbf{p}^{\mathcal{A}}_n
\end{aligned}
\tag{2.30}
$$

Expression (2.30) can be simplified by considering that $\Delta\mathbf{w} = \mathbf{w}_{n+1} - \mathbf{w}_n$:

$$
\begin{aligned}
&-\Delta t\, \mathbf{V}^{\mathcal{TC}}\left(\mathbf{E}^{\mathcal{CC}}\mathbf{w}^{\mathcal{C}}_n + \mathbf{E}^{\mathcal{CT}}\mathbf{w}^{\mathcal{T}}_{n+1} + \mathbf{E}^{\mathcal{CA}}\mathbf{w}^{\mathcal{A}}_{n+1} + \sigma^{\mathcal{C}}_0\right) \\
&-\Delta t\, \mathbf{V}^{\mathcal{TT}}\mathbf{p}^{\mathcal{T}}_n - \Delta t\, \mathbf{V}^{\mathcal{TA}}\mathbf{p}^{\mathcal{A}}_n.
\end{aligned}
\tag{2.31}
$$

We finally substitute $\mathbf{p}'^{\mathcal{C}}_n = \mathbf{E}^{\mathcal{CC}}\mathbf{w}^{\mathcal{C}}_n + \mathbf{E}^{\mathcal{CT}}\mathbf{w}^{\mathcal{T}}_{n+1} + \mathbf{E}^{\mathcal{CA}}\mathbf{w}^{\mathcal{A}}_{n+1} + \sigma^{\mathcal{C}}_0$ in expression (2.31):

$$
-\Delta t\, \mathbf{V}^{\mathcal{TC}}\mathbf{p}'^{\mathcal{C}}_n - \Delta t\, \mathbf{V}^{\mathcal{TT}}\mathbf{p}^{\mathcal{T}}_n - \Delta t\, \mathbf{V}^{\mathcal{TA}}\mathbf{p}^{\mathcal{A}}_n.
\tag{2.32}
$$

A similar rearrangement can be made on the 3rd component of the last term in equation (2.23)

obtaining:

$$-\Delta t\, \mathbf{V}^{\mathscr{A}\mathscr{C}} \mathbf{p}'^{\mathscr{C}}_n - \Delta t\, \mathbf{V}^{\mathscr{A}\mathscr{T}} \mathbf{p}^{\mathscr{T}}_n - \Delta t\, \mathbf{V}^{\mathscr{A}\mathscr{A}} \mathbf{p}^{\mathscr{A}}_n. \tag{2.33}$$

Finally, by replacing the three expressions (2.29), (2.32) and (2.33) with the respective three entries of the last term in the right hand side of (2.23) we obtain:

$$
\begin{bmatrix}
\mathbf{f}^{\mathscr{C}}_L - \mathbf{L}^{\mathscr{C}\mathscr{C}}\mathbf{b}^{\mathscr{C}} \\
\mathbf{f}^{\mathscr{T}}_L - \Delta\mathbf{w}^{\mathscr{T}} + \Delta t\, \mathbf{V}^{\mathscr{T}\mathscr{C}}\mathbf{b}^{\mathscr{C}} \\
\mathbf{f}^{\mathscr{A}}_L - \Delta\mathbf{w}^{\mathscr{A}} + \Delta t\, \mathbf{V}^{\mathscr{A}\mathscr{C}}\mathbf{b}^{\mathscr{C}}
\end{bmatrix}
=
\begin{bmatrix}
+\Delta t\, \mathbf{G}^{\mathscr{C}} - \mathbf{q}^{\mathscr{C}}_{\text{out}} + \Delta t\, \mathbf{q}^{\mathscr{C}}_{\text{in}}/\Delta A_e \\
+\Delta t\, \mathbf{G}^{\mathscr{T}} - \mathbf{q}^{\mathscr{T}}_{\text{out}} + \Delta t\, \mathbf{q}^{\mathscr{T}}_{\text{in}}/\Delta A_e - \Delta\mathbf{w}^{\mathscr{T}} \\
+\Delta t\, \mathbf{G}^{\mathscr{A}} - \mathbf{q}^{\mathscr{A}}_{\text{out}} + \Delta t\, \mathbf{q}^{\mathscr{A}}_{\text{in}}/\Delta A_e - \Delta\mathbf{w}^{\mathscr{A}}
\end{bmatrix}
+
$$

$$
+
\begin{bmatrix}
-\Delta t\, \left[\Delta t\, \mathbf{V} + \boldsymbol{C}_f\right]^{\mathscr{C}\mathscr{C}} \mathbf{p}'^{\mathscr{C}}_n - \Delta t\, \mathbf{V}^{\mathscr{C}\mathscr{T}}\mathbf{p}^{\mathscr{T}}_n - \Delta t\, \mathbf{V}^{\mathscr{C}\mathscr{A}}\mathbf{p}^{\mathscr{A}}_n + \boldsymbol{C}_f^{\mathscr{C}\mathscr{C}}\mathbf{p}^{\mathscr{C}}_n \\
-\Delta t\, \mathbf{V}^{\mathscr{T}\mathscr{C}}\mathbf{p}'^{\mathscr{C}}_n - \Delta t\, \mathbf{V}^{\mathscr{T}\mathscr{T}}\mathbf{p}^{\mathscr{T}}_n - \Delta t\, \mathbf{V}^{\mathscr{T}\mathscr{A}}\mathbf{p}^{\mathscr{A}}_n \\
-\Delta t\, \mathbf{V}^{\mathscr{A}\mathscr{C}}\mathbf{p}'^{\mathscr{C}}_n - \Delta t\, \mathbf{V}^{\mathscr{A}\mathscr{T}}\mathbf{p}^{\mathscr{T}}_n - \Delta t\, \mathbf{V}^{\mathscr{A}\mathscr{A}}\mathbf{p}^{\mathscr{A}}_n
\end{bmatrix}
\tag{2.34}
$$

2.5 Numerical solution of the non-linear system of equations

We can synthetically write the system of Eq. (2.22) as

$$\mathbf{A}\left(\mathbf{x}^n\right) \cdot \mathbf{x}^n = \mathbf{b}\left(\mathbf{x}^n\right). \tag{2.35}$$

This non-linear system must be solved for each trial position of the fracture front. We solve it using an Anderson Acceleration method of the classical fixed point iteration scheme (Anderson, 1965; Walker and Ni, 2011). This involves the multiple solution of the linearised system of equations

$$\mathbf{A}\left(\mathbf{x}^n_k\right) \cdot \mathbf{x}^n_{k+1} = \mathbf{b}\left(\mathbf{x}^n_k\right). \tag{2.36}$$

This system is non symmetric and non diagonal dominant despite although the elastic operator **E** and the finite difference operator **V** are both positive definite. We solve the linearised system of equations using the iterative method Bi-CGSTAB (van der Vorst, 1992) and a right preconditioning strategy:

$$
\begin{aligned}
\mathbf{A}\mathbf{P}^{-1}\mathbf{z} &= \mathbf{b} \\
\mathbf{x} &= \mathbf{P}^{-1}\mathbf{z}
\end{aligned}
\tag{2.37}
$$

We assume a preconditioner to be an approximate of the matrix of the system

$$\mathbf{P}^{-1} \sim \mathbf{A}^{-1} \tag{2.38}$$

such that its application allows for a proper reduction of the spectral radius of the preconditioned system. To develop a robust preconditioner, we follow the approach originally suggested by Peirce (2006).

- we first compute an approximate elastic operator $\tilde{\mathbf{E}}$. This is done similarly to what proposed by Peirce (2006). For each row of $\tilde{\mathbf{E}}$, we consider only the diagonal values and the off diagonal values which absolute value is above a given percentage of the diagonal

one,

- we then assemble the approximated system of equations $\tilde{\mathbf{A}}$ using the approximated operator $\tilde{\mathbf{E}}$,

- we finally compute the preconditioner $\tilde{\mathbf{P}}$ via an ILUT decomposition of the approximated system $\tilde{\mathbf{A}}$ (dual threshold incomplete LU factorization (Saad, 1994)).

This preconditioner has proven to be particularly efficient and robust, in line with the statistics presented in Peirce (2006).
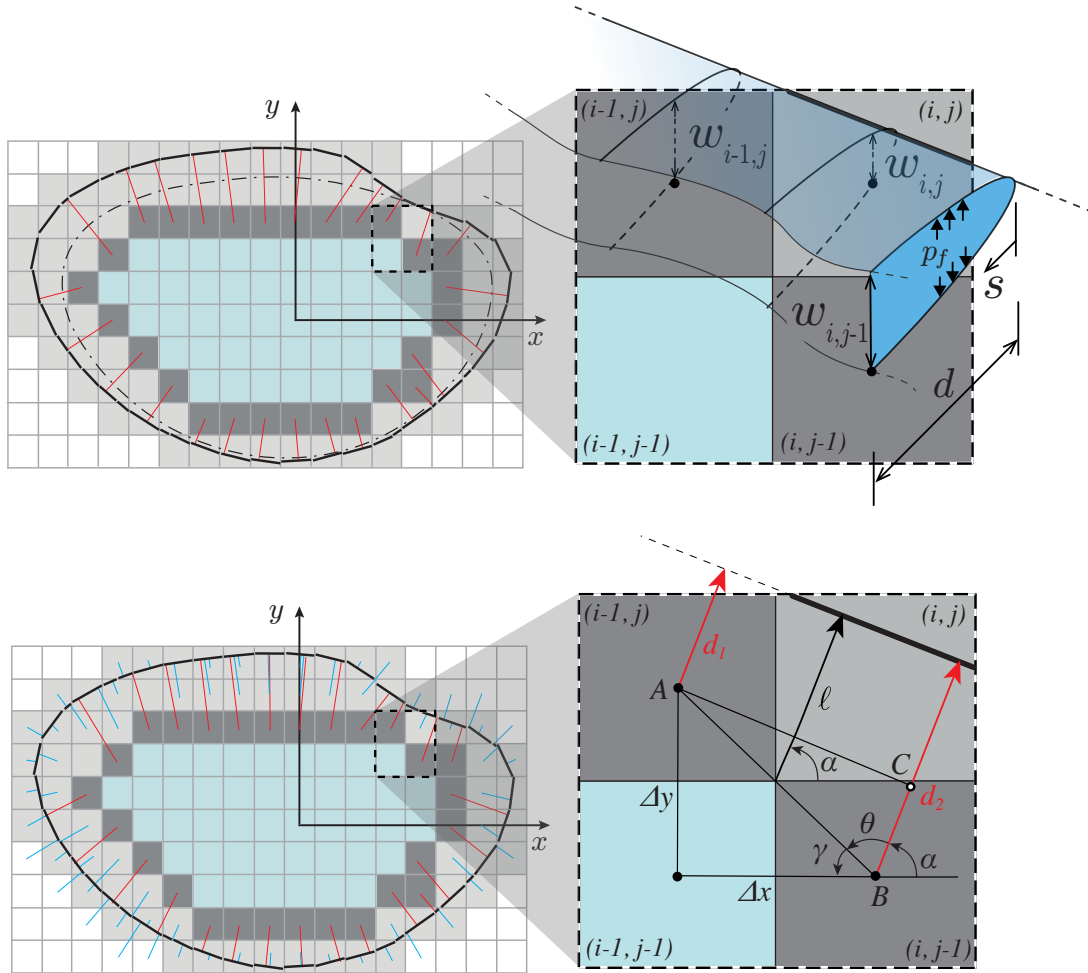
2.6 Front reconstruction

Figure 2.4 – On top, the distance to the fracture front at the survey cells is defined by inverting the asymptotic relation between the fracture opening and the distance to the front. The lower figure represents the geometrical interpretation of the front reconstruction algorithm in Peirce and Detournay (2008).

The signed distances are the values of the level set function. This function is defined as the minimum distance to the fracture front and the sign of this distance carries the information about the location of the point where it is evaluated. The level set is negative when evaluated within the fracture and positive otherwise. The level set can be computed at the center of each cell in the domain by solving the Eikonal equation

$$\left|\nabla d\left(x,y\right)\right| = 1, \tag{2.39}$$

where d is the level set function. The equation is solved by the fast marching method (Sethian, 1999). The boundary conditions for this equation are represented by the values of the level set function at the survey cells. The red segments in the top part of Fig. 2.4 mark these distances. The additional distances computed by solving the Eikonal equation are displayed with blue segments the bottom part of Fig. 2.4. By the expression "font reconstruction", we simply refer to the algorithm that allows the computation of the fracture front position in all the cells of the Cartesian mesh. The fracture front is a straight segment within each cell of the Cartesian mesh. The position of each segment is computed based on the knowledge of the level set around the fracture front. This position is defined locally within each cell by two pieces of information: 1) the angle α of the segment with respect to the horizontal line. 2) the largest distance ℓ to the front from a cell vertex located inside the fracture. The front reconstruction proposed in Peirce and Detournay (2008); Peirce (2015); Dontsov and Peirce (2017) allows one to reconstruct the front independently in each cell traversed by it. As a consequence the front is discontinuous between two neighbouring cells (it is only piece-wise linear). This may be unpleasant to see but it does not cause a problem for the accuracy of the solution. A geometrical interpretation of the front reconstruction algorithm is shown in the bottom part of Fig. 2.4. The angle α for the front located in cell (i, j) is defined by considering the triangle ABC and the two distances d_1 and d_2 in the neighbours cells. The assumption taken by the algorithm is that the vector d_1 is parallel to the vector d_2. The front curvature may be too large, and this assumption is violated. From a mathematical point of view the algorithm proposed in (Peirce and Detournay, 2008; Peirce, 2015; Dontsov and Peirce, 2017) fails when

$$|d_1 - d_2| > \sqrt{\Delta x^2 + \Delta y^2}. \tag{2.40}$$

A large curvature of the fracture front that leads to the failure of this algorithm can be the result of the presence of tough inclusions in the domain. A test case where a hydraulic fracture encounters four inclusions of tough material is displayed in Fig. 2.5. The right panel in subfigure b) shows the overall evolution of the fracture front and the last time step before failure. The details of the reconstructed front approaching the tough heterogeneity are shown in the left panel in subfigure c). For this test case, the simulation fails due to the front reconstruction algorithm when the condition in Eq. 2.6 is satisfied.
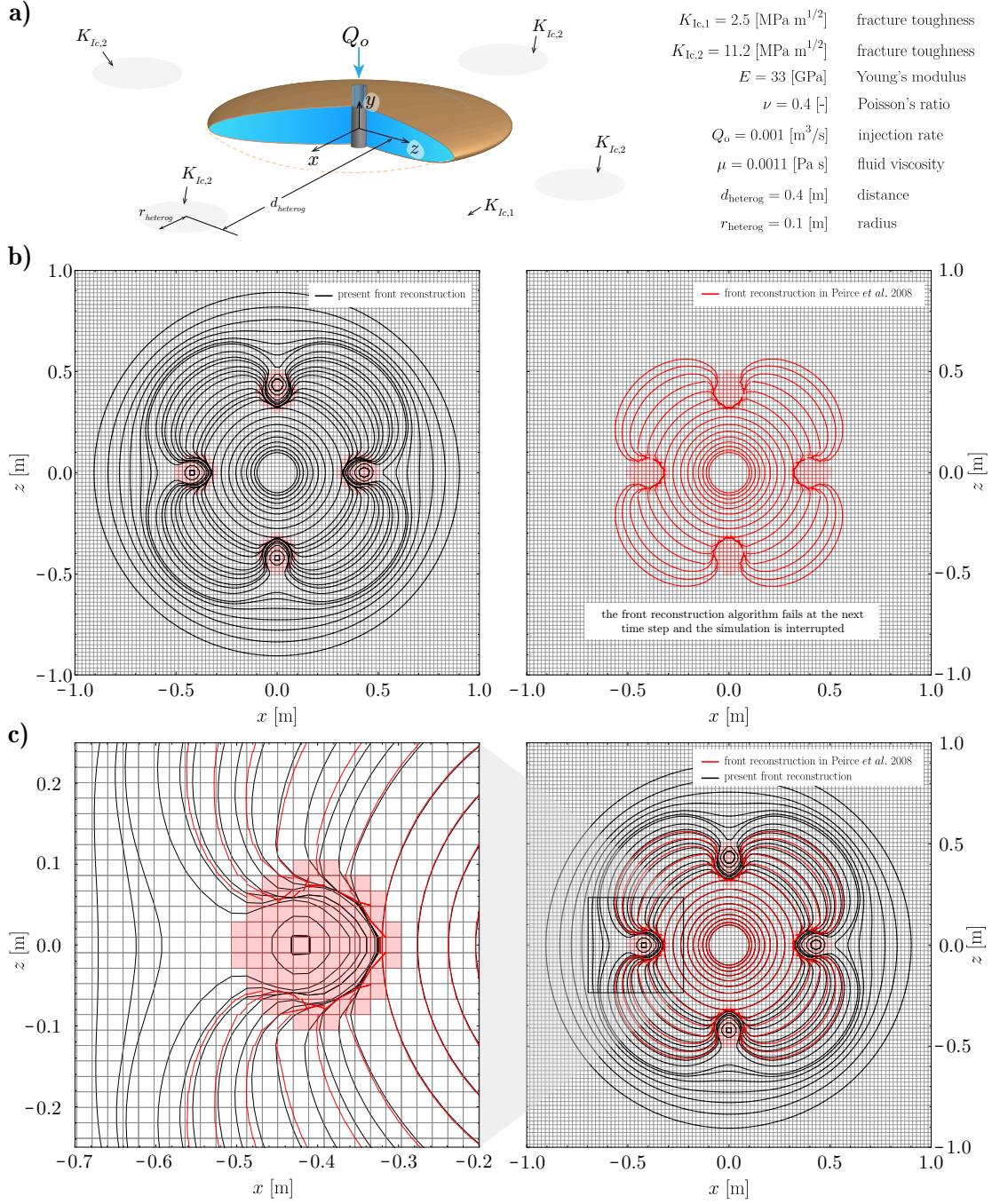
Figure 2.5 – Test case where a hydraulic fracture encounters four inclusions of higher fracture toughness. The front reconstruction algorithm proposed in Peirce and Detournay (2008); Peirce (2015); Dontsov and Peirce (2017) (red line) fails and the simulation ultimately crashes. The new front reconstruction algorithm is represented by the black line, and can simulate the creation of islands of un-broken materials.

In order to address this problem, we propose a new fracture front reconstruction algorithm

that does not fail in case of large front curvature while maintaining the same accuracy of the overall scheme. We can summarise this new algorithm as follows:

- consider a sub-Cartesian mesh obtained by simply joining all the cell centers of the main mesh. We refer to this mesh as "fictitious mesh" and to its cells as "fictitious cells". Both the Cartesian mesh and the "fictitious mesh" (dashed line) are displayed in the cartoon in Fig. 2.6.

- The values of the level set function are known at the cell centers of the elements in the original mesh. These correspond to the four vertexes of each "fictitious cell". Therefore, the level set is also known at the four vertexes of each "fictitious cell". We consider a bilinear interpolation of the level set between the four vertexes.

- The fracture front position is then defined by the curve where the bilinear interpolation assumes a value equal to zero. This is represented by the green curve in Fig. 2.6. We compute the intersections of such curve with the original Cartesian mesh. A trial front is consequently obtained by simply joining all points defined on the original Cartesian mesh.

- In most cases the steps above are just enough to obtain the final front. This means that, we know the two intersections between the front and the cell edges for each element traversed by the fracture front. However, in some cases and for few cells in the fracture, these same steps result in more than two intersections per cell. It is impossible to define a straight front within the cell if there are more than two intersections for a cell traversed by the front. An example is shown in Fig. 2.7. The red points in the figure are produced by the steps above. The solution adopted is to detect these situations and remove one point. In some cases there is more than one choice in deleting the point. The dashed lines in the example in Fig. 2.7 are two possible outcomes of the fracture front. Each of them corresponds to a different removed point. Resolving this ambiguity by removing one of the points does not impact significantly the accuracy of the overall scheme.

In Fig. 2.5, we compare this fracture front reconstruction algorithm with the one proposed in Peirce and Detournay (2008); Peirce (2015); Dontsov and Peirce (2017). Note the capability of the new algorithm to handle both the coalescence ahead of the heterogeneity, and the creation of an "island" of intact material.
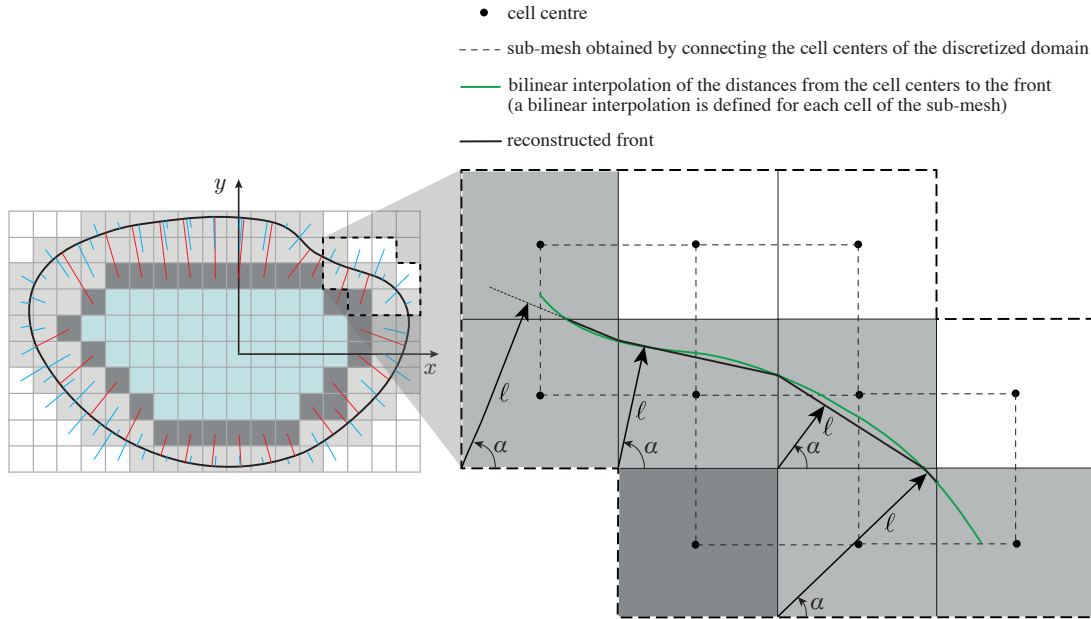
Figure 2.6 – Schematic representation of the new fracture front reconstruction algorithm.
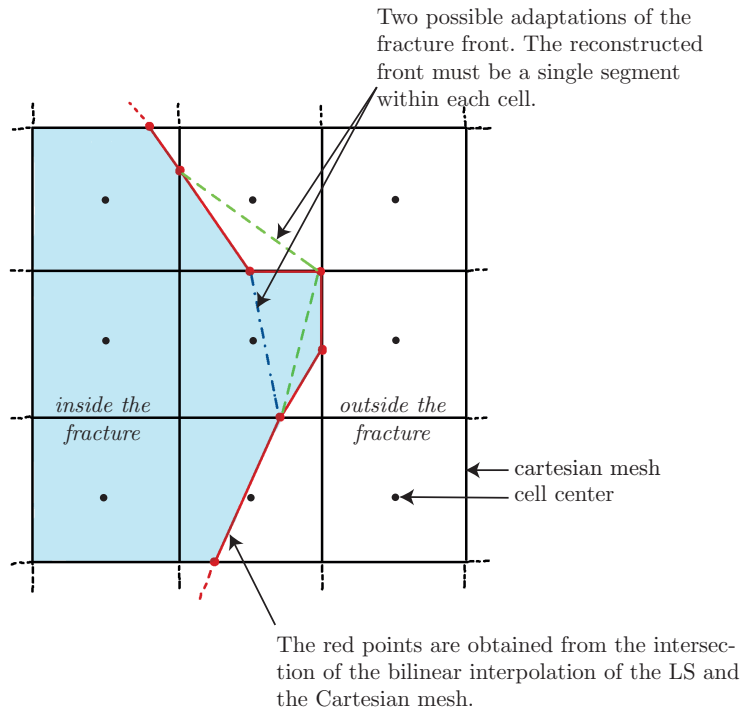
Figure 2.7 – Rare but possible ambiguities arising when using the new fracture front reconstruction algorithm.

2.7 Verification against analytical solution

Rice (1985) derived the first-order expression of the variation of the mode I stress intensity factor (SIF) induced by some small, but otherwise arbitrary, coplanar perturbation of the front of a semi-infinite tensile crack in an infinite body. However, Rice (1985)'s expression is accurate only to first order in the perturbation of the front. This was the motivation for Leblond et al. (2012)'s extension to second order of Rice (1985)'s first-order formula. Vasoya et al. (2013) applied Leblond et al. (2012)'s formula to some geometrically nonlinear analysis of quasistatic, coplanar crack propagation in media having a heterogeneous distribution of fracture toughness. They first extended Leblond et al. (2012)'s formula to the case where the unperturbed SIF, for the straight configuration of the front, depends on the position of this front within the crack plane. Such an extension was required to address the case where the unperturbed SIF becomes independent of the front position.
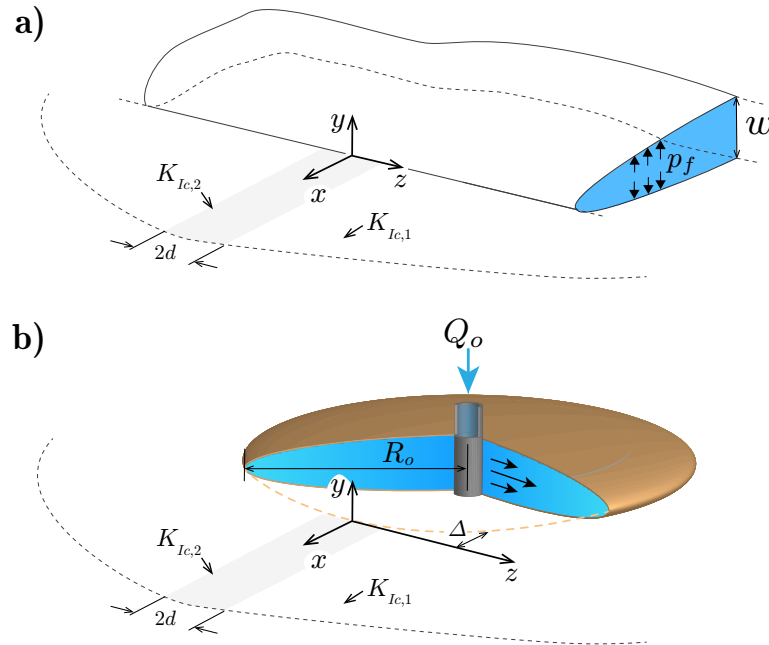
Figure 2.8 – a) Semi-infinite tensile crack in an infinite body. b)Penny shaped tensile crack in an infinite body. In both configurations the fractures are loaded internally by a uniformly pressurised fluid and they approach the same semi- infinite layer of high fracture toughness.

As an application, they have considered the case of a crack penetrating into a single obstacle of infinite length in the direction of propagation. For a given loading, provided that the energy release rate G is equal to G_c at every point of the crack front, the distribution of toughness determines the shape of this front. The equilibrium shape of the front is calculated up to second order in the contrast of toughness between the matrix and the obstacle. By simple superposition, we can relate this configuration to the case where the fracture is loaded internally

by a uniformly pressurised fluid. A geometrical representation of the initial configuration of this application is shown in Fig.2.8-a). Such configuration also corresponds, under certain conditions, to the case of a penny shaped fracture that is loaded by a uniformly pressurized fluid. The main differences between the two problems are:

- the different radius of curvature of the front while approaching the heterogeneity. The initial radius of curvature of the straight front is infinite while it is equal to the fracture radius in the case of a penny shape fracture.

- the geometry of the two problems is different, as one fracture is semi infinite while the other is finite.

However, when radius of curvature of the fracture R_o is much bigger than the finite size of the obstacle, $2d$, the equilibrium shape of the two problems should coincide in vicinity of the front. We investigated this possibility by means of numerical simulations. We start by adopting a fixed toughness contrast $\epsilon = 0.75$

$$\epsilon = \frac{K_{\text{Ic-2}}^2 - K_{\text{Ic-1}}^2}{K_{\text{Ic-1}}^2}, \tag{2.41}$$

where $K_{\text{Ic-2}}^2$ is the fracture toughness in the obstacle. We varied the ratio between the fracture radius R_o and the size of the obstacle $2d$ assuming $R_o/d = 27.5$, 34.6 and 48.4. We also decided to adopt different discretizations, resulting in a different number of cells in the obstacle. In particular, for the case $R_o/d = 27.5$ we used 13 cells, for $R_o/d = 34.6$ we used 7 cells and for $R_o/d = 48.4$ we used 3 cells. The superposition between the analytical solution $\Phi(z)$ and the numerical one in the top part of Fig. 2.9 shows a good agreement. Although the analytical and the numerical solutions are expected to be alike for the case $R_o/d = 48.4$, the lower number of cells in the discretization causes a larger difference between the analytical and the numerical predictions when compared to the case $R_o/d = 27.5$. The relative difference between the analytical and the numerical solutions shown in the bottom part of Fig. 2.9 confirms this point. In this plot we also compare the relative difference Δ between the initial radial and straight fronts. We find that the relative difference between the numerical and the analytical solutions far from the center scale as Δ/d. This is not the case when we use a finest discretization. This can be explained by the fact that the analytical solution we are comparing is only "second order accurate". Larger toughness contrasts between the obstacle and the surrounding medium imply larger deformations of the fracture front.
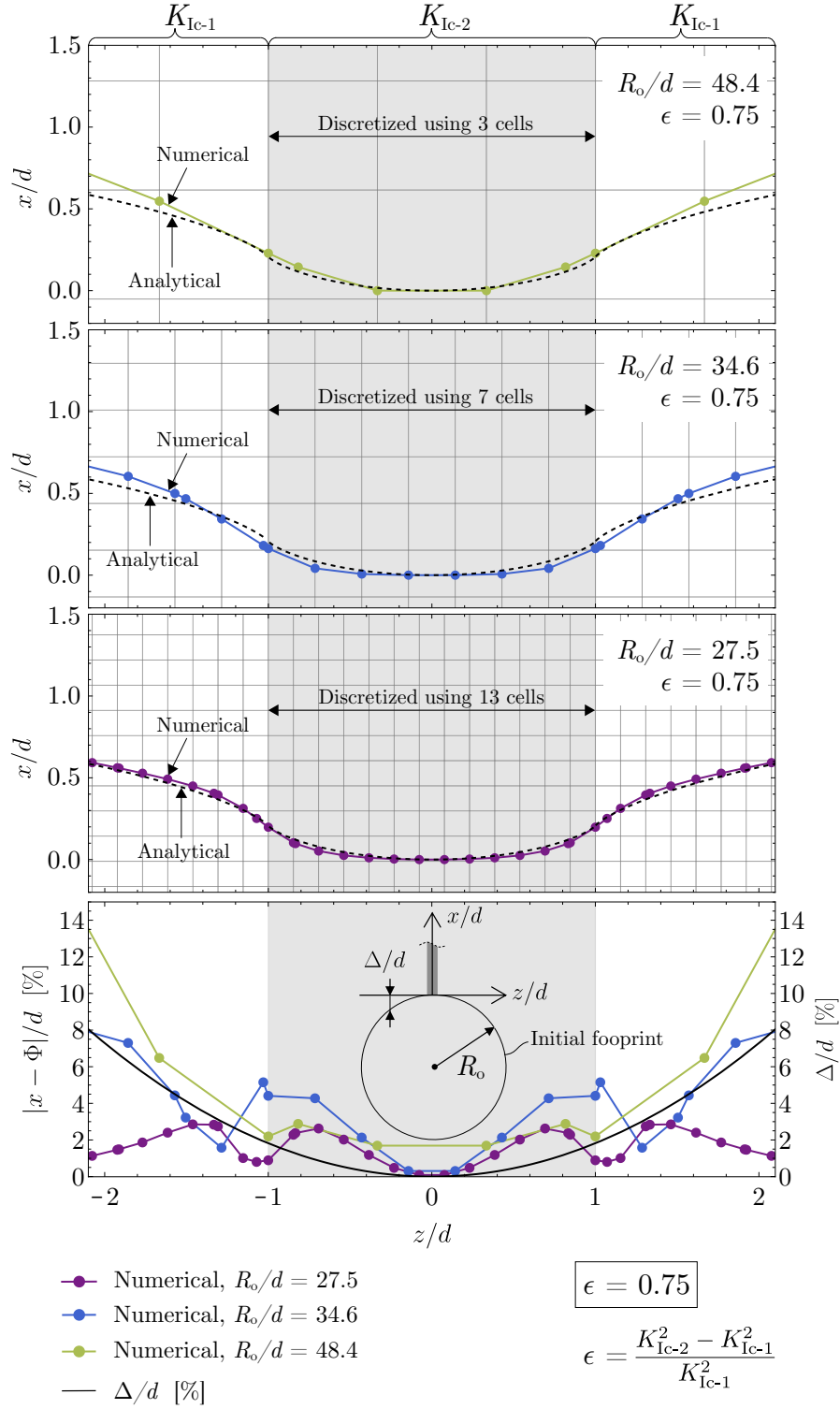
Figure 2.9 – Comparison between the analytical and numerical front configurations for two fractures propagating over a semi infinite obstacle of higher fracture toughness. We vary both, the number of cells in the obstacle and the ratio R_o/d between the initial radius R_o and the size of the obstacle $2d$.

Finally we considered the case with $R_o/d = 27.5$ and a fixed number of cells in the obstacle to study the variability of the results when varying the toughness contrast $\epsilon = 0.75$. Particularly, we considered $\epsilon = 0.25$, 0.5, 0.75, and 1.25. We find that the larger the toughness contrast the more the relative difference between the two solutions increases (see Fig. 2.10).
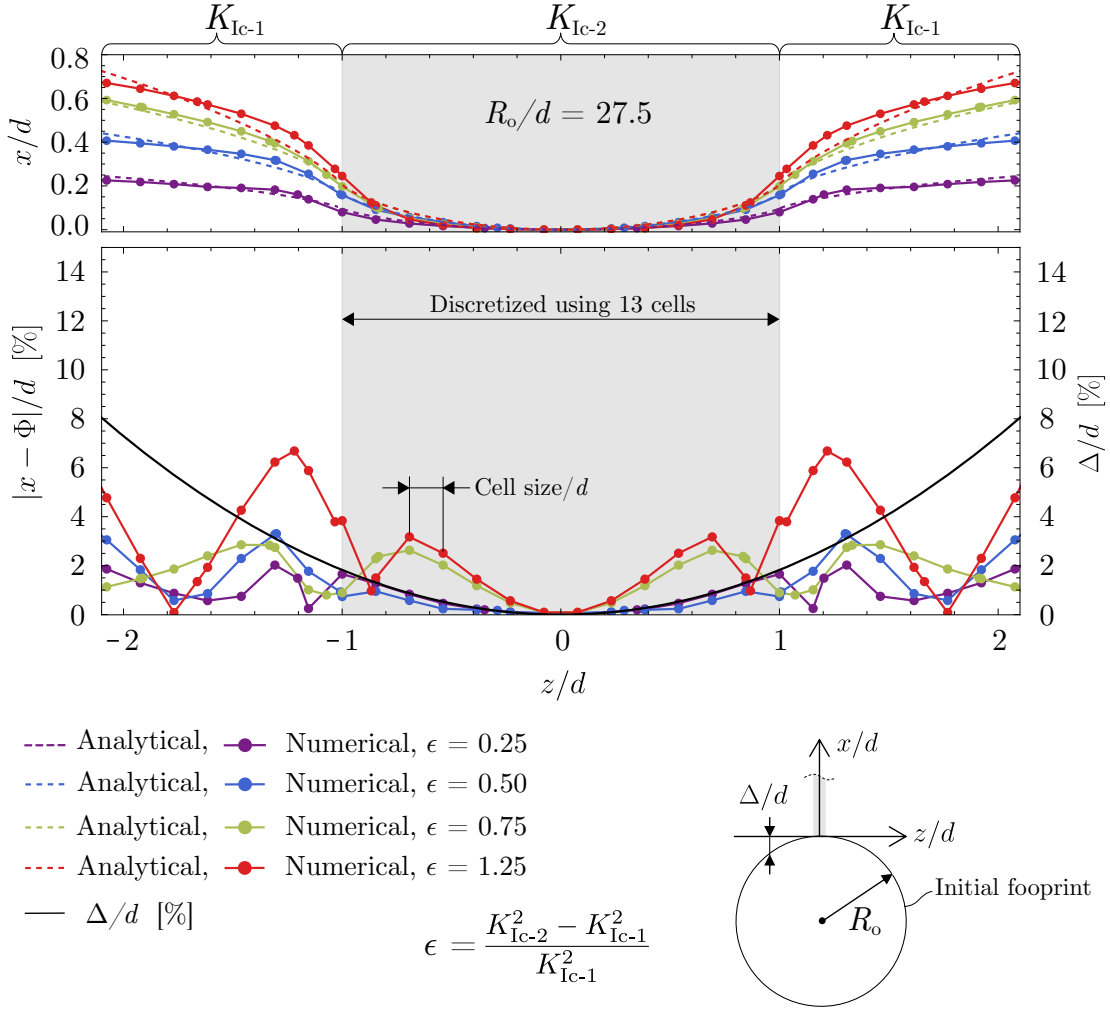
Figure 2.10 – Comparison between the analytical and numerical front configurations for two fractures propagating over a semi infinite obstacle of higher fracture toughness. We vary only the toughness contrast ϵ between the obstacle and the surrounding medium. We assume the same number of cells in the obstacle and the ratio R_o/d between the initial radius R_o and the size of the obstacle $2d$.

2.8 Conclusions

We have demonstrated that the current front reconstruction scheme adopted by the Implicit Level Set Algorithm (Peirce and Detournay, 2008; Peirce, 2015; Dontsov and Peirce, 2017) fails in some cases of large and localised fracture front curvatures. We have presented an improved

algorithm to reconstruct the fracture front that is capable of handling large curvature, such as those caused when tough heterogeneities pin the fracture front. We tested the algorithm against the analytical solution of a semi infinite fracture penetrating a single tough obstacle of infinite length in the direction of propagation. The next Chapter, will compare the new front reconstruction and the overall scheme to existing laboratory experiments.

3 Comparisons against experiments

Disclaimer and acknowledgements: The ideas and work presented in this chapter are original and represent my contributions, except for the comparison with the stress jump experiment. This comparison was made jointly with Dr B. Fryer.

Note: The last part of this chapter is currently being adapted into a scientific publication:
C. Peruzzo, B. Lecampion, "*Interaction and coplanar coalescence of two hydraulic fractures*", to be submitted to Int J. Eng. Sci., 2023
The comparison with the stress jump experiment shown in the first part of this chapter will be adapted into a scientific publication:
C. Peruzzo, B. Fryer, B. Lecampion, "*Conditions for hydraulic fracture height-growth arrest by a bi-lateral stress jump*", in prep., 2023

3.1 Introduction

Our numerical code Pyfrac has previously been benchmarked by Zia and Lecampion (2020) against analytical solutions for both radial and fully contained fractures that are either fully viscosity or fully toughness dominated. It was additionally validated by Zia and Lecampion (2019) against the experimental results of Wu et al. (2008) for the case of a hydraulic fracture encountering an asymmetrical stress jump. Here, however, further validation will be provided against the following experiments:

- the experimental results of Garagash et al. (2009); Jeffrey and Bunger (2009) for the case of a viscosity-dominated fracture encountering a symmetrical bi-lateral stress jump, equivalent in form the problem presented in Fig 3.1.

- the experimental results of O'Keeffe et al. (2018a); O'Keeffe (2019) for the case of a single penny shaped fracture propagating mostly in the toughness dominated regime.

- the experimental results of O'Keeffe et al. (2018b); O'Keeffe (2019) for the case of a two coplanar penny shaped fractures propagating in the toughness dominated regime.

3.2 Stress jump experiment

The experiment "scon7" of Jeffrey and Bunger (2009) is the same experiment as the "positive stress jump" experiment presented by Garagash et al. (2009). Therefore, the experiment will be referred to as "scon7" when discussing the results of both papers. This experiment was also modelled in Peirce (2015).

3.2.1 setup

The experiment is carried in polymethylmethacrylate (PMMA). The idea was to create step-like stress changes on an interface between two blocks, injecting a viscous fluid in the interface and propagating a hydraulic fracture. A conceptual scheme of the experimental setup is presented in Fig. 3.1. To produce the designed stress variations along the interface between the two PMMA blocks one surface of one block is machined with a prescribed profile. When the two, equally sized, PMMA blocks are pressed against each other the interface contact stress presents the required stress variation. No material bond is created between the two blocks, so the fracture toughness during the propagation is zero. A mixture of water, glucose and food dye is injected via a computer-controlled positive displacement pump. During the experiment different physical quantities were measured:

- The fracture opening was obtained from the video images by analyzing the decrease in light intensity associated with light passing through the fracturing fluid.

- The video images were also used to measure the evolution of the main fracture dimensions.

- The fluid pressure at the fracture inlet was measured via a pressure transducer.

- A local fracture opening measurement was made via a pair of linear variable differential transceivers (LVDTs). The position of this point with regard to the footprint is marked by the point "A" in Fig. 3.1-a).

For further details refer to Jeffrey and Bunger (2009).

3.2.2 Discussion of the results

The experiment scon7 was repeated in Pyfrac with, $Q_o = 1.7 \times 10^{-9} \mathrm{m}^3/s$, $\mu = 30.2$Pa s, and $\Delta\sigma = 4.3$MPa, $H = 25$mm, $K1C = 0$Pa$\sqrt{\mathrm{m}}$ $E' = 3.93$GPa. The simulation was performed twice with two different grid resolutions, once with 75 square vertical elements in the reservoir and

once with 25 square vertical elements. The results are presented in Fig. 3.1. The different discretizations used do not lead to a significant difference in the numerical results. The largest difference is probably appreciated when comparing the numerical and the experimental footprints at two different time steps (see Fig. 3.1-a)). The different comparisons of the numerical fracture opening across the stress jump presented in Fig. 3.1-c) do not show significant differences with the experimental observations. The experimental points around $X = -20$ mm that drop to zero do not have to be considered. In Fig 3.1-d) we present the comparison of the evolution of the fracture opening measured at point "A" via LVDTs and the evolution of the fluid pressure at the fracture inlet. Except for an initial period at the beginning of the experiment, the numerical results match the experimental data. The evolution of the half fracture length L shown in Fig. 3.1-d) presents a larger difference. This is caused by the fact that we assumed a constant injection rate for the whole duration of the simulation. Another variable of interest is the breakthrough distance λ. It is defined as the maximum penetration of the fracture front measured from the interface. The comparison between the numerical predictions match the experimental observations (see Fig. 3.1-e))
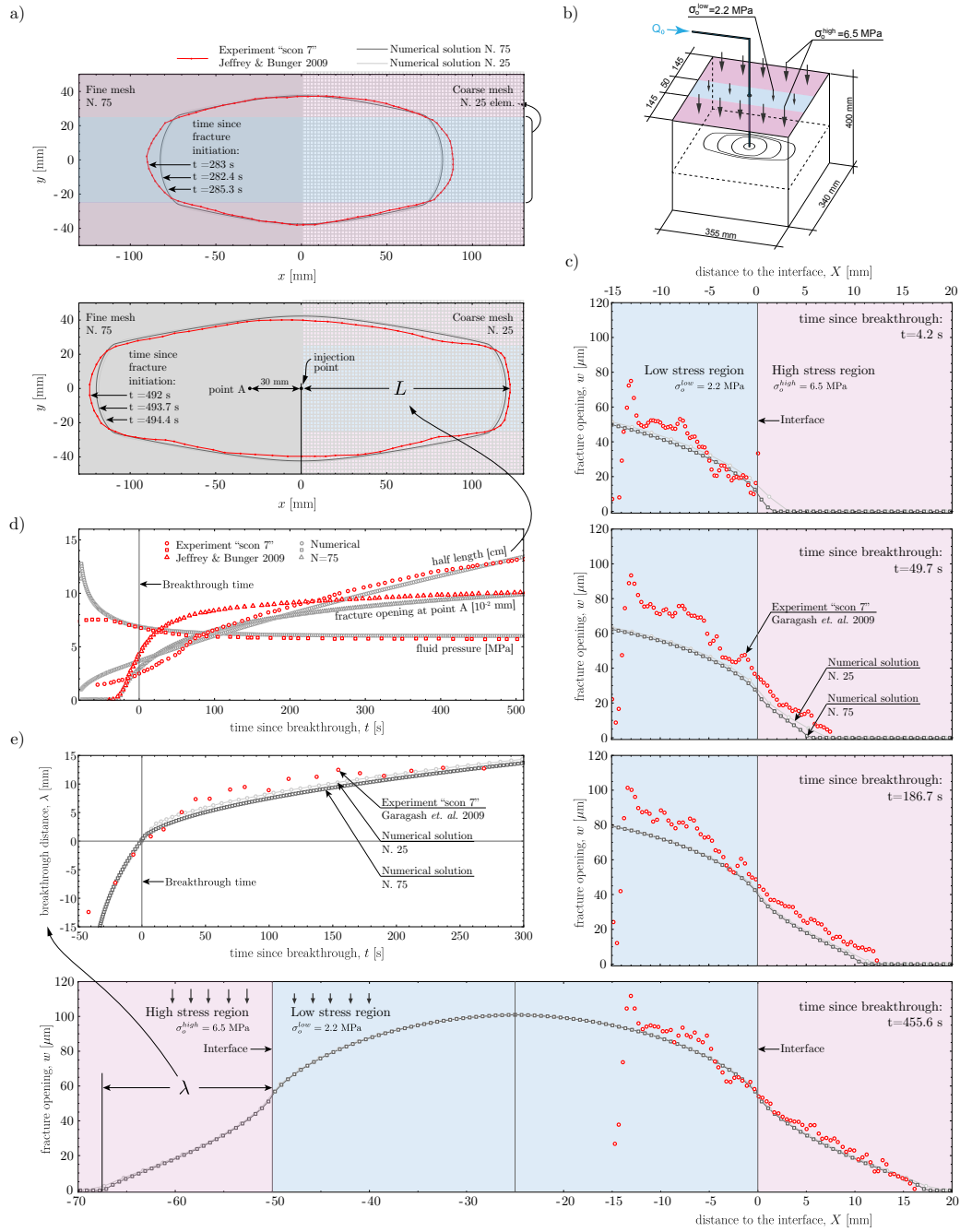
Figure 3.1 – Numerical versus experimental observations for the "stress jump" experiment. a) A comparison of the numerical fracture footprint against scon7 for a fine and coarse mesh at two different times. b) An overview of the experimental setup with the low and high stress regions shown in blue and pink, respectively. c) A comparison of the scon7 and numerical fracture openings at four different times for two different mesh resolutions. d) A comparison of the scon7 and numerical half lengths, fluid pressures, and fracture opening for a fine and coarse mesh. e) A comparison of the breakthrough distance for scon7 and the fine and coarse numerical mesh resolutions.

3.3 Single, radial, toughness dominated experiments

3.3.1 setup

A set of 18 experiments is carried out in a block of hydrogel. The setup of the experiments is shown in Fig. 3.2. The hydrogel block is closed on 5 sides and open on one side. The injection is performed by using a displacement syringe pump. To promote the planarity of the hydraulic fracture 4 plates of 1 mm thickness are inserted between the hydrogel and the mould where it was casted (see Fig. 3.2). The light attenuation measurement technique is used to obtain the fracture opening profile for each experiment. For further details refer to O'Keeffe et al. (2018a); O'Keeffe (2019). The numerical values of the experimental parameters used in the simulations are reported in Table 3.1. The accuracy related to the experimental derivation of these parametes is about 10%. All the experiments can be considered mostly toughness dominated.
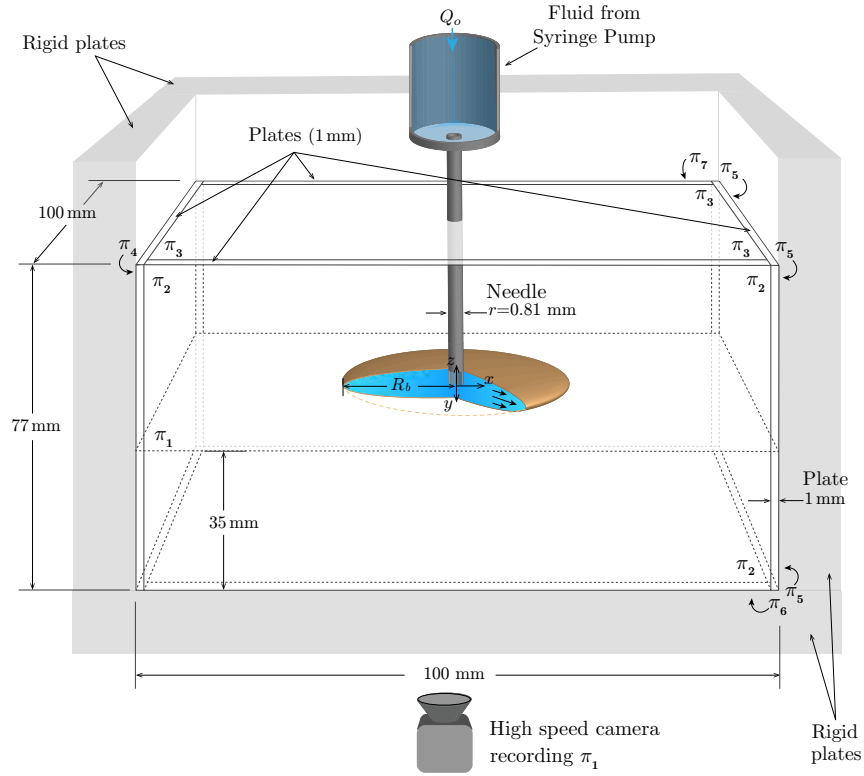
Figure 3.2 – Experimental setup used for the single fracture experiment.

exp. ID	E' [kPa]	μ [Pa s]	Q_o [mL/min]	K_{Ic} $\left[\text{kPa}\sqrt{\text{m}}\right]$
1	165	0.1	15	1.205
2	129	0.1	20	1.202
3	209	0.28	20	1.474
4	200	0.08	35	1.497
5	207	0.08	10	1.221
6	129	0.08	10	1.202
7	207	0.001	15	1.221
8	85	0.08	15	0.903
9	347	0.08	15	2.738
10	209	0.08	15	1.474
11	427	1	2	1.753
12	213	1	2	1.238
13	213	1.2	10	1.238
14	209	1.13	20	1.474
15	425	1.13	23	1.749
16	489	1.13	23	1.876
17	415	3.4	23	1.729
18	489	10	20	1.876

Table 3.1 – Parameters used in the numerical simulations of the single hydraulic fracture experiments.

3.3.2 Discussion of the results

The time evolution of the fracture radius for the 18 experiments is shown in Fig. 3.3 and numerical predictions generally captured it. In most cases the discrepancies are related to the time of fracture initiation. A close look at the Fig. 3.3 reveals that in the experiments n. 4, 5, 7, 9 and 16 the evolution of the fracture radius departs from the trend shown by the numerical solution. This can be understood because the numerical simulations do not account for the boundary effect. Additionally the fracture footprint in the experiment tends to drift its center away from the injection point reinforcing the boundary effect. In Fig. 3.4 we compare the opening profile near the fracture front to the analytical solution of a toughness dominated radial fracture. The results are related to the experiment n. 10. In the same figure we also present the comparison with the numerical solution (red curve). The mismatch between the numerical and analytical solutions is caused by the coarse numerical discretization we used. Finally, in Fig.3.5 we present a successful comparison between the numerical and the experimental fracture opening profiles for the experiment n. 18. In this rare case the numerical fracture radius (black line) matches almost perfectly the experimental one for the same time (see the bottom part of Fig. 3.5). It is important to note the "rigid body motion" of the experimental footprint. This implies that the fracture center moves away from the initial injection point.
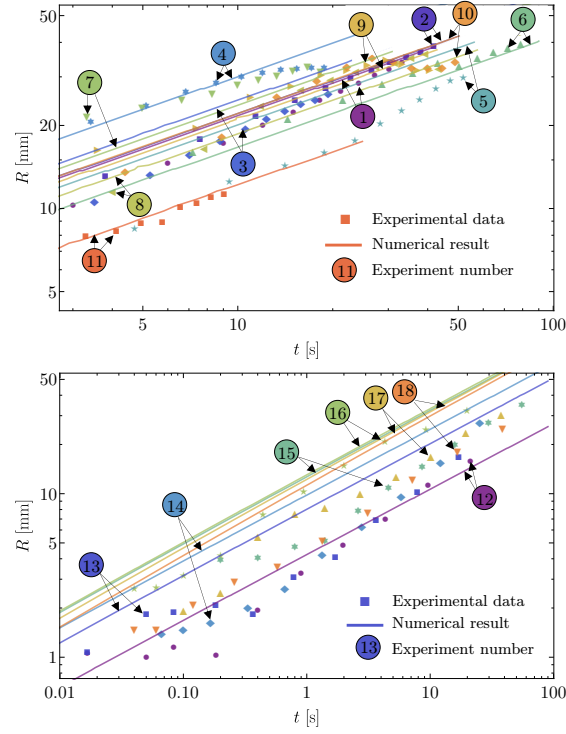
Figure 3.3 – Numerical versus experimental evolution of the fracture radius for 18 different single-fracture experiments.
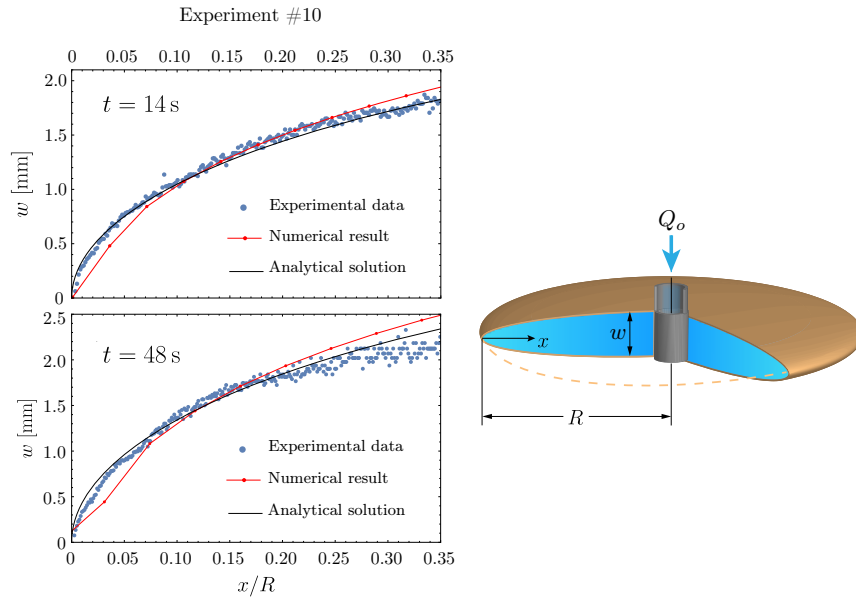
Figure 3.4 – Numerical, analytical and experimental comparison of the opening profile around the fracture front for at two times in Experiment n. 10 (single-fracture experiments).

Experiment #8

$t = 39.4$ [s]

Simulation

$t = 39.4$ [s]

10 mm

Footprint from
numerical
simulation
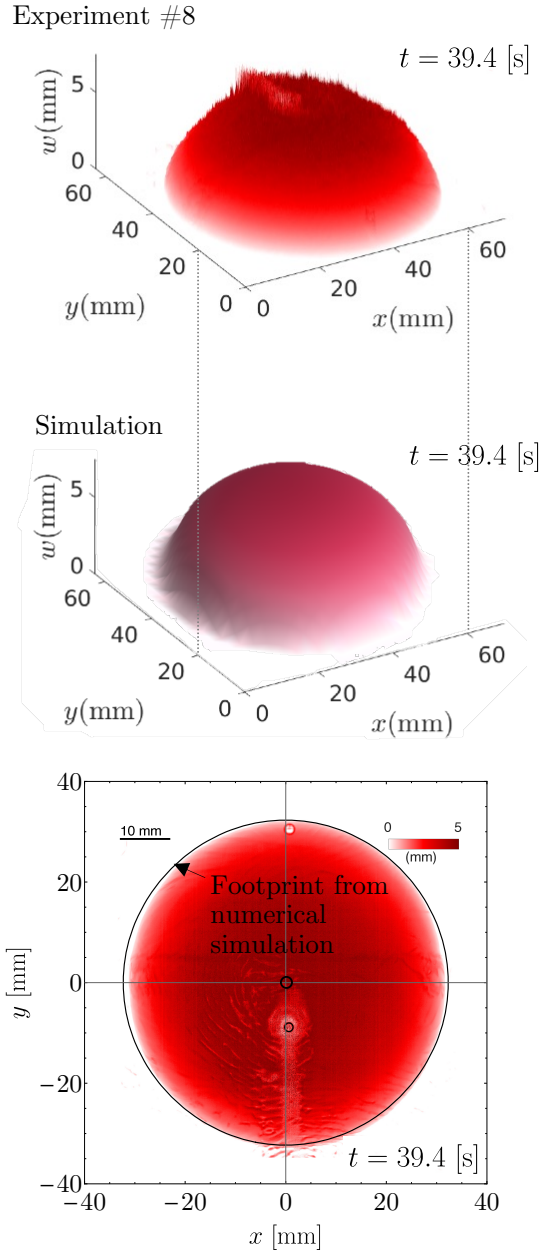
$t = 39.4$ [s]

Figure 3.5 – Numerical and experimental comparison of the 3D opening profile in Experiment
n. 10 for $t = 39.4$ s (single-fracture experiments).

3.4 Coalescence of two coplanar HF

In this section we present the comparison of the numerical predictions against a set of experiments where the simultaneous fluid injection generates two hydraulic fractures that first grow independently and then coalesce. The coalescence takes place on the same plane thanks to the presence of a sufficient amount of confining stress.

3.4.1 setup

The experimental setup is shown in Fig. 3.6 and is similar to the one presented in the previous section. However in this case the fluid is injected at two locations in the hydrogel. To measure the average fluid velocity within the fracture O'Keeffe et al. (2018b) used the optical method of Particle Image Velocimetry. In this flow visualisation technique a particular flow section with particles is illuminated to allow instantaneous velocity measurements. For further details refer to O'Keeffe et al. (2018b); O'Keeffe (2019). The numerical values of the experimental parameters used in the simulations are reported in Table 3.2. All the experiments can be considered toughness dominated.
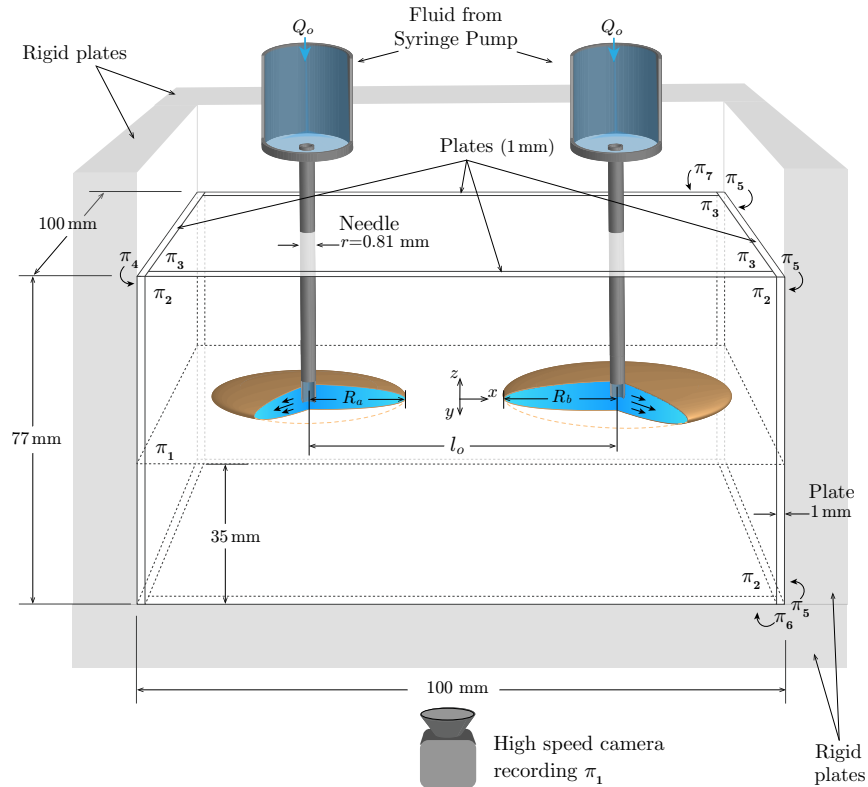
Figure 3.6 – Experimental setup for the double fracture experiment.

exp. ID	exp. ID reference	E [kPa]	μ [Pa s]	Q_o [mL/min]	K_{Ic} $\left[\text{kPa}\sqrt{\text{m}}\right]$
1	db03	97	1.13	5	2.166
2	db12	125	1.13	20	2.166
3	pivdb13	97	0.44	5	2.166

Table 3.2 – Parameters used in the numerical simulations of the double hydraulic fracture experiments.

3.4.2 Discussion of the results

Experiment 1

In Fig. 3.7 and 3.8 we selected a set of time instants for which we present the comparison of the numerically predicted fracture front (black line) and the experimental footprint. Even though the injections started simultaneously, the fracture initiation occurred at different times for the two fractures. To account for this in the numerical simulation we considered two different radii for the initial fractures. The selected radii correspond to the radius of the first observable fracture and to the radius of the needle used for the injection. Despite this caution the fracture footprints obtained by numerical simulation evolves only qualitatively as the ones shown in the experiment. In particular we see that the numerical footprints are more extended in the direction away from the coalescence point. A possible explanation for this phenomenon is that in the numerical simulations we assume that the propagation takes place in an infinite medium while the experiment takes place in a relatively small block of hydrogel. The numerical simulations and the experiments show that once the fractures have grown enough, they interact and attract each other. The closer the two fractures are the higher is the stress intensity factor at the closer parts of the fracture front. Although our numerical simulations do not exactly reproduce the time of coalescence, we obtain excellent comparisons if we shift in time the numerical results taking the time of coalescence as reference. An almost perfect match between the numerical simulation and the experiment is obtained for the 3D fracture opening profile around the point of coalescence. This is shown in Fig. 3.9. The "wiggles" or the "scattered points" seen in the experimental results are related to the light attenuation measurement technique used to obtain the fracture opening. To demonstrate the consistent level of accuracy obtained in comparing with this unique set of experiments we choose to continue reporting on the geometrical comparisons concerning a different experiment.
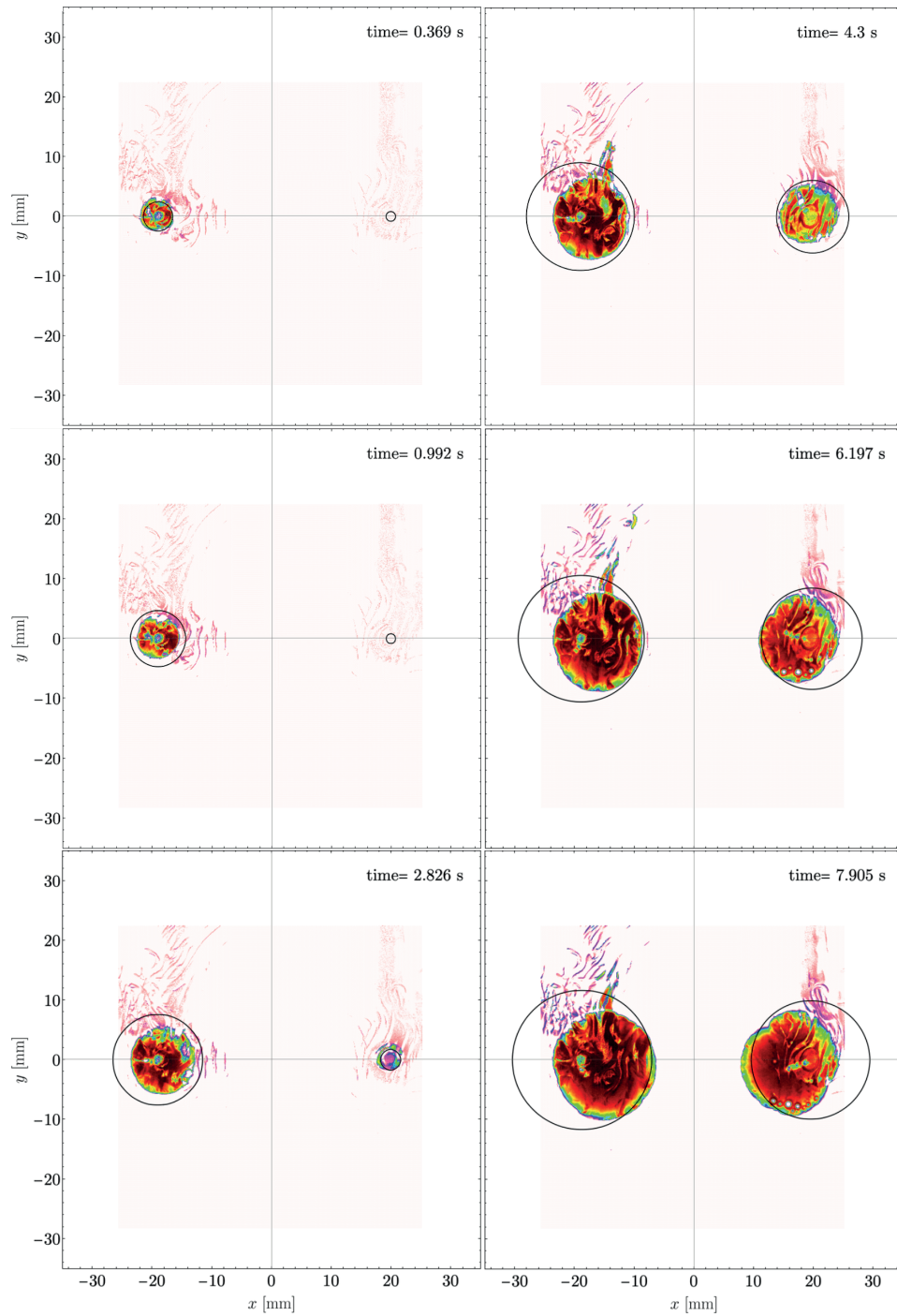
Figure 3.7 – EXP n.1 - Numerical (black line) versus experimental comparison of the fracture footprint before near the beginning of the simulation. Note the delayed initiation of the second fracture (top left).
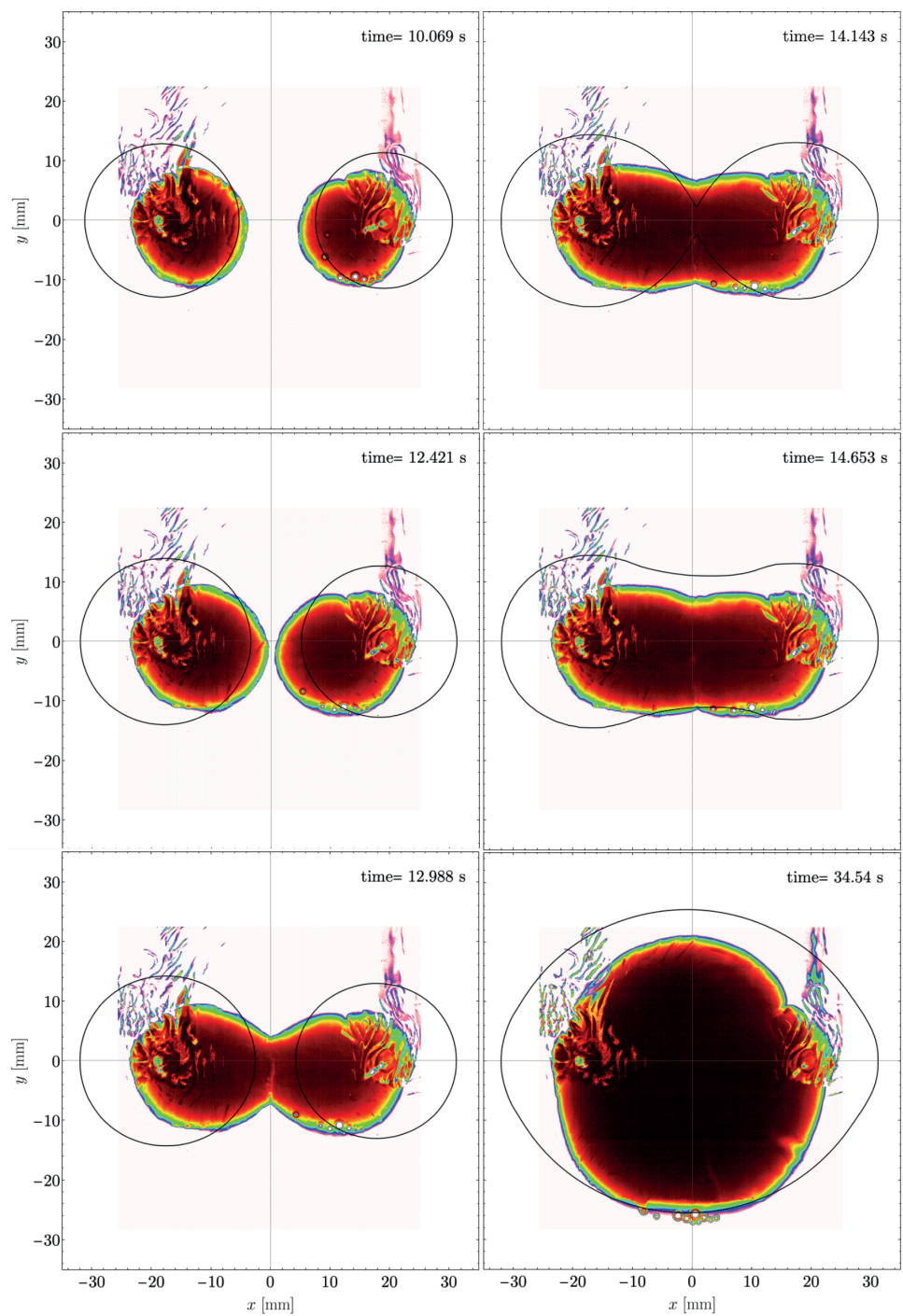
Figure 3.8 – EXP n.1 - Numerical (black line) versus experimental comparison of the fracture footprint before and after the time of coalescence.
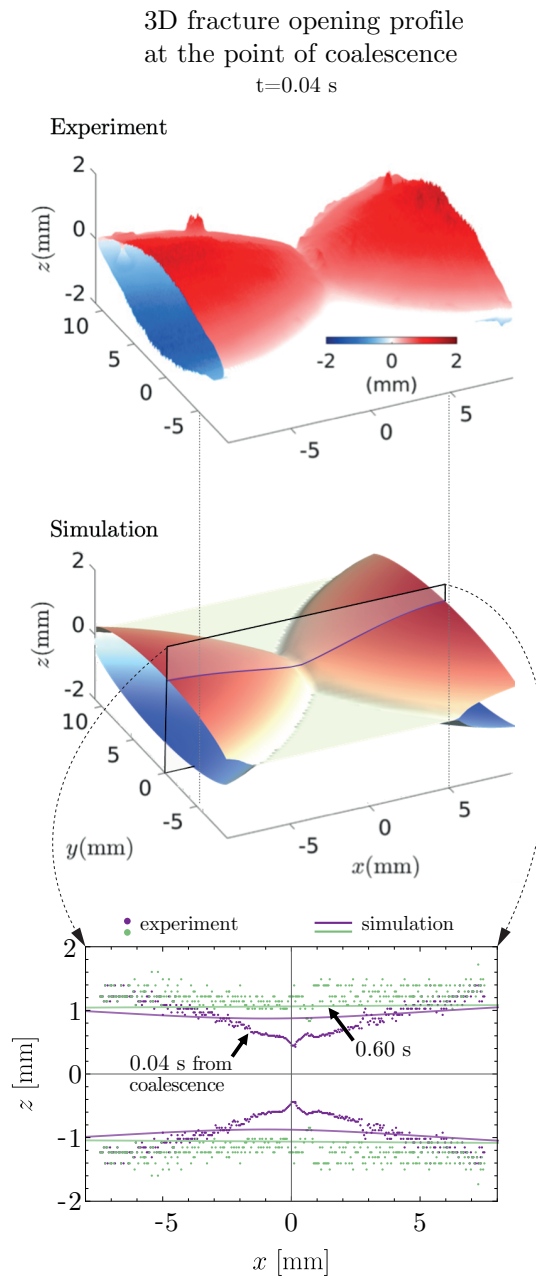
Figure 3.9 – EXP n.1 - Numerical versus experimental comparison of the 3D opening profile 0.04 s after coalescence (top). 2D comparison of the opening profile on the central plane $z - x$.

Experiment 2

As for the previous experiment, the light attenuation measurement technique is used to measure the fracture opening. In Fig. 3.10 we focus on the evolution of the fracture opening profile along two orthogonal planes intersecting the two fractures. Plane "B" in Fig. 3.10 is

passing through the two injection points and is orthogonal to the fracture plane. Plane "A" is orthogonal to plane "B" and it is passing through the point where the coalescence occurs. We consider the fracture opening profiles for few instants before and after the coalescence time (taken as reference). The evolution of the fracture opening profiles obtained numerically match the experimental observations around the point where the coalescence occurs. The scattering in the experimental data is due to the interference of the experimental setup with the light attenuation measurements. As in the previous experiment, we observe that the simulated fracture grows away from the point of coalescence more than what was observed in the experiment. We now turn to consider the evolution of the fracture opening near the injection points shown in Fig. 3.11. The drop of the fracture opening observed in the experiments was previously attributed to the passage of a shear wave O'Keeffe (2019). In our opinion, this drop is mostly due to a quasi static evolution of the fracture opening as a consequence of the coalescence. Our numerical results shown in Fig. 3.11 capture the same drop, with the same variation of fracture opening.
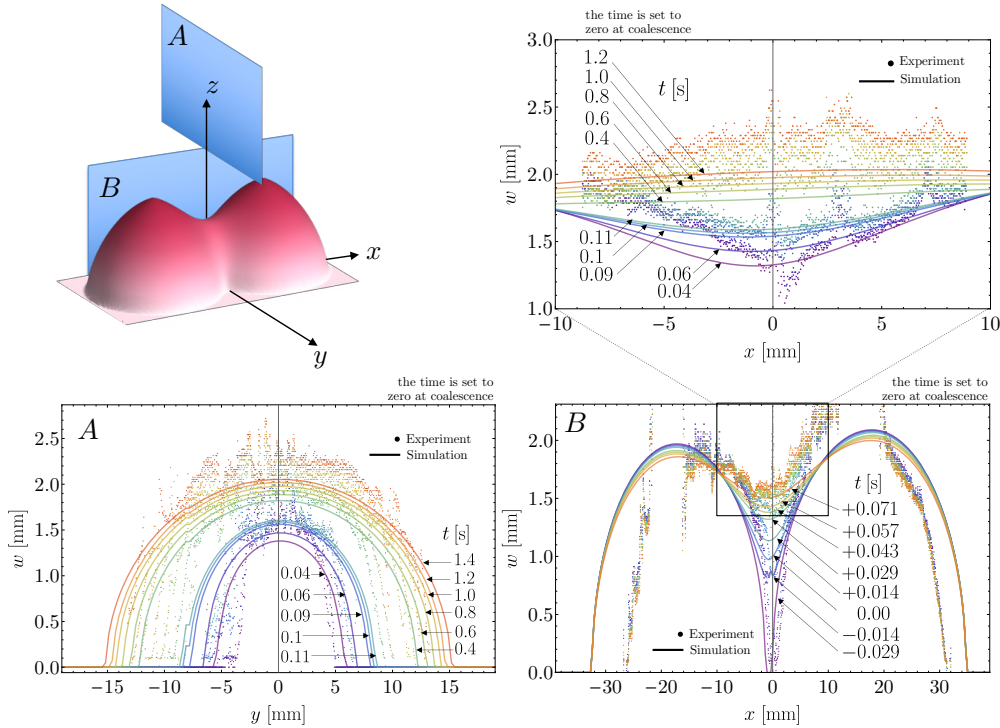
Figure 3.10 – EXP n.2 - Numerical versus experimental evolution of the fracture opening on the planes A and B.

Fracture opening at the
injection points:
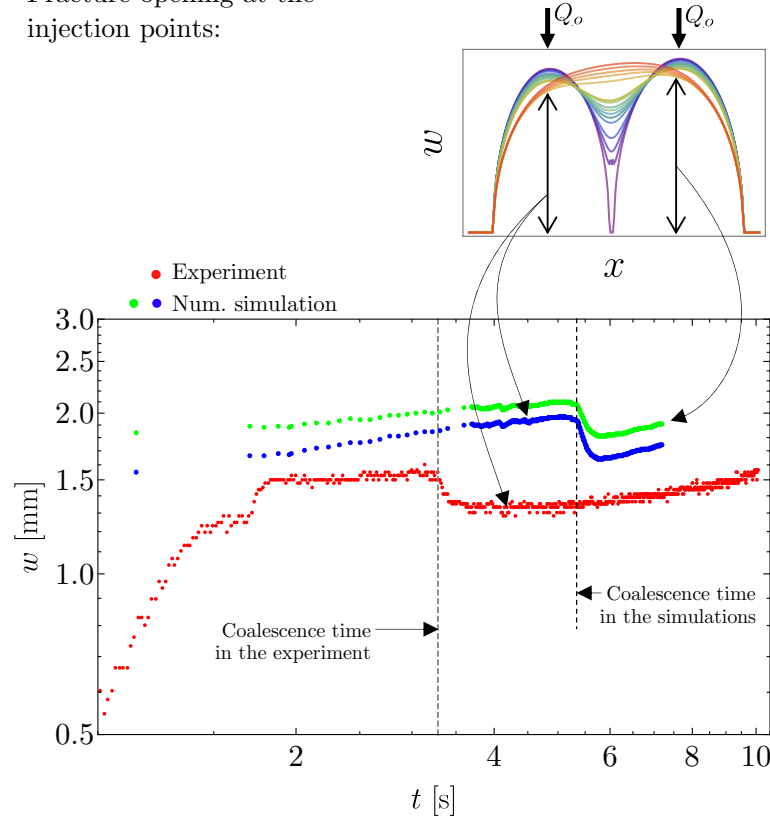
Figure 3.11 – EXP n.2 - Numerical versus experimental evolution of the fracture opening at the injection points. The sudden drop in the fracture opening upon coalescence is a geometrical effect captured by our quasi-static numerical simulations.

Experiment 3

In this experiment the fluid velocity in the fracture is measured via the particle image velocimetry method. This is the first time the fluid velocity inside a hydraulic fracture is compared to numerical simulations. We shifted in our numerical results in time to take the coalescence time as a reference. We start by analysing the average fluid velocity u_x along a cross section connecting the two injection points. In the top part of Fig. 3.12 we present the comparison for the fracture velocity u_x at an early stage of the interaction between the two fractures. In this case the order of magnitude of the fracture velocity is perfectly matched. However, a close look at the plot reveals that the fracture in the numerical simulations extends further in the direction away from the injection points. The diversion of part of the fluid in this direction causes a temporal mismatch between the numerical and the experimental results. In the central part of Fig. 3.12 we consider the velocity profiles immediately before the coalescence time. A close look at the velocity profiles around the coalescence point shows that the fluid starts to accelerate as the two fractures get closer. The numerical simulation captures quantitatively the values of fluid velocity up to -0.02s from the coalescence time. From time equal to -0.02s and

during the subsequent times (see the bottom plot of Fig. 3.12), the fluid velocities predicted by the numerical simulation do not match quantitatively with the experimental observations but they still match qualitatively. It must be noted that not only the numerical simulations are challenged by the rapid evolution of the system during coalescence but also the experimental technique used to measure the velocity in the experiment. We now examine the evolution of the fluid velocity u_y upon coalescence on a plane that is orthogonal to the injection points and passes through the coalescence point. The comparisons between the numerical predictions and the experimental measurements of the fluid velocity are shown in Fig. 3.13. The fluid velocity is larger for times closer to the coalescence time, and decreases later as the fracture regains its radial shape. The large discrepancies between the fluid velocities shown on the top plot in Fig. 3.13 are explained as the fracture footprints in the experiments and in the simulations have different extensions. As mentioned before this is probably caused by the finite boundaries of the specimen.
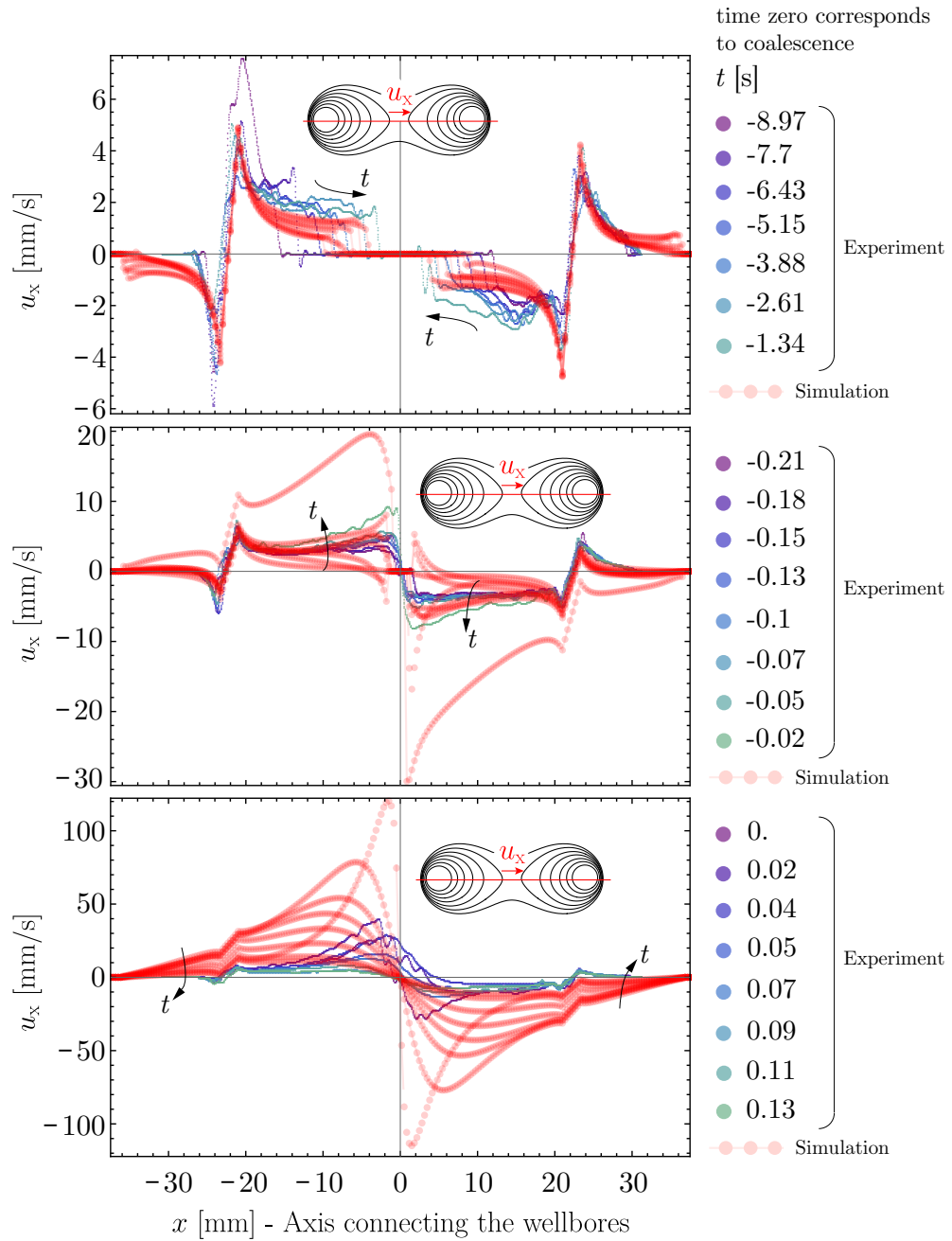
Figure 3.12 – EXP n.3 - Evolution of the fluid velocity along an axis connecting the injection points. Time equal to zero corresponds to the time of coalescence. The order of magnitude of the fluid velocity is captured until few seconds before the coalescence time.

The evolution of the fracture velocity upon coalescence is shown in Fig. 3.13.
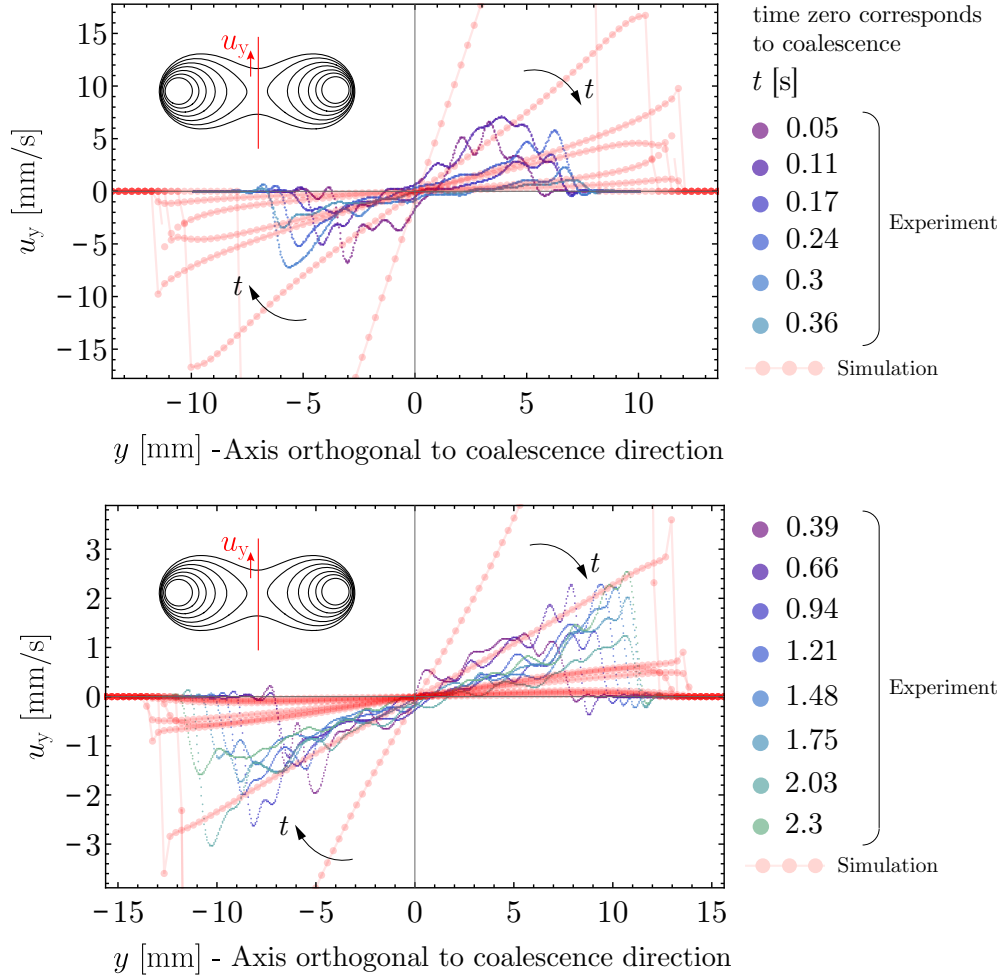
Figure 3.13 – EXP n.3 - Evolution of the fluid velocity along an axis orthogonal to the coalescence direction. Time equal to zero corresponds to the time of coalescence.

3.5   Conclusions

We have analyzed three different experiments. The propagation of a viscosity dominated fracture between two stress barriers. The propagation of single toughness dominated fracture and the interaction and coplanar coalescence of two hydraulic fractures. Our numerical scheme has proven capable of describing hydraulic fracture growth in all the experiments. The numerical simulations also matched the order of magnitude of the quantities observed. For the first time we have presented the comparison between the numerical predictions and the experimental measurements of the fluid velocity in the fracture.

4 Energy balance of a hydraulic fracture

Disclaimer and acknowledgements: My contributions to this chapter are: *i)* linking the energy balance of the solid and the fluid by introducing Newton's third law. *ii)* the extension of the energy balance to the case where the gravitational effects are present. *iii)* the idea of using the definition of the total differential of a function to express the elastic energy stored in the medium. The derivation of the energy balance was done together with Prof. B. Lecampion who pointed out that the scaling of the energy balance leads to the definition of the dimensionless toughness. I acknowledge the work of Andreas Möri who ran the simulations and post-processed the results to confirm that the extension of the energy balance to the case where the gravity effects are present is correct (not shown here). The numerical results presented in this chapter are the product of my contribution.

Note: This chapter is currently being adapted into a scientific publication:
C. Peruzzo, B. Lecampion, "*The energy balance of a hydraulic fracture*", to be submitted to Int J. Eng. Sci., 2023

4.1 Introduction

A hydraulic fracture can be viewed as a dissipative phenomenon where the mechanical energy entering the system is dissipated both in breaking the solid and in the flow of the viscous fluid towards the propagating front. Therefore, enough energy needs to be provided to the system from its boundaries for the process to continue. In this Chapter we derive the energy balance for a hydraulic fracture.

4.2 The power balance of the solid with a fracture

4.2.1 The energy release rate

We consider a body $\Omega_S \subseteq \mathbb{R}^3$ [1] with boundary $\partial \Omega_S = (\partial \Omega_{Su} \cup \partial \Omega_{ST})$ such that $(\partial \Omega_{Su} \cap \partial \Omega_{ST}) = \varnothing$, where $\partial \Omega_{Su}$ and $\partial \Omega_{ST}$ are respectively the part of the boundary where displacements u_i, and tractions T_i, $i = 1, 2, 3$ are prescribed. The fracture area is represented by the symbol a. The energy release rate is defined as (Keating and Sinclair, 1996; Zehnder, 2012):

$$-\frac{\partial \mathrm{W}}{\partial a} + \frac{\partial \mathrm{W}_{ext}}{\partial a}\bigg|_{\mathscr{F}=\text{const}} = G$$

where W and W_{ext} are the work of internal and external forces respectively. We can rewrite this equation as:

$$-\frac{\partial}{\partial a}(\mathrm{W} - \mathrm{W}_{ext}) = G$$

$$-\frac{\partial \phi}{\partial a} := G \tag{4.1}$$

where ϕ is the *total potential energy* of the system, i.e:

$$\phi = \frac{1}{2}\int_{\Omega_S} \sigma_{ij}\varepsilon_{ij}\mathrm{d}V - \int_{\partial \Omega_{ST}} T_i u_i \mathrm{d}s \tag{4.2}$$

Note that the last integral on the right is made only over the part of the boundary where the tractions are applied. By using the Clapeyron's theorem (in absence of body forces), the previous becomes:

$$\phi = \frac{1}{2}\int_{\partial \Omega_S} u_i T_i \mathrm{d}s - \int_{\partial \Omega_{ST}} u_i T_i \mathrm{d}s$$

we can split the first integral by recalling that $\partial \Omega = (\partial \Omega_u \cup \partial \Omega_T)$:

$$\phi = \frac{1}{2}\int_{\partial \Omega_{Su}} u_i T_i \mathrm{d}s + \frac{1}{2}\int_{\partial \Omega_{ST}} u_i T_i \mathrm{d}s - \int_{\partial \Omega_{ST}} u_i T_i \mathrm{d}s$$

$$\phi = \frac{1}{2}\int_{\partial \Omega_{Su}} u_i T_i \mathrm{d}s - \frac{1}{2}\int_{\partial \Omega_{ST}} u_i T_i \mathrm{d}s$$

following the definition given by Eq. (4.1), we obtain:

$$G = -\frac{1}{2}\frac{\partial}{\partial a}\left(\int_{\partial \Omega_{Su}} u_i T_i \mathrm{d}s\right) + \frac{1}{2}\frac{\partial}{\partial a}\left(\int_{\partial \Omega_{ST}} u_i T_i \mathrm{d}s\right) \tag{4.3}$$

---

[1] Note the "S" refers to "solid".

The derivative can not be immediately moved inside of the integral sign because the region of integration $\partial\Omega_{ST}$ depend on the fracture advancement $\mathrm{d}a$. However, we show that in case $\partial u_i / \partial a$ is not diverging, the derivatives with respect to the variation of fracture area can be taken within the integral sign. In particular, the second term on the right hand side can be expressed as:

$$\frac{1}{2}\frac{\partial}{\partial a}\int_{\partial\Omega_{ST}} T_i u_i \mathrm{d}s = \frac{1}{2}\lim_{\delta a\to 0}\left[\frac{1}{\delta a}\left(\int_{\partial\Omega_{ST}} T_i\left(a+\delta a\right)u_i\left(a+\delta a\right)\mathrm{d}s+\right.\right.$$

$$\left.\left.+\int_{\delta a} T_i\left(a+\delta a\right)u_i\left(a+\delta a\right)\mathrm{d}s - \int_{\partial\Omega_{ST}} T_i\left(a\right)u_i\left(a\right)\mathrm{d}s\right)\right] \tag{4.4}$$

Note that a similar expansion of the first term on the right hand side would not include the integral over the small quantity δa. In fact, we do not consider δa part of $\partial\Omega_{Su}$. We expand the terms in the integral of Eq. (4.4) using Taylor's theorem:

$$u_i\left(a+\delta a\right) = u_i\left(a\right) + \left.\frac{\partial u_i}{\partial a}\right|_a \delta a + \mathcal{O}\left(\delta a^2\right) \tag{4.5}$$

$$T_i\left(a+\delta a\right) = T_i\left(a\right) + \left.\frac{\partial T_i}{\partial a}\right|_a \delta a + \mathcal{O}\left(\delta a^2\right) \tag{4.6}$$

We focus on the integral over the small increment δa:

$$\lim_{\delta a\to 0}\left[\left(\frac{\int_{\delta a} T_i\left(a+\delta a\right)u_i\left(a+\delta a\right)\mathrm{d}S}{\delta a}\right)\right] =$$

$$\lim_{\delta a\to 0}\left[\frac{1}{\delta a}\int_{\delta a}\left(u_i T_i + u_i\frac{\partial T_i}{\partial a}\delta a + T_i\frac{\partial u_i}{\partial a}\delta a + \frac{\partial u_i}{\mathrm{d}a}\frac{\partial T_i}{\mathrm{d}a}\delta a^2 + O\left(\delta a^2\right)\right)\mathrm{d}s\right]$$

The external tractions acting on δa are zero when the fracture is of size a (i.e. $T_i\left(a\right)|_{\delta a} = 0$), thus the previous limit can be simplified as:

$$\lim_{\delta a\to 0}\left[\int_{\delta a}\left(u_i\frac{\partial T_i}{\partial a} + T_i\frac{\partial u_i}{\partial a} + \frac{\partial u_i}{\partial a}\frac{\partial T_i}{\partial a}\delta a + \frac{O\left(\delta a^2\right)}{\delta a}\right)\mathrm{d}s\right] \tag{4.7}$$

The term $u_i \partial T_i / \partial a$ is zero because the displacement field u_i is finite and the external tractions are fixed with respect to crack advancement. The limit in Eq. (4.7) further simplifies as:

$$\lim_{\delta a\to 0}\left[\int_{\delta a}\left(T_i\frac{\partial u_i}{\partial a} + \frac{\partial u_i}{\partial a}\frac{\partial T_i}{\partial a}\delta a + \frac{O\left(\delta a^2\right)}{\delta a}\right)\mathrm{d}s\right] \tag{4.8}$$

This limit is zero when the functions under the integral sign are finite quantities because the domain of integration goes to zero (thanks to the limiting process). The other possibility is that the function $\partial u_i / \partial a$ is singular such that the whole limit may diverge. A singular function $\partial u_i / \partial a$ implies that the displacement field does not change continuously as the fracture

advances. This case is not considered here and we assume that the limit is zero.

Upon substituting equations (4.5) and (4.6) in the remaining part of the limit in Eq. (4.4) we obtain:

$$\frac{\partial W_{\text{ext}}}{\partial a} = \frac{1}{2} \lim_{\delta a \to 0} \left[\frac{1}{\delta a} \left(\int_{\partial \Omega_{ST}} T_i\,(a + \delta a)\,u_i\,(a + \delta a)\,\mathrm{d}s + \right. \right.$$

$$\left. \left. - \int_{\partial \Omega_{ST}} T_i\,(a)\,u_i\,(a)\,\mathrm{d}s \right) \right] = \frac{1}{2} \int_{\partial \Omega_{ST}} \frac{\partial}{\partial a}\,(T_i u_i)\,\mathrm{d}s \tag{4.9}$$

Thus, we can write:

$$G = -\frac{1}{2} \int_{\partial \Omega_{Su}} \left(u_i \frac{\partial T_i}{\partial a} + \frac{\partial u_i}{\partial a} T_i \right) \mathrm{d}s + \frac{1}{2} \int_{\partial \Omega_{ST}} \left(u_i \frac{\partial T_i}{\partial a} + \frac{\partial u_i}{\partial a} T_i \right) \mathrm{d}s =$$

$$= -\frac{1}{2} \int_{\partial \Omega_{Su}} u_i \frac{\partial T_i}{\partial a} \mathrm{d}s + \frac{1}{2} \int_{\partial \Omega_{ST}} \frac{\partial u_i}{\partial a} T_i \mathrm{d}s$$

being the applied displacements u_i on $\partial \Omega_{Su}$ independent of the crack advancement δa, (i.e. $\frac{\partial u_i}{\partial a} = 0 \,\forall\, u_i \in \partial \Omega_{Su}$) and $\frac{\partial T_i}{\partial a} = 0 \,\forall\, T_i \in \partial \Omega_{ST}$. More generally it can be written:

$$G = \frac{1}{2} \int_{\partial \Omega_S} \left(\frac{\partial u_i}{\partial a} T_i - u_i \frac{\partial T_i}{\partial a} \right) \mathrm{d}s$$

4.2.2 The energy balance for the solid phase

Equation 4.3 can be expressed as a function of the crack velocity. First we note that $u_i = u_i\,(x_1, x_2, a\,(t))$, thus:

$$\mathrm{d}u_i = \frac{\partial u_i}{\partial x_1} \mathrm{d}x_1 + \frac{\partial u_i}{\partial x_2} \mathrm{d}x_2 + \frac{\partial u_i}{\partial a} \mathrm{d}a$$

that implies:

$$\frac{\mathrm{d}u_i}{\mathrm{d}t} = \frac{\partial u_i}{\partial x_1} \frac{\mathrm{d}x_1}{\mathrm{d}t} + \frac{\partial u_i}{\partial x_2} \frac{\mathrm{d}x_2}{\mathrm{d}t} + \frac{\partial u_i}{\partial a} \frac{\mathrm{d}a}{\mathrm{d}t}$$

Looking at a point fixed in space and assuming that the fracture propagates at one or more locations along the fracture front such that $\frac{\mathrm{d}a}{\mathrm{d}t} \neq 0$, we obtain:

$$\frac{\partial u_i}{\partial a} = \left(\frac{\mathrm{d}u_i}{\mathrm{d}t} \right) \left(\frac{\mathrm{d}a}{\mathrm{d}t} \right)^{-1}$$

The same applies to $T_i = T_i\,(x_1, x_2, a\,(t))$. In this case we have:

$$G \frac{\mathrm{d}a}{\mathrm{d}t} = \frac{1}{2} \int_{\partial \Omega_S} \left(\dot{u}_i T_i - u_i \dot{T}_i \right) \mathrm{d}s \qquad \geq G_c \frac{\mathrm{d}a}{\mathrm{d}t}$$

Upon adding the quantity $\frac{1}{2}\int_{\partial\Omega_S} T_i \dot{u}_i \mathrm{d}s$ to both sides and assuming $\mathbf{G} = G_c$

$$\underbrace{\frac{1}{2}\int_{\partial\Omega_S}\left(\dot{\mathbf{u}}\mathbf{T} + \mathbf{u}\dot{\mathbf{T}}\right)\mathrm{d}s + G_c\frac{\mathrm{d}a}{\mathrm{d}t}}_{\underbrace{\quad\quad\quad\quad}_{\mathscr{P}_i}\,\text{elast.\,en.\,rate}} = \underbrace{\int_{\partial\Omega_{ST}}\dot{\mathbf{u}}\mathbf{T}\mathrm{d}s}_{\mathscr{P}_e} \tag{4.10}$$

It is important to note that the fact that $\dot{u} = 0$ on $\partial\Omega_{Su}$ implies that $\int_{\partial\Omega_S} T_i \dot{u}_i \mathrm{d}s = \int_{\partial\Omega_{ST}} T_i \dot{u}_i \mathrm{d}s$. The previous expression can be written as:

$$\underbrace{\int_{\partial\Omega_S}\frac{\mathrm{d}}{\mathrm{d}t}\left(\frac{1}{2}\mathbf{u}\mathbf{T}\right)\mathrm{d}s + G_c\frac{\mathrm{d}a}{\mathrm{d}t}}_{\underbrace{\quad\quad\quad\quad}_{\mathscr{P}_i}\,\text{elast.\,en.\,rate}} = \underbrace{\int_{\partial\Omega_{ST}}\dot{\mathbf{u}}\mathbf{T}\mathrm{d}s}_{\mathscr{P}_e}$$

or

$$\underbrace{\int_{\partial\Omega_S}\frac{\mathrm{d}}{\mathrm{d}t}\left(\frac{1}{2}\mathbf{u}\mathbf{T}\right)\mathrm{d}s}_{\text{elast.\,en.\,rate}} + \underbrace{\int_{\Gamma} G_c\mathbf{v}\mathbf{n}\mathrm{d}\gamma}_{\text{elast.\,en.\,rate}} = \underbrace{\int_{\partial\Omega_{ST}}\dot{\mathbf{u}}\mathbf{T}\mathrm{d}s}_{\mathscr{P}_e}$$

where $\mathbf{v}$ is the local front velocity, $\mathscr{P}_e$ is the total external power exerted by the external forces. $\mathscr{P}_i$ is the internal power formed by the sum of the dissipated energy via fracture advancement and the rate of elastic energy stored into the medium. Note that the domain $\partial\Omega_S$ is fixed in time. We now refer the previous equations to a system subjected to an initial state of tractions $\mathbf{T}_0$. The initial displacements corresponding to the situation where the sole load $\mathbf{T}_0$ act in the system are assumed to be zero. The previous equations become:

$$\underbrace{\int_{\partial\Omega_S}\frac{\mathrm{d}}{\mathrm{d}t}\left[\frac{1}{2}\mathbf{u}\left(\mathbf{T}-\mathbf{T}_0\right)\right]\mathrm{d}s + \int_{\Gamma} G_c\mathbf{v}\mathbf{n}\mathrm{d}\gamma + \int_{\partial\Omega_{ST}}\dot{\mathbf{u}}\mathbf{T}_0\mathrm{d}s}_{\mathscr{P}_i} = \int_{\partial\Omega_{ST}}\dot{\mathbf{u}}\mathbf{T}\mathrm{d}s$$

4.3 The energy balance of a laminar fluid flow

In what follows, the principle of virtual power is derived. The balance of momentum for a volume of fluid, the definition of work done by a force and the constitutive law that relates stress and strain rates are used. The balance of momentum of a material volume τ of fluid bounded by the surface S is expressed by (Batchelor (2000)):

$$\int_{\Omega_F}\frac{\mathrm{D}\dot{u}_i}{\mathrm{D}t}\rho\mathrm{d}\tau = \int_{\Omega_F} F_i\rho\mathrm{d}\tau + \int_{\partial\Omega_F}\sigma_{ij}n_j\mathrm{d}s \quad i,j = 1,2,3 \tag{4.11}$$

where:

- $\dot{u}_i \left[\frac{L}{T}\right]$ is the $i-$component of the velocity vector $\dot{\mathbf{u}}$,

- t is time [T],

- $\frac{D()}{Dt} = \frac{\partial ()}{\partial t} + \dot{\mathbf{u}} \cdot \nabla ()$ is the operator giving the material derivative, it applies only to functions of t and $\dot{\mathbf{u}}$,

- ρ is the fluid density $\left[\frac{M}{L^3}\right]$,

- F_i is the $i-$component of the force per unit mass vector, defined per unit of mass of fluid $\left[\frac{L}{T^2}\right]$,

- σ_{ij} is the component ij of the second order stress tensor $\sigma \left[\frac{M}{LT^2}\right]$,

- n_j is the $j-$component of the normal vector to the small element of surface δS.

By using the divergence theorem Eq. (4.12) can be expressed as follows:

$$\int_{\Omega_F} \frac{D\dot{u}_i}{Dt}\rho d\tau = \int_{\Omega_F} F_i \rho d\tau + \int_{\Omega_F} \frac{\partial \sigma_{ij}}{\partial x_j} d\tau \tag{4.12}$$

we multiply both sides by $\dot{u}_i$ and add the term $\int \sigma_{ij}\frac{\partial \dot{u}_i}{\partial x_j}d\tau$:

$$\int_{\Omega_F} \sigma_{ij}\frac{\partial \dot{u}_i}{\partial x_j}d\tau + \int_{\Omega_F} \dot{u}_i\frac{D\dot{u}_i}{Dt}\rho d\tau = \int_{\Omega_F} \dot{u}_i F_i \rho d\tau + \int_{\Omega_F}\left(\dot{u}_i\frac{\partial \sigma_{ij}}{\partial x_j} + \sigma_{ij}\frac{\partial \dot{u}_i}{\partial x_j}\right)d\tau \tag{4.13}$$

and after applying the divergence theorem to the last integral on the right hand side the Principle of Virtual Powers is obtained[2]:

$$\underbrace{\int_{\Omega_F} \sigma_{ij}\frac{\partial \dot{u}_i}{\partial x_j}d\tau + \int_{\Omega_F} \frac{D}{Dt}\left(\frac{1}{2}\rho \dot{u}_i^2\right)d\tau}_{\mathscr{P}_i} = \underbrace{\int_{\Omega_F} \dot{u}_i F_i \rho d\tau + \int_{\partial\Omega_F} \dot{u}_i \sigma_{ij} n_j ds}_{\mathscr{P}_e} \tag{4.14}$$

The two integrals on the right hand side represent the rate of work (i.e. the power) done by the external actions done to the system (i.e. the volume of fluid). It is important to note that the last integral on the right hand side can represent both the rate of work done on the system by the external forces and the rate of work done by injecting fluid into the system at a given velocity and consequent pressure. This observation will be clearer later when the actual boundary conditions are given. The second integral on the left hand side represents the rate of change of kinetic energy $\frac{1}{2}\rho u_i^2$. The first integral on the left hand side embeds several different terms that will appear after introducing the relationship between stress and strain rates (i.e. the constitutive law).

The Navier-Stokes constitutive relation assumes that the Cauchy stress tensor σ is a function of the density ρ, temperature T and the velocity gradient $\nabla\dot{\mathbf{u}}$, i.e. $\sigma = f(\rho, T, \nabla\dot{\mathbf{u}})$. The velocity

---

[2]Note:$\dot{\mathbf{u}}\frac{D\dot{\mathbf{u}}}{Dt} = \dot{\mathbf{u}}\odot\frac{\partial\dot{\mathbf{u}}}{\partial t} + \dot{\mathbf{u}}\odot\dot{\mathbf{u}}\cdot\nabla\dot{\mathbf{u}} = \frac{\partial}{\partial t}\left(\frac{1}{2}\dot{\mathbf{u}}\odot\dot{\mathbf{u}}\right) + \dot{\mathbf{u}}\cdot\nabla\left(\frac{1}{2}\dot{\mathbf{u}}\odot\dot{\mathbf{u}}\right) = \frac{D}{Dt}\left(\frac{1}{2}\dot{\mathbf{u}}\odot\dot{\mathbf{u}}\right)$, and $\odot$ denotes the Hadamart product.

gradient $\nabla \dot{\mathbf{u}}$ can be decomposed as:

$$\nabla \dot{\mathbf{u}} = \mathbf{E} + \mathbf{R} = \frac{1}{2} \left(\nabla \dot{\mathbf{u}} + (\nabla \dot{\mathbf{u}})^T \right) + \frac{1}{2} \left(\nabla \dot{\mathbf{u}} - (\nabla \dot{\mathbf{u}})^T \right)$$

where $\mathbf{R}$ is a tensor representing a rigid rotation and $\mathbf{E}$ is the *strain rate tensor*; the first does not contribute to the rate of change of deformation and is subsequently excluded from the expression of the constitutive law. The strain rate tensor can be further decomposed in two parts:

$$\mathbf{E}_{ij} = \mathbf{D}_{ij} + \mathbf{S}_{ij} = \underbrace{\frac{1}{3} \frac{\partial \dot{u}_k}{\partial x_k} \delta_{ij}}_{\mathbf{D}_{ij}} + \underbrace{\frac{1}{2} \left(\frac{\partial \dot{u}_j}{\partial x_i} + \frac{\partial \dot{u}_i}{\partial x_j} \right) - \frac{1}{3} \frac{\partial \dot{u}_k}{\partial x_k} \delta_{ij}}_{\mathbf{S}_{ij}}$$

Where $\mathbf{D}$ and $\mathbf{S}$ are respectively the *rate of expansion tensor* and *rate of shear tensor*. The constitutive equation is then expressed as:

$$\sigma_{ij} = -p\delta_{ij} + \kappa \frac{\partial \dot{u}_k}{\partial x_k} \delta_{ij} + 2\mu \left[\frac{1}{2} \left(\frac{\partial \dot{u}_j}{\partial x_i} + \frac{\partial \dot{u}_i}{\partial x_j} \right) - \frac{1}{3} \frac{\partial \dot{u}_k}{\partial x_k} \delta_{ij} \right] \tag{4.15}$$

where κ is the *expansion viscosity* and μ is the *shear viscosity*. Note that $p = -\frac{1}{3}\sigma_{ii}$ is the thermodynamic equilibrium pressure while the departure from it, generally happening in a moving fluid, is take into account by the term $\kappa \frac{\partial \dot{u}_k}{\partial x_k} \delta_{ij}$ (see Batchelor (2000) for more details). Substituting Eq. (4.15) in Eq. (4.14) leads to:

$$
\begin{aligned}
& \underbrace{-\int_{\Omega_F} p\delta_{ij} \frac{\partial \dot{u}_i}{\partial x_j} \mathrm{d}\tau}_{\text{elast. en. rate}} + \underbrace{\int_{\Omega_F} \kappa \frac{\partial \dot{u}_k}{\partial x_k} \delta_{ij} \frac{\partial \dot{u}_i}{\partial x_j} \mathrm{d}\tau}_{\text{dissipation by expansion}} \\
& + \underbrace{\int_{\Omega_F} 2\mu \left[\frac{1}{2} \left(\frac{\partial \dot{u}_j}{\partial x_i} + \frac{\partial \dot{u}_i}{\partial x_j} \right) - \frac{1}{3} \frac{\partial \dot{u}_k}{\partial x_k} \delta_{ij} \right] \frac{\partial \dot{u}_i}{\partial x_j} \mathrm{d}\tau}_{\text{dissipation by shear}} + \\
& + \underbrace{\int_{\Omega_F} \frac{\mathrm{D}}{\mathrm{D}t} \left(\frac{1}{2} \rho \dot{u}_i^2 \right) \mathrm{d}\tau}_{\text{kinetic en. rate}} = \underbrace{\int_{\Omega_F} \dot{u}_i F_i \rho \mathrm{d}\tau + \int_{\partial\Omega_F} \dot{u}_i \sigma_{ij} n_j \mathrm{d}s}_{\mathscr{P}_e}
\end{aligned}
\tag{4.16}
$$

Introducing the mass balance

$$\frac{1}{\rho} \frac{\mathrm{D}\rho}{\mathrm{D}t} + \nabla \cdot \dot{\mathbf{u}} = 0,$$

and simplifying it for the case of an incompressible fluid leads to

$$\nabla \cdot \dot{\mathbf{u}} = \frac{\partial \dot{u}_k}{\partial x_k} = 0. \tag{4.17}$$

This result can be used to simplify Eq. (4.16):

$$-\int_{\Omega_F} p\delta_{ij}\frac{\partial \dot{u}_i}{\partial x_j}\mathrm{d}\tau + \int_{\Omega_F} \mu\left(\frac{\partial \dot{u}_j}{\partial x_i}+\frac{\partial \dot{u}_i}{\partial x_j}\right)\frac{\partial \dot{u}_i}{\partial x_j}\mathrm{d}\tau +$$
$$\underbrace{\qquad\qquad\qquad}_{\text{reversible power}}$$
$$+\underbrace{\int_{\Omega_F}\frac{\mathrm{D}}{\mathrm{D}t}\left(\frac{1}{2}\rho\dot{u}_i^2\right)\mathrm{d}\tau}_{\text{kinetic en. rate}} = \underbrace{\int_{\Omega_F}\dot{u}_i F_i\rho\mathrm{d}\tau + \int_{\partial\Omega_F}\dot{u}_i\sigma_{ij}n_j\mathrm{d}s}_{\mathscr{P}_e} \tag{4.18}$$

Note that Eq. (4.18) expresses a set of 3 distinct balances between internal and external power provided to the system. For the sake of clarity we express the balance in direction x_1 (i.e. for $i = 1$):

$$-\int_{\Omega_F} p\frac{\partial \dot{u}_1}{\partial x_1}\mathrm{d}\tau + \int_{\Omega_F}\mu\left(2\left(\frac{\partial \dot{u}_1}{\partial x_1}\right)^2 + \left(\frac{\partial \dot{u}_2}{\partial x_1}+\frac{\partial \dot{u}_1}{\partial x_2}\right)\frac{\partial \dot{u}_1}{\partial x_2}+\left(\frac{\partial \dot{u}_3}{\partial x_1}+\frac{\partial \dot{u}_1}{\partial x_3}\right)\frac{\partial \dot{u}_1}{\partial x_3}\right)\mathrm{d}\tau +$$
$$+\int_{\Omega_F}\frac{\mathrm{D}}{\mathrm{D}t}\left(\frac{1}{2}\rho\dot{u}_1^2\right)\mathrm{d}\tau = \int_{\Omega_F}\dot{u}_1 F_1\rho\mathrm{d}\tau + \int_{\partial\Omega_f}\dot{u}_1\left(\sigma_{11}n_1 + \sigma_{12}n_2 + \sigma_{13}n_3\right)\mathrm{d}s \tag{4.19}$$

A scalar balance is obtained by summing the separate balances over the three directions:

$$-\underbrace{\int_{\Omega_F} p\nabla\cdot\dot{\mathbf{u}}\mathrm{d}\tau + \int_{\Omega_F}2\mu\left(\nabla\cdot\dot{\mathbf{u}}\right)\cdot\left(\nabla\cdot\dot{\mathbf{u}}\right)\mathrm{d}\tau}_{\text{reversible power}} +$$
$$+\underbrace{\int_{\Omega_F}\mu\left(\left(\frac{\partial \dot{u}_1}{\partial x_2}+\frac{\partial \dot{u}_2}{\partial x_1}\right)^2 + \left(\frac{\partial \dot{u}_2}{\partial x_3}+\frac{\partial \dot{u}_3}{\partial x_2}\right)^2 + \left(\frac{\partial \dot{u}_1}{\partial x_3}+\frac{\partial \dot{u}_3}{\partial x_1}\right)^2\right)\mathrm{d}\tau}_{\text{dissipation by shear}} +$$
$$+\underbrace{\int_{\Omega_F}\frac{\mathrm{D}}{\mathrm{D}t}\left(\frac{1}{2}\rho\dot{\mathbf{u}}^2\right)\mathrm{d}\tau}_{\text{kinetic en. rate}} = \underbrace{\int_{\Omega_F}\dot{\mathbf{u}}\mathbf{F}\rho\mathrm{d}\tau + \int_{\partial\Omega_F}\dot{\mathbf{u}}\sigma\mathbf{n}\mathrm{d}s}_{\mathscr{P}_e} \tag{4.20}$$

using the assumption of fluid incompressibility (i.e.: Eq. (4.17)) leads to a number of simplifications [3]:

$$\underbrace{\int_{\Omega_F}\mu\left(\left(\frac{\partial \dot{u}_1}{\partial x_2}+\frac{\partial \dot{u}_2}{\partial x_1}\right)^2 + \left(\frac{\partial \dot{u}_2}{\partial x_3}+\frac{\partial \dot{u}_3}{\partial x_2}\right)^2 + \left(\frac{\partial \dot{u}_1}{\partial x_3}+\frac{\partial \dot{u}_3}{\partial x_1}\right)^2\right)\mathrm{d}\tau}_{\text{dissipation by shear}} +$$
$$+\underbrace{\int_{\Omega_F}\frac{\mathrm{D}}{\mathrm{D}t}\left(\frac{1}{2}\rho\dot{\mathbf{u}}^2\right)\mathrm{d}\tau}_{\text{kinetic en. rate}} = \underbrace{\int_{\Omega_F}\dot{\mathbf{u}}\mathbf{F}\rho\mathrm{d}\tau + \int_{\partial\Omega_F}\dot{\mathbf{u}}\sigma\mathbf{n}\mathrm{d}s}_{\mathscr{P}_e} \tag{4.21}$$

The previous equation needs to be written in dimensionless form to choose the terms that can be neglected thanks to the assumptions of lubrication flow. The approach already exposed in Szeri (2010) is repeated but applying it to an energy balance. The independent and dependent dimensionless variables can be defined as:

$$\bar{x}_i = x_i/x_{i*}, \ \bar{t} = t/t_*,$$

---

[3]Note that $(\nabla\cdot\dot{\mathbf{u}})\cdot(\nabla\cdot\dot{\mathbf{u}}) = 0$ because the conservation of mass for an incompressible fluid implies that $\nabla\cdot\dot{\mathbf{u}} = 0$.

$$\bar{u}_i = \dot{u}_i / \dot{u}_{i*}, \ \bar{p} = p/p_*, \ \bar{\sigma} = \sigma/p_*$$

where the characteristic dimensions are denoted with $()_*$. The assumptions that define the lubrication flow, guide the choice of these dimensions of the problem. This type of flow is distinguished by the fact that one spatial dimension of the fluid domain is much smaller than the other two; here it is assumed $x_3 \ll x_1$ and $x_3 \ll x_2$. Therefore a single length scale L can be chosen for both x_{1*} and x_{2*}, i.e.: $x_{1*} = x_{2*} = L$ and $x_{3*} = \varepsilon L$ with $\varepsilon \ll 1$. Similarly, the velocity parallel to the fracture plane is assumed to scale with single characteristic velocity $\dot{U}$, i.e.: $\dot{u}_{1*} = \dot{u}_{2*} = \dot{U}$. It follows that a choice for the characteristic time t_* is $t_* = L/\dot{U}$. The conservation of mass becomes:

$$\varepsilon \frac{\partial \bar{u}_1}{\partial \bar{x}_1} + \varepsilon \frac{\partial \bar{u}_2}{\partial \bar{x}_2} + \frac{\dot{u}_{3*}}{\dot{U}} \frac{\partial \bar{u}_3}{\partial \bar{x}_3} = 0$$

Given the choices of $t_* = L/\dot{U}$ and $x_{3*} = \varepsilon L$, the characteristic velocity $\dot{u}_{3*}$ is chosen as $\dot{u}_{3*} = \varepsilon \dot{U}$. Note that consequently the mass conservation simplifies as:

$$\frac{\partial \bar{u}_1}{\partial \bar{x}_1} + \frac{\partial \bar{u}_2}{\partial \bar{x}_2} + \frac{\partial \bar{u}_3}{\partial \bar{x}_3} = 0$$

Finally, only p_* remains to be defined. Writing the energy balance in dimensionless variables leads to[4]:

$$\mu \dot{U}^2 L \varepsilon^2 \int_{\Omega_F} \left(\left(\frac{\partial \bar{u}_1}{\partial \bar{x}_2} + \frac{\partial \bar{u}_2}{\partial \bar{x}_1} \right)^2 + 2 \left(\frac{\partial \bar{u}_2}{\partial \bar{x}_3} \frac{\partial \bar{u}_3}{\partial \bar{x}_2} + \frac{\partial \bar{u}_1}{\partial \bar{x}_3} \frac{\partial \bar{u}_3}{\partial \bar{x}_1} \right) \right) \mathrm{d}\bar{\tau} + $$
$$\underbrace{\qquad\qquad\qquad\qquad\qquad\qquad\qquad\qquad\qquad\qquad\qquad\qquad\qquad}_{\text{dissipation by shear}}$$

$$+ \mu \dot{U}^2 L \int_{\Omega_F} \left(\left(\frac{\partial \bar{u}_2}{\partial \bar{x}_3} \right)^2 + \left(\frac{\partial \bar{u}_1}{\partial \bar{x}_3} \right)^2 \right) \mathrm{d}\bar{\tau} + \mu \varepsilon^4 \dot{U}^2 L \int_{\Omega_F} \left(\left(\frac{\partial \bar{u}_3}{\partial \bar{x}_2} \right)^2 + \left(\frac{\partial \bar{u}_3}{\partial \bar{x}_1} \right)^2 \right) \mathrm{d}\bar{\tau} + $$
$$\underbrace{\qquad\qquad\qquad\qquad\qquad\qquad\qquad\qquad\qquad\qquad\qquad\qquad\qquad}_{\text{dissipation by shear}}$$

$$+ \underbrace{\rho \dot{U}^3 L^2 \varepsilon^2 \int_{\Omega_F} \frac{\mathrm{D}}{\mathrm{D}\bar{t}} \left(\frac{1}{2} \bar{u}^2 \right) \mathrm{d}\bar{\tau}}_{\text{kinetic en. rate}} = \underbrace{\rho F \dot{U} L^3 \varepsilon^2 \int_{\Omega_F} \left(\bar{u}_1 \bar{F}_1 + \bar{u}_2 \bar{F}_2 + \varepsilon \bar{u}_3 \bar{F}_3 \right) \mathrm{d}\bar{\tau} + p_* \varepsilon^2 \dot{U} L^2 \int_{\partial \Omega_F} \frac{\bar{\mathbf{u}} \bar{\sigma} \mathbf{n} \mathrm{d}\bar{s}}{\varepsilon}}_{\mathscr{P}_e}$$

dividing all the terms by the non-zero quantity $\mu \dot{U}^2 L$ and recognizing the Reynolds number

---

[4]Note that $\dot{\mathbf{u}} = \begin{bmatrix} \dot{U}\bar{u}_1 & \dot{U}\bar{u}_2 & \varepsilon \dot{U}\bar{u}_3 \end{bmatrix}$ and $\mathbf{n}\mathrm{d}s = \begin{bmatrix} \varepsilon L^2 \mathrm{d}\bar{s} & \varepsilon L^2 \mathrm{d}\bar{s} & L^2 \mathrm{d}\bar{s} \end{bmatrix}$

$\text{Re} = \frac{\rho \dot{U} \varepsilon L}{\mu} = \frac{\rho \dot{U} w}{\mu}$ the previous equation becomes:

$$\varepsilon^2 \int_{\Omega_F} \underbrace{\left(\left(\frac{\partial \bar{\dot{u}}_1}{\partial \bar{x}_2} + \frac{\partial \bar{\dot{u}}_2}{\partial \bar{x}_1} \right)^2 + 2 \left(\frac{\partial \bar{\dot{u}}_2}{\partial \bar{x}_3} \frac{\partial \bar{\dot{u}}_3}{\partial \bar{x}_2} + \frac{\partial \bar{\dot{u}}_1}{\partial \bar{x}_3} \frac{\partial \bar{\dot{u}}_3}{\partial \bar{x}_1} \right) \right) \mathrm{d}\bar{\tau}}_{\text{dissipation by shear}} +$$

$$+ \underbrace{\int_{\Omega_F} \left(\left(\frac{\partial \bar{\dot{u}}_2}{\partial \bar{x}_3} \right)^2 + \left(\frac{\partial \bar{\dot{u}}_1}{\partial \bar{x}_3} \right)^2 \right) \mathrm{d}\bar{\tau} + \varepsilon^4 \int_{\Omega_F} \left(\left(\frac{\partial \bar{\dot{u}}_3}{\partial \bar{x}_2} \right)^2 + \left(\frac{\partial \bar{\dot{u}}_3}{\partial \bar{x}_1} \right)^2 \right) \mathrm{d}\bar{\tau}}_{\text{dissipation by shear}} +$$

$$+ \varepsilon \text{Re} \underbrace{\int_{\Omega_F} \frac{\mathrm{D}}{\mathrm{D}\bar{t}} \left(\frac{1}{2} \bar{\mathbf{u}}^2 \right) \mathrm{d}\bar{\tau}}_{\text{kinetic en. rate}} = \underbrace{\left(\varepsilon \text{Re} \times \frac{FL}{\dot{U}^2} \right) \int_{\Omega_F} \left(\bar{\dot{u}}_1 \bar{F}_1 + \bar{\dot{u}}_2 \bar{F}_2 \right) \mathrm{d}\bar{\tau} + \varepsilon^2 \text{Re} \frac{FL}{\dot{U}^2} \int_{\Omega_F} \bar{\dot{u}}_3 F_3 \mathrm{d}\bar{\tau} + p_* \frac{L}{\mu \dot{U}} \varepsilon^2 \int_{\partial \Omega_F} \frac{\bar{\dot{u}} \bar{\sigma} \mathbf{n} \mathrm{d}\bar{s}}{\varepsilon}}_{\mathscr{P}_e}$$

$$(4.22)$$

It must be noted that different dimensionless groups multiply the different components of the energy balance. The characteristic pressure p_* has to be set to $p_* = \frac{\mu \dot{U}}{L \varepsilon^2}$ for the power exchanged at the boundary to be of order 1. It follows that:

$$\underbrace{\int_{\Omega_F} \left(\left(\frac{\partial \bar{\dot{u}}_2}{\partial \bar{x}_3} \right)^2 + \left(\frac{\partial \bar{\dot{u}}_1}{\partial \bar{x}_3} \right)^2 \right) \mathrm{d}\bar{\tau}}_{\mathscr{P}_i = \text{dissipation by shear}} = \underbrace{\varepsilon^2 \frac{\rho F L^2}{\mu \dot{U}} \int_{\Omega_F} \left(\bar{\dot{u}}_1 \bar{F}_1 + \bar{\dot{u}}_2 \bar{F}_2 \right) \mathrm{d}\bar{\tau} + \int_{\partial \Omega_F} \bar{\dot{u}} \bar{\sigma} \mathbf{n} \mathrm{d}\bar{s}}_{\mathscr{P}_e} \qquad (4.23)$$

The external power is essentially dissipated in the gradient of velocity perpendicular to the flow direction. Expressing the latter in dimensional form leads to:

$$\underbrace{\int_{\Omega_F} \mu \left(\left(\frac{\partial \dot{u}_2}{\partial x_3} \right)^2 + \left(\frac{\partial \dot{u}_1}{\partial x_3} \right)^2 \right) \mathrm{d}\tau}_{\mathscr{P}_i = \text{dissipation by shear}} = \underbrace{\int_{\Omega_F} \rho \left(\dot{u}_1 F_1 + \dot{u}_2 F_2 \right) \mathrm{d}\tau + \int_{\partial \Omega_F} \dot{u} \sigma \mathbf{n} \mathrm{d}s}_{\mathscr{P}_e} \qquad (4.24)$$

Performing the same dimensional analysis on the Navier-Stokes equations (i.e. Eq. (4.11)) and neglecting the terms the terms of order $\geq \mathcal{O}(\varepsilon)$ leads to (e.g. see Szeri (2010)):

$$\frac{\partial p}{\partial x_1} = \mu \frac{\partial^2 \dot{u}_1}{\partial x_3^2} - \rho F_1, \quad \frac{\partial p}{\partial x_2} = \mu \frac{\partial^2 \dot{u}_2}{\partial x_3^2} - \rho F_2, \quad \frac{\partial p}{\partial x_3} = 0 \qquad (4.25)$$

these results will now be used. Integrating the left hand side of Eq. (4.24) by parts along x_3 gives:

$$\underbrace{\int_{\Omega_F} \frac{\mu}{2} \left(\dot{u}_1^2 + \dot{u}_2^2 \right) \Big|_{-w/2}^{w/2} \mathrm{d}x_1 \mathrm{d}x_2 - \int_{\Omega_F} \left(\dot{u}_1 \mu \frac{\partial^2 \dot{u}_1}{\partial x_3^2} + \dot{u}_2 \mu \frac{\partial^2 \dot{u}_2}{\partial x_3^2} \right) \mathrm{d}\tau}_{\mathscr{P}_i = \text{dissipation by shear}} = \underbrace{\int_{\Omega_F} \rho \left(\dot{u}_1 F_1 + \dot{u}_2 F_2 \right) \mathrm{d}\tau + \int_{\partial \Omega_F} \dot{u} \sigma \mathbf{n} \mathrm{d}s}_{\mathscr{P}_e}$$

$$(4.26)$$

where w is the thickness of the domain in the x_3 direction. Assuming no slip boundary condition, that is $\dot{u}_i \left(x_1, x_2, \pm \frac{w}{2} \right) \equiv 0$ for $i = 1, 2$ and $\forall x_1, x_2$ implies that the first integral on the left hand side vanishes. Then, upon making use of the first 2 reduced Navier-Stokes equations

in (4.25) the previous becomes:

$$-\int_{\Omega_F}\left(\dot{u}_1\frac{\partial p}{\partial x_1}+\dot{u}_2\frac{\partial p}{\partial x_2}\right)d\tau-\underbrace{\int_{\Omega_F}\rho\left(\dot{u}_1F_1+\dot{u}_2F_2\right)d\tau}_{\mathscr{P}_i=\text{dissipation by shear}}=\underbrace{\int_{\Omega_F}\rho\left(\dot{u}_1F_1+\dot{u}_2F_2\right)d\tau+\int_{\partial\Omega_F}\dot{\mathbf{u}}\sigma\mathbf{n}ds}_{\mathscr{P}_e}$$

(4.27)

The 3rd Equation in (4.25) implies that $p = p(x_1, x_2)$ allowing us to rewrite the left hand side integral in Eq. (4.27) as:

$$-\underbrace{\int_{\Omega_F}\left(\left(\int_{-w/2}^{w/2}\dot{u}_1dx_3\right)\frac{\partial p}{\partial x_1}+\left(\int_{-w/2}^{w/2}\dot{u}_2dx_3\right)\frac{\partial p}{\partial x_2}\right)dx_1dx_2-\int_{\Omega_F}\rho\left(q_1F_1+q_2F_2\right)dx_1dx_2}_{\mathscr{P}_i=\text{dissipation by shear}}$$
$$=\underbrace{\int_{\Omega_F}\rho\left(\left(\int_{-w/2}^{w/2}\dot{u}_1dx_3\right)F_1+\left(\int_{-w/2}^{w/2}\dot{u}_2dx_3\right)F_2\right)dx_1dx_2+\int_{\partial\Omega_F}\dot{\mathbf{u}}\sigma\mathbf{n}ds}_{\mathscr{P}_e}$$

(4.28)

and upon introducing the average velocities

$$v_i=\frac{\int_{-w/2}^{w/2}\dot{u}_idx_3}{\int_{-w/2}^{w/2}dx_3}=\frac{1}{w}\int_{-w/2}^{w/2}\dot{u}_idx_3\quad i=1,2$$

(4.29)

and fluxes

$$q_i=wv_i\quad i=1,2$$

(4.30)

Eq. (4.28) finally becomes (with $\mathbf{T}=\sigma\mathbf{n}$):

$$-\underbrace{\int_{\Omega_F}\left[q_1\left(\frac{\partial p}{\partial x_1}+\rho F_1\right)+q_2\left(\frac{\partial p}{\partial x_2}+\rho F_2\right)\right]dx_1dx_2}_{\mathscr{P}_i=\text{dissipation by shear}}$$
$$=\underbrace{\int_{\Omega_F}\rho\left(q_1F_1+q_2F_2\right)dx_1dx_2+\int_{\partial\Omega_F}\dot{\mathbf{u}}\mathbf{T}ds}_{\mathscr{P}_e}$$

(4.31)

This equation can be alternatively expressed only as a function of the average fluid velocity. For this purpose, the first two of Eq. (4.25) have to be integrated along x_3 between $\pm\frac{w}{2}$ assuming no slip boundary condition, that is $\dot{u}_i\left(x_1,x_2,\pm\frac{w}{2}\right)\equiv0$ for $i=1,2$ and $\forall x_1,x_2$. It results:

$$\dot{u}_i(x_1,x_2,x_3)=\frac{1}{2\mu}\left(\frac{\partial p}{\partial x_i}+\rho F_i\right)\left(x_3^2-\frac{w^2}{4}\right)\quad i=1,2$$

(4.32)

this shows that in a vertical cross section the velocity distribution is parabolic. Substituting (4.32) into Eq. (4.29) results:

$$v_i(x_1,x_2)=-\frac{1}{12\mu}\left(\frac{\partial p}{\partial x_i}+\rho F_i\right)w^2\quad i=1,2$$

(4.33)

Note that if instead of the fluid pressure p we consider $p = p_{net}+\sigma_o(x_1,x_2)$, where $\sigma_o(x_1,x_2)$

is the in-situ stress orthogonal to the fracture plane, the previous becomes:

$$v_i(x_1, x_2) = -\frac{1}{12\mu}\left(\frac{\partial p_{net}}{\partial x_i} + \frac{\partial \sigma_o}{\partial x_i} + \rho F_i\right)w^2 \quad i = 1, 2 \tag{4.34}$$

and further assuming that $\frac{\partial \sigma_o}{\partial x_i} = -\rho_s F_i$ we have:

$$v_i(x_1, x_2) = -\frac{1}{12\mu}\left(\frac{\partial p_{net}}{\partial x_i} + (\rho - \rho_s)F_i\right)w^2 \quad i = 1, 2 \tag{4.35}$$

Substituting the latter Eq. (4.33) and Eq. (4.30) in the left hand side of (4.31) leads to an alternative expression of the internal energy that makes use of the average fluid velocity $v_i(x_1, x_2)$ $i = 1, 2$:

$$\underbrace{12\mu\int_{\Omega_F}\frac{1}{w}\left(v_1^2 + v_2^2\right)\mathrm{d}x_1\mathrm{d}x_2}_{\mathscr{P}_i = \text{dissipation by shear}}$$

$$= \underbrace{\int_{\Omega_F}w\rho\left(v_1 F_1 + v_2 F_2\right)\mathrm{d}x_1\mathrm{d}x_2 + \int_{\partial\Omega_F}\dot{\mathbf{u}}\mathbf{T}\mathrm{d}s}_{\mathscr{P}_e} \tag{4.36}$$

where $\mathbf{T} = \sigma\mathbf{n}$. The energy balance is finally obtained by integrating either Eq. (4.31) or (4.36).

4.3.1 The energy balance of a fluid driven fracture

Equation (4.36) represents the equivalence between the rate of energy dissipated into the system and the energy provided to it. The fluid boundary can be regarded as to be composed of two different parts $\partial\Omega_F = \partial\Omega_{F-inj} \cup \partial\Omega_{F-S}$. The part of the boundary where the fluid enters or exits the domain (e.g. via injection or leakoff) is identified by $\partial\Omega_{F-inj}$ and the other one, in contact with the elastic material, is identified by $\partial\Omega_{F-S}$. We finally obtain:

$$\underbrace{12\mu\int_{\Omega_F}\frac{1}{w}\left(v_1^2 + v_2^2\right)\mathrm{d}x_1\mathrm{d}x_2}_{\mathscr{P}_i(\text{fluid}) = \text{dissipation by shear}} =$$

$$= \underbrace{\int_{\Omega_F}w\rho\left(v_1 F_1 + v_2 F_2\right)\mathrm{d}x_1\mathrm{d}x_2 + \int_{\partial\Omega_{F-inj}}\dot{\mathbf{u}}\mathbf{T}\mathrm{d}s + \int_{\partial\Omega_{F-S}}\dot{\mathbf{u}}\mathbf{T}\mathrm{d}s}_{\mathscr{P}_e(\text{fluid})} = \tag{4.37}$$

$$= \underbrace{\int_{\Omega_F}w\rho\left(v_1 F_1 + v_2 F_2\right)\mathrm{d}x_1\mathrm{d}x_2 + Q_o p_o - \int_{\partial\Omega_{F-S}}\mathbf{v}_L\mathbf{T}\mathrm{d}s + \int_{\partial\Omega_{F-S}}\dot{\mathbf{u}}\mathbf{T}\mathrm{d}s}_{\mathscr{P}_e(\text{fluid})}$$

we particularize the expression on the where $Q_o p_o$ is the power entering the system via the fluid injection at the constant rate Q_o and inlet pressure p_o. The fluid leaves the system from the crack faces at a velocity $\mathbf{v}_L(\mathbf{x}, t)$. The power entering the fluid system is minus the one

entering the elastic system, i.e.:

$$\underbrace{\int_{\partial\Omega_{F-S}} \dot{\mathbf{u}}\mathbf{T}\mathrm{d}s}_{\mathscr{P}_e(\text{fluid})} = -\underbrace{\int_{\partial\Omega_S} \dot{\mathbf{u}}\mathbf{T}\mathrm{d}s}_{\mathscr{P}_e(\text{solid})}$$

Remembering that:

$$\underbrace{\int_{\partial\Omega_S} \frac{\mathrm{d}}{\mathrm{d}t}\left[\frac{1}{2}\mathbf{u}\,(\mathbf{T}-\mathbf{T_0})\right]\mathrm{d}s + \int_{\Gamma} G_c\mathbf{v}\mathbf{n}\mathrm{d}\gamma + \int_{\partial\Omega_{ST}} \dot{\mathbf{u}}\mathbf{T_0}\mathrm{d}s}_{\mathscr{P}_i} = \int_{\partial\Omega_{ST}} \dot{\mathbf{u}}\mathbf{T}\mathrm{d}s$$

with $\partial\Omega_s$ denoting the solid boundary, we obtain:

$$\underbrace{\int_{\partial\Omega_{F-S}} \dot{\mathbf{u}}\mathbf{T}\mathrm{d}s}_{\mathscr{P}_e(\text{fluid})} = -\left(\underbrace{\int_{\partial\Omega_S} \frac{\mathrm{d}}{\mathrm{d}t}\left[\frac{1}{2}\mathbf{u}\,(\mathbf{T}-\mathbf{T_0})\right]\mathrm{d}s}_{\text{rate of elastic energy}} + \underbrace{\mathbf{G_c}\frac{\mathrm{d}a}{\mathrm{d}t}}_{\text{fracture energy rate}} + \int_{\partial\Omega_{ST}} \dot{\mathbf{u}}\mathbf{T_0}\right) \tag{4.38}$$

substituting Eq. (4.38) into Eq. (4.37) leads to:

$$\underbrace{\underbrace{12\mu\int_{\partial\Omega_F}\frac{\mathbf{v}^2}{w}\mathrm{d}s}_{\text{dissipation by shear}} + \underbrace{\int_{\partial\Omega_S}\frac{\mathrm{d}}{\mathrm{d}t}\left[\frac{1}{2}\mathbf{u}\,(\mathbf{T}-\mathbf{T_0})\right]\mathrm{d}s}_{\text{rate of elastic energy}} + \underbrace{\int_{\Gamma} G_c\mathbf{v}\mathbf{n}\mathrm{d}\gamma}_{\text{fracture energy rate}} + \int_{\partial\Omega_{ST}}\dot{\mathbf{u}}\mathbf{T_0}}_{\mathscr{P}_i(\text{fluid and solid})} =$$

$$\underbrace{\int_{\partial\Omega_F} w\rho\,(v_1 F_1 + v_2 F_2)\,\mathrm{d}s + Q_o p_o - \int_{\partial\Omega_{F-S}} \mathbf{v}_L\mathbf{T}\mathrm{d}s}_{\mathscr{P}_e(\text{fluid})} \tag{4.39}$$

By considering that:

- the fracture consists of two opposite surfaces with two opposite oriented surfaces.

- the normal component of the traction vector $\mathbf{T}$ equals the fluid pressure p.

- the fluid pressure is related to the net pressure via the relation $p = p_{net} + \sigma_o(x_1, x_2)$ where $\sigma_o(x_1, x_2)$ is the component of the in-situ stress normal to the fracture plane.

- for a planar fracture mode-I decouples from the other two fracture modes

one can express the previous equation as:

$$\underbrace{12\mu \int_{\partial\Omega_F} \frac{\mathbf{v}^2}{w}\mathrm{d}s}_{\text{dissipation by shear}} + \underbrace{\int_{\partial\Omega_{F-S}} \frac{\mathrm{d}}{\mathrm{d}t}\left(\frac{1}{2}w \times p_{net}\right)\mathrm{d}s}_{\text{rate of elastic energy}} + \underbrace{\int_\Gamma G_c\mathbf{v}\mathbf{n}\mathrm{d}\gamma}_{\text{fracture energy rate}} + \underbrace{\int_{\partial\Omega_{F-S}} \frac{\mathrm{d}w}{\mathrm{d}t} \times \sigma_o(x_1,x_2)\mathrm{d}s+}_{\text{reversible power}} =$$

$$\underbrace{= \int_{\partial\Omega_F} w\rho\,(v_1 F_1 + v_2 F_2)\,\mathrm{d}s + Q_o \times \left(p_{net}(0,0) + \sigma_o(0,0)\right) - \int_{\partial\Omega_{F-S}} \mathbf{v}_L \times \left(p_{net} + \sigma_o(x_1,x_2)\right)\mathrm{d}s}_{\mathscr{P}_e\text{(fluid)}}$$

$$\tag{4.40}$$

with $\mathscr{P}_i$(fluid and solid) under the first line.

$$\underbrace{12\mu \int_{\partial\Omega_F} \frac{\mathbf{v}^2}{w}\mathrm{d}s}_{\substack{\text{Power}\\\text{dissipated}\\\text{by viscous fluid flow}}} + \underbrace{\int_{\partial\Omega_{F-S}} \frac{\mathrm{d}}{\mathrm{d}t}\left(\frac{1}{2}w\,p\right)\mathrm{d}s}_{\substack{\text{Power}\\\text{stored as elastic}\\\text{deformation of the solid}\\\text{medium}}} + \underbrace{\int_\Gamma G_c\mathbf{v}\,\mathbf{n}\mathrm{d}\gamma}_{\substack{\text{Power}\\\text{dissipated to}\\\text{create new}\\\text{fracture surfaces}}} = \underbrace{Q_o p_o}_{\substack{\text{External}\\\text{Power}}}$$
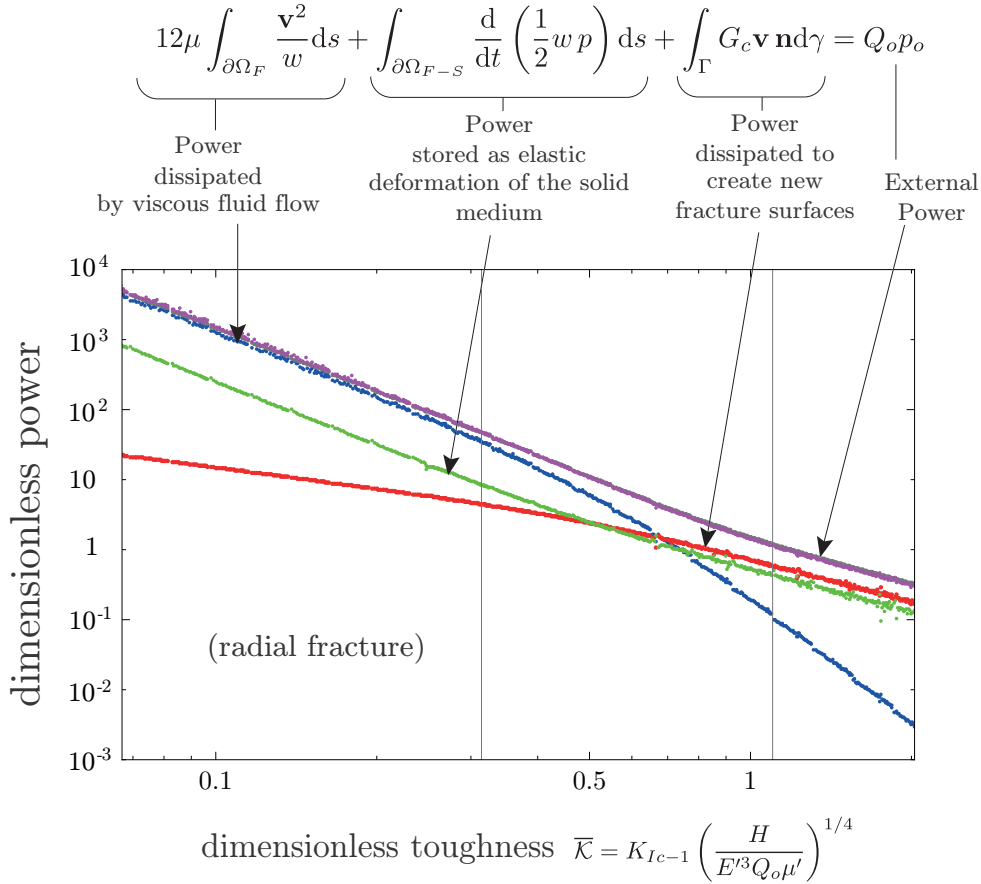
Figure 4.1 – Different terms of the power balance for a radial hydraulic fracture.

As an example we consider the case where a penny shaped fracture propagates in a homogeneous and impermeable medium. We simplify the power balance by excluding the work linked to the confining stress σ_o. In Figure 4.1 we show the evolution of each term of the balance. In the figure, each term is made dimensionless by the following quantity: $Q_o\left(K_{\text{Ic}}^6/\left(E'^3 Q_o\mu'\right)\right)^{1/2} = Q_o p_{mk}$. The horizontal axis reports the dimensionless toughness $\overline{\mathcal{K}}$. This dimensionless number can be derived by nondimensionalizing the power balance by the

same scaling approach reported in Savitski and Detournay (2002). In this case we assume that, for the radial fracture, the characteristic size of the domain scales as the fracture diameter H. For small values of the dimensionless toughness the main energy dissipation mechanism is the flow of the viscous fluid. Conversely, for large values of $\overline{\mathcal{K}}$, the main energy dissipation mechanism is the creation of new fracture surfaces.

4.4 Conclusions

In this chapter we have derived the energy balance for a hydraulic fracture. For the case of a simple radial fracture we have demonstrated that the main energy dissipation mechanism evolves as a function of the fracture size.

5 Conditions for the local arrest of a hydraulic fracture by a toughness heterogeneity

Disclaimer and acknowledgements: The idea of using the energy balance for a steadily moving semi-infinite hydraulic fracture to express the arrest criterion for a propagating hydraulic fracture is my contribution. Prof. B. Lecampion has fully developed the approach described in the subsection "matching the far field opening across the jump for the semi-infinite HF" and has contributed in some steps of deriving the energy balance of a semi infinite hydraulic fracture. He also improved the written presentation of the results.

Note: This chapter is currently being adapted into a scientific publication:
C. Peruzzo, B. Lecampion, "*Conditions for the local arrest of a hydraulic fracture by a region of larger toughness*", to be submitted to Mechanics of Materials, 2023

In this chapter we will answer to the following research question. When is a heterogeneity of fracture toughness is capable of arresting locally the propagation of a hydraulic fracture?

5.1   Problem definition
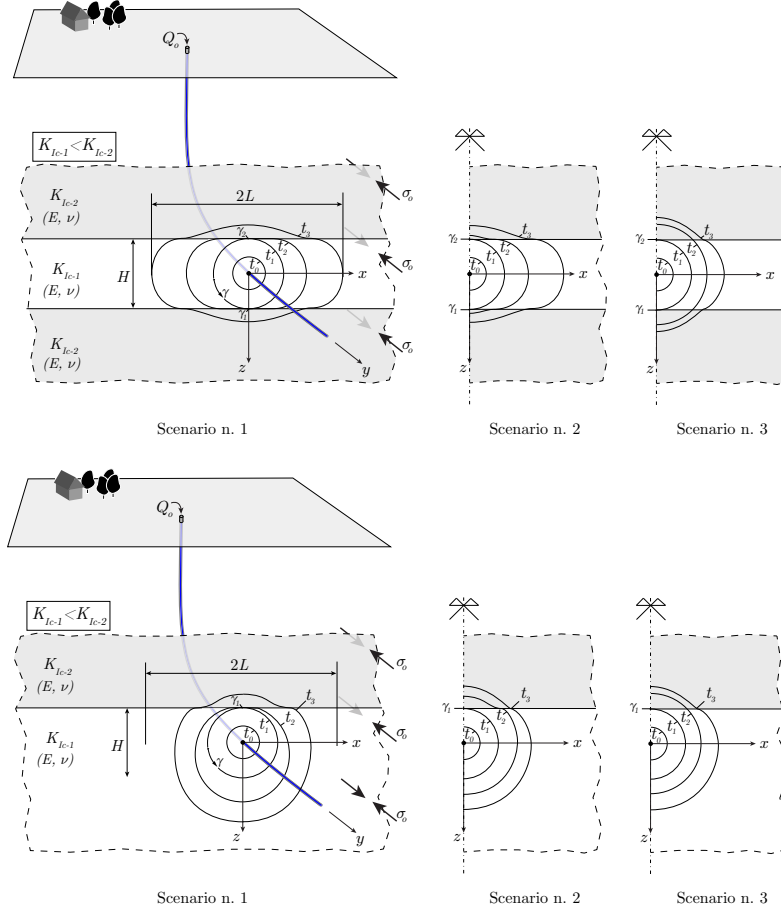
Figure 5.1 – Sketch representing the three-layer configuration considered throughout this work and the three different possible scenarios occurring upon the fracture has touched the interfaces. In the 1st scenario the propagation stops at the interfaces and continues along with the central layer (footprint t_2) before breaking through into the bounding layers (footprint t_3). In both the 2nd and 3rd scenarios, the breakthrough happens immediately at footprint t_1. In the 2nd scenario the velocity after breakthrough V^+ around γ_i, $i = 1, 2$ is smaller than V^-, the one immediately before touching the interface. In the 3rd scenario $V^+ \approx V^-$ i.e. it is not immediately affected by the presence of the heterogeneity.

Our primary interest stems from the practical configuration of a hydraulic fracture propagating initially in a layer bounded symmetrically by two layers of higher fracture toughness. However, as we shall see, our results can be generalized to other configurations. To frame our arguments, we consider three layers of the same impermeable linear-elastic material, characterized by uniform Young's modulus E, Poisson's ratio ν and uniform confining stress σ_o acting perpendicularly to the plane $x - z$ in Figure 5.1. The central layer has thickness H while

the others extend indefinitely above and below. The material in the central layer differs from the others by its fracture energy G_{c-1} which is smaller than the one of the bounding layers G_{c-2}. Throughout the rest of the document we will either refer to G_{c-i} $i = 1,2$, or to the fracture toughness $K_{Ic-i} = \sqrt{E'G_{c-i}}$ where $E' = E/(1-v^2)$ (Irwin, 1957). An incompressible Newtonian fluid of viscosity μ is injected at the center of the middle layer. The injection proceeds at a constant rate Q_o and drives the propagation of a penny shaped fracture. The fracture is characterized by the diameter $2L(t)$ evolving in time t, the fracture opening $w(x,z,t)$ and the net pressure $p(x,z,t)$ or, equivalently, by the fluid pressure $p_f(x,z,t) = p(x,z,t) + \sigma_o$. The injection source lengthscale (the wellbore diameter) is assumed to be much smaller than the fracture length, so the injection can be considered to take place at a point. We also assume that the fluid lag remains negligible during the entire process. This condition is ensured by the relation $\mu'VE'^2/\sigma_o^3 \ll 1$ where V is the front velocity (Garagash and Detournay, 1998). The equation that govern this moving boundary problem relate to elasticity, fluid flow and fracture propagation. The balance of momentum for the solid can be reduced to a scalar boundary integral equation for mode I planar fracture (Hills et al., 2013; Crouch S.L., 1983),

$$p(x,z) = p_f(x,z) - \sigma_o = -\frac{E'}{8\pi} \int_{\Sigma(t)} \frac{w(x',z',t)}{\left[(x'-x)^2 + (z'-z)^2\right]^{3/2}} dx'dz',$$ (5.1)

where the Σ represents the fracture's trace on the middle fracture plane. The local fluid volume conservation inside the fracture in the case of an impermeable rock reads (Batchelor, 1967):

$$\frac{\partial w(x,z,t)}{\partial t} + \nabla \cdot \mathbf{q} - \delta(x)\delta(z)Q_o(x,z,t) = 0 \,,$$ (5.2)

that integrated both in time and in space reduces to the global volume balance

$$\int_{\Sigma(t)} w(x',z',t) dx'dz' = Q_o t \,.$$ (5.3)

The width-averaged balance of momentum for the fluid in laminar conditions is:

$$\mathbf{q} = \begin{bmatrix} q_x & q_z \end{bmatrix} = -\frac{w(x,z,t)^3}{\mu'}\nabla p(x,z,t) \quad \mu' = 12\mu$$ (5.4)

and the quasi-static fracture propagation conditions locally reads:

$$\begin{cases} V(\gamma)G_c(\gamma) \geq 0 \\ (G - G_c(\gamma))V(\gamma) = 0 \end{cases} \quad \forall \gamma \in \Gamma$$ (5.5)

where G is the energy release rate, $V(\gamma) = \mathbf{v}(x,z) \cdot \mathbf{n}(\gamma)$ is the magnitude of the local fracture front velocity at the curvilinear coordinate γ along the front and $\mathbf{n}(\gamma)$ is the normal to the front. As shown in Savitski and Detournay (2002), when the hydraulic fracture propagates in a homogeneous medium, i.e. before reaching the interfaces in our case, the solution of equations 5.1,5.2, (or 5.3), 5.4 and 5.5 in terms of L, w and p depends on a single dimensionless number. The nondimensionalization of these equations leads to two alternative definitions for

it. If it is assumed that the viscous dissipations involved in the fluid flow are of $\mathcal{O}(1)$ compared to the energy required to break the material (*viscosity scaling*), the dimensionless number appearing upon nondimensionalization is the *dimensionless toughness*

$$\mathcal{K}_R = \left(\frac{K_{Ic-1}^{18}}{E'^{13} Q_o^3 \mu'^5} \right)^{1/18} t^{1/9}$$

(with the subscript "R" reminding that the parameter refers to the case of a radial fracture geometry). By reversing the assumptions (*toughness scaling*), the dimensionless number appearing upon the nondimensionalization is $\mathcal{M}_R = \left(\frac{\mu'^5 E'^{13} Q_o^3}{K_{Ic-1}^{18}} \right)^{1/5} t^{-2/5}$ denoted *dimensionless viscosity*. As shown in Chapter 4, $\mathcal{K}_R^2$, or equivalently $\mathcal{M}_R^{-5/9}$, is exactly the ratio between the two energy dissipation mechanisms occurring during the hydraulic fracturing process. In the case of a radial fracture, their expressions show that this ratio evolves with time. Thus, the hydraulic fracture solution changes from the *viscosity dominated regime (*at *early time)* where the energy required by the viscous flow of the fluid is much larger than the fracture energy, to the *toughness dominated regime (*at *late time)* where the opposite holds (Savitski and Detournay, 2002). This suggests that, at the time t_{touch} when the fracture touches the interfaces, either the value of dimensionless toughness $\mathcal{K}_R(t = t_{\text{touch}}, K_{Ic-1})$ or $\mathcal{M}_R(t = t_{\text{touch}}, K_{Ic-1})$, together with the toughness ratio K_{Ic-2}/K_{Ic-1}, are expected to control the fracture behavior. It is convenient to introduce the length scale H in both $\mathcal{K}_R(t_{\text{touch}}, K_{Ic-1})$ and $\mathcal{M}_R(t_{touch}, K_{Ic-1})$ in place of t_{touch}. By substituting $t_{\text{touch}} : L_{R-M}(t) = H$ in $\mathcal{K}_R(t, K_{Ic-1})$ we obtain:

$$\overline{\mathcal{K}}(H, K_{Ic-1}) = K_{Ic-1} \left(\frac{H}{E'^3 Q_o \mu'} \right)^{1/4} \tag{5.6}$$

Analogously by substituting $t_{\text{touch}} : L_{R-K}(t) = H$ in $\mathcal{M}_R(t, K_{Ic-1})$ we obtain $\overline{\mathcal{M}} = \overline{\mathcal{K}}^{-4}$. The functions $L_{R-M}(t)$ and $L_{R-K}(t)$ are the solutions of the penny shaped hydraulic fracture problem in the viscosity dominated and in the toughness dominated regime respectively (Savitski and Detournay, 2002).

We assume that the change in fracture toughness occur abruptly at the layers interface, and that the fracture propagates on the same plane after touching them (i.e. no deviation of the fracture plane) This represents one possible limiting case for layer's interfaces in sedimentary rock formations. Thus, the possible scenarios are restricted to the ones represented in Figure 5.1. In all the three scenarios a penny-shaped fracture is propagates at a velocity V in the central layer at $t = t_0$. During the whole propagation, V is assumed to remain small enough such that any inertial effect can be neglected. At time $t_1 = t_{\text{touch}}$, the fracture touches the interfaces at two points, γ_1 and γ_2, along the front. Then, the three scenarios differ in relation to the change of velocity happening around γ_i $i = 1, 2$. Since inertia is negligible for hydraulic fracture growth, the velocity changes instantaneously from $V^- > 0$ to V^+ and the scenarios are characterized as follows:

- *Scenario n. 1* (transient containment - transiently arrested height growth): $V^+ = 0$, any

point of the fracture front stops immediately upon reaching the interfaces. The fracture growth develops only in the central layer. The fluid flow is nonzero only along the x direction, except for a region near the injection point where the flow transitions from radial to unidirectional. The fracture remains contained between the two interfaces for a finite time Δt_c. Possibly $\Delta t_c \to 0$. As shown later, in case of a finite viscosity such a containment time is never infinite: $\Delta t_c < \infty$.

- *Scenario n. 2* (no containment - slowed height growth): $0 < V^+ < V^-$, the propagation in the new medium continues albeit with a lower velocity. The fracture footprint deviates from a radial geometry. It is important to note that the limit $V^+ \to 0$ in Scenario n. 2 corresponds to the limit $\Delta t_c \to 0$ in Scenario n. 1.

- *Scenario n. 3* (unperturbed propagation): $V^+ = V^-$, the fracture crosses the interface maintaining (temporarily) the same velocity. This corresponds to the limit $\overline{\mathcal{K}} \to 0$. The fracture footprint remains radial for some time before the heterogeneity affects it. In any case, no containment is possible.

5.2 The existence of fracture containment

In the previous section, we have introduced the dimensionless parameters that govern the problem: K_{Ic-2}/K_{Ic-1} and $\overline{\mathcal{K}}$ (or $\mathcal{K}_R(t = t_{\text{touch}}, K_{Ic-1})$). They can be retrieved by nondimensionalizing the energy balance expressed for the case where G_c is heterogeneous along the front (generalising the derivation of Lecampion and Detournay (2007)). In absence of leak-off and other energy losses, the energy balance in rate from reduces to:

$$\underbrace{\underbrace{\mu' \int_\Sigma \frac{\mathbf{v} \cdot \mathbf{v}}{w} \mathrm{d}s}_{\text{viscous dissipation}} + \underbrace{\oint_\Gamma G(\gamma) \mathbf{v} \cdot \mathbf{n} \mathrm{d}\gamma}_{\text{energy rel. rate}} + \underbrace{\int_\Sigma \frac{1}{2} \frac{\mathrm{d}}{\mathrm{d}t} \left(w \times (p_f - \sigma_o) \right) \mathrm{d}s}_{\text{rate of elastic energy accretion}}}_{\mathcal{P}_i} = \underbrace{Q_o p_o(t)}_{\mathcal{P}_e} \tag{5.7}$$

where $\Gamma \equiv \partial \Sigma$ is the crack front. We denote the fluid velocity with $\mathbf{v}(x, z)$ and the net pressure at the injection as $p(x = 0, y = 0, t) = p_o(t) = p_{fo}(t) - \sigma_o$. The external power provided to the system $\mathcal{P}_e(t)$ (on the right hand side), is balanced by three contributions that, all together, constitute the internal power $\mathcal{P}_i(t)$: i) the energy dissipation associated with viscous fluid flow inside the fracture, ii) the energy dissipation associated with new fracture creation and iii) the accretion of elastic energy stored in the solid medium. The nondimensionalization of the energy balance, following the same approach as in Savitski and Detournay (2002), reveals that the problem is a function of only two dimensionless parameters $\mathcal{K}_R(t, K_{Ic-1})$ and $\mathcal{K}_R(t, K_{Ic-2})$. Or alternatively, $\mathcal{K}_R(t, K_{Ic-1})$ and the ratio Instead of $\mathcal{K}_R(t, K_{Ic-2})/\mathcal{K}_R(t, K_{Ic-1}) = K_{Ic-2}/K_{Ic-1}$. To retrieve $\overline{\mathcal{K}}$, we express the dimensionless number $\mathcal{K}_R(t, K_{Ic-1})$ as $\mathcal{K}_R(t_{\text{touch}}, K_{Ic-1})$ and we replace t_{touch} as done in the previous section. Moreover, the energy balance makes it evident that the states of the system, associated to a negligible energy spent in the creation of new fractures are described by the combination $\overline{\mathcal{K}} \ll 1$ and $K_{Ic-2}/K_{Ic-1} \ll 1$. This limit corresponds to

Chapter 5. Conditions for the local arrest of a hydraulic fracture by a toughness heterogeneity

Scenario n. 3 (unperturbed propagation) described before. For other values of the parameters $\overline{\mathcal{K}}$ and K_{Ic-2}/K_{Ic-1} it is possible to fall either in scenario n. 2 (no containment - slowed height growth) or n. 1 (transient containment - transiently arrested height growth). The limit between these scenarios (or limit of occurrence of fracture containment) is defined by a function that relates the two dimensionless parameters: the function $K_{Ic-2}/K_{Ic-1}\left(\overline{\mathcal{K}}\right):\left[V^+ = 0 \text{ and } \Delta t_c = 0\right]$. In what follows we prove the existence of fracture containment and determine this function analytically. To obtain this estimate, we follow two different approaches that eventually lead to two results that differ only about 2% from one another. In both case, we consider the fracture at the moment it touches the interfaces as shown in the cartoon on the top right part of Figure 5.2. Then we study the region around the point along the fracture front that touches one of the interfaces (see the top left part of Figure 5.2). As shown experimentally both in homogeneous (see Bunger and Detournay (2008) or bottom plot in Figure 5.2) and heterogeneous cases (see Garagash et al. (2009)), in this region, the fields $w(x,z)$ and $p_f(x,z)$ reduce to the ones of a plane-strain steadily-moving fluid driven fracture for which asymptotic solutions exist (Garagash, 2009; Garagash et al., 2011). In such an approximation, the fluid velocity coincides with the front velocity V. For finite fractures, up to a distance h from the propagating front, the width-average fluid velocity $\mathbf{v}_f$ and fracture front velocity $\mathbf{v}_s$ can be regarded to be approximately equal, i.e.: $\|\mathbf{v}_f\| \approx \|\mathbf{v}_s(\gamma)\| \approx V$. This applies in case the fluid-lag can be considered negligible:

$$\lim_{\alpha \to 0}\left[\mathbf{v}_f\left(\alpha\mathbf{n}\left(\gamma\right)\right) - \mathbf{v}_s(\gamma)\right] = 0 \quad \forall \gamma \in \Gamma, \, \alpha \in \mathbb{R}^-$$

The fracture opening in a semi-infinite steadily-moving hydraulic fracture has two asymptotic limits separated by a transition length scale ℓ_{mk}. At a distance $\hat{z} \ll \ell_{mk}$ from the propagating front the energy dissipated in the creation of new fractures dominates the one spent in the fluid flow. In this region $w(\hat{z} \ll \ell_{mk}) \to \hat{w}_k = \sqrt{32/\pi}K_{Ic}E'^{-1}\hat{z}^{1/2}$ and the solution is independent of the fluid viscosity. The opposite holds at a distance $\hat{z} \gg \ell_{mk}$ where $w(\hat{z} \gg \ell_{mk}) \to \hat{w}_m = 2^{1/3}3^{5/6}\left(\mu'VE'^{-1}\right)^{1/3}\hat{z}^{2/3}$ (see Garagash (2009); Garagash et al. (2011)). The transition length scale ℓ_{mk} separates the two different asymptotic behaviors characterizing $\hat{w}/w_{mk}$, and it is defined such that $\hat{w}_m(\hat{z}) = \hat{w}_k(\ell_{mk}) \implies \ell_{mk} = K_{Ic}^6/\left(E'^4\mu'^2V^2\right)$. The corresponding scale for the opening is $\hat{w}_m(\ell_{mk}) = \hat{w}_k(\ell_{mk}) = w_{mk} = K_{Ic}^4/\left(E'^3\mu'V\right)$. The bottom plot in Figure 5.2 shows the evolution of the dimensionless opening $\hat{w}/w_{mk}$ as a function of the dimensionless distance $\hat{z}/\ell_{mk}$ from the tip of the steadily-moving hydraulic fracture. When the front touches the interface at $t = t_{\text{touch}}$, the lack of inertia forces makes the system to change instantaneously from the state characterized by G_{c-1}, V^-, w^- and p^-, to a new one, characterized by G_{c-2}, V^+, w^+ and p^+.

The two approaches to find $K_{Ic-2}/K_{Ic-1}\left(\overline{\mathcal{K}}\right):\left[V^+ = 0 \text{ and } \Delta t_c = 0\right]$ differ on the hypothesis that relates the two states of the system. In the first approach, we assume that the energy dissipated by the system does not manifest a sudden change. In the second approach, we assume the fracture opening at the injection point to be equal before and after the fracture touches the interface: $w^-(0,0,t_{\text{touch}}) = w^+(0,0,t_{\text{touch}})$. In the next three sub-sections, we present the two approaches and their comparison to numerical predictions obtained using

the fully-coupled hydraulic fracturing solver PyFrac (Zia and Lecampion, 2020).
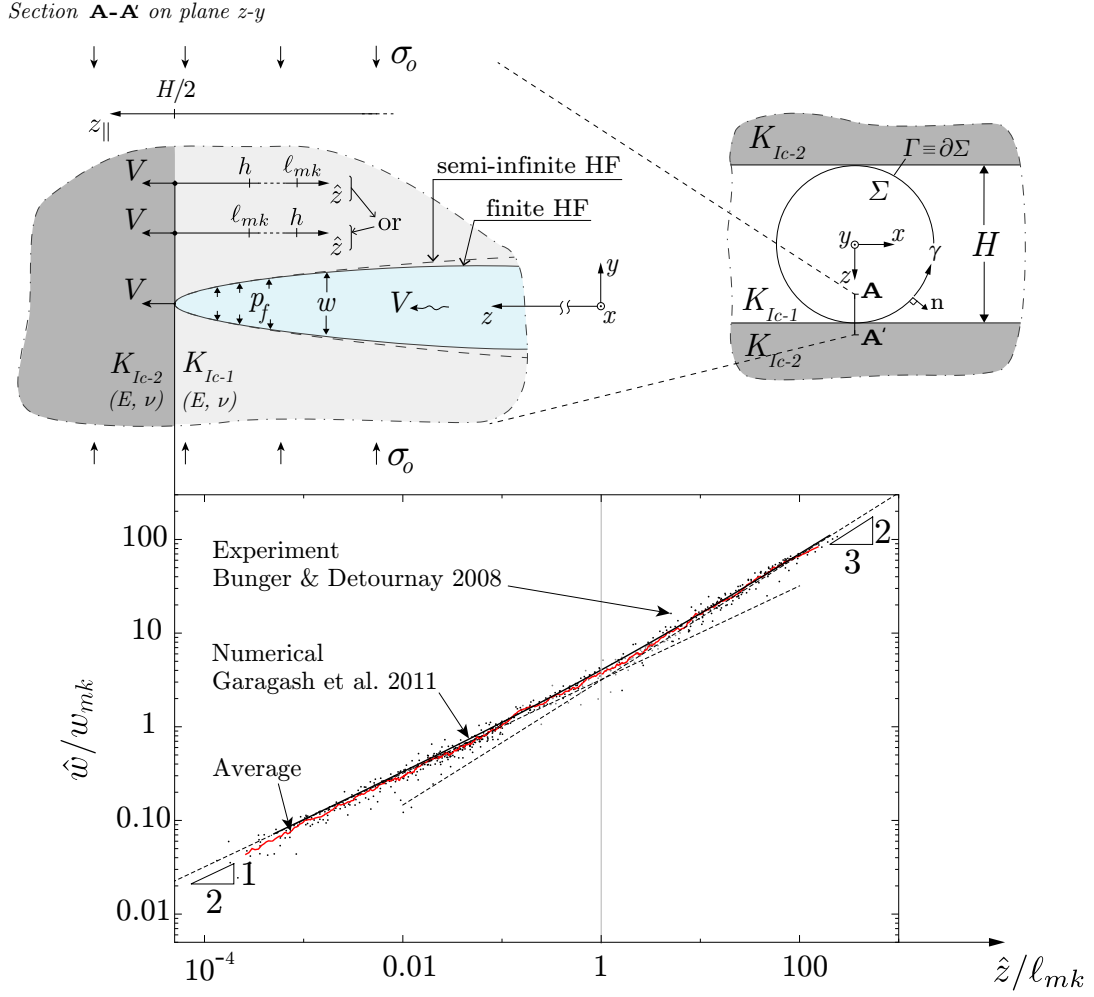
Figure 5.2 – The cartoon on the top-right shows the fracture footprint at the time it has reached the layers interfaces. The interior of the fracture middle's plane is denoted by Σ and its front $\Gamma = \partial \Sigma$ is parametrized by the curvilinear coordinate γ. $\forall \gamma \in \Gamma \, \mathbf{n}(\gamma) :=$ normal vector. The cartoon on the top-left represents a cross section A-A' of the radial fracture along the plane $z - y$ of the tip region $\{(x, z) : x = 0 \text{ and } z \gtrsim h\}$. The coordinate system $\hat{z}$ is attached to the fracture tip and moves with its velocity V. The plot at the bottom (redrawn from Bunger and Detournay (2008)) shows the opening profile $\hat{w}$ of a plane-strain semi-infinite fracture obtained theoretically and experimentally. Two cases are considered $h \gg \ell_{mk}$ and $h \ll \ell_{mk}$. ℓ_{mk} is the length-scale over which w and p_f are influenced from energy dissipation occurring at the tip.

5.2.1   A semi-infinite HF encountering a toughness jump

Energy balance across the jump for the semi-infinite HF

The energy balance in Eq. 5.7 is valid for *any* 3D planar fluid driven fracture. In particular, we can express it for the region close to the crack tip at coordinates $(x, z) = (0, H/2)$ shown in Figure 5.2, and further assume the geometry being described by a plane-strain, semi-infinite and steadily-moving fluid-driven fracture. We limit the integrals to the interval $z \in [H/2 - h, H/2]$. After changing to the reference system $\hat{z}$ moving with the same speed V of the tip $(\mathrm{d}()/\mathrm{d}t = -V\mathrm{d}()/\mathrm{d}\hat{z})$, we obtain:

$$\underbrace{\mu' V^2 \int_0^h \frac{1}{\hat{w}} \mathrm{d}\hat{z}}_{\text{viscous dissipation rate}} + \underbrace{G \times V}_{\text{energy rel. rate}} + \underbrace{\int_0^h \frac{1}{2} \frac{\mathrm{d}}{\mathrm{d}\hat{z}} \left(\hat{w} \times (\hat{p}_f - \sigma_o)\right) \mathrm{d}\hat{z}}_{\text{rate of elastic energy accretion}} = \underbrace{V \hat{w}(h) \hat{p}(h)}_{\mathscr{P}_e} \tag{5.8}$$

where $\hat{f}$ highlights the fact that the field f is expressed in the moving reference system $\hat{z}$ $(\hat{f} = f(\hat{z}))$ (see Appendix A for more details). By recalling that $\hat{p}(h) = \left(\hat{p}_f(h) - \sigma_o\right)$ and that $\hat{w}(0)\hat{p}(0) = 0$ (Garagash, 2009; Garagash et al., 2011), the previous equation reduces to:

$$\underbrace{\underbrace{G}_{\text{fracture energy rel.}} + \underbrace{\mu' V \int_0^h \frac{1}{\hat{w}} \mathrm{d}\hat{z}}_{\text{viscous dissipation}}}_{\text{Total internal dissipated energy}} = \underbrace{\frac{1}{2}\hat{w}(h)\hat{p}(h)}_{\text{quota of ext. energy dissipated}} \tag{5.9}$$

The latter is formally an energy balance valid at any given time. Furthermore, the first term on the right hand side corresponds to the quota of external energy provided to the system that is dissipated during the process by viscous flow and fracturing. Substituting the previous equation into the propagation condition 5.5, we obtain:

$$\begin{cases} \left(\underbrace{\frac{1}{2}\hat{w}(h)\hat{p}(h)}_{\text{quota of ext. energy dissipated}} - \underbrace{\mu' V \int_0^h \frac{1}{\hat{w}} \mathrm{d}\hat{z}}_{\text{viscous dissipation}} - G_c \right) V = 0 \qquad \forall \gamma \in \Gamma \\ V \geq 0 \end{cases} \tag{5.10}$$

We now apply this propagation condition at the moment when such a semi-infinite hydraulic fracture touches the fracture toughness boundary (see Figure 5.2). In the state characterized by G_{c-1}, V^-, $\hat{w}^-$ and $\hat{p}^-$, since $V^- > 0$, we have

$$\frac{1}{2}\hat{w}^-(h)\hat{p}^-(h) = V^- \mu' \int_0^h \frac{1}{\hat{w}^-} \mathrm{d}\hat{z} + G_{c-1} \tag{5.11}$$

We then assume that the energy enters the system at $\hat{z} = h$, and that the quota of external

energy does not change:

$$\frac{1}{2}\hat{w}^-(h)\hat{p}^-(h) \equiv \frac{1}{2}\hat{w}^+(h)\hat{p}^+(h) \quad \text{at } t = t_{\text{touch}} \tag{5.12}$$

This assumption is justified by the fact that the change of material fracture energy happens suddenly at time t_{touch}.

Considering Eq. 5.10 for the propagation in the medium n. 2 and substituting Eqs. 5.11 and 5.12 therein leads to:

$$\left\{ \begin{array}{c} \left[\underbrace{\left(V^-\mu'\int_0^h \frac{1}{\hat{w}^-}d\hat{z} + G_{c-1}\right)}_{\text{total dissipation in medium n.1}} - \underbrace{\left(V^+\mu'\int_0^h \frac{1}{\hat{w}^+}d\hat{z} + G_{c-2}\right)}_{\text{total dissipation in medium n.2}} \right] V^+ = 0 \\ V^+ \geq 0 \end{array} \right. \tag{5.13}$$

This new form of the propagation condition includes all the dissipation mechanisms and provides a relationship that justifies the three different scenarios at $t = t_{\text{touch}}$.

- In case the local velocity changes from $V^- > 0$ to $V^+ > 0$ the system 5.13 reduces to:

$$V^-\mu'\int_0^h \frac{1}{\hat{w}^-}d\hat{z} + G_{c-1} = V^+\mu'\int_0^h \frac{1}{\hat{w}^+}d\hat{z} + G_{c-2} \tag{5.14}$$

We rescale the fracture opening $\hat{w}(\hat{z})$ by introducing the characteristic length-scale ℓ_{mk} and opening w_{mk} such that $w(\hat{z}/\ell_{mk}) = w_{mk}\Omega(\hat{z}/\ell_{mk})$. ℓ_{mk} is the length-scale over which w and p_f are influenced from energy dissipation occurring at the tip:

$$\left(\int_0^{h/\ell_{mk-1}} \frac{1}{\Omega^-(\hat{z}/\ell_{mk-1})}d(\hat{z}/\ell_{mk-1}) + 1\right)G_{c-1} = \left(\int_0^{h/\ell_{mk-2}} \frac{1}{\Omega^+(\hat{z}/\ell_{mk-2})}d(\hat{z}/\ell_{mk-2}) + 1\right)G_{c-2}$$

A simple approximation, up to a few percent error, for the function $w(\hat{z}/\ell_{mk})$ has been proposed by Dontsov and Peirce (2015) where: $w(\hat{z}/\ell_{mk}) = w_{mk}\Omega(\hat{z}/\ell_{mk})$ and $\Omega(s) = \sqrt{\frac{32}{\pi}}\left(1 + \frac{9}{64}\sqrt{\frac{3}{2}}\pi^{3/2}\sqrt{s}\right)^{1/3}\sqrt{s}$ with $s = \hat{z}/\ell_{mk}$. It allows us to express each integral in the previous equation as:

$$\int_0^{\frac{h}{\ell_{mk-i}}} \frac{1}{\Omega^-\left(\frac{\hat{z}}{\ell_{mk-i}}\right)}d\left(\frac{\hat{z}}{\ell_{mk-i}}\right) = \frac{-32 \times 3^{1/3} + \left(128\sqrt{6} + 54\pi^{3/2}\sqrt{\frac{h}{\ell_{mk-i}}}\right)^{2/3}}{6 \times 3^{5/6}\pi} \quad i = 1, 2 \tag{5.15}$$

A simple inspection of this result reveals that the energy dissipated in the fluid flow is proportional to $(h/\ell_{mk})^{1/3}$. In virtue of that, we can approximate Eq. 5.14 as:

$$\left[hE'\mu'^2(V^-)^2\right]^{1/3} + G_{c-1} = \left[hE'\mu'^2(V^+)^2\right]^{1/3} + G_{c-2}$$

This equation demonstrates that a positive toughness jump $G_{c-2}/G_{c-1} > 1$ implies that

upon touching the interface $V^- > V^+ > 0$.

- In case $V^+ = 0$ and $\Delta t_c \geq 0$ the system 5.13 reduces to:

$$\left(V^- \mu' \int_0^h \frac{1}{w^-} d\hat{z} + G_{c-1} \right) \leq G_{c-2} \tag{5.16}$$

where the equivalence corresponds to the special case of $\Delta t_c = 0$. Using ℓ_{mk-1} and w_{mk-1} to scale the integral of Eq. 5.16 leads to:

$$\frac{K_{Ic-2}}{K_{Ic-1}} = \left(1 + \int_0^{h/\ell_{mk-1}} \frac{1}{\Omega^-(\hat{z}/\ell_{mk-1})} d(\hat{z}/\ell_{mk-1}) \right)^{1/2} \tag{5.17}$$

where $w(\hat{z}/\ell_{mk}) = w_{mk}\Omega(\hat{z}/\ell_{mk})$. By substituting the result in Eq. 5.15 in the previous equation we finally obtain the ratio of toughness between the two materials which is sufficient to stop the propagation of a semi-infinite HF in the limiting case of zero time of containment ($\Delta t_c = 0$)

$$\frac{K_{Ic-2}}{K_{Ic-1}} = \sqrt{1 + \frac{-32 \times 3^{1/3} + \left(128\sqrt{6} + 54\pi^{3/2}\sqrt{\frac{h}{\ell_{mk-1}}} \right)^{2/3}}{6 \times 3^{5/6}\pi}} \tag{5.18}$$

We recall that, in this equation, h represents the distance from the crack tip at which we truncate the energy balance for the semi-infinite fracture problem. A physical meaning to h will be given when considering the problem in the context of a finite fracture problem.

Matching the far field opening across the jump for the semi-infinite HF

Here we present a similar, somewhat simpler, approach to obtain an estimate for the ratio of toughness between the two materials that is sufficient to stop the propagation of a semi-infinite HF in the limiting case of zero time of containment:$\Delta t_c = 0$. At time $t = t_{\text{touch}}$ the system changes from the state characterized by G_{c-1}, V^-, $w^-(\hat{z})$, to the one characterized by G_{c-2}, V^+, $w^+(\hat{z})$. We assume that at a distance $\hat{z} = h$ from the fracture front the fracture opening remains unchanged:

$$w^-(h, t_{\text{touch}}) = w^+(h, t_{\text{touch}}) \tag{5.19}$$

Making use of the approximation $w(\hat{z}/\ell_{mk})$ proposed by Dontsov and Peirce (2015), the previous equation reduces to:

$$V^+ = V^- - \frac{64}{9}\sqrt{\frac{2}{3\pi^3}} \frac{\left(K_{Ic-2}^3 - K_{Ic-1}^3 \right)}{\mu' E'^2 \sqrt{h}} \tag{5.20}$$

Note that this expression is valid only at time $t = t_{\text{touch}}$. It shows similar properties of the system:

- $V^+ = 0$ when the second term on the right hand side of the previous equation is $\geq V^-$. This corresponds to *Scenario n. 1* (transient containment - transiently arrested height growth);

- $V^+ < V^-$ when $K_{Ic-2} > K_{Ic-1}$, this corresponds to *Scenario n. 2* (no containment - slowed height growth);

- $V^+ \to V^-$ when $\frac{(K_{Ic-2}^3 - K_{Ic-1}^3)}{\mu' E'^2 \sqrt{h}} \to 0$ that corresponds to *Scenario n. 3* (unperturbed propagation);

By assuming that $V^+ = 0$, Eq. 5.20 can be re-expressed to obtain the minimum toughness ratio require to stop the semi-infinite hydraulic fracture at the interface:

$$\frac{K_{Ic-2}}{K_{Ic-1}} = \left(1 + \frac{9}{64} \sqrt{\frac{3\pi^3}{2}} \sqrt{h/\ell_{mk-1}} \right)^{1/3} \tag{5.21}$$

5.2.2 Application to a finite HF encountering a toughness jump

To estimate the function $K_{Ic-2}/K_{Ic-1}\left(\overline{\mathscr{K}}\right) : \left[V^+ = 0 \text{ and } \Delta t_c = 0\right]$, we consider the penny-shaped hydraulic fracture at the moment it touches the interfaces as shown in the top right part of Fig. 5.2. In a layer close to the fracture front the solution reduces to the one of a semi-infinite hydraulic fracture moving at the local front speed (top left part of Fig. 5.2). For this reason, we have previously estimated the function $K_{Ic-2}/K_{Ic-1}(h/\ell_{mk-1}) : \left[V^+ = 0 \text{ and } \Delta t_c = 0\right]$ for the semi-infinite fracture problem (i.e.: Eqs. 5.21 or 5.18). To derive these estimates, we have introduced a generic distance h where either the fracture opening, or the external energy, have been assumed independent from the toughness variation occurring at the front. To link the semi-infinite fracture problem to the actual one, we match h to the fracture radius at t_{touch} i.e.: $h = H/2$ and we set the velocity V^- to be the one of the radial fracture. This is equivalent to introducing both, the characteristic length scale of the finite fracture H and the global volume balance via the radial velocity V^-. This approach is essentially the same as the one discussed in Garagash (2009) to investigate the propagation regimes of a finite hydraulic fracture.

Energy balance across the jump for a finite HF

We introduce $h = H/2$ and the velocity of the viscosity dominated regime V_M at t_{touch}, in the dimensionless number h/ℓ_{mk} obtaining (without reporting prefactors): $H/\ell_{mk} = \overline{\mathscr{K}}^{-6}$. Thus, Eq. 5.18, in the viscosity scaling, becomes:

$$\frac{K_{Ic-2}}{K_{Ic-1}}\left(\overline{\mathscr{K}}\right) = \frac{1}{3\sqrt{2\pi}} \sqrt{-32\sqrt{3} + 18\pi + 2^{1/3}3^{1/6}\left(221.703 + \frac{70.6819}{\overline{\mathscr{K}}^3}\right)^{2/3}} \quad \overline{\mathscr{K}} < 1 \tag{5.22}$$

Chapter 5. Conditions for the local arrest of a hydraulic fracture by a toughness heterogeneity

For the toughness scaling we express the velocity of the toughness dominated regime V_K at t_{touch} obtaining, (without reporting the prefactors): $H/\ell_{mk} = \overline{\mathcal{M}}^{-3/2}$ with $\overline{\mathcal{M}} = \overline{\mathcal{K}}^{-4}$. Then, Eq. 5.18 becomes:

$$\frac{K_{Ic-2}}{K_{Ic-1}}\left(\overline{\mathcal{M}}\right) = \sqrt{1 + \frac{1}{180\pi}\left[-320\sqrt{3} + 3^{1/6}5^{1/3}\left(2560\sqrt{3} + 162\sqrt{2}\pi\overline{\mathcal{M}}\right)^{2/3}\right]} \quad \overline{\mathcal{M}} < 1 \qquad (5.23)$$

Taking a Maclaurin expansion of Eqs. 5.22, we obtain:

$$\frac{K_{Ic-2}}{K_{Ic-1}}\left(\overline{\mathcal{K}} \to 0\right) \propto \overline{\mathcal{K}}^{-1} + \mathcal{O}\left(\overline{\mathcal{K}}\right) \qquad (5.24)$$

This demonstrates that, in the cases where there is a finite amount of fracture toughness in the system, a toughness ratio that allows the fracture containment always exist. Then, taking a Maclaurin expansion of Eq. 5.23 result in: $\frac{K_{Ic-2}}{K_{Ic-1}}\left(\overline{\mathcal{M}} \to 0\right) \propto 1 + \mathcal{O}\left(\overline{\mathcal{M}}\right)$. This shows that in case of negligible dissipation due to the viscous flow (compared to the one involved in the creation of new fractures) an arbitrarily small increase of fracture toughness along the front is sufficient to locally stop the fracture propagation.

Matching the opening across the jump for a finite HF

Similarly to what has been done in the previous paragraph, we introduce $h = H/2$ and $V_M(t_{\text{touch}})$ (*viscosity scaling*) or $V_K(t_{\text{touch}})$ (*toughness scaling*) with the right prefactors Savitski and Detournay (2002), in Eq. 5.21:

$$\frac{K_{Ic-2}}{K_{Ic-1}} = \left(1 + \frac{0.3188}{\overline{\mathcal{K}}^3}\right)^{1/3} \quad \overline{\mathcal{K}} < 1 \qquad (5.25)$$

$$\frac{K_{Ic-2}}{K_{Ic-1}} = \left(1 + \frac{27\pi}{640}\sqrt{\frac{3}{2}}\overline{\mathcal{M}}\right)^{1/3} \quad \overline{\mathcal{M}} < 1 \qquad (5.26)$$

When taking a Maclaurin expansion of these equations, the same limits that have been found previously by energy conservation arguments can be retrieved up to a prefactor of order one.

5.2.3 Comparisons

In the top part of Fig. 5.3, we plot the estimates of the function $K_{Ic-2}/K_{Ic-1}\left(\overline{\mathcal{K}}\right) : \left[V^+ = 0 \text{ and } \Delta t_c = 0\right]$ provided by the different approaches discussed: the "energy approach" and the "$w(H)$-matching" approach. The equations 5.22, 5.25 are valid for $\overline{\mathcal{K}} \ll 1$ while Eqs. 5.23 and 5.26 are valid for $\overline{\mathcal{K}} \gg 1$. These estimates divide the parametric space $\left(\overline{\mathcal{K}}, K_{Ic-2}/K_{Ic-1}\right)$ in two regions as shown in the top plot of Fig. 5.3. The upper region consists of all points above $K_{Ic-2}/K_{Ic-1}\left(\overline{\mathcal{K}}\right) : \left[V^+ = 0 \text{ and } \Delta t_c = 0\right]$ and it is characterized by a period containment $\Delta t_c > 0$. Conversely, in the region below $K_{Ic-2}/K_{Ic-1}\left(\overline{\mathcal{K}}\right) : \left[V^+ = 0 \text{ and } \Delta t_c = 0\right]$ the break-

through takes place as soon as the fracture has reached the interface. The relative difference between the two estimates is plotted in the bottom part of Fig. 5.3. It is computed by taking as a reference the "$w(H)$-matching" approach. The relative difference is comprised between 1% and 2% showing that the different assumptions behind the two approaches lead to similar results in the whole parametric space.
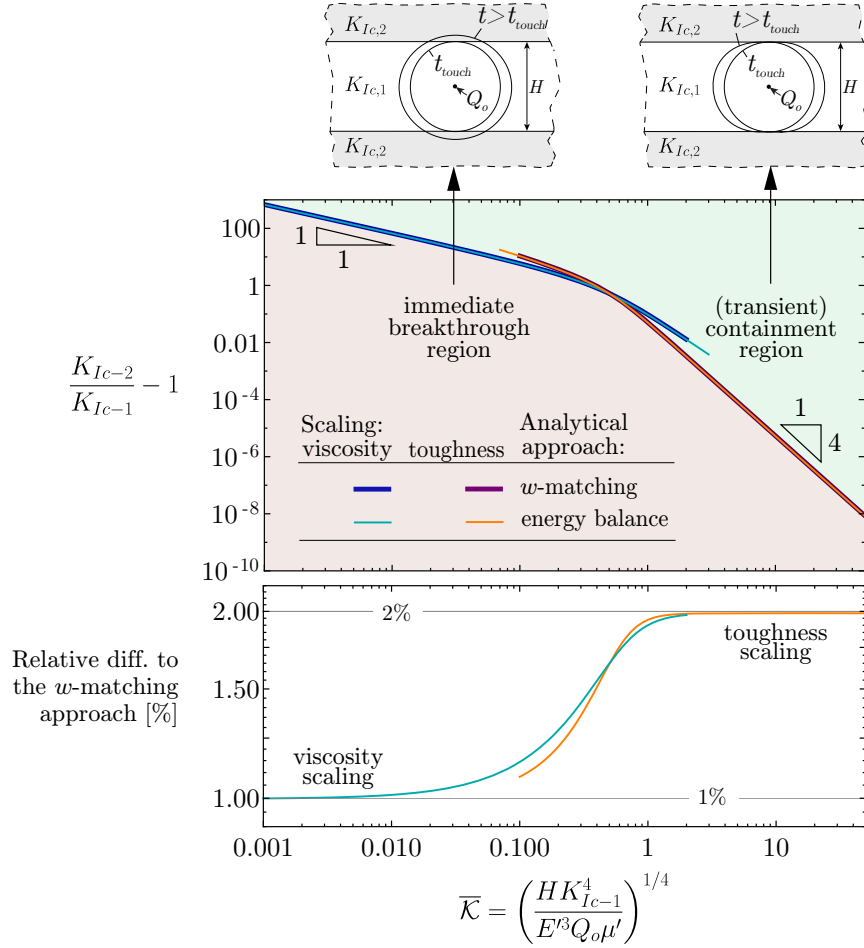
Figure 5.3 – Comparison between the estimates of the function $K_{Ic-2}/K_{Ic-1}\left(\overline{\mathcal{K}}\right)$: $\left[V^+ = 0 \text{ and } \Delta t_c = 0\right]$ provided by two different approaches. The top plot shows, in the viscosity scaling, Eqs. 5.22 with a thin green line, 5.25 with a thick blue line and, in the toughness scaling, Eqs. 5.23 (thin orange line) 5.26 (thick purple line). The bottom plot shows the relative difference between the two approaches in the respective ranges of validity

In Fig. 5.4, we compare the estimates provided by Eqs. 5.25 (dashed blue curve) and 5.26 (dashed red curve) with the numerical estimation obtained by using the 3D-Planar hydraulic fracture simulator Pyfrac Zia and Lecampion (2020) (green stars). The numerical solution is obtained by stating that the breakthrough takes place when the aspect ratio of the fracture is two percent larger than one: $L/(0.5H) = 1.02$. The largest relative difference between the

analytical estimates and the numerical results is 38%±2.5% in the limit $\overline{\mathcal{K}} \to 0$. While Eqs. 5.25 and 5.26 have been obtained by replacing V^- in Eq. 5.21 with the fracture velocity either in the viscosity (M-) or in the toughness dominated regime (K-regime), the numerical simulations allows us to use the actual V^- at t_{touch}. The related curve is represented by the orange crosses in Fig. 5.4. Similarly, the black line with circular markers is obtained by inserting in Eq. 5.21 the velocity V^- computed numerically by Madyarova (2003) for a radial hydraulic fracture.
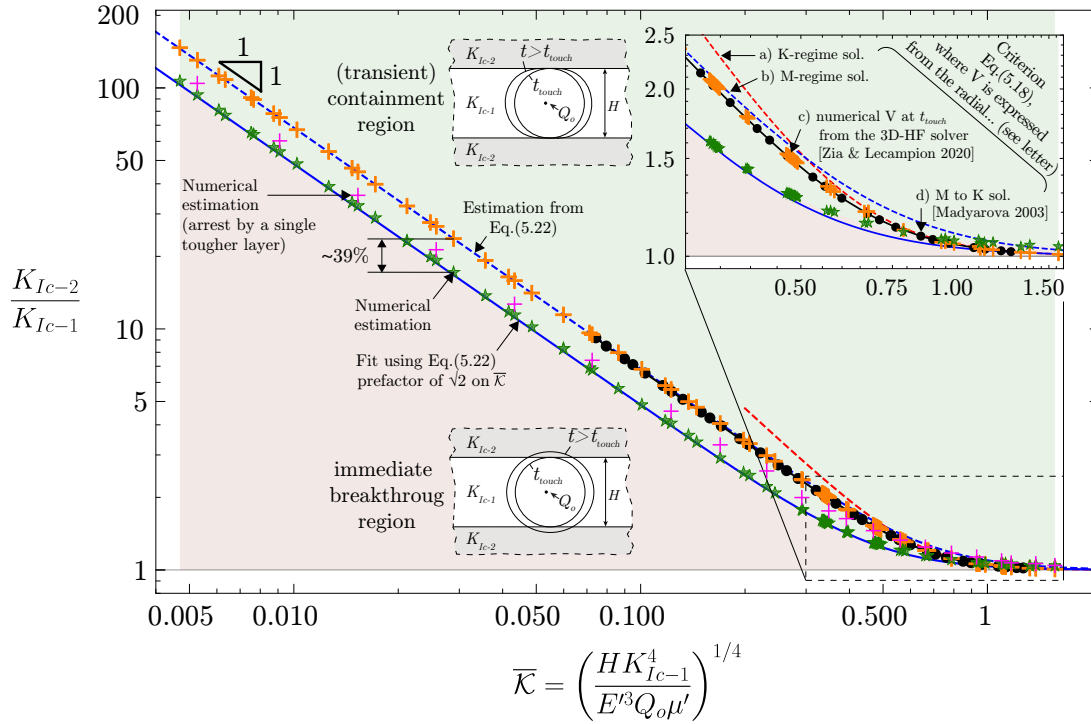
Figure 5.4 – Parametric space of the problem delimiting regions of immediate breakthrough (red), and local arrest (green) for a hydraulic fracture encountering an infinite toughness heterogeneity. The green stars represent points where the breakthrough happens almost immediately (aspect ratio at breakthrough = 1.02). They correspond to the numerical solution obtained using the 3D-Planar hydraulic fracture simulator PyFac Zia and Lecampion (2020). The orange crosses correspond to the semi-analytical equation 5.21 evaluated with the actual numerical estimate of the fracture velocity V^-. The same equation has been evaluated using the velocity obtained numerically in Madyarova (2003). The corresponding results are plotted using a black line with black dots as markers.

5.3 Conclusions

In this chapter, focusing on the case of hydraulic fracture propagating from a point source encountering a symmetrical jump of fracture toughness, we have established a relationship for the local arrest of the fracture as a function of i) the intensity of the fracture toughness heterogeneity ($K_{Ic,2}/K_{Ic,1}$) and ii) the ratio of the energy dissipated in surface creation versus fluid

flow in the fracture at the instant where it touches the heterogeneity ($\overline{\mathcal{K}}$). Using arguments based on the near-tip behavior of a steadily moving hydraulic fracture, we have established analytical expressions for the minimum toughness ratio in the viscosity dominated and toughness dominated regimes. These analytical predictions are in-line with fully-coupled planar 3D simulations. Notably, the minimum toughness ratio scales as $1/\overline{\mathcal{K}}$ when the fracture propagates in the viscosity dominated regime, and obviously tends to one in the toughness dominated regime. Although established with the case of a symmetrical toughness jump in mind (the case of two bounding layers), these results are actually valid for any type of toughness heterogeneity as their expression are local by nature. In practice, the minimum toughness ratio as a function of the propagation regime $\overline{\mathcal{K}}$ for a local arrest to occur is not the final quantity of interest. If arrested by a layer of larger toughness, it remains to quantify how long the hydraulic fracture will remain arrested: this is the subject of the next chapter.

6 Fracture containment by two layers of higher fracture toughness

Note: This chapter is currently being adapted into a scientific publication:
C. Peruzzo, B. Lecampion, "*How long a planar 3D hydraulic fracture remains contained by two layers of larger toughness*", to be submitted to Int. J. Eng. Sci., 2023

6.1   Introduction

In this work, we consider a hydraulic fracture propagating initially radially in a layer bounded by two layers having a larger fracture toughness than the central layer. At the moment when the hydraulic fracture touches the tougher layers, it can either break through immediately into the bounding layers or can be transiently contained and grow with a blade-like / PKN geometry, at least for a while. Recent work has quantified the minimum ratio of fracture toughness required for the containment to occur as a function of the ratio between viscous and fracture energy dissipation, see Peruzzo and Lecampion (2023). In the following, for toughness values above this minimum ratio of fracture toughness, that is the case when containment does occur, we estimate the amount of time the fracture remains contained between the bounding layers. We quantify the duration of containment as a function of both the ratio of fracture toughness and the main energy dissipation mechanism at the moment when the fracture reaches the

interfaces of the tougher layers. Our semi-analytical predictions are compared to numerical ones obtained with the fully-coupled 3D-planar hydraulic fracture simulator PyFrac (Zia and Lecampion, 2020). Throughout this work, we assume the hypotheses of quasi-static linear hydraulic fracture mechanics (Detournay, 2016) and focus on 3D-planar fracture propagation in an infinite impermeable medium driven by the injection of a Newtonian fluid at a constant rate.

6.2 Order of magnitude of the fracture toughness contrast between rock layers

Adjacent rock strata can have different mode-I fracture toughness. Before quantifying the effect of such a toughness contrast on hydraulic fracture propagation, we first discuss the order of magnitude of the variation of fracture toughness observed in rocks. We found solely one work (Senseny and Pfeifle, 1984) that estimated the natural distribution of fracture toughness between layers considering hectometers-long successions of layers at depths $\gtrsim 1\,$km from the surface of the Earth. In particular, the published data consists of the vertical distribution of fracture toughness measured at a number of depths in three wellbores in the Rulison Field – Piceance Basin, Garfield County, Colorado, USA. The same method ("short rod specimen" test (Barker, 1977)) was used in all the samples to measure the fracture toughness. The three plots in Figure 6.1a) reproduce the data sets b_k for each borehole ($k = 1, 2, 3$). Each point in the plots reports the average fracture toughness in a thin layer from which up to 6 fracture toughness measurements were performed from just as many samples. We consider the layers to be thin because they have an average thickness of 0.53 m (Std. Dev. of 1.03 m, min. thickness of 0.10 m, max of 7.00 m), which is much smaller than the extent of the investigated ranges of depth (min > 300 m). To estimate how frequently a given toughness contrast $\left(K_{Ic-i}/K_{Ic-j}\right)_k \geq 1$ is within each wellbore k, we start by taking all the possible combinations of layers $(i, j)_k$ with $i \neq j$. Then, for each data set b_k, we count the number of toughness ratios $\left(K_{Ic-i}/K_{Ic-j}\right)_k$ falling in a given interval of amplitude 0.1. The results are shown in the histogram at the top of Figure 6.1b). We note that only in few occasions is the toughness ratio $\left(K_{Ic-i}/K_{Ic-j}\right)_k \geq 2$. By inspecting the data set b_1 in Figure 6.1a), most of the toughness ratios > 2, shown in Figure 6.1b), are due to the presence of just one layer with very low fracture toughness. In order to compare the results between the different data sets, we computed both the relative and the cumulative relative frequency of a given toughness ratio. The results are shown in Figure 6.1c) The cumulative relative frequency evolution does not substantially differ among different b_k. This can be explained by the relatively small distance between the three wellbores (min ~ 30 m, max ~ 152 m (Atkinson et al., 1981)). The cumulative relative frequency shows that, by randomly taking a combination of layers $(i, j)_k$ with $i \neq j$ and $k \in [1, 3]$, a toughness ratio $K_{Ic-max}/K_{Ic-min} \in (1, 2]$ can be found in $\approx 80\%$ of the cases. This result can not yet be safely considered to represent an order of magnitude, without considering other examples.
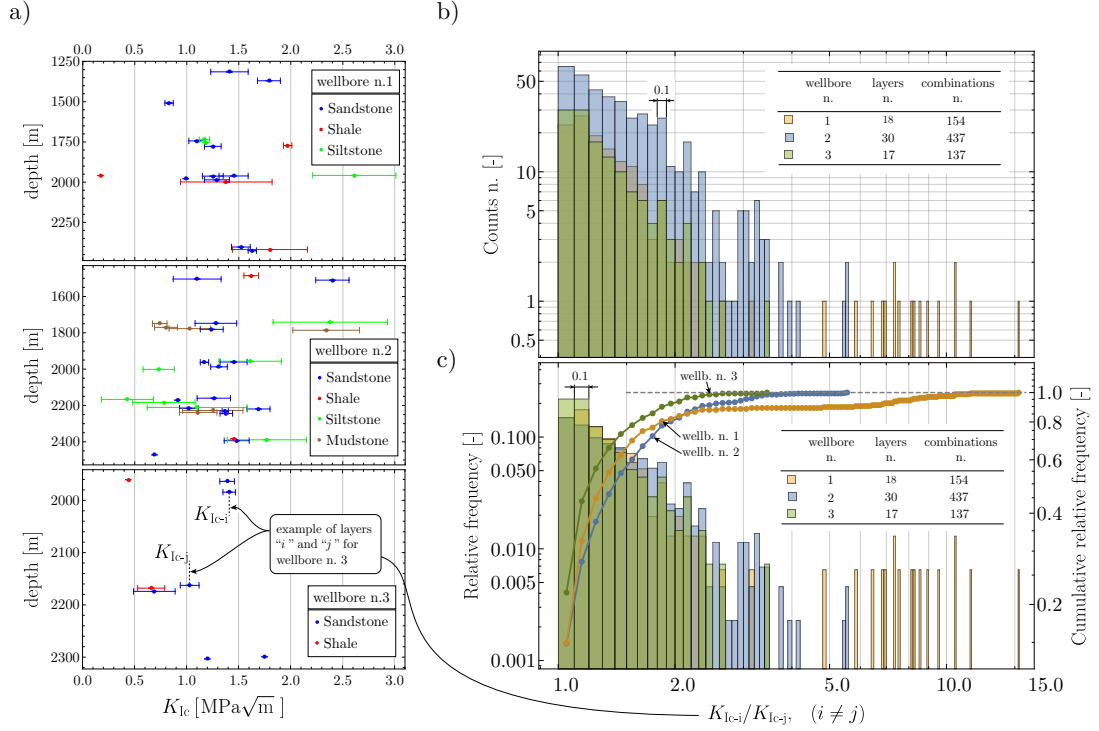
Figure 6.1 – *a*) Mode-I fracture toughness (K_{Ic}) at different depths from 3 different boreholes. Data reproduced from Senseny and Pfeifle (1984). The horizontal error bar represents the error in the measurements, while the vertical one (barely visible) represents the thickness of layer *i* where $K_{\mathrm{Ic}-i}$ was measured. *b*) histogram of toughness ratios $K_{\mathrm{Ic}-i}/K_{\mathrm{Ic}-j} > 1$ (const. intervals of size 0.1). *c*) shows, on the left vertical axis, the histogram of the relative frequency of toughness ratio. The cumulative relative frequency is shown on the right axis.

Unfortunately, due to the absence of other similar works, we also analyze fracture toughness measurements of rock samples that have not necessarily been obtained from a natural succession of rock layers nor measured by the same experimental protocol / author(s). We consider published results where, within the same work, fracture toughness measurements are reported either for different lithologies (see Table 6.2) or for different rock units of the same lithology (see Table 6.1). Then, for each work, we compute the maximum toughness ratio that can be observed among the measurements. In almost all the cases in tables 6.2 and 6.1, the largest toughness ratio is greater than 2. This evidence only confirms that the interval (1, 2] estimated from the work of Senseny and Pfeifle (1984) is not an outlier. From all the data presented, it emerges that typical values of mode-I *toughness ratios*, measured from rock samples of decimeter-scale, happen to be mostly in a range $\approx$ (1, 2]. Since the published data that can be used for this estimation is both limited in terms of the number of measurements and heterogeneous in its quality, we do not claim this conclusion to be definitive - but this range can be considered to give a realistic order of magnitude for the variation of laboratory derived fracture toughness between different sedimentary rocks.

Lithology	n. of rock units	$K_{Ic}\,[\mathrm{MPa\,m}^{1/2}]$	$\frac{K_{Ic-max}}{K_{Ic-min}}$	Ref.
Sandstone	3	$0.36 \le K_{Ic} \le 0.89$	2.5	Nara et al., 2012
	3	$0.37 \le K_{Ic} \le 1.1$	2.9	Roy et al., 2017
	5	$0.49 \le K_{Ic} \le 1.60$	3.3	Noël et al., 2021
	3	$0.98 \le K_{Ic} \le 2.12$	2.2	Thiercelin, 1989
	3	$0.53 \le K_{Ic} \le 0.73$	1.38	Chandler et al., 2016
Limestone	3	$0.48 \le K_{Ic} \le 0.92$	1.9	Chandler et al., 2016
	2	$1.36 \le K_{Ic} \le 2.06$	1.5	Gunsallus et al., 1984

Table 6.1 – Mode-I fracture toughness ranges for typical rocks in conventional and unconventional reservoirs (Schmoker and Oscarson, 1995; Zou, 2013). For each lithology, we report the range of fracture toughness measured by each research group under the same conditions (group specific) but testing different rock units of the same lithology. The ratio K_{Ic-max}/K_{Ic-min} represents the ratio between the extremes of each range. Comparisons between rows are not possible because of the different testing methods and conditions used in the different works. Each value of fracture toughness is the average of at least 2 samples of the same rock unit within the same lithology.

6.3 Problem definition

We consider three layers made of the same impermeable linear-elastic material, characterized by a uniform Young's modulus E, Poisson's ratio v, and uniform confining stress σ_o acting perpendicularly to the plane $x - z$ in Figure 6.2-a). The central layer has thickness H, while the others extend indefinitely above and below. The material in the central layer differs from the others by its fracture energy G_{c-1} which is smaller than the one of the bounding layers G_{c-2}. Throughout the rest of this work, we will either refer to G_{c-i} $i = 1, 2$, or to the fracture toughness $K_{Ic-i} = \sqrt{E' G_{c-i}}$ where $E' = E/(1 - v^2)$ (Irwin, 1957). An incompressible Newtonian fluid of viscosity μ is injected at the center of the middle layer. The injection proceeds at a constant rate Q_o and drives the propagation of a penny shape fracture initially. The fracture is characterized by its diameter $2L(t)$ evolving in time t, the fracture opening $w(x, z, t)$, and the net pressure $p(x, z, t)$ or, equivalently, by the fluid pressure $p_f(x, z, t) = p(x, z, t) + \sigma_o$. In addition to the usual hypotheses of linear hydraulic fracture mechanics (Detournay, 2016), we further assume that:

- the dimension of the injection source (the wellbore diameter) is assumed to be much smaller than the fracture length such that the injection can be considered to take place at a point.

- the fluid lag is assumed to remain negligible during the entire process. This condition

Lithology	n. of rock units	$K_{Ic}\left[\mathrm{MPa\,m}^{1/2}\right]$	$\frac{K_{Ic-max}}{K_{Ic-min}}$	Ref.
Granite[a]	1	2.14	5.9	Nara et al., 2012
Sandstone[a]	3	$0.36 \leq K_{Ic} \leq 0.89$		
Shale[b]	1	0.31	3.4	Roy et al., 2017
Sandstone*	3	$0.37 \leq K_{Ic} \leq 1.1$		
Mudstone*	1	2.12	4.9	Thiercelin, 1989
Shale*	1	0.43		
Sandstone*	3	$0.98 \leq K_{Ic} \leq 2.12$		
Shale[a]	1	0.44	2.1	Chandler et al., 2016
Shale[b]	1	0.44		
Limestone*	3	$0.48 \leq K_{Ic} \leq 0.92$		
Sandstone*	3	$0.53 \leq K_{Ic} \leq 0.73$		
Dolostone*	5	$1.66 \leq K_{Ic} \leq 2.47$	1.8	Gunsallus et al., 1984
Sandstone*	1	1.47		
Limestone*	2	$1.36 \leq K_{Ic} \leq 2.06$		

*= no explicit information are given about the direction of crack propagation with respect to the bedding planes. Otherwise: [a] = arrester direction,[b] = divider direction

Table 6.2 – Comparison of Mode-I fracture toughness K_{Ic} between lithologies studied by the same research group. Comparisons between rows are not possible because of the different methods and protocols used to measure fracture toughness. Each fracture toughness value reported is the average of at least 2 samples for the same rock unit.

is ensured when $\mu V E'^2/\sigma_o^3 \ll 1$ where V is the fracture front velocity (Garagash and Detournay, 1998). This is typically the case for deep fractures in rocks for which σ_o is sufficiently large (Lecampion and Detournay, 2007).

- the fracture is assumed to propagate on the same plane after touching the interfaces between the layers. This represents one possible limiting case for the interaction of a hydraulic fracture with a layer's interfaces in sedimentary rock formations (see Bunger and Lecampion (2017) for more discussion).

- gravity effects are negligible, an assumption we further discuss at the end of this paper.

The equations governing this moving boundary problem relate to elasticity, fluid flow, and fracture propagation. The quasi-static balance of momentum for the elastic solid can be reduced to a scalar boundary integral equation for a single mode I planar 3D fracture (Hills

et al., 2013; Crouch S.L., 1983),

$$p(x,z) = p_f(x,z) - \sigma_o = -\frac{E'}{8\pi} \int_{\Sigma(t)} \frac{w(x',z',t)}{\left[(x'-x)^2 + (z'-z)^2\right]^{3/2}} dx' dz',$$ (6.1)

where the Σ represents the fracture's trace on the middle fracture plane. Lubrication flow apply in the fracture, and the local fluid volume conservation in the case of an impermeable rock reads (Batchelor, 1967):

$$\frac{\partial w(x,z,t)}{\partial t} + \nabla \cdot \mathbf{q} - \delta(x)\delta(z)Q_o(x,z,t) = 0 ,$$ (6.2)

which provides after integrating both time and space the global volume balance

$$\int_{\Sigma(t)} w(x',z',t) dx' dz' = Q_o t .$$ (6.3)

The width-averaged balance of momentum for the fluid under laminar flow gives the well-known Poiseuille relation:

$$\mathbf{q} = \left[\begin{array}{cc} q_x & q_z \end{array}\right] = -\frac{w(x,z,t)^3}{\mu'} \nabla p(x,z,t) \quad \mu' = 12\mu$$ (6.4)

and the quasi-static fracture propagation conditions locally reads:

$$\left\{ \begin{array}{c} V(\gamma)G_c(\gamma) \geq 0 \\ (G - G_c(\gamma))V(\gamma) = 0 \end{array} \right. \quad \forall \gamma \in \Gamma$$ (6.5)

where G is the energy release rate, $V(\gamma) = \mathbf{v}(x,z) \cdot \mathbf{n}(\gamma)$ is the magnitude of the local fracture front velocity at the curvilinear coordinate γ along the front and $\mathbf{n}(\gamma)$ is the normal to the front. In the absence of a fluid lag, both the width and the fluid flux normal to the front vanishes at the crack front (see Detournay and Peirce (2014) for discussion).

Under the previous assumptions, at $t_1 = t_{\text{touch}}$ when the fracture touches the interfaces, three scenarios are possible, as sketched in Figure 6.2-a) (see Peruzzo and Lecampion (2023)). These three scenarios differ in relation to the change of velocity at the top and bottom points γ_1 and γ_2, where the fracture front first touches the tougher layers (see Figure 6.2).

a)

b)
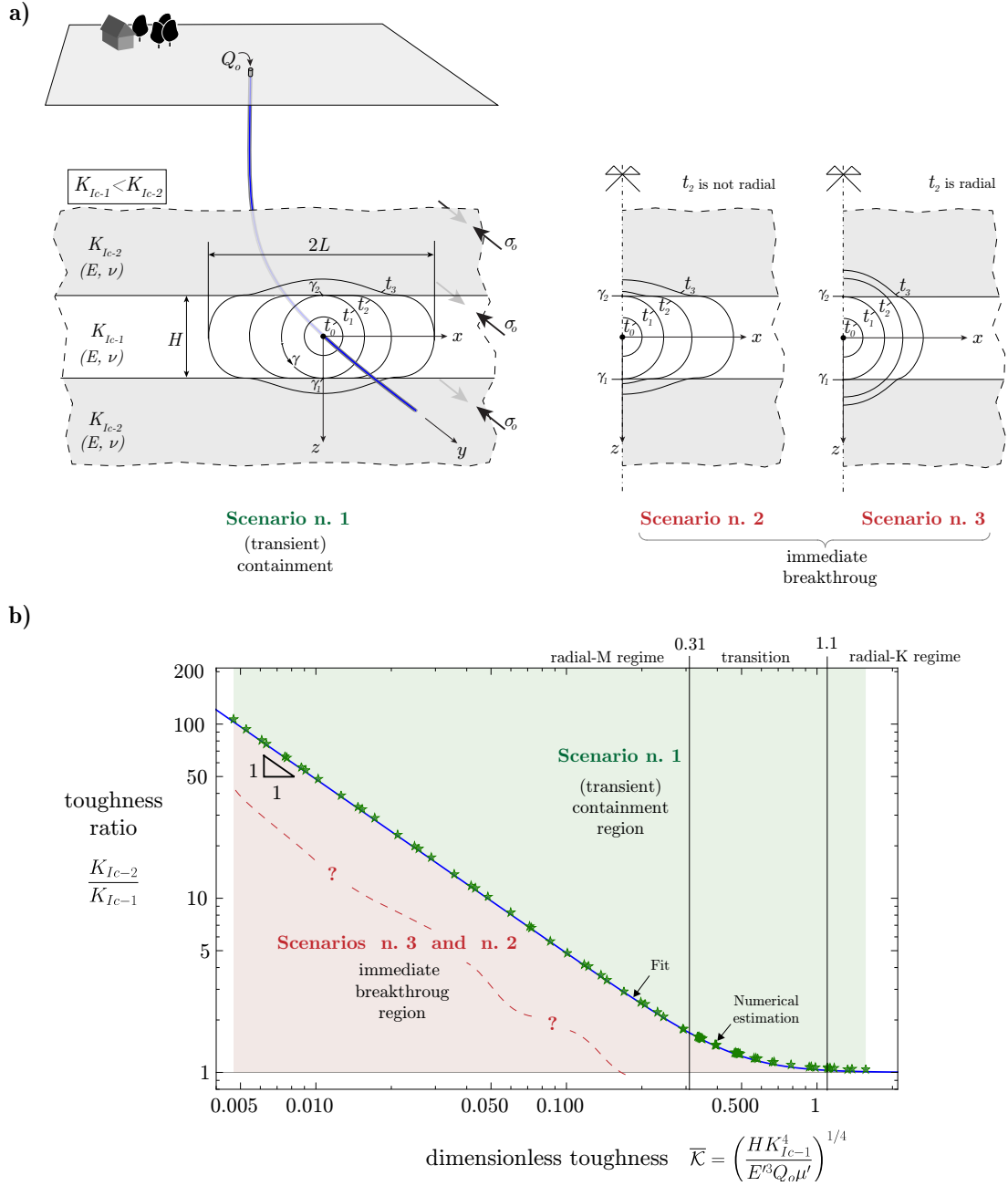
Figure 6.2 – *a*) Sketch representing the three-layer configuration considered throughout this work and the different possible evolution of the fracture upon reaching the interfaces with the bounding layers. *b*) parametric space that represents the separations between the different scenarios. Both, *a*) and *b*) are adapted from Peruzzo and Lecampion (2023).

- *Scenario n. 1* (transient containment - or alternatively transiently arrested height growth): the fracture front stops immediately upon reaching the interfaces. The fracture then grows only horizontally in the central layer. The fluid flow occurs only along the

x direction, with the exception of the region near the injection point where the flow transitions from radial to unidirectional. The fracture then remains confined between the two interfaces for a finite amount of time Δt_c, albeit possibly small. Moreover, as it will be shown later, in the case of a finite amount of fluid viscosity, the containment time Δt_c is always finite.

- *Scenario n. 2* (no containment - slowed height growth): the propagation continues immediately in the new medium albeit at a lower velocity. The fracture footprint deviates significantly from a radial geometry.

- *Scenario n. 3* (unperturbed propagation): the fracture crosses the interface maintaining (temporarily) a radial shape. After some time, the fracture senses the larger toughness which then starts to affect the shape of the fracture front. In any case, no containment is possible.

In Peruzzo and Lecampion (2023), the limit between *Scenario n. 1* and the *Scenarios n. 2 & 3* has been obtained as a function of two dimensionless numbers: the ratio of fracture toughness between the layers K_{Ic-2}/K_{Ic-1} and the dimensionless toughness of the initially radial fracture when it touches the interfaces:

$$\overline{\mathcal{K}} = K_{Ic-1} \left(\frac{H}{E'^3 Q_o \mu'} \right)^{1/4} \tag{6.6}$$

The limit in such parametric space is shown in Fig. 6.2-b) (see Peruzzo and Lecampion (2023)). It is important to recall the meaning of the dimensionless toughness $\overline{\mathcal{K}}$ as we will estimate Δt_c as function of $\overline{\mathcal{K}}$ and K_{Ic-2}/K_{Ic-1}. Before the fracture reaches the interfaces, the solution of equations 6.1,6.2, (or 6.3), 6.4 and 6.5 in terms of L, w and p, depends on a single dimensionless number as shown by Savitski and Detournay (2002). This number can be expressed in the form of a *dimensionless toughness*

$$\mathcal{K}_R = K_{Ic-1} \left(\frac{1}{E'^{13} Q_o^3 \mu'^5} \right)^{1/18} t^{1/9} \tag{6.7}$$

(where the subscript "R" reminds us that it refers to the case of a radial fracture). Note the dependence of this number on time. The parameter $\overline{\mathcal{K}}$ corresponds to the value of $\mathcal{K}_R$ at the time a viscosity dominated hydraulic fracture reaches a diameter H. In particular, we define t_{touch} as the time t such that $L_{R-M}(t) \equiv H$, where the function $L_{R-M}(t)$ represents how the characteristic radius of a penny shaped hydraulic fracture scales with time in the viscosity dominated regime (see for example Eq. (27) in Savitski and Detournay (2002)). To find the expression for $\overline{\mathcal{K}}$ in Eq.(6.6), we simply substitute this estimate for t_{touch} in $\mathcal{K}_R$. According to Savitski and Detournay (2002), (pending a factor $\sqrt{32/\pi}$ used in this previous contribution) when the dimensionless toughness $\mathcal{K}_R \gtrsim 1.097$, a penny shaped fracture propagates in the toughness dominated regime whereas, when $\mathcal{K}_\mathcal{R} \lesssim 0.313$ the fracture grows in the viscosity dominated regime. Naturally, these limits apply to $\overline{\mathcal{K}}$ as well, and they are marked in Fig. 6.2-b).

6.4 Quantification of the duration of fracture containment

6.4.1 Fully confined fractures: the transition from K to M

In the limit $K_{Ic-2}/K_{Ic-1} \to \infty$, the fracture will remain contained between the bounding layers indefinitely. The aspect ratio of the fracture $L/(0.5H)$ increases as the fracture spreads along the x direction as injection continues. For a sufficiently large aspect ratio, the problem can be approximated by a constant height fracture model known as the PKN model (Perkins and Kern, 1961; Nordgren, 1972; Adachi and Peirce, 2007). Such a well-known hydraulic fracture model assumes that:

1. The fracture footprint has a rectangular/blade-like shape. In other words, the fracture height H (see Fig. 6.2) is constant,

2. For each coordinate x, the net pressure $p(x)$ is only a function of x, rather than both x and z: the fluid flow becomes unidirectional.

3. Any cross-section on a plane parallel to $z - y$ in Fig. 6.2-a) has an elliptical shape, independently from the value of the aspect ratio $L/(0.5H)$.

Upon the introduction of these assumptions in the system of Eqs. (6.1), (6.2), (6.4) and (6.5) two limiting solutions can be derived. The first one is the viscosity dominated regime for a PKN fracture where fracture energy/toughness is negligible. This viscosity limit corresponds to the original hypothesis layout in Perkins and Kern (1961), and Nordgren (1972) (see also Kemp (1990)). A more accurate solution was obtained in Kovalyshen and Detournay (2009) as:

$$w_{PKN-M}(x=0,z,t) = 2.2142 \left(\frac{\mu Q_o^2}{E'H}\right)^{1/5} t^{1/5} \sqrt{1 - \left(\frac{2z}{H}\right)^2}$$
$$p_{PKN-M}(x=0,z,t) = 1.1071 \left(\frac{\mu E'^4 Q_o^2}{H^6}\right)^{1/5} t^{1/5} \qquad (6.8)$$
$$L_{PKN-M}(t) = 0.660422 \left(\frac{2}{\pi^3}\right)^{1/5} \left(\frac{E'Q_o^3}{\mu H^4}\right)^{1/5} t^{4/5}$$

We will denote it shortly as the PKN-M solution (M for viscosity). The second limiting solution corresponds to the toughness dominated regime for a PKN fracture, where the energy dissipated in the viscous fluid flow is neglected entirely. Such a PKN-K solution (K for toughness) was derived in Sarvaramini and Garagash (2015):

$$w_{PKN-K}(x,z,t) = \frac{4}{\sqrt{\pi}} \frac{K_{Ic}\sqrt{H}}{E'} \sqrt{1 - \left(\frac{2z}{H}\right)^2}$$
$$p_{PKN-K}(x,z,t) = 2\frac{K_{Ic}}{\sqrt{\pi H}} \qquad (6.9)$$
$$L_{PKN-K}(t) = \frac{E'Q_o}{\sqrt{\pi}K_{Ic}H^{3/2}} t$$

As already noted in Dontsov (2021) Garagash (2023), a PKN fracture evolves from the "early time" toughness-dominated to the "late time" viscosity-dominated regime. This behavior can be explained intuitively after observing that the energy dissipated in the fluid flow is proportional to the fracture length (see L in Fig. 6.2 a)) while the energy dissipated in the

creation of new fracture surfaces is proportional to the extension of the propagating front (see H in Fig. 6.2 -a)). Since the latter quantity remains constant while the former increases, the viscous fluid flow, therefore, dominates at "late time". On the contrary, in the case of a fracture propagating with a radial shape, the late time behavior is toughness dominated. Indeed for a radial fracture, the ratio between the energy dissipation mechanisms in Eq. (6.7) increases with the fracture diameter and thus time (as per Eq. (6.6)). The characteristic transition-times between the toughness and viscosity-dominated regimes for both the radial and PKN fracture geometries are recalled in Table 6.3. In the same Table, the other characteristic scales are also reported for completeness (fracture size L, the net pressure p and fracture opening w), all are evaluated at the transition time between the two limiting regimes. These quantities can be

PKN fracture		Radial fracture	
t_{K-M}	$\dfrac{H^{7/2}K_{Ic}^5}{E'^4\mu Q_o^2}$	t_{M-K}	$\left(\dfrac{E'^{13}Q_o^3\mu'^5}{K_{Ic}^{18}}\right)^{1/2}$
p_{K-M}	$\dfrac{K_{Ic}}{\sqrt{H}}$	p_{M-K}	$\left(\dfrac{K_{Ic}^6}{E'^3\mu'Q_o}\right)^{1/2}$
w_{K-M}	$\dfrac{\sqrt{H}K_{Ic}}{E'}$	w_{M-K}	$\left(\dfrac{E'\mu'Q_o}{K_{Ic}^2}\right)^{1/2}$
L_{K-M}	$\dfrac{H^2K_{Ic}^4}{E'^3\mu Q_o}$	L_{M-K}	$\dfrac{E'^3\mu'Q_o}{K_{Ic}^4}$

Table 6.3 – Transition scales for time t, net pressure p, fracture opening w, and fracture length/radius L in the PKN and radial models respectively.

used to express the ratio between the powers dissipated in the two dissipation mechanisms. For example, a PKN fracture of length $L \gg L_{K-M(PKN)}$ propagates in the PKN-M regime, while if $L \ll L_{K-M(PKN)}$ it propagates in the toughness dominated regime. Moreover, they can also be used to relate the fracture evolution from the initial radial propagation (prior to reaching the interfaces) to the elongated (blade-shaped) fracture described by the PKN model. The radial fracture can reach the layer boundaries at different times during the transition from the viscosity-dominated regime (radial-M) $\overline{\mathcal{K}} \ll 1$ to the toughness-dominated regime (radial-K) $\overline{\mathcal{K}} \gg 1$. We can actually express the dimensionless toughness $\overline{\mathcal{K}}$, using the following ratio of length-scales:

$$\overline{\mathcal{K}}^4 = \frac{H}{L_{M-K(RADIAL)}}. \tag{6.10}$$

By recalling how the propagation regimes are linked to the values of $\overline{\mathcal{K}}$, we observe that:

$$\begin{cases} H \ll L_{M-K(RADIAL)} \Rightarrow \text{radial-M regime at } t_{\text{touch}} \\ H \gg L_{M-K(RADIAL)} \Rightarrow \text{radial-K regime at } t_{\text{touch}} \end{cases} \tag{6.11}$$

In addition, up to a constant prefactor, the ratios between the radial and the PKN transition length-scales are actually related as:

$$\frac{H}{L_{M-K(RADIAL)}} = \frac{L_{K-M(PKN)}}{H} \tag{6.12}$$

This implies that the ratio between the energy dissipation mechanisms when the fracture is being confined is also reflected in the subsequent PKN behavior:

$$\begin{cases} H \ll L_{M-K(RADIAL)} \Rightarrow H \gg L_{K-M(PKN)} \Rightarrow \text{PKN-M regime at } t_{\text{touch}} \\ H \gg L_{M-K(RADIAL)} \Rightarrow H \ll L_{K-M(PKN)} \Rightarrow \text{PKN-K regime at } t_{\text{touch}} \end{cases} \tag{6.13}$$

As a result, we finally obtain that:

$$\begin{cases} \text{radial-M regime at } t_{\text{touch}} \Rightarrow \text{PKN-M regime at } t_{\text{touch}} \\ \text{radial-K regime at } t_{\text{touch}} \Rightarrow \text{PKN-K regime at } t_{\text{touch}} \end{cases} \tag{6.14}$$

The same reasoning can be conducted in terms of time-scales. We first have to note that the transition time-scales of the radial and the PKN fractures are linked (see Table 6.3 for their respective expressions). In fact, up to a prefactor of $\mathcal{O}(1)$:

$$\overline{\mathcal{K}} = \left(\frac{t_{K-M(PKN)}}{t_{M-K(RADIAL)}} \right)^{1/14} \tag{6.15}$$

Moreover, by recalling that $\overline{\mathcal{K}} = \mathcal{K}(t_{\text{touch-M}})$ and that $\mathcal{K}(t) = \left(t/t_{M-K(RADIAL)}\right)^{1/9}$, we obtain the following relation between the transition time-scales for a strictly radial and a strictly PKN hydraulic fracture and the time at which the radial fracture reaches (touches) the interface:

$$\left(\frac{t_{\text{touch-M}}}{t_{M-K(RADIAL)}} \right)^{5} = \left(\frac{t_{K-M(PKN)}}{t_{\text{touch-M}}} \right)^{9} \tag{6.16}$$

As a result, if a radial fracture touches the interfaces in the Radial-M regime that is $t_{\text{touch}} < t_{M-K(RADIAL)}$, respectively in the Radial-K regime ($t_{\text{touch}} > t_{M-K(RADIAL)}$) then the PKN fracture will propagate in the PKN-M regime with $t_{\text{touch}} > t_{K-M(PKN)}$, respectively in the PKN-K regime ($t_{\text{touch}} < t_{K-M(PKN)}$).

It is important to keep in mind that the PKN-behaviour is not immediately established when the radial fracture reaches the interfaces. The fracture aspect ratio $L/(0.5H)$ has to increase sufficiently above unity for the PKN model to be valid (Adachi and Peirce, 2007). In Fig. 6.3, we show a comprehensive description of the transition from radial to PKN-like fracture propagation. In particular, we compare the numerical solution of the 3D-planar problem (colored dotted curves) to the different radial and PKN solutions (black continuous and dashed lines). The plots in this figure represent the fracture length L in the x-direction (parallel to the layers), the fracture length z_{max} in the z-direction (orthogonal to the layers), the inlet net pressure $p(0,0,t)$, and fracture opening $w(0,0,t)$, as a function of t. In Figs. 6.3-d), -e), and f), these quantities are nondimensionalized by their corresponding values at the times

of touching the interfaces. In Figs. 6.3-a), -b), and c) the scales correspond to the ones reported in Table 6.3. We present a total of six different numerical simulations, each of them characterized by a different value of dimensionless toughness $\overline{\mathcal{K}}$ and marked by a different color. The dimensional values of the parameters chosen for each simulation are reported in the Appendix. The time when each fracture touches the interfaces is marked by a red dot. The curves characterized by $\overline{\mathcal{K}} = 5.68$ and $\overline{\mathcal{K}} = 0.0568$ in Fig. 6.3-a), -b), and c) touch the interfaces in the radial-K and radial-M regimes, respectively. As predicted by the scaling relations 6.13, after a small transition period, these tend to the PKN-K and PKN-M regimes respectively. The simulation $\overline{\mathcal{K}} = 5.68$ has been interrupted before the transition to the PKN-M regime was reached due to the large computational cost that it would have involved. Instead, the transition from the PKN-K to the PKN-M regime is partially represented by the set of simulations with $\overline{\mathcal{K}} = 1.01, 0.568, 0.319$. The plot in Fig. 6.3-d) shows the evolution of the fracture length L as a function of time, while the fracture grown in the z direction is reported in the Appendix . The inset quantifies the relative difference between the two limiting PKN solutions. For $\overline{\mathcal{K}} = 5.68$, the relative difference is computed with respect to the PKN-K solution, while for $\overline{\mathcal{K}} = 0.180$ and $\overline{\mathcal{K}} = 0.0568$, the PKN-M is taken as a reference. Interestingly, the difference to the PKN-M solution is less than about $\sim 1\%$ only when the fracture aspect ratio has reached $L/(0.5H) \sim 5$. For $\overline{\mathcal{K}} = 5.68$, this aspect ratio has to increase as much as $L/(0.5H) \sim 20$ for the relative difference to be of $\sim 1\%$. The plot in Fig. 6.3-e) shows that, during the transition from the radial-M to the PKN-M behaviour, the net pressure at the injection point reaches a minimum that is only $\sim 17\%$ less than the PKN-K pressure. The pressure at the injection point in the radial-M analytical solution is log-singular. When it is rescaled by $p_{radial-M}(t_{\text{touch}})$ it becomes $p_{radial-M}(t)/p_{radial-M}(t_{\text{touch}}) = (t/t_{\text{touch}})^{-1/3}$. Nevertheless, To circumvent the log-singularity at the inlet, we consider the scaled-pressure equal to the pressure of the radial-M solution at t_{touch} and at a small distance from the injection point $(0.01446 \times H)$. To highlight this on the plot in Fig. 6.3-e), we have used a dashed line to represent the PKN-M analytical solution. Interestingly, the plot in Fig. 6.3-f) shows that the fracture opening between t/t_{touch} and $\sim 2t/t_{\text{touch}}$ is evolving more or less independently of $\bar{\mathcal{K}}$. Such independence with respect to the ratio of viscous to fracture energy dissipation is only observed on the fracture opening. The inset in Fig. 6.3-f) quantifies the relative difference to the PKN solutions. The green dots (lower curve) and the brown dots (upper curve) represent the relative difference of the numerical solutions to the PKN-M solution for $\overline{\mathcal{K}} = 0.180$ and $\overline{\mathcal{K}} = 0.0568$. The reason why the relative difference is smaller for $\overline{\mathcal{K}} = 0.180$ is due to the different numerical accuracy achieved with different spatial discretizations. Denoting ℓ_{cell} the size of an element of the mesh, $H/\ell_{cell} = 47.6$ for the first simulation, respectively $H/\ell_{cell} = 33.72$ for the second. The purple and scattered dots refer to $\overline{\mathcal{K}} = 5.68$ and are obtained by comparing to the PKN-K solution. The plots presented in Fig. 6.3 confirm the validity of the two limiting solutions of the PKN model and their underlying assumptions. For aspect ratio $L/0.5H \gtrsim 5$, an initially viscosity dominated hydraulic fracture differs by less than 5% from the PKN-M solution. The same is not true for initially toughness dominated fractures. These require $L/0.5H \gtrsim 20$ for the evolution of L to differ less than 5% to the PKN-K solution.

Figure 6.3 – Transition from radial to a fully contained PKN hydraulic fractures in the limit $K_{Ic,2}/K_{Ic,1} \to \infty$. Sub-figures *a*), *b*) and *c*) show the evolution of fracture length L, net pressure p and opening w. Sub-figure *d*), *e*), and *f*) present the same results but scaled by using the corresponding quantities at t_{touch}. Different colors are used to distinguish the different values of the dimensionless toughness $\overline{\mathcal{K}}$. The red dots mark the instant when the radial fracture touches the bounding layers. The black-continuous lines represent the PKN-K and PKN-M analytical solutions. The black-dashed line is parallel to the PKN-M solution. Dotted curves with the same color in different plots represent the results of the same simulations. The dots match the time-discretization in the numerical scheme.

The Figs. 6.4-a), -b), and -c) represent a zoom into the corresponding Figs. 6.3-a), -b), and c). Here, we compare the numerical solution obtained with the 3D-planar numerical solver PyFrac (Zia and Lecampion, 2020) with the numerical solution of the (1D-)PKN model reported in Dontsov (2021) or Garagash (2023) (black line). Note that the large relative difference of the fluid pressure in Fig. 6.4-b) is due to the fact that the pressure obtained from the 3D

simulations is related to the injection point, whereas in the (1D-)PKN model the fluid is injected from a line source. Figs. 6.4-d), and -e) represent the relative difference of the (1D-)PKN model solution to the limiting solutions PKN-K and PKN-M as a function of time. In Fig. 6.4-d), it is shown the relative difference of the crack length evolution whereas Fig. 6.4-e) represents the relative difference of either inlet fluid pressure or inlet fracture opening. The oscillations in the left part of the plot are artifacts associated with the numerical scheme used.
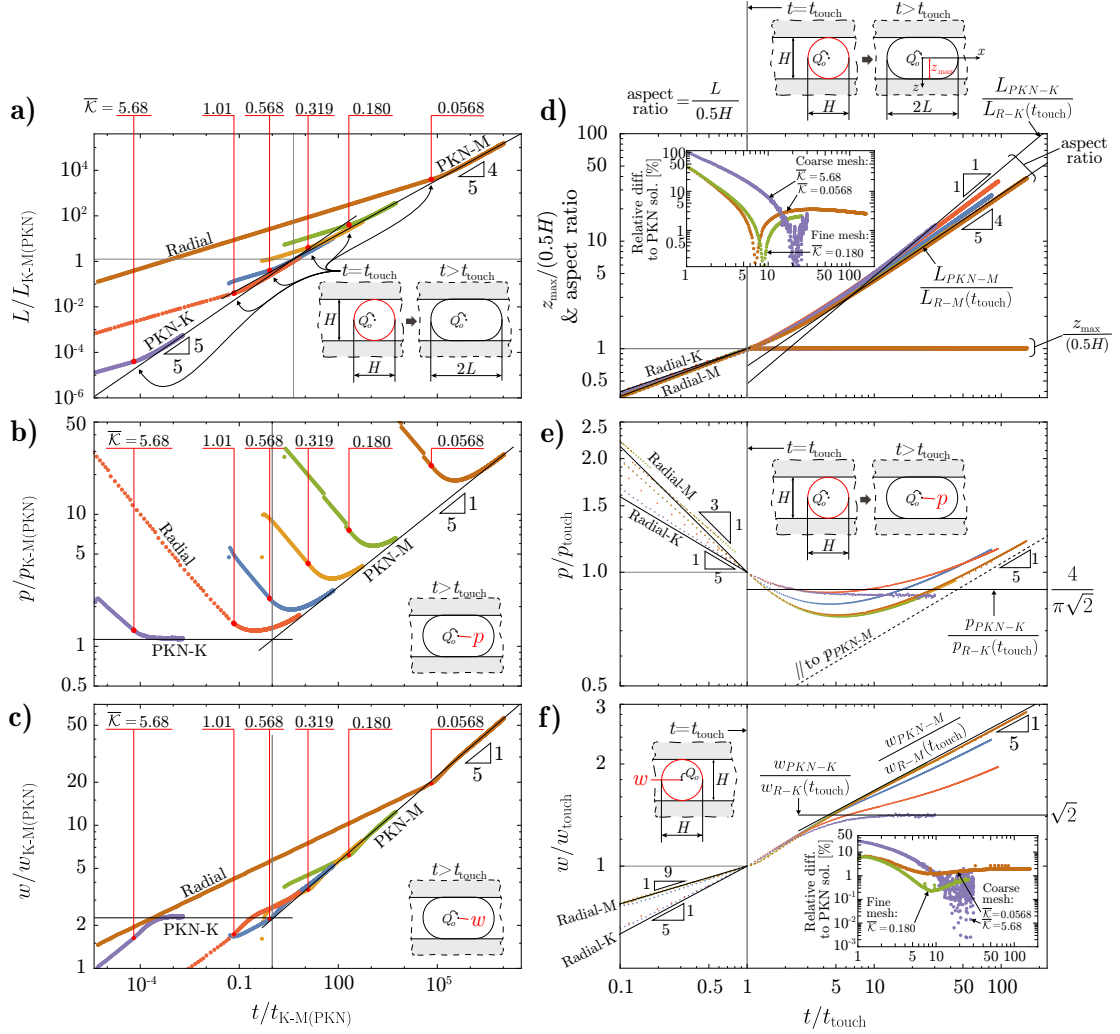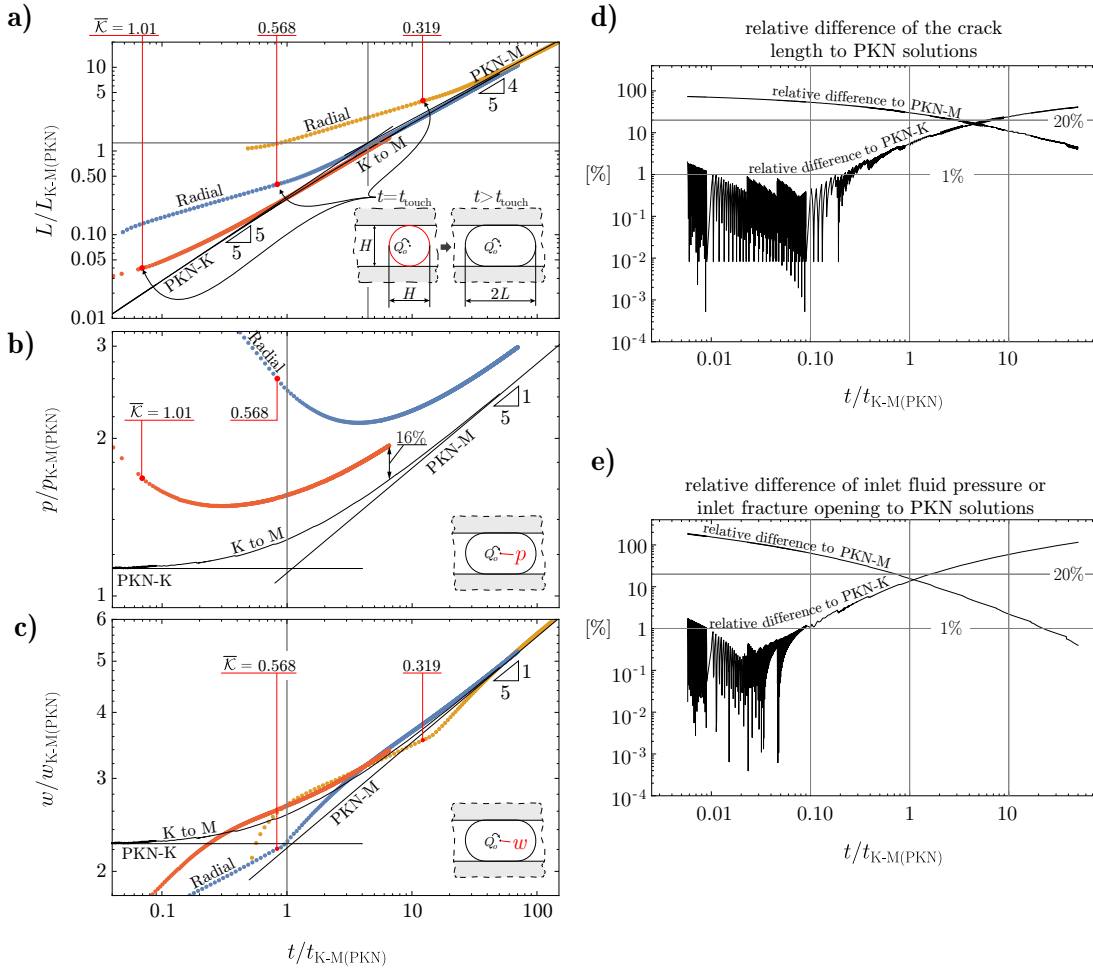

Figure 6.4 – Transition from a radial to a fully contained PKN hydraulic fracture in the limit $K_{Ic,2}/K_{Ic,1} \to \infty$. Sub-figures *a*), *b*), and *c*) are a zoom of the corresponding sub-figures 6.3*a*), *b*), and *c*) where the newly added black lines represent the numerical solution to the (1D-)PKN model reported e.g. in Dontsov (2021) or Garagash (2023). Subfigures *d*), and *e*) report the relative difference of the latter to the PKN-K and PKN-M solutions as a function of the dimensionless time.

6.4.2 The breakthrough time

The toughness dominated PKN limit (PKN-K)

A closer look at the transition from radial to PKN
In the case of zero viscosity, (PKN-K regime), the system of governing equations simplifies further. A key ingredient necessary to derive the analytical solution of the PKN-K regime (Sarvaramini and Garagash, 2015), is the expression of the energy release rate G_{PKN-K} for a such a constant height fracture. It was originally obtained by Dvorak and Laws (1986, 1987) following the idea of Gille (1985) for such a blade like fracture geometry:

$$G_{PKN-K} = \frac{\pi H p^2}{4E'} \Rightarrow K_{I\,PKN-K} = \frac{\sqrt{\pi}}{2} p \sqrt{H} \tag{6.17}$$

Theoretically, Eq. (6.17) represents an exact limit for a fracture with an infinitely large aspect ratio. Ho and Suo (1993) conjectured that the energy release rate of a radial crack that gets confined by two layers quickly approaches this value (6.17) as the fracture aspect ratio $L/(0.5H)$ increases. In Fig. 6.5, we provide quantitative evidence. We compare the analytical expressions for the stress intensity factors of the radial $K_{I\,\text{radial}-K}$ and blade-like $K_{I\,PKN-K} = \sqrt{G_{PKN-K} \times E'}$ geometries against the numerical results obtained by 3D-planar simulations spanning the transition (in the case of an inviscid fracturing fluid). For an aspect ratio $L/(0.5H)$ greater than ~ 2, the relative difference between the analytical and the numerical is about $\sim 1\%$ (see inset in Fig. 6.5). To understand the larger relative difference $\sim 10\%$ for $L/(0.5H) \lesssim 0.5$ and its increase for $L/(0.5H) > 5$, it is important to keep in mind that, numerically, the fracture is growing over a fixed Cartesian mesh. A low number of elements discretizes the fracture at the beginning of the simulation $(L/(0.5H) \lesssim 0.5)$, which leads to an initially large value of the relative difference with respect to the analytical radial-K solution. The increase of the relative difference for a larger aspect ratio $(L/(0.5H) > 5)$ can be understood by recalling a theoretical result obtained in Gao and Rice (1987) which states that for a uniformly loaded mode I fracture, the fracture geometry is known up to a zero-order perturbation. The fracture footprint's position is thus defined up to a "rigid" body motion: an additive constant along the $x-$ and $z-$directions for $L/(0.5H) < 1$ and only along the $x-$direction for $L/(0.5H) \geq 1$. When the number of cells discretizing the fracture is "low", the numerical scheme prevents "artificially" such rigid body motion.When the number of cells increases, the fixed point scheme for the new fracture footprint in the implicit level set algorithm has a harder time converging, due to this rigid body motion. This has a negative impact on the accuracy of the solution. More details about the numerical solution of the system of equations for the zero-viscosity limit and the numerical estimate of G are reported in the Appendix.
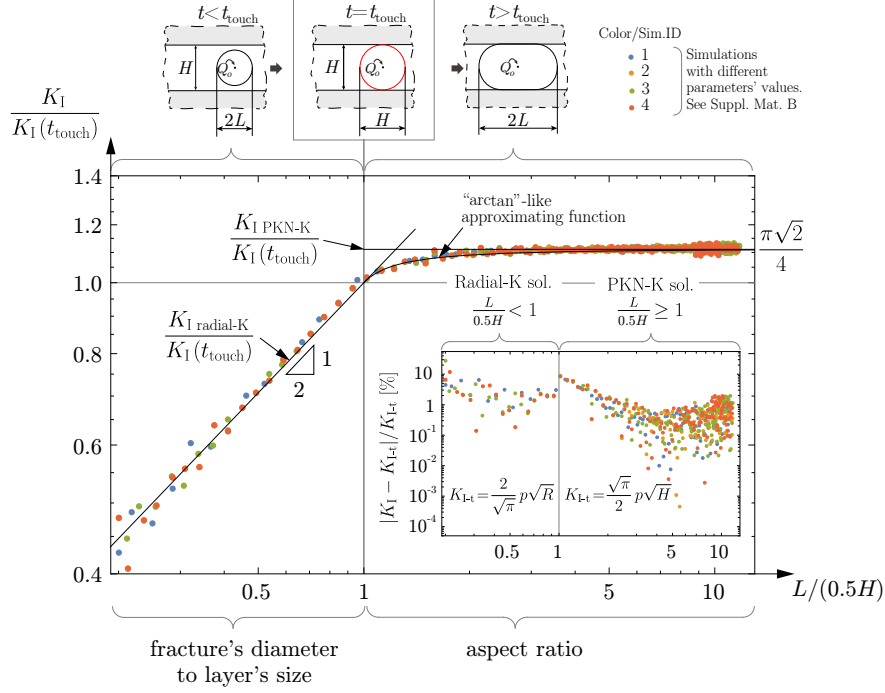
Figure 6.5 – Evolution of the "global" stress intensity factor $K_I = \sqrt{G \times E'}$ for a fracture that gets confined by two layers of higher fracture toughness and propagates driven by the injection of an inviscid fluid. The dots represent the numerical results of 3D-planar simulations. The different colors represent simulations with different parameters (see the Appendix). The black straight lines represent the radial-K ($t < t_{\text{touch}}$) and PKN-K analytical solutions to which we computed the relative *error* for $t < t_{\text{touch}}$ and the relative *difference* for $t \geq t_{\text{touch}}$ shown in the inset. The spaces between dots of the same color match the time-discretization used by the numerical scheme.

Given the accuracy of the estimate for G_{PKN-K} in Eq. (6.17), even for relatively small values of the aspect ratio $L/(0.5H)$, it is interesting to compare the PKN-K solution to numerical simulations of the transition from a radial to a contained geometry. The curves in Fig. 6.6 correspond to two choices of toughness contrasts: $K_{Ic-2}/K_{Ic-1} = 1.47$ and $K_{Ic-2}/K_{Ic-1} = 1.30$, respectively. The first corresponds to a case where the fracture transitions to PKN-K while in the other case, the fracture breaks through before. We first limit our attention to the case where the fracture is able to make the transition to PKN-K. In Fig. 6.6-a), we display the evolution of the fracture radius ($t/t_{\text{touch}} \leq 1$) or half length L ($t/t_{\text{touch}} \geq 1$) scaled by the thickness of the layer H. The inset shows the relative difference of the numerical curve marked by $K_{Ic-2}/K_{Ic-1} = 1.47$ to the pertinent analytical solutions. In Fig. 6.6-b), we plot the evolution of the maximum front position $z_{\max}$. While from the figure it appears that for $K_{Ic-2}/K_{Ic-1} = 1.47$, after t_{touch}, the front position $z_{\max}$ remains constant, the inset shows that the height growth is not always arrested.

The evolution of the fracture opening at the injection point and net pressure in the fracture

are displayed in Figs. 6.6-c), and -d). This last quantity is uniform over the fracture, because the viscosity of the injected fluid is zero. The relative difference of the numerical curves for $K_{Ic-2}/K_{Ic-1} = 1.47$ to the PKN-K solution amounts to few percents for $L/(0.5H) > 1$ (see inset of Figs. 6.6c, d). Note that while both the fluid pressure and the fracture opening differ of less than 5% to the PKN-K solution for $L/(0.5H) \sim 3$, the aspect ratio has to increase up to $L/(0.5H) \sim 8$ before the fracture length matches the PKN-K solution within the same accuracy.
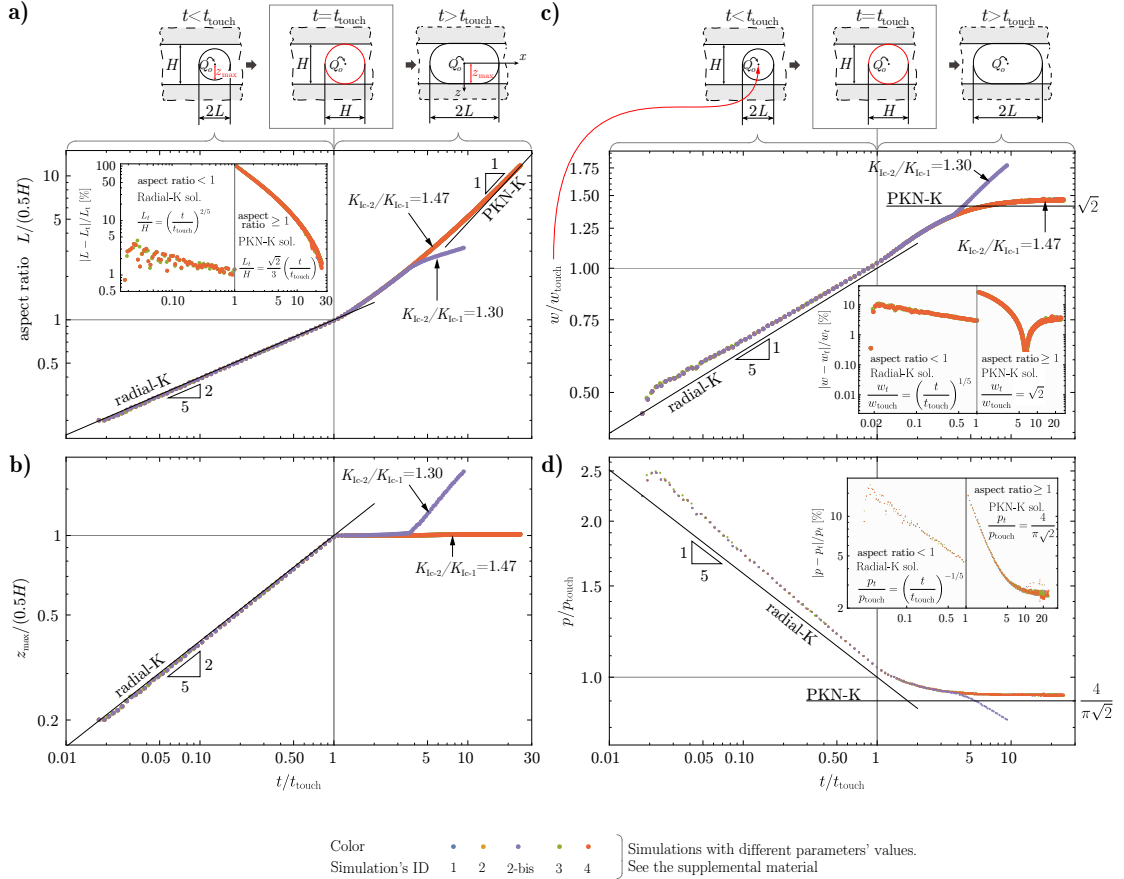
Figure 6.6 – Fracture behavior in case of inviscid fracturing fluid / large toughness limit.The dimensionless *a*) fracture length *L*, *b*) max *z*-coordinate of the front, *c*) opening *w* at the injection point and *d*) pressure *p* are represented as a function of the dimensionless time *t*. The insets of all the sub-figures show the corresponding relative *error* to the radial-K analytical solution for $t < t_{\text{touch}}$ and the relative *difference* to the PKN-K solution for $t > t_{\text{touch}}$. In all the plots, the colors distinguish the parameters used in the simulations (see the Appendix for the values of the different parameters). The spaces between dots of the same color match the time-discretization used by the numerical scheme.

Prediction of the containment duration

The stress intensity factor $K_I^{\perp}$ at the point $x = 0$, $z = H/2$, where the fracture touches the bounding layer evolves after t_{touch} as the fracture gets elongated along the $x-$direction. The

fracture will remain confined as long as

$$K_I^\perp \leq K_{Ic,2}. \tag{6.18}$$

The evolution of $K_I^\perp$ allows us to quantify the time

$$\Delta t_c = t_\text{breakthrough} - t_\text{touch} \tag{6.19}$$

during which the fracture remains confined. As previously discussed, when the aspect ratio $L/(0.5H) \gg 1$ (for $t \gg t_\text{touch}$), the hypotheses behind the PKN model are verified. In particular, on a plane orthogonal to the propagation direction, the fracture cross section is elliptical, and the stress intensity factor at the interface with the bounding layers is given by the solution of a uniformly loaded 2D-plane strain fracture (Tada et al., 2000)

$$K_I^\perp = \sqrt{\frac{\pi}{2}} \times p\sqrt{H}$$

Because the pressure in the fracture becomes ultimately constant in the PKN-K regime the stress intensity factor $K_I^\perp$ becomes also constant. Substituting the pressure from the PKN-K solution (see Eq. (6.9)) we obtain:

$$K_I^\perp\big|_{PKN-K} = \sqrt{2} \times K_{Ic-1} \tag{6.20}$$

We can make three important observations:

- during the transition from radial-K to PKN-K, the stress intensity factor $K_I^\perp$ (at $x = 0$, $z = H/2$) increases from $K_{Ic,1}$ to $\sqrt{2} \times K_{Ic-1}$.

- if the toughness $K_{Ic,2}$ is larger than $K_I^\perp\big|_{PKN-K}$ (that is $K_{Ic-2} \geq \sqrt{2}K_{Ic-1}$), the radial fracture will transition to the PKN-K (otherwise it will necessarily breakthrough).

- once the fracture propagates in the PKN-K regime, in the case of inviscid fluid, the time of containment Δt_c is infinite.

We verified this result by two numerical experiments in which the two different values for K_{Ic-2}/K_{Ic-1} are chosen to be slightly smaller and larger than $\sqrt{2}$ ($K_{Ic-2}/K_{Ic-1} = 1.30$ and $K_{Ic-2}/K_{Ic-1} = 1.47$, respectively) - see Fig. 6.6. For the smaller value of toughness ratio, the breakthrough happens, as expected, before the PKN-K solution is reached. For $K_{Ic-2}/K_{Ic-1} = 1.47 > \sqrt{2}$, the fracture remains fully contained. Interestingly, such a ratio of $\sqrt{2}$ between the stress intensity factors in the two directions has been already observed in the context of ply failure of composite laminates (see Eq. (14) in Dvorak and Laws, 1986).

The evolution of $K_I^\perp$ can be expressed in terms of the numerical evolution of the fracture opening $w(x = 0, z = 0, t)$, at the injection point. Not only for both $t = t_\text{touch}$ (radial-K regime) and $t \gg t_\text{touch}$ (PKN-K regime) the fracture opening profile is elliptical, but also during the

transition, as demonstrated by the results of 3D-planar numerical simulations shown in Fig. 6.7. The top plot shows the fracture opening (normalized by its maximum value $w_{\max}$) along a section parallel to the plane $y - z$ at different times. The bottom plot of Fig. 6.7 shows the actual relative difference of the numerical solution to the elliptic profile $w_{\text{elliptic}}(z)$. The relative difference (far from the fracture front) is below 1% indicating that the opening profile can be considered elliptical, such that:

$$w(x = 0, z, t) = w(x = 0, z = 0, t) \sqrt{1 - \left(\frac{z}{H/2}\right)^2} \tag{6.21}$$

Knowing the opening behavior on a plane orthogonal to the fracture front allows us to obtain the stress intensity factor $K_I^{\perp}$ from the linear elastic fracture mechanics asymptote(Rice, 1968):

$$K_I^{\perp} = \lim_{s \to 0} \left(\sqrt{\frac{\pi}{32}} \times E' \frac{w(s)}{\sqrt{s}} \right) \tag{6.22}$$

where $s = H/2 - z$ is the normal distance to the fracture front in the vertical direction. We can express the evolution of $K_I^{\perp}$ for time greater than t_{touch} as:

$$K_I^{\perp}(t) = \sqrt{2} \times K_{Ic-1} \frac{w(x = 0, z = 0, t)}{w_{PKN-K}(z = 0)} \tag{6.23}$$

where w_{PKN-K} is the toughness dominated PKN solution (6.9). The condition for containment and a numerical estimate of the fracture opening at the injection point (Fig. 6.6-c)) allow us to extend the prediction of the containment time for value of the toughness ratio lower than $\sqrt{2}$. Indeed, $\Delta t_c (K_{Ic-2}/K_{Ic-1})$ is implicitly defined as:

$$\frac{K_{Ic-2}}{K_{Ic-1}} = \sqrt{2} \times \frac{w(x = 0, z = 0, \Delta t_c)}{w_{PKN-K}(z = 0)} \tag{6.24}$$

The corresponding inversion for Δt_c is plotted in Fig. 6.8-a). The "coarse mesh" results refer to a simulation with a resolution $H/\ell_{cell} = 49.3$, while the "fine" mesh correspond to a resolution of $H/\ell_{cell} = 98.7$. The inset shows the prediction of the aspect ratio at the breakthrough, and as a function of the toughness ratio.
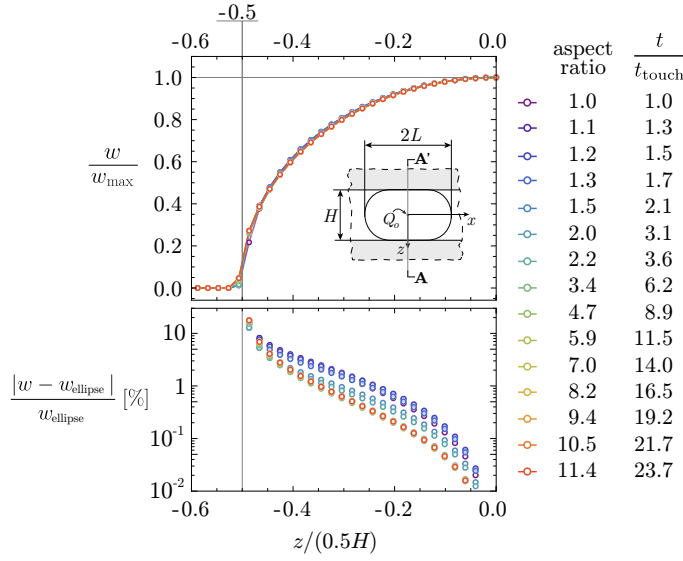
Figure 6.7 – Dimensionless fracture opening along section A-A' at $x = 0$ for a toughness dominated confined fracture (top). The different colors correspond to different fracture aspect ratios and times. The bottom figure displays the relative difference of the numerical solution from an elliptic profile. The spaces between dots of the same color match the numerical spatial discretization used.

In Fig. 6.8-a), the predictions of $\Delta t_c / t_{\text{touch}}$ for $K_{Ic-2} / K_{Ic-1} = 1.1$, 1.2, and 1.3 are highlighted as red paths. These predictions are then compared against numerical simulations in Fig. 6.8-b) and c), where the maximum z-coordinate is plotted as a function of time. Figure 6.8-b), analogous to the one in Fig. 6.6-b), shows the three different simulations departing from $z_{max} / (0.5H) = 1$ at their respective breakthrough times. Before this time, the fracture front slowly advances in the new layer, and then the process accelerates as soon as the breakthrough occurs over a larger portion of the front. The curves represented by gray and black dots are related to simulations where the interface between the bounding layers is respectively inclined at 30° and parallel to the discretization. We refer to these cases as "regular discretization" and "inclined discretization", and both have the same element sizes. If it is evident that the discretization orientation does not significantly impact the overall trend, it matters with regard to the accuracy of the observed breakthrough time. In fact, in the case of "regular discretization", the breakthrough time happens slightly earlier. This last point can be appreciated in Fig. 6.8 c). The percentages in the plot refer to the relative error between the predicted breakthrough time and the one estimated numerically (as the time when $z_{\text{max}} / (0.5H) - 1 \gtrsim 10^{-3}$).
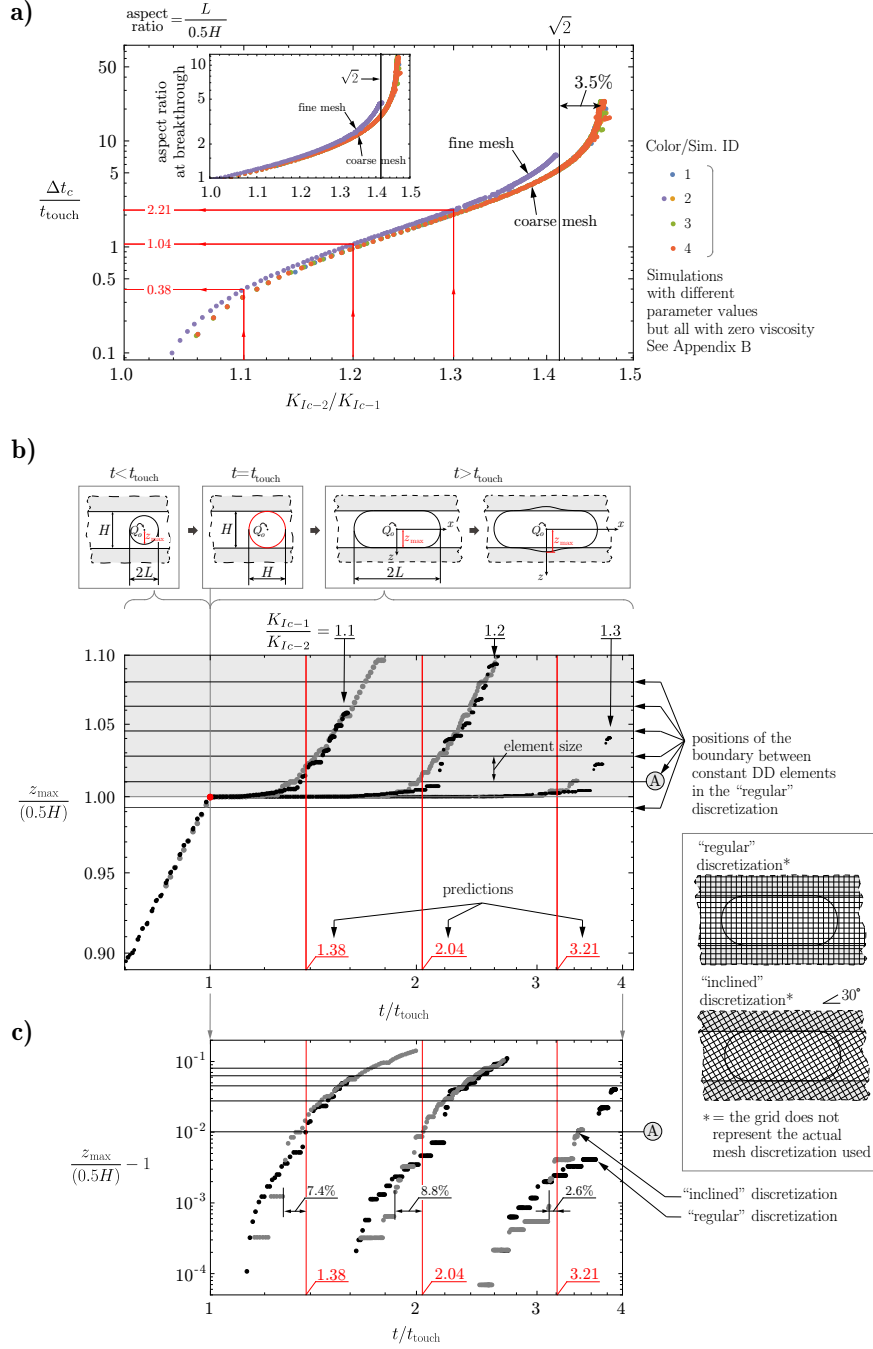
Figure 6.8 – *a*) Predicted dimensionless time during which a toughness dominated fracture remains contained ($\Delta t_c / t_{\text{touch}}$) as a function of the toughness ratio. The inset shows the corresponding fracture aspect ratio at $t_{\text{breakthrough}}$. The red lines mark the predicted values of $\Delta t_c / t_{\text{touch}}$ for $K_{Ic-2}/K_{Ic-1} = 1.1$, 1.2, and 1.3. The spaces between dots of the same color match the time-discretization used in the numerical simulation. *b*) The three dotted curves represent the time evolution of the half size of the fracture (in the vertical direction) - the fracture height - for $K_{Ic-2}/K_{Ic-1} = 1.1$, 1.2, and 1.3 respectively. The red lines represent the predictions obtained from subfigure *a*). Figure *c*) represents a zoom of subfigure *b*) for $t/t_{\text{touch}} \in [1; 4.0]$.

The finite viscosity & finite toughness case

We now consider cases where the fracture toughness and the fluid viscosity are finite. The fracture containment now depends on both the toughness ratio K_{Ic-2}/K_{Ic-1} and the dimensionless toughness $\overline{\mathcal{K}}$ (Eq. 6.10), which quantifies the ratio of energy spent in fracture creation over viscous flow at the instant where the hydraulic fracture reaches the tougher layer. As in the case $K_{Ic-2}/K_{Ic-1} \to \infty$, for high values of K_{Ic-2}/K_{Ic-1}, the newly formed PKN fracture transitions to the PKN-M regime for any value of $\overline{\mathcal{K}}$ (see Fig. 6.3). By recalling that the stress intensity factor $K_I^{\perp}$ scales with the fracture opening (Eq. (6.23)), and that this grows as $t^{1/5}$ (Eq. (6.8)), we conclude that breakthrough always occurs. The analytical expression for the breakthrough time $t_{\text{breakthrough-M}}$ (for large K_{Ic-2}/K_{Ic-1}) follows by combining the evolution of $K_I^{\perp}$ with the containment condition (Eq. (6.18)):

$$\frac{t_{\text{breakthrough-M}}}{t_{\text{K-M}(PKN)}} = 0.19443 \times \left(\frac{K_{Ic-2}}{K_{Ic-1}}\right)^5 \tag{6.25}$$

To express the duration of fracture containment Δt_c (6.19) analytically, we further need to estimate the time t_{touch} when the radial fracture reaches a diameter equal to the layer height H. We can estimate t_{touch} when either the fracture reaches the interfaces in the viscosity dominated ($\overline{\mathcal{K}} \leq 0.31$) or in the toughness dominated ($\overline{\mathcal{K}} \geq 1.1$) regime. The two expressions for t_{touch} are respectively (Savitski and Detournay, 2002):

$$t_{\text{touch-M}} = 0.4727 \left(\frac{H^9 \mu'}{E' Q_o^3}\right)^{1/4}$$
$$t_{\text{touch-K}} = \frac{\sqrt{2\pi}}{3} \frac{K_{Ic-1} H^{5/2}}{E' Q_o} \tag{6.26}$$

The duration of fracture containment Δt_c (6.19) in the viscosity dominated regime is then simply:

$$\frac{\Delta t_c}{t_{\text{touch-M}}} = \frac{t_{\text{breakthrough-M}}}{t_{\text{touch-M}}} - 1$$
$$= 4.9359 \times \overline{\mathcal{K}}^5 \left(\frac{K_{Ic-2}}{K_{Ic-1}}\right)^5 - 1 \quad \text{for} \left\{ \begin{array}{c} \overline{\mathcal{K}} \leq 0.31 \\ K_{Ic-2}/K_{Ic-1} \gtrsim \overline{\mathcal{K}}^{-1} \end{array} \right. \tag{6.27}$$

Note that for a fixed value of containment time Δt_c, the value of toughness ratio K_{Ic-2}/K_{Ic-1} scales as $\overline{\mathcal{K}}^{-1}$. This is precisely how the minimum amount of toughness ratio K_{Ic-2}/K_{Ic-1} required to arrest hydraulic fracture scales in the viscosity dominated regime ($\overline{\mathcal{K}} \leq 0.31$). Therefore, it should be no surprise that the series of isolines (of constant $\Delta t_c/t_{\text{touch-M}}$) shown on the left part of the parametric space in Fig. 6.10-a), -b), and c) are inclined with slope -1. The very first isoline $K_{Ic-2}/K_{Ic-1} = \overline{\mathcal{K}}^{-1}$ corresponds to the amount of time $\Delta t_c = 4 \times t_{\text{touch-M}}$ that the fracture needs to transition from radial-M to the PKN-M regime. This value is obtained by requiring that both the opening evolution at the injection point follows the PKN-M solution (see Fig. 6.3) and the opening profile differs less than $\lesssim 2\%$ form an ellipse, see Fig. 6.11 -a), -b), -c), -d).

The predictions provided by Eq. (6.27) for $\left(\overline{\mathcal{K}}, K_{Ic-2}/K_{Ic-1}\right)$ respectively equal to $(0.32, 3.5)$, $(0.32, 4.0)$ and $(0.18, 6.5)$ are tested against numerical simulations (see Fig. 6.12 a) and b)). In all cases, the relative difference between the analytical predictions and the numerical results are below 10% (see Fig. 6.12 b)). For $\overline{\mathcal{K}} = 0.32$, we obtained higher values (respectively 6.2% and 8.2%) than for $\overline{\mathcal{K}} = 0.18$ (1.8%) because $\overline{\mathcal{K}} = 0.32$ is right at the validity limit of the viscosity-dominated regime solution.

For the remaining interval, going from t_{touch} to $t_{\text{touch}} + (4 \times t_{\text{touch-M}})$, that corresponds to low values of the toughness ratio K_{Ic-2}/K_{Ic-1} (but at the same time sufficient to arrest the propagation), we have estimated numerically the containment time over a wide range of $\overline{\mathcal{K}} \in [0.0047, 1.57]$. Note that this range covers the values of $\overline{\mathcal{K}} \approx 1$ and low values of the toughness ratio K_{Ic-2}/K_{Ic-1} for which no analytical predictions are possible. The results are presented by the colored dots in Fig. 6.10-b) and c). The color code expresses the actual value of $\Delta t_c/t_{\text{touch}}$ while a line connects the points where the aspect ratio at breakthrough is the same. The details concerning the numerical exploration of the parametric space are reported in the Appendix.

We now turn to express the duration of fracture containment Δt_c (6.19) in the toughness dominated regime ($\overline{\mathcal{K}} \geq 1.1$) and for large K_{Ic-2}/K_{Ic-1}. Analogously to the viscosity-dominated case, but now using $t_{\text{touch-K}}$, we obtain:

$$
\begin{aligned}
\frac{\Delta t_c}{t_{\text{touch-K}}} &= \frac{t_{\text{breakthrough-M}}}{t_{\text{touch-K}}} - 1 \\
&= 2.79235 \times \overline{\mathcal{K}}^4 \left(\frac{K_{Ic-2}}{K_{Ic-1}}\right)^5 - 1 \text{ for } \begin{cases} \overline{\mathcal{K}} \geq 1.62 \\ K_{Ic-2}/K_{Ic-1} > 3 \end{cases} \\
&\approx \frac{t_{\text{breakthrough-M}}}{t_{\text{K-M}(PKN)}}
\end{aligned}
\tag{6.28}
$$

Note that for a fixed value of containment time Δt_c, the value of toughness ratio K_{Ic-2}/K_{Ic-1} scales as $\overline{\mathcal{K}}^{-4/5}$ while the minimum value of toughness ratio K_{Ic-2}/K_{Ic-1} sufficient to arrest the propagation goes to one, independently from $\overline{\mathcal{K}}$ (see Fig. 6.10-a) -b) and c)). This apparent contradiction is reconciled by the fact that:

- for small values of toughness ratio ($K_{Ic-2}/K_{Ic-1} < \sqrt{2}$), the breakthrough happens in the transition between the radial and the PKN-K regime ($\overline{\mathcal{K}}$). The predictions for $\Delta t_c (K_{Ic-2}/K_{Ic-1})$ obtained in the limit of infinite toughness ($\overline{\mathcal{K}} \to \infty$), are displayed in Fig. 6.8 providing a good approximation in this case. This is confirmed by the comparison shown in Fig. 6.10-d), where the numerical estimates for the containment time for $\overline{\mathcal{K}} = 1.56$ (star symbols) are close to the predictions for the zero viscosity case of Fig. 6.8.

- for values of toughness ratio $K_{Ic-2}/K_{Ic-1} \geq \sqrt{2}$ (for which indefinite containment occur when $\overline{\mathcal{K}} \to \infty$), the fracture propagates in the PKN-K regime for an amount of time $\Delta t_{\text{const} K_I^{\perp}}$ during which the stress intensity factor $K_I^{\perp}$ remains constant, as the contained
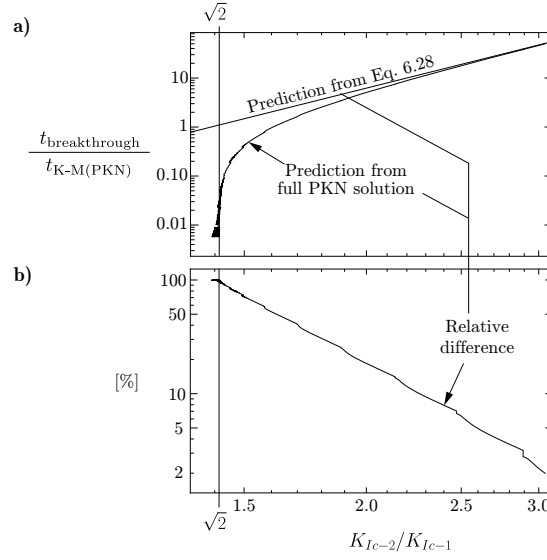
Figure 6.9 – *a*) Comparison between the predictions provided by Eq. (6.28) and the full PKN solution. *b*) shows the relative difference between the two curves in *a*).

fracture elongates transitioning to the PKN-M regime where the stress intensity factor increases as $K_I^\perp \propto t^{1/5}$. This creates a "jump" in the containment time that is visible in Fig 6.10-a). The reason why $K_I^\perp$ remains constant, is that the fracture opening remains constant in the PKN-K regime. The corresponding "latency period" $\Delta t_{\text{const}\,K_I^\perp}$ can be estimated as the difference between the time when the fracture (opening) departs from the PKN-K solution (that is $\sim 0.1 \times t_{K-M(PKN)}$ from Fig. 6.4-e)) and the time that is required to transition to the PKN-K solution (that is $\sim 10 \times t_{\text{touch}}$ from Fig. 6.6-c)):

$$\Delta t_{\text{const}\,K_I^\perp} \approx \underbrace{0.1 \times t_{K-M(PKN)}}_{\substack{\text{end of} \\ \text{PKN-K propagation}}} - \underbrace{10 \times t_{\text{touch}-K}}_{\substack{\text{beginning of} \\ \text{PKN-K propagation}}} \tag{6.29}$$

The large toughness ratio K_{Ic-2}/K_{Ic-1} predictions (Eq. 6.28) are not valid immediately after the end of the PKN-K propagation because the breakthrough can take place in the transition from PKN-K to PKN-M. To complete the predictions of the containment time for the cases $K_{Ic-2}/K_{Ic-1} \geq \sqrt{2}$ and $K_{Ic-2}/K_{Ic-1} \leq 3$, we take the solution $w(x=0, z=0, t)$ obtained by solving numerically the (1D-)PKN model (see the black line in Fig. 6.4-c)) and we compute the evolution of the stress intensity factor $K_I^\perp$ (Eq. 6.23). Then, by combining it with the propagation condition (6.18) we explicit the breakthrough time $t_{\text{breakthrough}}$ as a function of $K_{Ic-2}/K_{Ic-1} \geq \sqrt{2}$. The result is marked by the label "prediction from the full PKN solution" in Fig. 6.9-a). It is interesting to compare this prediction to the one obtained for large toughness ratio K_{Ic-2}/K_{Ic-1} (Eq. (6.28)). The relative difference between these two predictions is below $\sim 2\%$, when $K_{Ic-2}/K_{Ic-1} > 3$ (see Fig. 6.9-b).
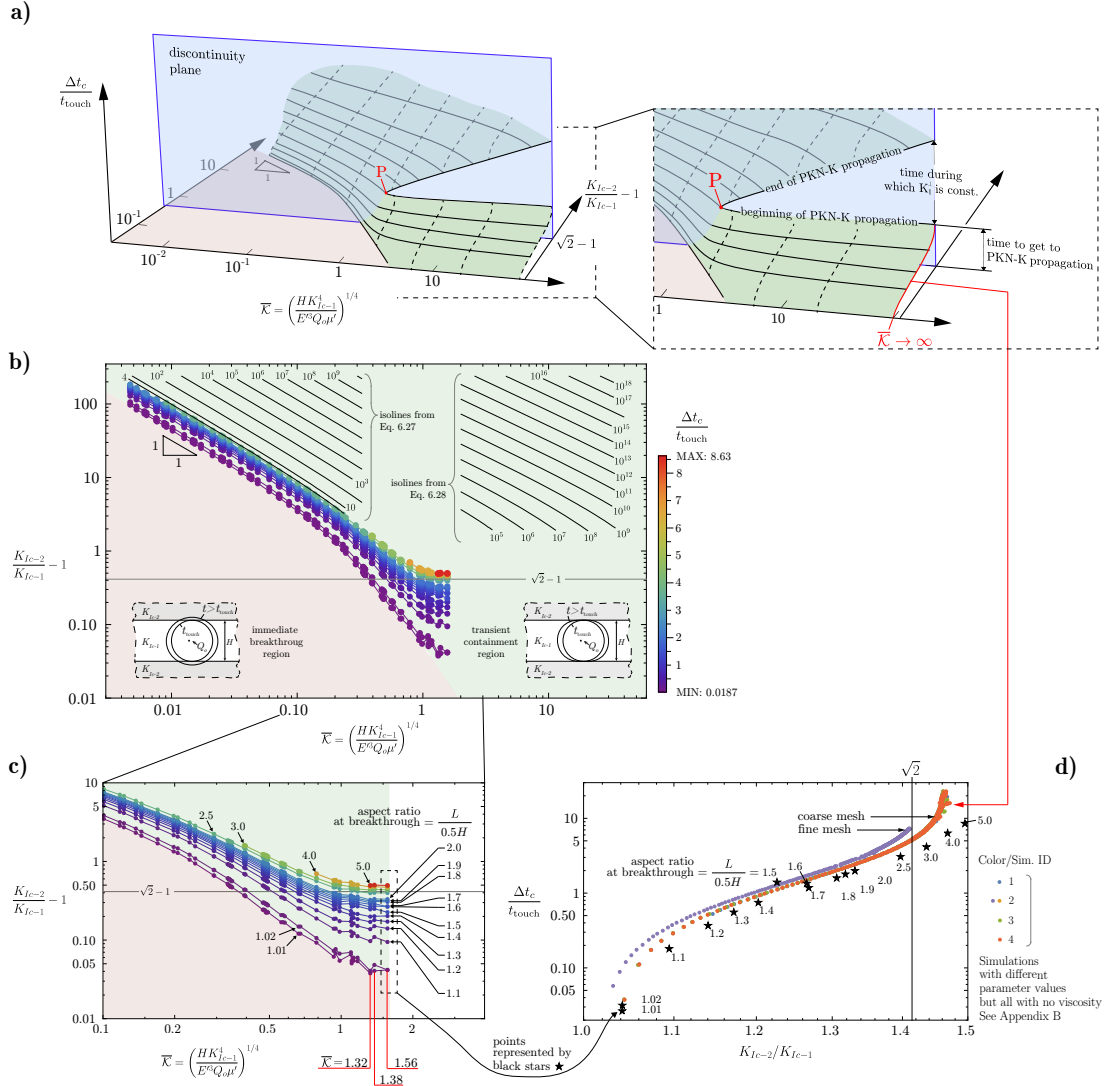
Figure 6.10 – *a*) Schematic of the parametric space $\left(\Delta t_c/t_{\text{touch}}, \overline{\mathcal{K}}, K_{Ic-2}/K_{Ic-1}-1\right)$. *b*) quantitative representation of the same parametric space as a contour plot. The color-code of each dot expresses the dimensionless breakthrough time $\Delta t_c/t_{\text{touch}}$, while the dots of same aspect ratio $L/(0.5H)$ at breakthrough are joined by a line. *c*) is a zoom over a region of sub-figure *b*). *d*) shows the superposition of $\Delta t_c/t_{\text{touch}}$ for $\overline{\mathcal{K}} = 1.56$ and for $\overline{\mathcal{K}} \to \infty$ taken from Fig. 6.8-*a*).

Now, we want to define where the jump of $\Delta t_c/t_{\text{touch}}$ begins along the $\overline{\mathcal{K}}$ axis of the parametric space $\left(\Delta t_c/t_{\text{touch}}, \overline{\mathcal{K}}, K_{Ic-2}/K_{Ic-1}-1\right)$. We marked this position through the red point "P" in Fig. 6.10-a). The "beginning of the discontinuity" corresponds to the case where the "beginning time of propagation as a PKN-K fracture" coincides with the transition to the PKN-M regime. In other words, in that case, the stress intensity factor $K_I^\perp$ keeps increasing continuously without being constant for a finite period of time. This equals setting $\Delta t_{\text{const} K_I^\perp} =$

0 in Eq.(6.29), from which we obtain:

$$\overline{\mathcal{K}}(P) \approx 1.62 \tag{6.30}$$

It is interesting to check numerically that for $\overline{\mathcal{K}} \lesssim 1.62$ the containment time $\Delta t_c / t_{\text{touch}}$ as a function of K_{Ic-2}/K_{Ic-1} does not present a discontinuity for $K_{Ic-2}/K_{Ic-1} \geq \sqrt{2}$. For this purpose, we computed numerically the function $\Delta t_c / t_{\text{touch}}$ as a function of K_{Ic-2}/K_{Ic-1} for $\overline{\mathcal{K}} = 1.56$. The results are shown with the black stars in Fig. 6.9-d) and they are compared to the case $\overline{\mathcal{K}} \to \infty$ of Fig. 6.8-a). Clearly no discontinuity is observed for $K_{Ic-2}/K_{Ic-1} \sim \sqrt{2}$.

Figure 6.11 – Fracture opening along the section A-A' at $x = 0$ for a viscosity dominated confined fracture (*a* and *c*). The different colors correspond to different fracture aspect ratios $L/(0.5H)$ and dimensionless times t/t_{touch}. The bottom figures *b*) and *d*) report the relative difference of the numerical solution from an elliptic profile. The spaces between dots of the same color match the spatial-discretization used in the numerical simulation.

Figure 6.12 – Analytical vs. numerical predictions of the containment time for viscosity dominated fractures. *a*) the 3 dotted curves represent the time evolution of the half size of the fracture (in the vertical direction). The spaces between dots of the same color match the time-discretization used in the numerical simulation. The red lines represent the predictions by Eq. (6.27). *b*) represents a zoom of subfigure *a*) for $t/t_{touch} \in [5;40]$.

6.5 Orders of magnitude in practice

In Tables 6.4 and 6.5, we computed the dimensionless toughness $\overline{\mathcal{K}}$, the containment time Δt_c, and aspect ratio at breakthrough for two practical applications: a open-hole micro-hydraulic fracturing test (Haimson, 1993), and a hydraulic fracturing treatment for well stimulation. For all cases, the estimates are computed assuming $K_{Ic-2}/K_{Ic-1} \leq 2$ because this can be already considered as a large value for the variation of toughness (see section 6.2). The values have

been obtained from the parametric space in Fig. 6.10-b), from Figs. 6.4 and by using the analytical estimates previously derived.

Micro-hydraulic fracturing tests

The open-hole micro hydraulic fracturing test is used to estimate the minimum in-situ principal stress σ_o in a rock formation. The measurement is based on the interpretation of the fluid pressure evolution during both hydraulic fracture propagation and closure phases that follow a prescribed injection schedule (Haimson and Cornet, 2003; Thiercelin et al., 1996; Desroches et al., 2021). The fluid is injected in a wellbore interval around the targeted depth where the stress is measured. Before the injection phase, the interval is hydraulically isolated from the rest of the wellbore by inflating two expansible elastic chambers (packers) respectively at the beginning and at the end of the interval. A fluid is then injected to initiate and propagate a hydraulic fracture. In a successful test, the interval has to remain hydraulically isolated from the rest of the wellbore, and the hydraulic fracture has to grow past the region subjected to the largest wellbore-induced stress perturbation. If the hydraulic fracture extends above the packers, it can create a hydraulic connection (packer bypass), interrupting the test before being completed. The presence of layers of higher fracture toughness above and below the targeted wellbore interval could potentially be a mechanism that prevents packer bypass and allows the fracture to grow further away from the wellbore. Table 6.4 considers typical values for the parameters characterizing the problem. Two values of injection rate are considered $1.6667 \times 10^{-6} \mathrm{m}^3/\mathrm{s}$ and $2.5 \times 10^{-5} \mathrm{m}^3/\mathrm{s}$ (respectively 0.1 liters/min and 1.5 liters/min) within the typical range of flow rates used to test low-permeability formations (Thiercelin and Desroches, 1993; Thiercelin et al., 1996; Haimson and Cornet, 2003). The injected fluids are assumed to be water and water-diluted drilling mud. Despite the latter being more viscous (and possibly non-Newtonian), we assume a constant viscosity of 0.025 Pa s (Caenn et al., 2011). We considered two possible layers heights H accounting for the fact that the distance between the packers is typically in the range $1-2$ m and the packer length is about 0.5 m (Desroches et al., 2021). We have combined the values of viscosity, injection rate, and fracture height to obtain the widest range of $\overline{\mathcal{K}}$ that is possible with the chosen parameters. The results in Table 6.4 show that for the cases of low injection rate, low fluid viscosity, and large layer height, the fracture can be considered contained for the whole test duration. Note that the stress perturbation induced by the wellbore and the inflated packers may potentially promote fracture breakthrough. This particular point deserves further investigation.

Hydraulic fracturing well stimulation treatment

We consider the limiting cases of a hydraulic fracturing treatment performed either with a low viscosity fluid (slick water with $\mu = 0.005$ Pa s.) but a large injection rate or with a large viscosity fluid (polymer gel with $\mu = 1.0$ Pa s)/lower injection rates.

A reference range of injection rates is $5.9 \times 10^{-3} - 1.99 \times 10^{-1} \mathrm{m}^3/\mathrm{s}$ ($3 - 100.$ bbl/min) (Economides and Nolte, 2000). For each case we consider a few sub-cases varying the value of K_{Ic-1}

a) Micro-hydraulic fracturing test[*]

Q_o [m^3/s]	μ [Pa s]	H [m]	K_{Ic-1} [MPa$\sqrt{\text{m}}$]	$\overline{\mathcal{K}}$ [-]	$t_{\text{touch-M}}$ [s]	$t_{\text{touch-K}}$ [s]	Δt_c [s]	aspect ratio at bt.
1.667×10^{-6} (0.1 L/min)	0.001	2.	1.0	1.3	-	88	$\lesssim 4400$	$\lesssim 24$
2.5×10^{-5} (1.5 L/min)	0.025	1.	1.0	0.25	2.3	-	$\sim 0.$	$\sim 1.$

[*] $K_{Ic-2}/K_{Ic-1} \leq 2$, $E = 30$ GPa and $\nu = 0.25$ in all the considered cases

Table 6.4 – Dimensionless toughness $\overline{\mathcal{K}}$, and containment time Δt_c computed for some cases of open-hole micro-hydraulic fracturing test. In all cases $K_{Ic-2}/K_{Ic-1} \leq 2$ is assumed. The aspect ratio at breakthrough is defined as $L/0.5H$ (see Fig. 6.2-a).

because it appears with the largest exponent in the definition of $\overline{\mathcal{K}}$ (Eq. (5.6)). In particular, it is known (Garagash, 2023) that the fracture toughness observed in-situ may be larger than the one measured at the laboratory scale (Liu et al., 2019). We observe that for a large value of fracture toughness of the central layer, the fracture may be transiently contained even for a relatively low jump in toughness ($K_{Ic-2}/K_{Ic-1} \leq 2$).

The results provided in this work do not consider the effect of gravity on hydraulic fracture propagation. The effects of gravity can be neglected if the fracture height is smaller than the critical length-scale for buoyant growth $H \lesssim L_b$ with $L_b = \left(K_{Ic-1} / \left(\gamma_{\text{solid}} - \gamma_{\text{fluid}} \right) \right)^{2/3}$ is the buoyancy length-scale (see Lister and Kerr (1991)) and γ the specific weight. Assuming $K_{Ic-1} = 2$ MPa$\sqrt{\text{m}}$ and $\gamma_{\text{solid}} - \gamma_{\text{fluid}} = 16$ kN/m^3, we obtain $L_b = 26$ m. An estimate larger than the few meters scale of a micro-hydraulic fracturing treatment (for which buoyant effects are thus negligible), but possibly on par with the scales of hydraulic fractures observed in well stimulation operations.

6.6 Conclusions

In this work, we have estimated how long two bounding layers of higher fracture toughness can contain the propagation of a hydraulic fracture between them, therefore restricting its vertical propagation as per Fig. 6.2-a). We demonstrated that provided the injection at a constant rate continues for long enough, the hydraulic fracture will eventually always breakthrough. A toughness ratio above $\sqrt{2}$ significantly increases the containment time when the propagation regime is toughness dominated at the time when the hydraulic fracture touches the bounding layers.

These results can be applied to the non-symmetric scenario where the toughness distribution in the three layers is $K_{Ic-2} - K_{Ic-1} - K_{Ic-3}$ with $K_{Ic-3} > K_{Ic-2} > K_{Ic-1}$. In this case, the toughness ratio K_{Ic-2}/K_{Ic-1} will determine the first (and possibly the only) breakthrough.

b) Hydraulic fracturing treatment[*]

Q_o [m³/s] ([bbl/min])	μ [Pa s]	H [m]	K_{Ic-1} [MPa$\sqrt{m}$]	$\overline{\mathcal{K}}$ [-]	$t_{\text{touch-M}}$ [s]	$t_{\text{touch-K}}$ [s]	Δt_c [s]	aspect atio at bt.
6.0×10^{-3} (3.0)	1.0	20	2.0	0.11	82	-	0.	1.
		20	10.0	0.54	82	78	$\sim 350.$	$\lesssim 4.0$
		40	2.0	0.13	388	-	0.	1.
		40	10.0	0.64	6.5	3.1	$< 60.$	< 5.0
3.0×10^{-2} (15.)	0.005	20	2.0	0.27	6.5	-	$\sim 0.$	$\sim 1.$
		20	10.0	1.40	-	16	$\lesssim 10^3$	-
		40	2.0	0.32	31	-	$\sim 6.$	~ 1.1
		40	10.0	1.60	-	88	$\lesssim 10^4$	-

[*]$K_{Ic-2}/K_{Ic-1} \leq 2$, $E = 30$ GPa and $\nu = 0.25$ in all the considered cases

Table 6.5 – Dimensionless toughness $\overline{\mathcal{K}}$, and containment time Δt_c computed for some cases of hydraulic fracturing well stimulation treatment. The unit in brackets is bbl/min=barrel per minute. The aspect ratio at breakthrough is defined as $L/0.5H$ (see Fig. 6.2-a)). When $\overline{\mathcal{K}} \gtrsim 1.1$ ($\overline{\mathcal{K}} \lesssim 0.34$) only $t_{\text{touch-K}}$ ($t_{\text{touch-M}}$) is computed, otherwise both $t_{\text{touch-M}}$ and $t_{\text{touch-K}}$ are computed.

Other factors, not considered here, can also have a first-order impact on the estimate of breakthrough time, notably: heterogeneity of elastic properties between layers, fluid leak-off in the surrounding medium, non-Newtonian fluid rheologies (Moukhtari and Lecampion, 2018), different types of injection (line source, varying injection rate) Garagash (2023). Finally, upon breakthrough, a substantial amount of time is required for the fracture to regain a radial shape. As a result, the estimations provided in this work have to be considered as a lower bound for the time during which the hydraulic fracture propagates in an elongated shape with a larger horizontal than vertical extent. The results presented here provide a basis for a proper in-depth investigation of the effect of multiple layers on the vertical containment of hydraulic fracture.

7 Multilayers of heterogeneous fracture toughness

Disclaimer and acknowledgements: The ideas and the work presented in this chapter are my contributions.

Note: This chapter is currently being adapted into a scientific publication:
C. Peruzzo, B. Lecampion, "*Hydraulic fracture containment emerging from a layered distribution of fracture energy*", in prep., 2023

7.1 Introduction

Unconventional hydrocarbon reservoirs are primarily located in sedimentary basins, which can exhibit heterogeneities on two-length scales. The large-scale heterogeneity is associated with the arrangement of various lithologies into layer-like formations, with layer thicknesses ranging from several centimeters to tens of meters (see, for example, Fig. 6.1). Conversely, the small-scale heterogeneity relates to features smaller than layer thickness. It is a result of anisotropy caused by the depositional and diagenetic processes of sedimentary rocks. For instance, shale is an anisotropic rock with a layered structure composed of thicker and thinner layers (referred to as bedding planes)(Sone and Zoback, 2013). The mechanical properties of shale, such as fracture toughness and elasticity, vary significantly in different directions relative to these bedding planes, requiring a Transverse Isotropic model to describe its elastic behavior. The two main directions of concern for fracture toughness variations are the arrester direction, where the fracture plane is perpendicular to the bedding planes, and the divider direction, where the fracture plane is parallel to the bedding planes. A simple way to understand these two directions is to consider cutting a log of wood with an axe - the arrester direction would correspond to the blade striking the wood perpendicular to the fibers, while the divider

direction would correspond to a cut parallel to the fibers[1]. The few available measurements indicate that the fracture toughness can be 1.05 up to 1.5 times larger in the arrester compared to the divider direction (Chandler et al., 2016; K. et al., 2017).

The present chapter examines the effect of layer-like heterogeneities of fracture toughness on hydraulic fracture propagation. In sedimentary basins, it is common for hydraulic fractures to propagate on a vertical plane due to the frequent horizontal orientation of the minimum in situ stress. As the fracture propagates through a layered material, it can be assumed that at least two portions of the fracture front advance in the arrester direction while the remaining two portions progress in the divider direction. The fracture toughness of the remaining portion of the front, which is not oriented in either the arrester or the divider direction, is dependent on the direction of propagation. In recent work, Zia et al. (2018) conjectured that when the size of the layers is much smaller than the fracture size (at the limit infinitesimal) it is feasible to define a fracture toughness that varies with the direction of propagation. Various trial functions were used to represent the direction-dependent toughness to test this hypothesis. The numerical simulations showed that the late-time propagation, dominated by toughness, exhibits self-similarity. Additionally, the late-time aspect ratio was found to be dependent on the specific expression for the direction-dependent toughness function used.

This study, presents a novel approach to investigating the hydraulic fracture behavior in materials with layer-like toughness heterogeneities. Unlike the approach proposed by Zia et al. (2018), who considered the size of the layers to be much smaller than the fracture size, we consider layers with dimensions comparable to the initial hydraulic fracture size. Our approach involves examining the interaction and propagation of the hydraulic fracture through the layers, which reveals a repetitive pattern. This enables us to identify two possible late-time fracture behaviors that emerge when the fracture size is significantly larger than the layer size. In one scenario, the fracture propagates with a practically constant aspect ratio, while in the second scenario, the fracture is practically contained. By contained, we mean that the fracture velocity in the vertical direction (arrester direction) becomes negligible compared to that in the horizontal direction (divider direction). This latter scenario was not predicted by the direction-dependent toughness approach presented in Zia et al. (2018).

Prior to presenting our method, it is important to note other studies investigating the impact of layer-like variations in fracture toughness on hydraulic fracture propagation. The work of Dontsov and Suarez-Rivera (2021) evaluates the homogenization of small scale variations in fracture toughness through 3D planar simulations, where "small scale" refers to dimensions smaller than the element size in their numerical discretization. The authors propose that the fracture toughness in the direction of propagation parallel to the layering can be obtained from the average fracture energy, while in the vertical direction (arrester), the maximum fracture toughness should be considered. However, caution should be exercised in applying

---

[1]This particular illustration simplifies the differentiation of the two orientations by virtue of the fact that the act of striking a log with an axe only affords two potential outcomes. In contrast, within layered materials, there exists a third possibility wherein a fracture plane aligns with a bedding plane.

the first result, as the average fracture energy argument is only applicable when the shape of the fracture front remains unchanged during propagation (as described in Rice (1988) or Gao and Rice (1989)). The second result has been theoretically confirmed by Hossain et al. (2014) and recently by Fies et al. (2022a,b) through their examination of a 1D hydraulic fracture propagating through a periodic distribution of fracture toughness, where they demonstrate that during the "late time" or toughness dominated phase, the higher fracture toughness dominates the propagation.

7.2 Problem formulation

We consider the case where a hydraulic fracture propagates in a medium consisting of a repetitive sequence of layers with similar mechanical properties. For simplicity, only one property varies between layers: fracture toughness. We could consider any repetitive distribution of fracture toughness but we choose a "simple" one: the sequence is constructed by alternating a tougher layer of height H_2 of fracture toughness $K_{\text{Ic-2}}$ to a layer of height $H_1 \geq H_2$ and $K_{\text{Ic-1}} \leq K_{\text{Ic-2}}$. A schematic representation of the problem is displayed in Fig. 7.1.

7.3 The effect of layers on an initially viscosity dominated fracture

We begin by considering the case where a radial hydraulic fracture is propagating in the viscosity dominated regime (which is always the case at an early time). Assuming that the initial fracture propagates in one of the layers helps the clarity of the presentation but does not influence the "late time" fracture behaviour. The length-scale of the initial fracture can cover several layer sizes. However, for clarity, we assume that the initial fracture size is less or equal to the size of a layer such that the fracture toughness along the front is uniform. The injection can be located in either layer n. 1 or n. 2, and it does not affect the "late time" propagation. First, we consider the injection point placed in the less tough layer. If the fracture is viscosity dominated ($\overline{\mathscr{K}} \ll 1$) when reaching the interfaces with the bounding layers, it might not even be affected by the toughness jump. In this case, the propagation continues maintaining a radial shape initially. As the radius increases, the power dissipated in creating new fracture surfaces becomes more relevant compared to the power dissipated in the viscous flow [2]. Consequently, the toughness variation between the layers starts to play an increasingly important role in the fracture propagation, and the shape of the fracture becomes more elongated in the direction of the layers. In this phase, the vertical propagation is not (yet) stopped when the fracture front reaches a new interface with a tougher layer. Instead, the vertical velocity reduces upon penetrating the high toughness layer. Once the overall fracture height h is sufficiently large, a layer of higher fracture toughness ($K_{\text{Ic-2}}$) can arrest (for a finite amount of time) the height growth. In Chapter 5, we have already derived the conditions that lead to the arrest of the propagating fracture. Once the vertical velocity is zero, the propagation continues only in the direction parallel to the layers. This situation is similar to the three layer

---

[2]This is confirmed by recalling that the dimensionless toughness $\overline{\mathscr{K}}$ scales with the fracture size.
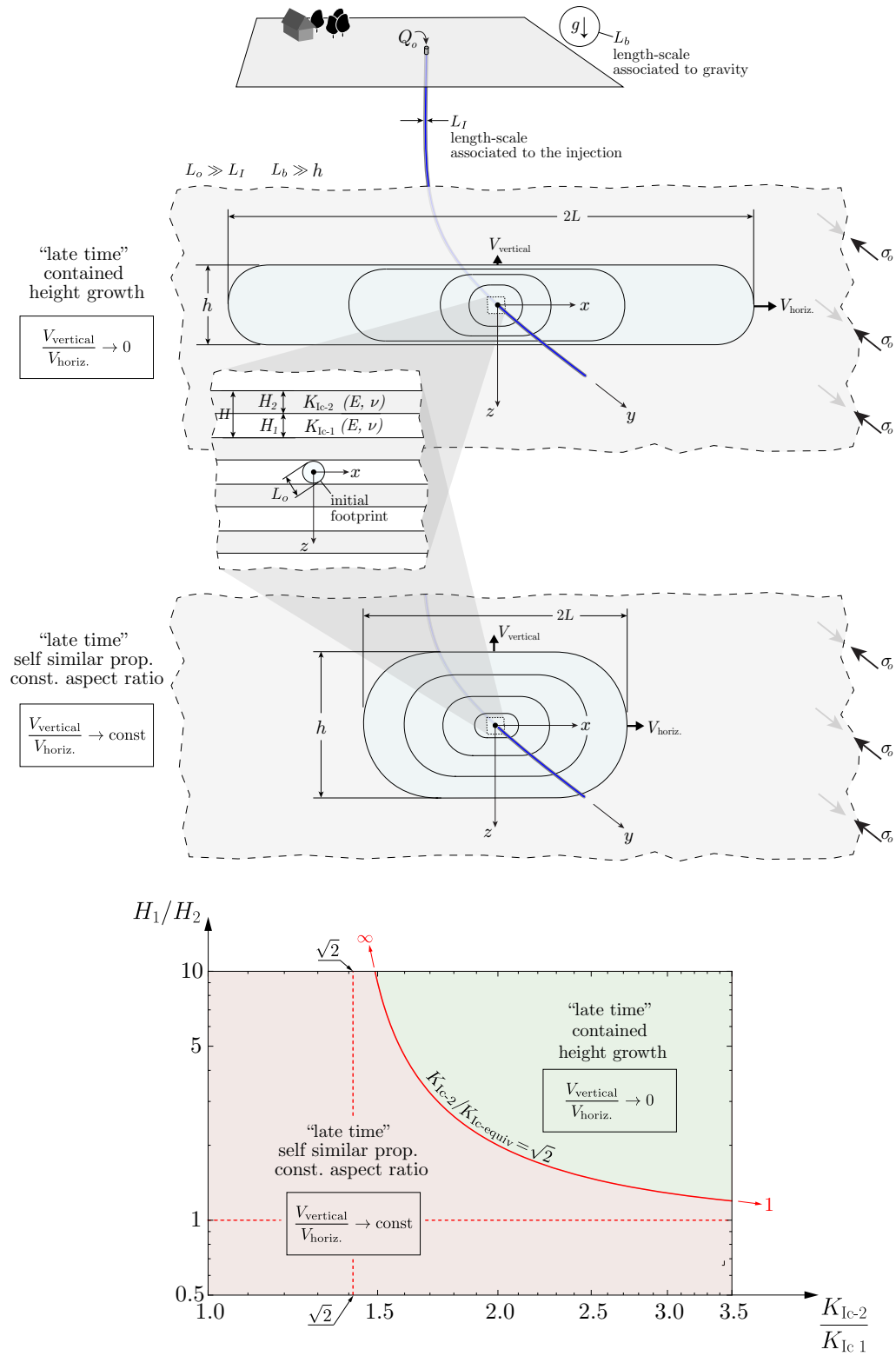
Figure 7.1 – Scheme representing the two possible "late time" evolutions of a hydraulic fracture propagating in a layered material. On the bottom the two late time behaviours are identified in the parametric space.

scenario previously described in Chapter 6. The only difference concerning that case is that the contained fracture was propagating in a homogeneous medium, while in this case, the fracture propagates traversing a parallel sequence of layers. However, we assume it is possible to replace the heterogeneous distribution of fracture toughness with an equivalent fracture toughness $K_{\text{Ic-equiv}}$. This assumption will be justified in a subsequent section. The value of $K_{\text{Ic-equiv}}$ is clearly smaller than $K_{\text{Ic-2}}$ and higher than $K_{\text{Ic-1}}$ and it depends on the relative layer heights H_2/H_1. The containment problem can be formulated as shown in the three-layer scenario described in Chapter 6.

7.4   The repeated pattern during the propagation in a layered medium

In the interaction of a hydraulic fracture with a layered medium, a discernible, repetitive pattern emerges that becomes evident when two layers of higher fracture toughness arrest vertical propagation. Initially, we consider a radial fracture propagating in a low toughness layer, with a "sufficiently large" toughness contrast to immediately arrest vertical propagation (Figure 7.2-A). If this is not the case, propagation will be arrested by a subsequent layer. As the contained fracture becomes more elongated in the horizontal direction, the stress intensity factor $K_I^{\perp}$ at the interface with the bounding layers increases. When $K_I^{\perp}$ exceeds $K_{\text{Ic-2}}$, the fracture restarts propagation in the vertical direction. After the breakthrough, the fracture propagates in both the vertical and horizontal directions (Figure 7.2-B), until the fracture front vertically reaches the layers of lower fracture toughness. At this point, vertical propagation abruptly accelerates locally until the next layer of higher fracture toughness is reached (Figure 7.2-C). Meanwhile, horizontal propagation is practically arrested. The fracture then has a cross-like shape and propagates mainly in the newly penetrated layers until a global "rectangular" shape is reached (Figure 7.2-D). At this point, the propagation restarts globally only in the horizontal direction, and the fracture elongates until the next breakthrough (Figure 7.2-E). This process then repeats. In Figure 7.3-F, the fracture propagates in both the vertical and the horizontal directions. When reaching the layers of lower fracture toughness, the fracture accelerates (Figure 7.3-G) before being stopped by a new pair of layers of higher fracture toughness. The cross-shaped fracture then regains a rectangular or blade-like shape (Figure 7.3-H). Subsequently, the global contained propagation starts again.

7.5   The mechanism that leads to the "late time" fracture containment

7.5.1   The main idea

Between two subsequent breakthroughs, the overall fracture height h increases, and the equivalent fracture toughness in the horizontal direction $K_{\text{Ic-equiv}}$ tends to be a constant. As a consequence, the newly formed contained fracture will become more and more toughness dominated ($h/L_{K-M(PKN)} \propto 1/h$) from which it follows that (see Chapter 6) the containment
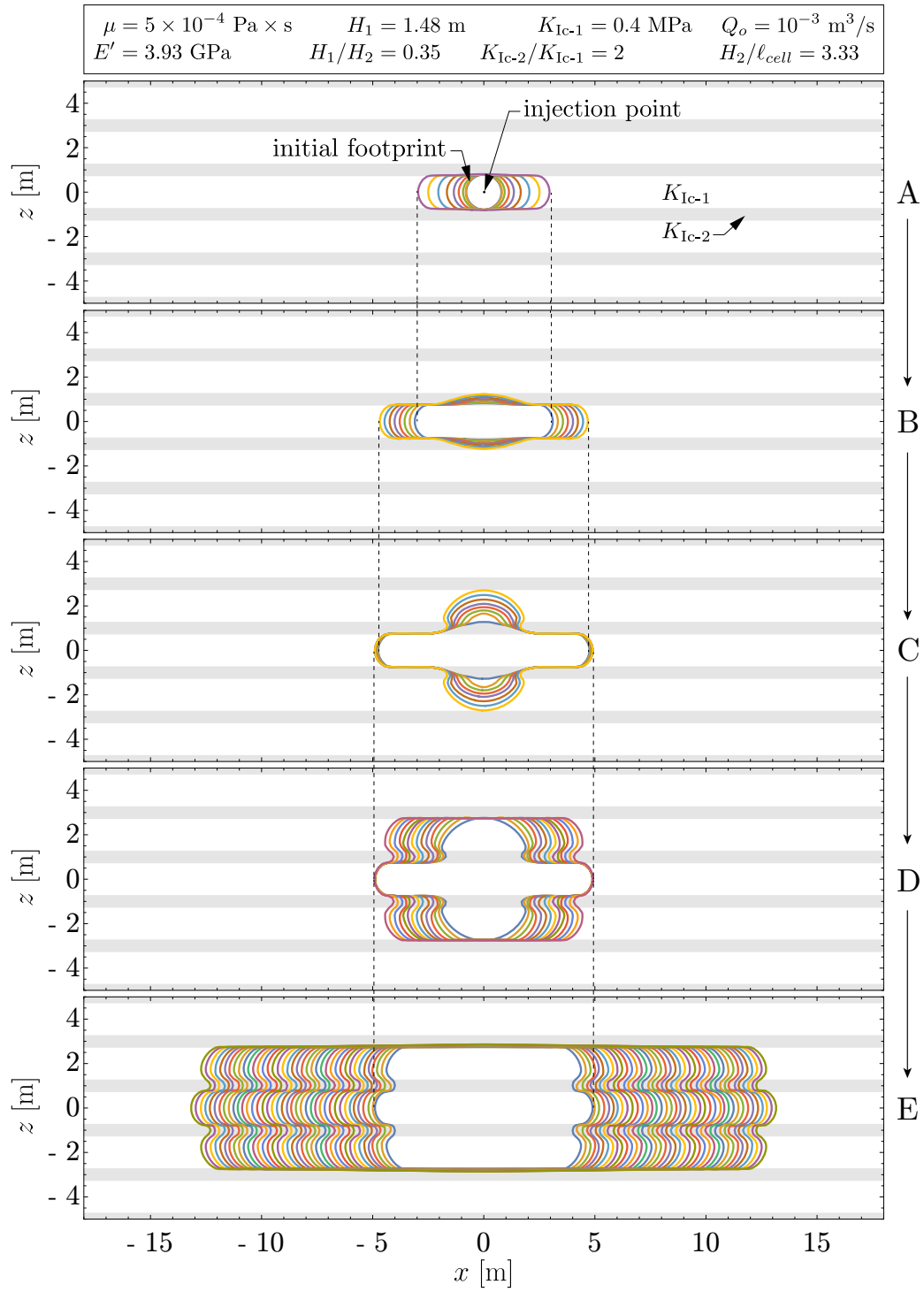
Figure 7.2 – Repeated pattern during the propagation through a layered medium. A) contained propagation, B) breakthrough in the high toughness layer, C) breakthrough in the low toughness layer, D) propagation only in the recently fractured layer and E) the propagation resumes in the horizontal direction along the whole fracture height.

Figure 7.3 – Repeated pattern during the propagation through a layered medium. This figure continues from Fig. 7.2. E) The fracture propagation is contained by the high toughness layers, F) breakthrough in the high toughness layer, G) breakthrough in the low toughness layer, H) the fracture propagates only in the recently fractured layer and E) the propagation resumes in the horizontal direction along the whole fracture height.

time Δt_c increases as $t_{K-M(PKN)} \propto h^{7/2}$ when $K_{\text{Ic-2}}/K_{\text{Ic-equiv}} \geq \sqrt{2}$. In other words, we want to demonstrate that for toughness contrasts $K_{\text{Ic-2}}/K_{\text{Ic-equiv}} \geq \sqrt{2}$ the aspect ratio of the fracture increases with time (while propagating over a number of several layers) and it "practically" reaches an equilibrium height. For this purpose, we compute the ratio between the average velocities of fracture propagation in the vertical (V_{vertical}) and horizontal ($V_{\text{horizontal}}$) directions. This ratio can be simplified as:

$$\frac{V_{\text{vertical}}}{V_{\text{horizontal}}} = \frac{\Delta h}{\Delta t} \times \frac{\Delta t}{\Delta(2L)} = \frac{\Delta h}{\Delta(2L)} \tag{7.1}$$

The increments of fracture height Δh, and total fracture length ($\Delta(2L)$) are evaluated between two subsequent fracture breakthroughs. The value of Δh is thus given by $\Delta h = 2 \times H$, where $H = H_1 + H_2$. On the other hand, when $K_{\text{Ic-2}}/K_{\text{Ic-equiv}} \geq \sqrt{2}$ the fracture length at breakthrough ($2L$) scales as $L_{K-M(PKN)}(h)$. Therefore, we can express $\Delta(2L)$ as $L_{K-M(PKN)}(h + \Delta h) - L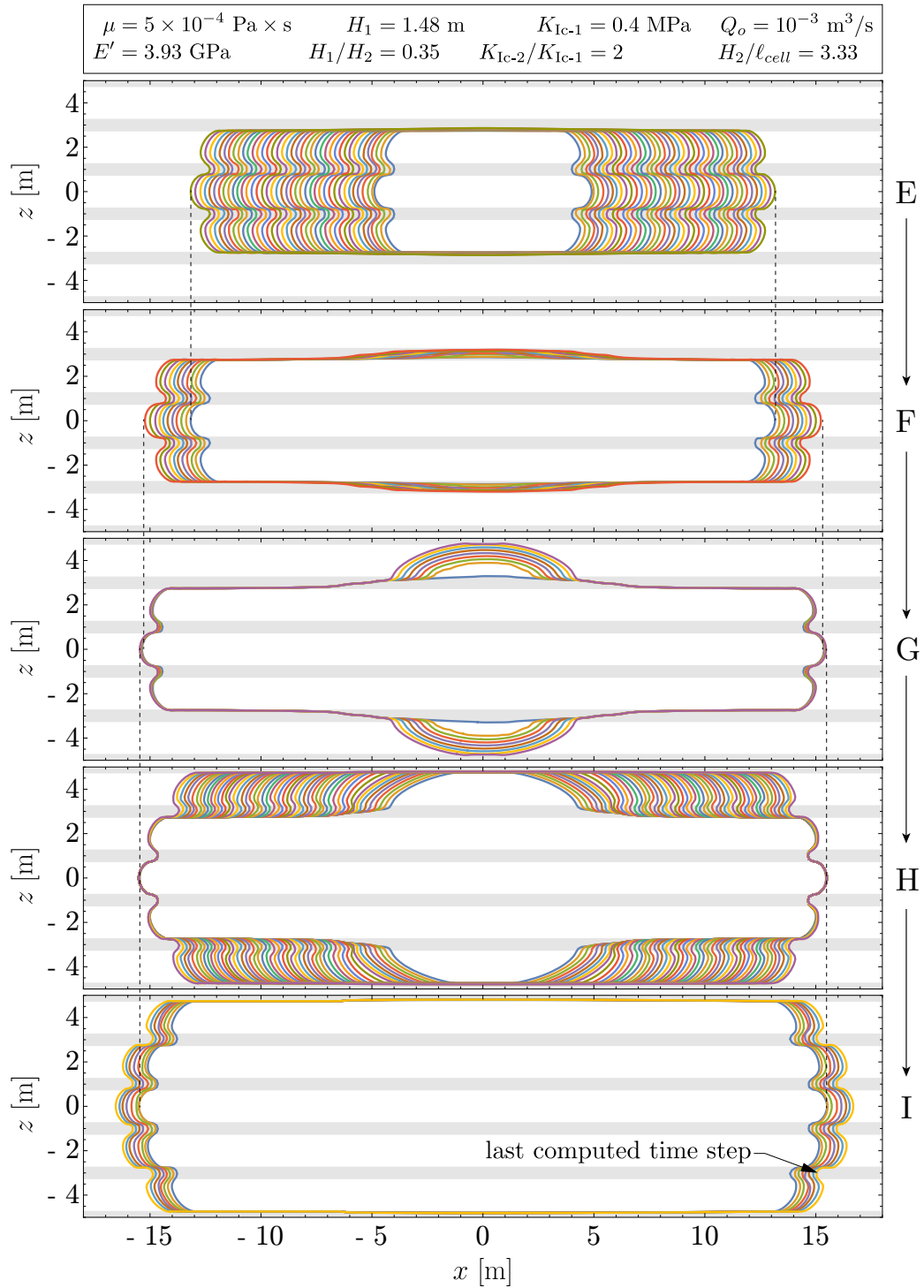_{K-M(PKN)}(h)$. While doing this, we are neglecting the increase of length occurring from the first breakthrough to the moment when the fracture gets contained again. We can also approximate the current fracture height h as a simple multiple of the repetitive height H, where $H = H_1 + H_2$, such that $h \approx n \times H$ with n being the integer number of layers pair ($n > 2$). The ratio between the velocities (Eq. (7.1)) becomes:

$$\frac{V_{\text{vertical}}}{V_{\text{horizontal}}} \approx \frac{1}{2} \times \frac{1}{1+n} \frac{E'^3 \mu Q_o}{H K_{\text{Ic-equiv}}^4} \tag{7.2}$$

For large n, $1/(n+1) \approx 1/n$ such that the previous equation can be further approximated as:

$$\frac{V_{\text{vertical}}}{V_{\text{horizontal}}} \approx \frac{1}{24} \times \frac{1}{\overline{\mathcal{K}}^4}, \qquad \overline{\mathcal{K}} = K_{\text{Ic-equiv}} \left(\frac{h}{E'^3 \mu' Q_o} \right)^{1/4} \tag{7.3}$$

The factor $1/24$ appears because of the use of μ in Eq. (7.2) and $\mu' = 12\mu$ in Eq. (7.3). Equation (7.3) proves that as the fracture height h becomes larger the ratio of both velocities tends to zero. As a consequence the fracture height will practically become constant.

7.5.2 The equivalent toughness $K_{\text{Ic-equiv}}$

Definition of $K_{\text{Ic-equiv}}$

The propagation of a contained fracture in the direction parallel to a sequence of layers of different fracture toughness can be described by considering an "equivalent" homogeneous medium. In other words, we can replace the fracture toughness distribution of the layers $K_{\text{Ic}}(z)$ by considering a uniform toughness $K_{\text{Ic-equiv}}$. This is possible if:

- the contained fracture is sufficiently elongated in the layers direction x (aspect ratio $L/(0.5h) \gtrsim 10$), such that the finite dimension along the x-direction does not affect the stress intensity factor at the propagating front.

Figure 7.4 – Correlation between the equivalent fracture toughness $K_{\text{Ic-equiv}}$ and the number n of repetitions of the pair of layers 1 and 2 in the fracture's height. a) saturation of the toughening effect (or size dependent fracture toughness). b) shows that the toughening effect saturates as $1/n$.
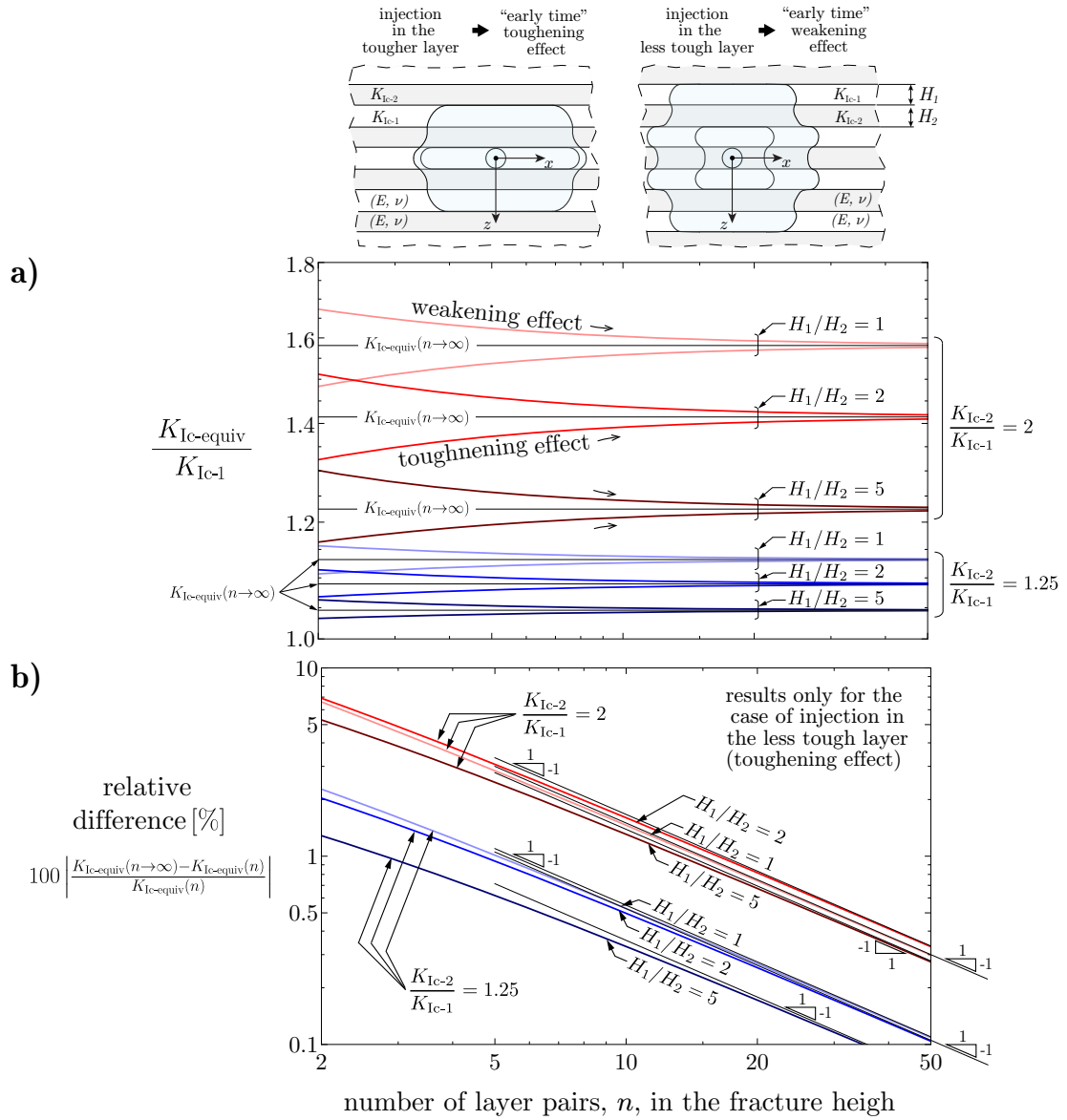
- the front does not change shape as it propagates. In other words, it simply translates in the x-direction.

If these conditions are satisfied, the equivalent toughness can be calculated by equating the energy release of the homogeneous and heterogeneous systems during a unit translation of the crack front in the x-direction (see Rice (1988) or Gao and Rice (1989)):

$$K_{\text{Ic-equiv}}^2 = \left\langle [K_{Ic}(z)]^2 \right\rangle \tag{7.4}$$

where the angle brackets $\langle \cdot \rangle$ denote an average along the z-direction.

The case of a square-wave toughness distribution

We consider a square-wave fracture toughness distribution characterised by values $K_{\text{Ic-1}}$ with wavelength H_1 (i.e. the thickness of the layer) and $K_{\text{Ic-2}}$ with wavelength H_2. We express the equivalent fracture toughness according to Eq. 7.4. Two different expressions can be derived depending on the location where the injection takes place (layer 1 or 2):

$$
\begin{aligned}
\frac{K_{\text{Ic-equiv}}}{K_{\text{Ic-1}}} &= \sqrt{\frac{n\left[1 + \frac{H_2}{H_1}\left(\frac{K_{\text{Ic-2}}}{K_{\text{Ic-1}}}\right)^2\right] + \frac{H_2}{H_1}\left(\frac{K_{\text{Ic-2}}}{K_{\text{Ic-1}}}\right)^2}{n\left(\frac{H_2}{H_1} + 1\right) + \frac{H_2}{H_1}}} \qquad \begin{array}{l}\text{injection in}\\ \text{layer n. 2}\end{array} \\[2em]
\frac{K_{\text{Ic-equiv}}}{K_{\text{Ic-1}}} &= \sqrt{\frac{n\left[\frac{H_1}{H_2} + \left(\frac{K_{\text{Ic-2}}}{K_{\text{Ic-1}}}\right)^2\right] + \frac{H_1}{H_2}}{n\left(\frac{H_1}{H_2} + 1\right) + \frac{H_1}{H_2}}} \qquad \begin{array}{l}\text{injection in}\\ \text{layer n. 1}\end{array}
\end{aligned}
\tag{7.5}
$$

where n is an integer number that represents the number of repetitions of the pair of layers 1 and 2 in the height of the fracture. In other words, n is the smallest integer value representing the number of times that the value H is contained within the height (h) of the fracture. As the fracture intersects a growing number of layers, the value of $K_{\text{Ic-equiv}}$ approaches a constant value $K_{\text{Ic-equiv}(n\to\infty)}$. This value is obtained by taking the limit of both equations for $n \to \infty$. In both case the limit is:

$$\frac{K_{\text{Ic-equiv}(n\to\infty)}}{K_{\text{Ic-1}}} = \sqrt{\frac{\frac{H_1}{H_2} + \left(\frac{K_{\text{Ic-2}}}{K_{\text{Ic-1}}}\right)^2}{\frac{H_1}{H_2} + 1}} \tag{7.6}$$

However, depending on the location of the injection point, the same value $K_{\text{Ic-equiv}(n\to\infty)}$ is approached in two different ways as n increases. When the injection point is located in layer n. 1, the equivalent toughness is always smaller than $K_{\text{Ic-equiv}(n\to\infty)}$ and it increases with n. In this case, we can say that increasing the number of layers has a "toughening effect" on the equivalent fracture toughness. The opposite is true when the injection point is located in layer n. 2. Increasing the number of layers has a "weakening effect" on the equivalent fracture toughness for this case. This result is shown in Fig. 7.4-a). The largest is the toughness

contrast $K_{\text{Ic-2}}/K_{\text{Ic-1}}$ between the layers, the more layers the fracture needs to intersect before $K_{\text{Ic-equiv}}$ approaches $K_{\text{Ic-equiv}(n\to\infty)}$. This is shown clearly in Fig. 7.4-b). When either one of the two layers is very small compared to the other, $H_1/H_2 \gg 1$ or $H_1/H_2 \ll 1$, the toughening and the weakening effects saturate over a smaller number of layers. This is shown in Fig. 7.5. Since these effects depend on the fracture size (via the number of layers traversed by the fracture footprint), they are possible mechanisms that could explain the size-dependent fracture toughness observed in some works related to hydraulic fracturing (see Liu et al. (2019) for discussion).

Validation against numerical simulations

We want to demonstrate that when the fracture aspect ratio $L/(0.5h)$ is sufficiently large, the fracture behaviour tends to the PKN-K solution evaluated using the equivalent toughness $K_{\text{Ic-equiv}}$, as defined in Eq. (7.5). We consider a set of contained hydraulic fractures of different height (h) which propagate in the toughness dominated regime in a layered material. Along the height of each fracture, there is a different number of layers pairs n such that a different value of $K_{\text{Ic-equiv}}$ characterizes each simulation. We have considered values of n ranging from 4 to 12. The corresponding layer distributions are displayed in the top part of Fig. 7.6. When the fracture reaches an aspect ratio $L/(0.5h) \gtrsim 10$ the fracture opening at the center differs only about 4 to 6.5% from the analytical solution. This relative error is acceptable because it is similar to the order of magnitude observed in the homogeneous case (see Fig. 6.6-c)). We note that the evolution of the fracture opening in Fig. 7.6 is oscillating. This can be explained by considering the combined effect of: i) the explicit front advancement algorithm used, ii) the very coarse discretisation of the fracture front compared to the layers heigh ($H_2/\ell_{cell} = (0.4\text{m})/(0.15\text{m}) \simeq 2.7$), iii) the assumption that for each front segment, fracture toughness is constant, iv) the iterative loop on the front direction associated to the direction dependent toughness implemented to regularise the jump between the layers, and v) the fact that the fracture propagates in the toughness dominated regime. It is now possible to explain the occurrence of transient local and artificial front pinning in certain footprint evolutions, as observed in the upper portion of Fig. 7.6. The fact that the fracture propagates in the toughness dominated regime already implies that the fracture behaviour is affected by a small local variation of fracture toughness. Now, imagine a front segment that is located in the layer of lower toughness for half of his length and in the layer of higher toughness for the other half. The algorithm evaluates the values of fracture toughness at the two segment ends [3] and it always selects the lower toughness value despite the fact that, in this case, a higher value is more appropriate. Imagine also that the chosen value of fracture toughness remains unchanged during the direction dependent toughness loop. Then the asymptotic tip solution is inverted using this toughness value to obtain the new front position. A lower value of toughness leads to overestimating the propagation in the layer of higher toughness. Then, such an estimate can not be further corrected by the algorithm because (for these simulations) we have used an explicit front advancing algorithm. Consequently, the front is locally pinned,

---

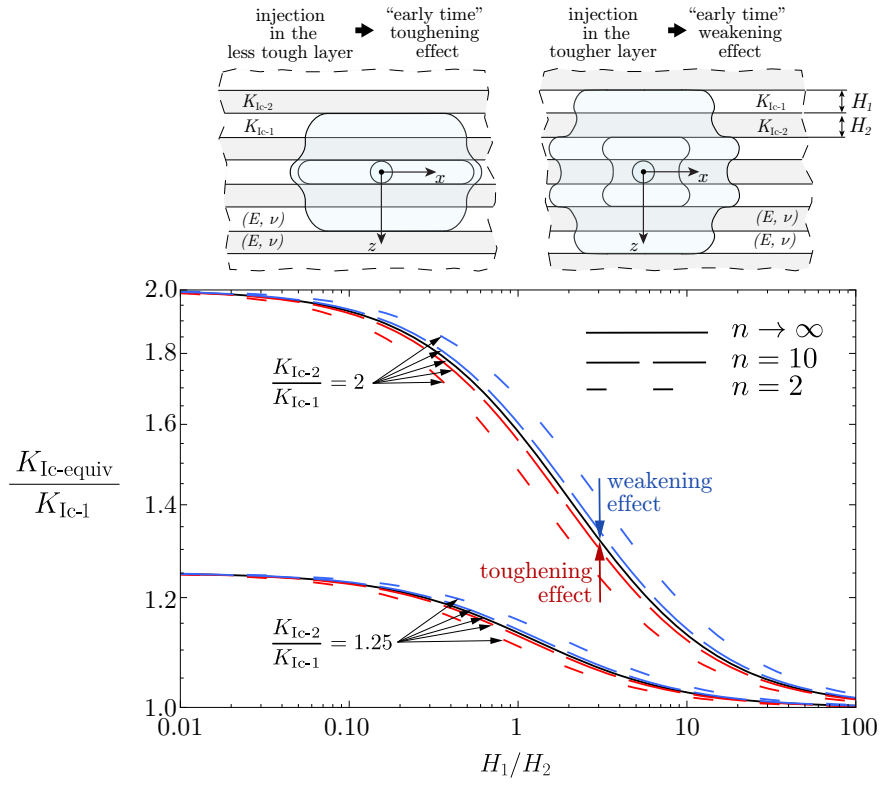[3]The toughness field is not discretised and it is defined by a function of the coordinates x and z.

Figure 7.5 – Correlation of the equivalent fracture toughness $K_{\text{Ic-equiv}}$ and the relative layers heigh H_1/H_2.

resulting in a local increase of fracture opening. As the fracture opening increases, the stress intensity factor follows, causing a de-pinning phase to occur and the concomitant reduction of fracture opening (see Fig. 7.6). Note that this problem can be solved while maintaining the explicit front advancing algorithm. In fact, it is sufficient to increase the discretisation of the front in the thinner layer of height H_2. A proof of this are the results displayed in Figs. 7.2 and 7.3. Although we used an explicit front advancing algorithm, the footprint evolution does not present the artificial pinning observed in Fig. 7.6. Note that similar ratios of energy dissipations characterize the set of simulations considered.

A final comment is needed concerning the evolution of the fracture footprint in the case of $n = 12$. Such a case is somewhat different from the others because after a few steps the fracture propagates only towards the right side. This also happens in the cases $n = 10$ and $n = 8$, but then the propagation in the arrested direction restarted. This can be understood by recalling a theoretical result obtained in Gao and Rice (1987) which states that for a uniformly loaded mode I fracture, the fracture geometry is known up to a zero order perturbation. The position of the fracture footprint is thus defined up to a "rigid" body motion: an additive constant along the $x-$ direction. In the case of contained propagation in a homogeneous medium, we have seen that when the number of cells discretising the fracture height is "low", the numerical scheme prevents "artificially" such rigid body motion. On the other hand, when the number of cells increases, the fixed point scheme for the new fracture footprint in the implicit level set algorithm has a harder time converging due to this rigid body motion. The theoretical result obtained in Gao and Rice (1987) remains valid for the heterogeneous distribution of fracture toughness that we considered. The heterogeneity is symmetric with respect to the plane $z - y$. Because the number of cells discretising the initial fracture front increases from case $n = 4$ to case $n = 12$, the localised front pinnings have different effects on the overall propagation. Particularly, for the case $n = 12$ it causes the entire fracture to propagate only on one side.

7.5.3 Impact of the toughening and weakening effects on the "late time" behaviour

For a periodic square-wave-like toughness distribution, the equivalent fracture toughness $K_{\text{Ic-equiv}}$ truly approaches $K_{\text{Ic-equiv}(n\rightarrow\infty)}$ only in the limit of an infinite number of layers. In the case where the initial fracture propagates from the "less tough" layer, the equivalent toughness increases from the lower limit $K_{\text{Ic-1}}$ to its final value. On the contrary, in the case where the initial fracture propagates from the "tougher" layer, the equivalent toughness decreases from the upper limit $K_{\text{Ic-2}}$ to its final value. To verify that these behaviours do not exclude the possibility that the fracture becomes contained at "late time" we compute again the ratio between the vertical and the horizontal velocities accounting for the size dependence of the equivalent toughness. In other words:

$$\frac{V_{\text{vertical}}}{V_{\text{horizontal}}} = \frac{\Delta h}{\Delta(2L)} = \frac{2H}{L_{K-M(PKN)}\left(h + 2H, K_{\text{Ic-equiv}}(n+2)\right) - L_{K-M(PKN)}\left(h, K_{\text{Ic-equiv}}(n)\right)} \quad (7.7)$$

In both cases, for a large n, the ratio of velocities scales as $\propto 1/n$, confirming the existence of the contained "late time" behaviour. Here, we report the expression for the case where the fracture propagates from the "less tough" layer:

$$\frac{V_{\text{vertical}}}{V_{\text{horizontal}}} \approx f\left(H_1/H_2, K_{\text{Ic-2}}/K_{\text{Ic-1}}, n\right)\frac{E'^3\mu Q_o}{HK_{\text{Ic-1}}^4}$$

$$f(\text{a},\text{b},n) = \frac{2}{\frac{(n+2)^2\left((n+2)\left(\text{a}+\text{b}^2\right)+\text{a}\right)^2}{(\text{a}(n+3)+n+2)^2} - \frac{n^2\left(\text{a}n+\text{a}+\text{b}^2 n\right)^2}{(\text{a}n+\text{a}+n)^2}}$$

$$(7.8)$$

7.5.4   The conditions that lead to "late-time" fracture containment

For a given periodic toughness distribution the equivalent fracture toughness $K_{\text{Ic-equiv}}$ becomes (practically) constant when the fracture has propagated through a sufficiently large number of repetitive units n. In analogy to the three layers case considered in Chapter 6, the jump in the containment time is only activated when:

$$\frac{K_2}{K_{\text{Ic-equiv}(n\rightarrow\infty)}} \geq \sqrt{2} \tag{7.9}$$

This is the condition that leads to "late-time" fracture containment. For toughness ratios below $\sqrt{2}$ the breakthrough will happen before a PKN-K fracture can be formed. In other words, when the toughness ratio is less than $\sqrt{2}$ there is no separation between the vertical fracture length-scale h and the horizontal one $2L$. Each time the fracture is arrested after growing vertically of a given quantity Δh, the propagation increases laterally of the same quantity ΔL. While the vertical increment Δh remains the same in time because of the distribution of fracture toughness, the increment ΔL becomes constant as $K_{\text{Ic-equiv}}$ approaches $K_{\text{Ic-equiv}(n\rightarrow\infty)}$. For this reason if $K_2/K_{\text{Ic-equiv}(n\rightarrow\infty)} < \sqrt{2}$ the late time propagation is self-similar and the aspect ratio is constant. Only when the separation of length-scales takes place the position of the propagating front does not affect the stress intensity factor at the center (until the transition to PKN-M).

Now, if we consider a square-wave variation of fracture toughness the condition that ensures "late-time" fracture containment (Eq. (7.9)) becomes:

$$\frac{H_1}{H_2} \geq \frac{1}{1-\left(\frac{\sqrt{2}}{K_{\text{Ic-2}}/K_{\text{Ic-1}}}\right)^2} \tag{7.10}$$

For this particular toughness distribution, a necessary condition to have a "late time" fracture containment is that the toughness ratio between the layers must be $K_{\text{Ic-2}}/K_{\text{Ic-1}} \geq \sqrt{2}$. Another necessary condition is that the height H_1 related to the less tough layer must be larger than that of the tougher layer H_2. These two conditions correspond to the two asymptotes in the
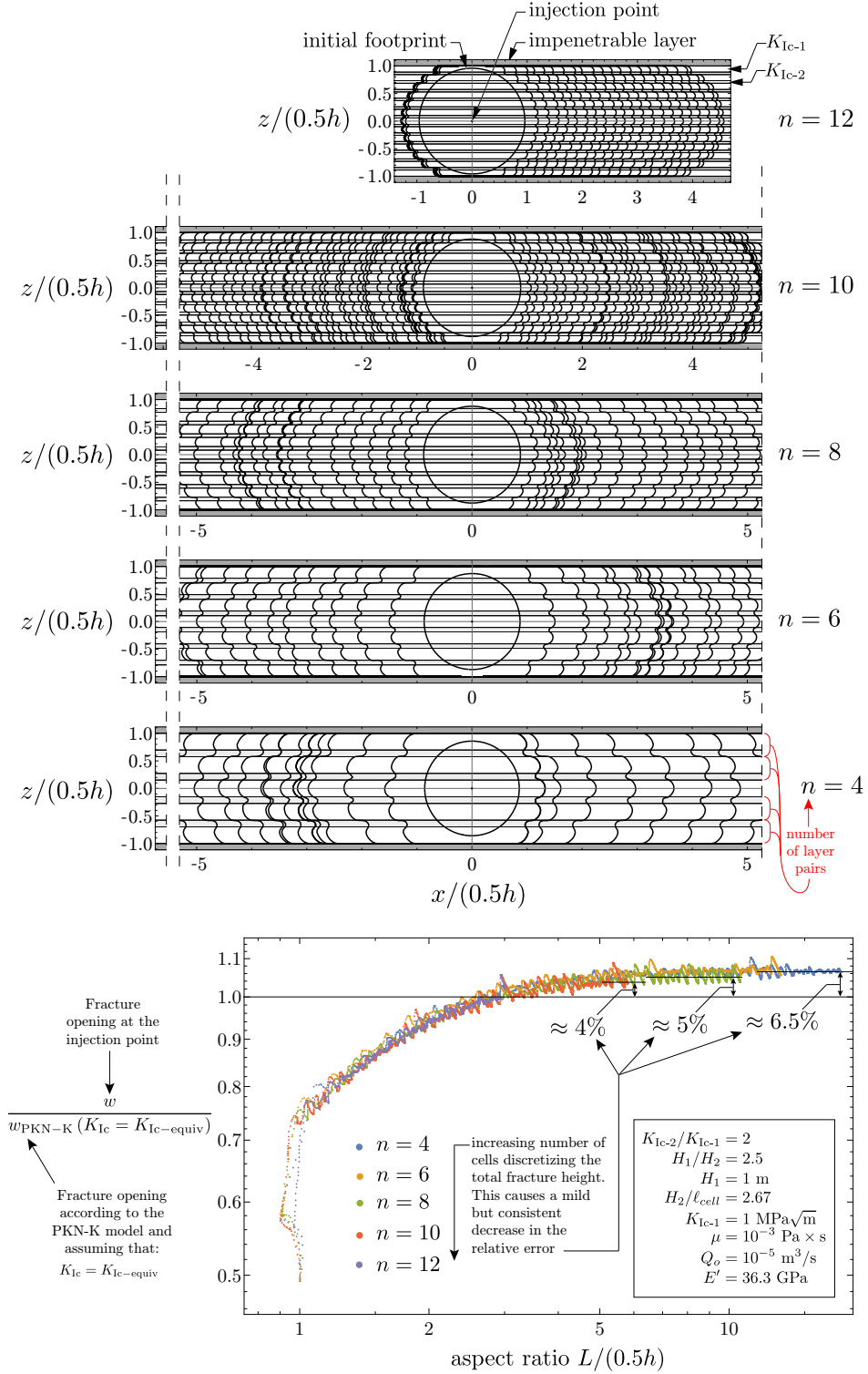
Figure 7.6 – Numerical versus analytical predictions of the fracture opening at the injection point. We considered toughness dominated hydraulic fractures propagating parallel to different toughness distributions. On the top we display the setup of the numerical simulations together with a number of footprints.
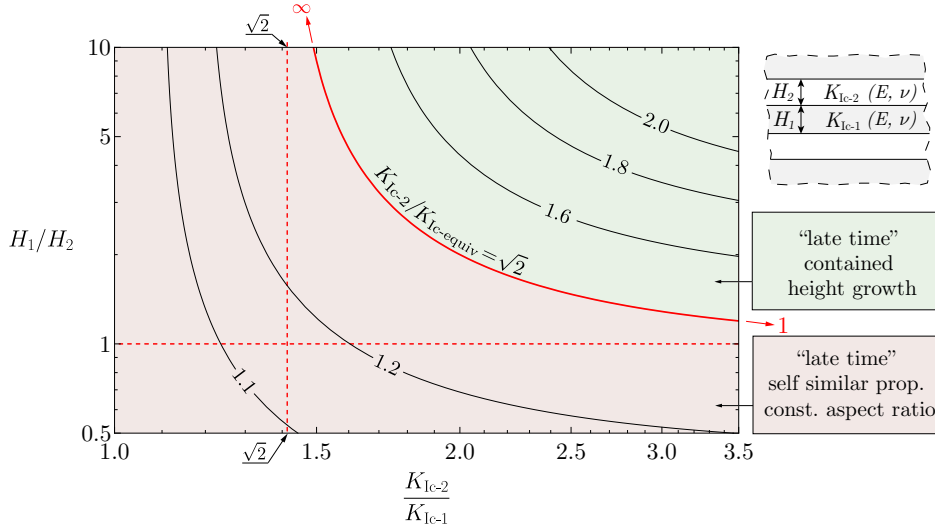
Figure 7.7 – Parametric space that defines the conditions under which the late time containment of a hydraulic fracture is established. The isolines are related to constant values of the toughness ratio $K_2/K_{\text{Ic-equiv}(n\to\infty)}$.

parametric space in Fig. 7.7 by red dashed lines. In the same parametric space we show the position of the isoline corresponding to $\frac{K_2}{K_{\text{Ic-equiv}(n\to\infty)}} = \sqrt{2}$ using a red continuous line. The position of the other isolines is obtained similarly as:

$$\frac{K_{\text{Ic-2}}}{K_{\text{Ic-equiv}(n\to\infty)}} = \text{const} \rightarrow \frac{H_1}{H_1} = \frac{\left(\frac{K_{\text{Ic-2}}}{K_{\text{Ic-1}}}\right)^2 \left[1 - (\text{const})^2\right]}{(\text{const})^2 - \left(\frac{K_{\text{Ic-2}}}{K_{\text{Ic-1}}}\right)^2} \tag{7.11}$$

By inspecting Fig. 7.7 and keeping in mind that the usual toughness contrast $K_{\text{Ic-2}}/K_{\text{Ic-1}}$ measured at the laboratory scale is in the range $K_{\text{Ic-2}}/K_{\text{Ic-1}} \in (1, 2)$ we can expect the ratio $K_2/K_{\text{Ic-equiv}(n\to\infty)}$ to be in the range $(1, 1.8)$.

7.6 Scale of applicability

Provided that $K_2/K_{\text{Ic-equiv}(n\to\infty)} \geq \sqrt{2}$, the "late-time" containment mechanism occurs regardless the initial propagation regime. Even if the hydraulic fracture is initially viscosity dominated, as the fracture height h becomes larger, the transition length-scale $L_{KM(PKN)} \propto h^2$ will dominate. However, the results provided in this work do not consider the effect of gravity on hydraulic fracture propagation. If the fracture height h is larger than the critical lengthscale for buoyant growth L_b, the gravity effect must be taken into account. We can estimate the buoyancy lengthscale as $L_b = \left(K_{Ic-1}/\left(\gamma_{\text{solid}} - \gamma_{\text{fluid}}\right)\right)^{2/3}$ (see Lister and Kerr (1991)), where γ is the specific weight. Assuming $K_{Ic-1} = 2\,\text{MPa}\sqrt{\text{m}}$ and $\gamma_{\text{solid}} - \gamma_{\text{fluid}} = 16\,\text{kN/m}^3$, we obtain $L_b = 26\,\text{m}$. An estimate larger than the few meters scale of a micro-hydraulic fracturing treat-

ment (for which buoyant effects are thus negligible), but possibly on par with the scales of hydraulic fractures observed in well stimulation operations. Another limitation to the applicability of the mechanism that we have described is that Linear Elastic Fracture Mechanics is assumed to be valid at all scales.

7.7 Orders of magnitude in practice

Micro-hydraulic fracturing test[*]								
Q_o $[\text{m}^3/\text{s}]$	μ [Pa s]	h [m]	H_1 [m]	H_2 [m]	$K_{\text{Ic-1}}$	$K_{\text{Ic-2}}$ $[\text{MPa}\sqrt{\text{m}}]$	$\dfrac{h}{L_{KM(PKN)}}$	$\dfrac{V_{\text{vert.}}}{V_{\text{horiz.}}}$
1.6667×10^{-6} (0.1 L/min)	10^{-3}	1.	0.09	0.01	1.1	1.65	0.09	0.014
2.5×10^{-5} (1.5 L/min)	0.025	2.	0.146	0.054	1.45	2.61	0.89	0.42
[*]$E = 30$ GPa and $\nu = 0.25$ in all the considered cases								

Table 7.1 – Ratio between the average vertical velocity and the average horizontal velocity computed for some cases of open-hole micro-hydraulic fracturing test. The lengthscale $L_{KM(PKN)}$ is computed using $K_{\text{Ic-equiv}}(h)$.

We consider a few examples of two practical applications: the open-hole micro-hydraulic fracturing test (Haimson, 1993) and the hydraulic fracturing treatment for well stimulation. For each of them, we use Eq. (7.8)[4] to compute the ratio between the vertical and the horizontal velocity ($V_{\text{vert.}}/V_{\text{horiz.}}$) for a given fracture size h. For all the cases, we choose values of layer heights H_1, H_2 and toughness contrast $K_{\text{Ic-2}}/K_{\text{Ic-1}}$ such that $K_{\text{Ic-2}}/K_{\text{Ic-equiv}} \geq \sqrt{2}$. When $V_{\text{vert.}}/V_{\text{horiz.}} \ll 1$ the fracture can be considered practically contained; otherwise, the containment mechanism does not occur. We also compute the ratio between the fracture size h and the transition lengthscale $L_{KM(PKN)}$ to check that, for $V_{\text{vert.}}/V_{\text{horiz.}} \ll 1$, the born PKN-like fracture is in the toughness dominated regime. The numerical values chosen for the injection rate Q_o, fluid viscosity μ, fracture height h, Young's modulus E and Poisson's ratio ν correspond to the usual values encountered in the corresponding applications. For further clarifications regarding the chosen values, the reader is referred to the section "Orders of magnitude in practice" of Chapter 6. The estimates of $V_{\text{vert.}}/V_{\text{horiz.}}$ for the cases of open-hole micro-hydraulic fracturing test reported in Table 7.1 demonstrate that the fracture can be practically contained. In particular, for the "low-injection" and "low-viscosity" case, the ratio $V_{\text{vert.}}/V_{\text{horiz.}}$ is about 1% when $h = 1$ m. A larger value $V_{\text{vert.}}/V_{\text{horiz.}} = 0.42$ for $h = 2$m is obtained in the "high-injection", and "high-viscosity" case. In the case of a hydraulic fracturing treatment, the fracture propagates mostly in the viscosity dominated regime. Therefore, even relatively high values of fracture toughness, such as 1.8 and 2.6MPa m$^{1/2}$ cannot create the containment effect (see Table 7.2). By reducing the injection rate to a value one order of magnitude lower than what is commonly used in practical applications, the velocity ratio $V_{\text{vert.}}/V_{\text{horiz.}}$ becomes 0.3 for $h = 40$ m(see Table 7.2).

---

[4]The results do not change significantly when Eq. (7.2) is used instead of Eq. (7.8).

Hydraulic fracturing treatment[*]								
Q_o $[\text{m}^3/\text{s}]$	μ [Pa s]	h [m]	H_1 [m]	H_2 [m]	$K_{\text{Ic-1}}$	$K_{\text{Ic-2}}$ $[\text{MPa}\sqrt{\text{m}}]$	$\dfrac{h}{L_{KM(PKN)}}$	$\dfrac{V_{\text{vert.}}}{V_{\text{horiz.}}}$
6.0×10^{-3} (360 L/min)	1.	40.	0.96	0.04	1.8	2.61	10.8	5.25
3.0×10^{-2} (1800 L/min)	0.005						430.	210
6.0×10^{-4} (36 L/min)	0.005	40.	1.58	0.42	1.2	2.0	0.61	0.29
			0.40	0.10			0.61	0.30
[*] $E = 30$ GPa and $\nu = 0.25$ in all the considered cases								

Table 7.2 – Ratio between the average vertical velocity and the average horizontal velocity computed for some cases of hydraulic fracturing treatment. The lengthscale $L_{KM(PKN)}$ is computed using $K_{\text{Ic-equiv}}(h)$.

7.8 Conclusions

In this work, we have considered a hydraulic fracture propagating in a layered material characterised by a periodic distribution of fracture toughness. We have demonstrated that the "late time" hydraulic fracture propagation can be self similar (with constant aspect ratio), or practically contained. The ratio between the highest fracture toughness in the periodic system and an "equivalent" fracture toughness determines the "late time" behaviour. In particular, when this ratio is above $\sqrt{2}$ the fracture will be practically contained at "late time". The "equivalent" fracture toughness must be computed from the average fracture energy of the repeated layers. Other factors, not considered here, can also have a first order impact on the estimate of breakthrough time, notably: heterogeneity of elastic properties between layers, fluid leak-off in the surrounding medium, non-Newtonian fluid rheologies (Moukhtari and Lecampion, 2018), different type of injections (line source, varying injection rate) Garagash (2023). Finally we must mention that this work does not consider the nucleation and coalescence with secondary fractures. The secondary fractures are those that could form in the "less tough" material because of the stress concentration induced by the nearby fracture front that is propagating in the "tougher material".

8 Conclusions

8.1 Main findings

In the framework of this thesis, we have contributed to the improvement of the Implicit Level Set Algorithm by proposing a new strategy to reconstruct the fracture front. We have demonstrated that the current algorithm available in the literature breaks for high front curvature. The newly proposed strategy uses a bilinear interpolation of the level set field between neighbouring cells to find the front intersections with the underlying Cartesian discretization. Throughout the thesis, we have proven the accuracy of the new front reconstruction scheme by comparing it to a number of analytical solutions, such as the toughness and viscosity dominated radial solutions, and the toughness and viscosity dominated PKN solutions. We also compared the numerical scheme to the analytical solution for the front deformation caused by the presence of a tough obstacle. We have also considered comparisons against laboratory experiments involving strong deformations of the fracture front. In particular, we have demonstrated that the Implicit Level Set Algorithm can successfully predict the interaction and coalescence of a pair of three dimensional and planar hydraulic fractures. For the first time, we have shown a qualitative and almost quantitative comparison of the fluid flow velocity to the one observed in the experiment. We then used this numerical tool to investigate the effect of toughness heterogeneities on hydraulic fracture propagation, focusing on the limiting case of an impermeable medium. We have established the conditions under which a region of higher fracture toughness can stop hydraulic fracture propagation. We have then considered the important case where the fracture encounters and arrests its propagation at the interfaces with two semi-infinite layers of higher fracture toughness. We have demonstrated that the fracture between these two tough layers can never be indefinitely contained. In other words, the fracture will always breakthrough in the bounding layers. We have quantified the amount of time the fracture propagates contained, between the two layers before breaking through. We found that this time is larger when the radial hydraulic fracture reaches the bounding layers in the toughness dominated regime. For this case, we found that the containment time strongly depends on the toughness contrast between the layers. A finite jump in the containment time is observed between the cases where the toughness ratio is below and above

$\sqrt{2}$. We have elucidated the mechanical reason for this jump. We have finally extended our study to the case where the hydraulic fracture interacts with a periodic distribution of fracture toughness. We have demonstrated that a size dependent fracture toughness can be observed when the fracture propagates in the toughness dominated regime over a small number of layers. Depending on the toughness distribution between the layers, this "early time" size dependent fracture toughness can either be "weakening" or "strengthening". We have then considered the "late time" toughness dominated propagation corresponding to the case where the hydraulic fracture has propagated over a large number of layers such that the size dependent fracture toughness can not be manifested. We have demonstrated two possible "late time" evolutions of the fracture. In one case, the fracture propagates maintaining a constant aspect ratio (self-similar propagation), while in the other, the aspect ratio keeps increasing, resulting in a "practically contained" propagation. This last case is similar to the one where the fracture is contained between two tough layers. As a result of this thesis, we can conclude that the effect of layers of toughness heterogeneities on the containment of hydraulic fractures strongly depends on their propagation regime. By combining low injection rates with a low viscosity fluid there is a potential to promote fracture containment in small scale industrial applications such as the micro-hydraulic fracturing tests.

8.2 Perspectives

Several research questions in direct relation to this work would deserve further investigations. In the following, we list some possible future studies on this topic. We divide them into two different themes: experimental developments, analytical and numerical developments.

Experimental developments

- An experiment should be made to prove the two different "late time" hydraulic fracture behaviours that we derived in the case of a fracture propagating through a layered material. 3D printing technology can be used to create a layered material structure where the size of each layer can be as small as a few mm.

- An experiment can be made to simulate the interaction and coalescence of two coplanar hydraulic fractures in the viscosity dominated regime.

Analytical and Numerical developments

- The scaling of the phenomenon of the coplanar coalescence of two hydraulic fractures is still lacking both, in the toughness and viscosity dominated propagation regime.

- It would be interesting to extend the analysis of the experiment related to the coalescence of two hydraulic fractures by accounting for the presence of finite boundaries.

- Further verification is needed for the ILSA scheme in the case of self-coalescence of a fracture front. A self-coalescing fracture front appears, for example, when the fracture cannot propagate through an inclusion of higher fracture toughness. In this case, the fracture propagates around the inclusion, then it coalesces ahead, leaving behind an island of intact material. As the fracture propagates, the island of intact material becomes smaller and smaller until self-coalescence of the fracture front.

- Another topic not explored before is the effect of randomly distributed toughness heterogeneities on hydraulic fracture propagation. In particular, it would be essential to establish under which conditions the hydraulic fracture leaves behind its fracture front "islands" of tougher and unbroken material.

- When a hydraulic fracture approaches the interface with a "less tough" layer, a fracture can nucleate ahead of the interface. The two fractures then interact and coalesce. This phenomenon was not included in the numerical simulations, and it could represent a reason for an anticipated breakthrough.

- The results obtained for the case of a hydraulic fracture contained between two tough layers should be extended, accounting for a possible contrast in elastic properties between the layers.

- In the context of the hydraulic fracture interaction with different layers, we have assumed that the propagation remains coplanar. This hypothesis can be relaxed, allowing for a possible propagation on the interfacial plane between the layers.

- The existing numerical tool further developed during this thesis can be extended to describe more physical effects. To mention a few examples, it would be possible to extend the code to account for the interaction of several parallel hydraulic fractures or the case where the fluid front does not coincide with the fracture front.

A Appendix

The energy balance in Eq. 5.7 expressed in a Cartesian reference system is reduced here to a plane strain geometry consisting of a semi-infinite fracture. For this purpose, we set $x = 0$ and we limit the integrals to the interval $z \in [H/2 - h, H/2]$ obtaining:

$$\underbrace{\underbrace{G \times V}_{\text{fracture energy rel. rate}} + \underbrace{\mu' V^2 \int_{H/2-h}^{H/2} \frac{1}{w} \mathrm{d}z}_{\text{viscous dissipation rate}} + \underbrace{\int_{H/2-h}^{H/2} \frac{1}{2} \frac{\mathrm{D}}{\mathrm{D}t} \left(w \times (p_f - \sigma_o) \right) \mathrm{d}z}_{\text{rate of elastic energy accretion}}}_{\mathscr{P}_i} = \underbrace{V w(h) p(h)}_{\mathscr{P}_e} \quad \text{(A.1)}$$

The reference system z is fixed in time. We consider a new coordinate system $\bar{z}$ that has its origin at the fracture tip and moves at its same constant velocity V, see Fig. A.1. In this reference system the total derivative in the previous equation reduces to:

$$\frac{\mathrm{D}(\cdot)}{\mathrm{D}t} = \frac{\mathrm{d}(\cdot)}{\mathrm{d}t} + \frac{\mathrm{d}(\cdot)}{\mathrm{d}\bar{z}} \frac{\mathrm{d}\bar{z}}{\mathrm{d}t}$$
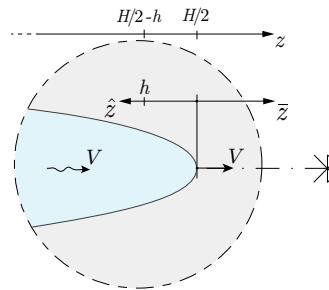

Figure A.1 – Reference systems for a semi-infinite steadily-moving hydraulic fracture. The origin of the reference system x is fixed in time, while the one of systems $\hat{x}$ and $\bar{x}$ is moving at the constant velocity of the fracture front V.

Appendix A. Appendix

When expressed in the a reference system $\hat{z} = -\bar{z}$, as shown in Fig. A.1, the previous becomes:

$$\frac{D(\cdot)}{Dt} = \frac{d(\cdot)}{dt} + (-1)\frac{d(\cdot)}{d\hat{z}}(-1)\frac{d\hat{z}}{dt}$$

now defining $V = (-1)\frac{d\hat{z}}{dt}$ and considering that $V = \text{const}$ implies that:

$$\frac{D(\cdot)}{Dt} = -\frac{d(\cdot)}{d\hat{z}}V$$

At time t the fracture front is at position $H/2$ and the relation between the coordinate systems $\hat{z}$ and z is:

$$z = H/2 - \hat{z} \Rightarrow \frac{dz}{d\hat{z}} = -1$$

Thus, the 1st integral on the left hand side of Eq. A.1 becomes:

$$\mu'V^2 \int_{H/2-h}^{H/2} \frac{1}{w}dz = \mu'V^2 \int_{h}^{0} \frac{1}{\hat{w}}(-1)d\hat{z} = \mu'V^2 \int_{0}^{h} \frac{1}{\hat{w}}d\hat{z}$$

where $w = w(z)$ and $\hat{w} = \hat{w}(\hat{z})$. The 2nd integral on the left hand side of Eq. A.1 becomes:

$$\frac{1}{2}\int_{H/2-h}^{H/2} \frac{D}{Dt}(w \times p)dz = \frac{1}{2}\int_{h}^{0} \frac{D}{Dt}(w \times p)(-1)d\hat{z} = -\frac{1}{2}V\int_{0}^{h} \frac{d}{d\hat{z}}(w \times p)d\hat{z} = \frac{1}{2}V\left[w(0)p(0) - w(h)p(h)\right]$$

By noting that the term $w(0)p(0) = 0$ (e.g. Garagash (2009); Garagash et al. (2011)) Eq. A.1 reduces to:

$$\underbrace{\underbrace{G}_{\text{fracture energy rel.}} + \underbrace{\mu'V\int_{0}^{h} \frac{1}{\hat{w}}d\hat{z}}_{\text{viscous dissipation}}}_{\text{Total internal dissipated energy}} = \underbrace{\frac{1}{2}\hat{w}(h)\hat{p}(h)}_{\text{quota of ext. energy dissipated}}$$

B Appendix

B.0.1 Supplemental material to Figures 4.1 and 4.2

The parameters used in the numerical simulations related to Figs. 4.1 and 4.2 are: fluid viscosity μ, Young's modulus E, Poisson's ratio ν, injection rate Q_o, layer's height H and fracture toughness K_{Ic}. Their numerical values for different simulations are reported in Table B.1 .

$\overline{\mathcal{K}}$	μ [Pa s]	K_{Ic-MIN} [MPa $m^{1/2}$]	K_{Ic-MAX} [MPa $m^{1/2}$]	ν [−]	E [GPa]	H [m]	Q_o [m³/s]
5.68	1×10^{-8}		4.0				
1.01	1×10^{-4}						
0.568	1×10^{-3}	0.4	2.0	0.4	3.3	2.96	0.001
0.319	1×10^{-2}						
0.180	1×10^{-1}		4.0				
0.0568	1×10^{4}						

Table B.1 – Parameters used in the numerical simulations related to Figs. 4.3 and 4.4.

In Fig. B.1 we show the evolution of the max front coordinate z_{max} for the set of simulations in Table B.1. When the propagation is radial, i.e. for $t/t_{\text{touch}} < 1$, the growth of z_{max} lies in between the radial-M ($\propto t^{4/9}$) and the radial-K ($\propto t^{2/5}$) regimes. For $t/t_{\text{touch}} > 1$ the propagation is confined. The small increments of z_{max} that can be seen in the figure are related to the numerical regularization of the toughness jump between the layers. A a linear ramp, taking place over a distance much smaller than the radial discretization, has been imposed for the toughness variation between the layers. Thus, z_{max} can either slowly grow or it can undergo small numerical oscillations (see the plot at the top of Fig. B.1). When the front is close to the interface between two elements of the discretization can get artificially

"attracted" to the new element. In order to prevent this effect from happening we impose that the interface between the bounding layers is located in the middle of one element.
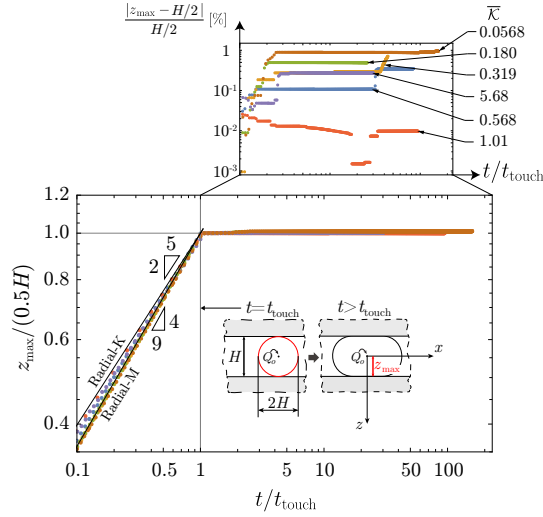

Figure B.1 – Evolution of the max front coordinate z_{max} as a function of time for the set of simulations in Table B.1.

B.0.2 Supplemental material to Figures 4.3, 4.4 and 4.5

In Table B.2 we show the parameters used in the numerical simulations reported in Fig. 4.3, 4.4 and 4.5.

sim ID	K_{Ic-MIN} $\left[\text{MPa}\,m^{1/2}\right]$	K_{Ic-MAX} $\left[\text{MPa}\,m^{1/2}\right]$	ν $[-]$	E [GPa]	H [m]	Q_o $\left[\text{m}^3/\text{s}\right]$
1		0.735		3.3	2.96	1×10^{-3}
2	0.400	0.735	0.4	33.0	2.96	1×10^{-3}
2-bis		0.650				
3		0.735		3.3	29.6	1×10^{-3}
4		0.735		3.3	2.96	1×10^{-4}

Table B.2 – Parameters used in the numerical simulations reported in Figs. 4.3, 4.4 and 4.5.

B.0.3 Numerical solution of a volume-control hydraulic fracture

The equations governing the problem of a fracture propagating under the injection of an inviscid fluid are Eqs. (M 3.1), (M 3.3) and (M 3.5) of the main manuscript. The numerical scheme to the solution of these equations is essentially the one discussed in Peirce and

Detournay (2008). Here we are reporting the numerical strategies used to efficiently solve the system of Eqs. (M 3.1) and (M 3.3), at each time step, and for a trial fracture front position. The system of equations is discretized using a Cartesian mesh and can be written as (see Peirce and Detournay (2008)):

$$
\begin{bmatrix}
 & & -1 \\
 & \mathbb{E} & & \cdots \\
 & & -1 \\
1 & \cdots & 1 & 0
\end{bmatrix}
\begin{bmatrix}
w_1 \\
\cdots \\
w_N \\
p_f
\end{bmatrix}
=
\begin{bmatrix}
-\sigma_o\,(x_i, z_i) \\
\cdots \\
-\sigma_o\,(x_i, z_i) \\
Q_o t / \left(\Delta x \Delta y \beta_i\right)
\end{bmatrix}
\tag{B.1}
$$

where $\mathbb{E}$ is the discretized elasticity (Eq.(M 3.1)), p_f is the fluid pressure and σ_o is the confining stress, $\Delta x, \Delta y$ are the cell sizes and β_i is a coefficient that accounts for the partially filled cells that are traversed by the fracture front.

Iterative solution of the system of equations

The system in Eq. (B.1) belongs to the class of saddle point problems and can be rewritten as Benzi et al. (2005):

$$
\begin{bmatrix}
A & B_1^T \\
B_2 & C
\end{bmatrix}
\begin{bmatrix}
w \\
p
\end{bmatrix}
=
\begin{bmatrix}
f \\
g
\end{bmatrix}
\tag{B.2}
$$

where $A \equiv \mathbb{E}$ is a positive definite matrix, $B_1 = \begin{bmatrix} -1 & \cdots & -1 \end{bmatrix}$, $B_2 = -B_1$ and $C \equiv 0$. To the solution of the system we used the GMRES method in combination to the following upper triangular preconditioner Benzi et al. (2005):

$$
P = \begin{bmatrix}
\hat{A} & B_1^T \\
0 & \hat{S}
\end{bmatrix}
\qquad
P^{-1} = \begin{bmatrix}
\hat{A}^{-1} & -B_1^T \hat{S}^{-1} \hat{A}^{-1} \\
0 & \hat{S}^{-1}
\end{bmatrix}
\tag{B.3}
$$

where $\hat{A}$ is a diagonal matrix with the same entries of the matrix A and $\hat{S} = -B_2 \hat{A} B_1^T$ is the approximated Schur complement of the system.

B.0.4 Numerical integration of the energy release rate

The method that we used to estimate the energy release rate G is essentially the "*energy or compliance method*" presented in Watwood (1970). The difference is that here the numerical solution that we used is obtained by the Displacement Discontinuity Method. We will briefly recall the procedure. Consider a 3D-planar fracture of surface Σ embedded in an infinite medium. When its faces are loaded by an internal net pressure p, the elastic energy stored into the medium U amounts to:

$$
U = \frac{1}{2} \int_{A(t)} p\,(x, z)\, w\,(x, z)\, \mathrm{dx dz}
\tag{B.4}
$$

G can be approximated by considering 2 fracture footprints, one at a time t_n and one at a time $t_{n+1} = t_n + \triangle t$ with $\triangle t \to 0$:

$$G = \left(\frac{\partial U}{\partial \Sigma}\right)_p \simeq \left(\frac{\Delta U}{\Delta \Sigma}\right)_p = \left(\frac{U_{n+1} - U_n}{\Sigma_{n+1} - \Sigma_n}\right)_p$$

At time t_n, the integral in Eq. (B.4) has been computed by discretizing the fracture footprint, using N_c^n rectangular cells, each of area A_c. The coefficients η_i accounts for cells that are only partially traversed by the fracture front, i.e. partially opened (the fracture front position is tracked as in Peirce and Detournay (2008)). They express the ratio between the fractured area and the total cell area A_c (i.e. $\eta_i = 1$ for a cell completely inside the fracture footprint). The term U_{n+1} in the previous equation can be written as:

$$U_{n+1} \simeq \frac{1}{2} A_c p \left(\sum_{i=1}^{N_c^{n+1}} w_i \eta_i\right)_{n+1}$$

Finally, by combining the previous equations, G can be estimated by:

$$G \simeq \frac{p}{2} \frac{\left(\sum_{i=1}^{N_c^{n+1}} w_i \eta_i\right)_{n+1} - \left(\sum_{i=1}^{N_c^n} w_i \eta_i\right)_n}{\left(\sum_{i=1}^{N_c^{n+1}} \eta_i\right)_{n+1} - \left(\sum_{i=1}^{N_c^n} \eta_i\right)_n}$$

B.0.5 Numerical exploration of the parametric space $\left(K_{Ic-2}/K_{Ic-1}; \overline{\mathscr{K}}; \Delta t_c/t_{\textbf{touch}}\right)$

We have determined numerically the value of $\Delta t_c/t_{\text{touch}}$ for a wide range of coordinates in the parametric space $\left(K_{Ic-2}/K_{Ic-1}, \overline{\mathscr{K}}\right)$ with $\overline{\mathscr{K}} \in [0.0047, 1.57]$. Since $\Delta t_c/t_{\text{touch}}$ must scale as the aspect ratio at breakthrough we have chosen to explore the parametric space by fixing this last quantity together with $\overline{\mathscr{K}}$ and we iterated (via a fixed point scheme) on the value of K_{Ic-2}/K_{Ic-1} until convergence. The convergence was reached as soon as one of the following criteria was met:

- the relative difference between the upper and the lower toughness ratios is < 0.001.

- the penetration in the bounding layers at $t_{\text{breakthrough}}$ is in the range $(0, \ell_{cell}/100)$.

Both an acceptable numerical accuracy and computational time were ensured by discretizing the central layer such that $H/\ell_{cell} \in [54.3, 98.6]$. The results are presented by the colored dots in Fig. 4.8-b) and -c).

Bibliography

Adachi, J. and Peirce, A. (2007). Asymptotic analysis of an elasticity equation for a finger-like hydraulic fracture. *Journal of Elasticity*, 90(1):43–69.

Anderson, D. G. (1965). Iterative procedures for nonlinear integral equations. *Journal of the ACM (JACM)*, 12(4):547–560.

Atkinson, C., Northrop, D., and Mann, R. (1981). The department of energy's western gas sands project multi-well experiment. In *All Days*. SPE.

Barker, L. (1977). A simplified method for measuring plane strain fracture toughness. *Engineering Fracture Mechanics*, 9(2):361–369.

Batchelor, G. (1967). *An Introduction to Fluid Dynamics*. Cambridge Mathematical Library. Cambridge University Press.

Batchelor, G. K. (2000). *An Introduction to Fluid Dynamics*. Cambridge Mathematical Library. Cambridge University Press.

Benzi, M., Golub, G., and Liesen, J. (2005). Numerical solution of saddle point problems. *Acta numerica*, 14:1–137.

Bunger, A. and Detournay, E. (2008). Experimental validation of the tip asymptotics for a fluid-driven crack. *Journal of the Mechanics and Physics of Solids*, 56(11):3101–3115.

Bunger, A. and Lecampion, B. (2017). *Four Critical Issues for Successful Hydraulic Fracturing Applications*, chapter 16, page 551:593. CRC Press.

Caenn, R., Darley, H., and Gray, G. (2011). *Composition and properties of drilling and completion fluids*. Gulf professional publishing.

Caswell, T. E. and Milliken, R. E. (2017). Evidence for hydraulic fracturing at gale crater, mars: Implications for burial depth of the yellowknife bay formation. *Earth and Planetary Science Letters*, 468:72–84.

Chacon, E., Barrera, V., Jeffrey, R., and van As, A. (2004). Hydraulic fracturing used to precondition ore and reduce fragment size for block caving. *A. Karzulovic and M.A. Alfaro (Eds), MassMin August*, pages 529–534.

Bibliography

Chandler, M. R., Meredith, P. G., Brantut, N., and Crawford, B. R. (2016). Fracture toughness anisotropy in shale. *Journal of Geophysical Research: Solid Earth*, 121(3):1706–1729.

Chen, Z., Jeffrey, R., and Zhang, X. (2015). Numerical modeling of three-dimensional t-shaped hydraulic fractures in coal seams using a cohesive zone finite element model. *Hydraulic Fracturing Journal*, 2(2):20–37.

Clarke, H., Eisner, L., Styles, P., and Turner, P. (2014). Felt seismicity associated with shale gas hydraulic fracturing: The first documented example in europe. *Geophysical Research Letters*, 41(23):8308–8314.

Cleary, M. (1978). Primary factors governing hydraulic fractures in heterogeneous stratified porous formations. Report n. UCRL-13884; CONF-781112-10.

Council, N. R. (2013). *Induced seismicity potential in energy technologies.* National Academies Press.

Crouch S.L., Starfield A.M., R. F. (1983). *Boundary Element Methods in Solid Mechanics.* George Allen & Unwin (London).

Daneshy, A. (1978). Hydraulic fracture propagation in layered formations. *Society of Petroleum Engineers Journal*, 18(01):33–41.

Das, S. B., Joughin, I., Behn, M. D., Howat, I. M., King, M. A., Lizarralde, D., and Bhatia, M. P. (2008). Fracture propagation to the base of the greenland ice sheet during supraglacial lake drainage. *Science*, 320(5877):778–781.

Desroches, J., Detournay, E., Lenoach, B., Papanastasiou, P., Pearson, J. R. A., Thiercelin, M., and Cheng, A. (1994). The crack tip region in hydraulic fracturing. *Proceedings of the Royal Society of London. Series A: Mathematical and Physical Sciences*, 447(1929):39–48.

Desroches, J., Peyret, E., Gisolf, A., Wilcox, A., Di Giovanni, M., de Jong, A., Sepehri, S., Garrard, R., and Giger, S. (2021). Stress measurement campaign in scientific deep boreholes: Focus on tool and methods. In *SPWLA 62nd Annual Logging Symposium.* OnePetro.

Desroches, J. and Thiercelin, M. (1993). Modelling the propagation and closure of micro-hydraulic fractures. *International Journal of Rock Mechanics and Mining Sciences I& Geomechanics Abstracts*, 30(7):1231–1234.

Detournay, E. (2016). Mechanics of hydraulic fractures. *Annual Review of Fluid Mechanics*, 48(1):311–339.

Detournay, E. and Peirce, A. (2014). On the moving boundary conditions for a hydraulic fracture. *International Journal of Engineering Science*, 84:147–155.

Dontsov, E. (2021). Analysis of a constant height hydraulic fracture.

Dontsov, E. and Peirce, A. (2015). A non-singular integral equation formulation to analyse multiscale behaviour in semi-infinite hydraulic fractures. *Journal of Fluid Mechanics*, 781:R1.

Dontsov, E. and Peirce, A. (2017). A multiscale implicit level set algorithm (ILSA) to model hydraulic fracture propagation incorporating combined viscous, toughness, and leak-off asymptotics. *Computer Methods in Applied Mechanics and Engineering*, 313:53–84.

Dontsov, E. and Suarez-Rivera, R. (2021). Representation of high resolution rock properties on a coarser grid for hydraulic fracture modeling. *Journal of Petroleum Science and Engineering*, 198:108144.

Dvorak, G. and Laws, N. (1986). Analysis of first ply failure in composite laminates. *Engineering Fracture Mechanics*, 25(5):763–770.

Dvorak, G. and Laws, N. (1987). Analysis of progressive matrix cracking in composite laminates ii. first ply failure. *Journal of Composite Materials*, 21(4):309–329.

Economides, M. and Nolte, K. (2000). *Reservoir Stimulation*. John Wiley & Sons.

EPA., U. (2016). Hydraulic fracturing for oil and gas: Impacts from the hydraulic fracturing water cycle on drinking water resources in the united states (final report). Technical report, U.S. Environmental Protection Agency, Washington, DC, EPA/600/R-16/236F.

Eyre, T. S., Eaton, D. W., Garagash, D. I., Zecevic, M., Venieri, M., Weir, R., and Lawton, D. C. (2019). The role of aseismic slip in hydraulic fracturing–induced seismicity. *Science advances*, 5(8):eaav7172.

Fies, G. D., Peck, D., Dutko, M., and Mishuris, G. (2022a). On averaging of toughness heterogeneity when modelling hydraulic fracture evolution. *U.S. Rock Mechanics/Geomechanics Symposium*. ARMA-2022-2135.

Fies, G. D., Peck, D., Dutko, M., and Mishuris, G. (2022b). A temporal averaging–based approach to toughness homogenisation in heterogeneous material. *Mathematics and Mechanics of Solids*, page 108128652211175.

Gao, H. and Rice, J. (1987). Somewhat circular tensile cracks. *International Journal of Fracture*, 33(3):155–174.

Gao, H. and Rice, J. R. (1989). A first-order perturbation analysis of crack trapping by arrays of obstacles. *Journal of Applied Mechanics*, 56(4):828–836.

Garagash, D. (2009). Scaling of physical processes in fluid-driven fracture: perspective from the tip. In *IUTAM symposium on scaling in solid mechanics*, pages 91–100. Springer.

Garagash, D. (2023). Fluid-driven crack tunneling in a layer. *in preparation*.

Bibliography

Garagash, D., Bunger, A., and Rohde, A. (2009). Leading edge of a hydraulic fracture crossing a stress boundary (paper no. t02. 008). In *Proceedings of 12th international conference on fracture, Ottawa, July 12–17 2009.*

Garagash, D. and Detournay, E. (1998). Similarity solution of a semi-infinite fluid-driven fracture in a linear elastic solid. *Comptes Rendus de l'Académie des Sciences - Series IIB - Mechanics-Physics-Chemistry-Astronomy*, 326(5):285–292.

Garagash, D., Detournay, E., and Adachi, J. (2011). Multiscale tip asymptotics in hydraulic fracture with leak-off. *Journal of Fluid Mechanics*, 669:260–297.

Gille, G. (1985). Strength of thin films and coatings. *Current topics in materials science*, 12:420–471.

Gu, H. and Siebrits, E. (2008). Effect of formation modulus contrast on hydraulic fracture height containment. *SPE Production & Operations*, 23(02):170–176.

Haimson, B. (1993). 14 - the hydraulic fracturing method of stress measurement: Theory and practice. In HUDSON, J. A., editor, *Rock Testing and Site Characterization*, pages 395–412. Pergamon, Oxford.

Haimson, B. and Cornet, F. (2003). Isrm suggested methods for rock stress estimation—part 3: hydraulic fracturing (hf) and/or hydraulic testing of pre-existing fractures (htpf). *International Journal of Rock Mechanics and Mining Sciences*, 40(7):1011–1020. Special Issue of the IJRMMS: Rock Stress Estimation ISRM Suggested Methods and Associated Supporting Papers.

Hanson, M., Shaffer, R., and Anderson, G. (1981). Effects of various parameters on hydraulic fracturing geometry. *Society of Petroleum Engineers Journal*, 21(04):435–443.

Hills, D., Kelly, P., Dai, D., and Korsunsky, A. (2013). *Solution of Crack Problems: The Distributed Dislocation Technique.* Solid Mechanics and Its Applications. Springer Netherlands.

Ho, S. and Suo, Z. (1993). Tunneling cracks in constrained layers. *Journal of Applied Mechanics*, 60(4):890–894.

Holland, A. A. (2013). Earthquakes triggered by hydraulic fracturing in south-central oklahoma. *Bulletin of the Seismological Society of America*, 103(3):1784–1792.

Hossain, M., Hsueh, C.-J., Bourdin, B., and Bhattacharya, K. (2014). Effective toughness of heterogeneous media. *Journal of the Mechanics and Physics of Solids*, 71:15–32.

Hubbert, M. and Willis, D. (1957). Mechanics of hydraulic fracturing. *Transactions of the AIME*, 210(01):153–168.

Irwin, G. (1957). Analysis of stresses and strains near the end of a crack traversing a plate. *Journal of Applied Mechanics*, 24(3):361–364.

Jébrak, M. (1997). Hydrothermal breccias in vein-type ore deposits: A review of mechanisms, morphology and size distribution. *Ore Geology Reviews*, 12(3):111–134.

Jeffrey, R., Bunger, A., Lecampion, B., Zhang, X., Chen, Z., van As, A., Allison, D., de Beer, W., Dudley, J., Siebrits, E., Thiercelin, M., and Mainguy, M. (2009). Measuring hydraulic fracture growth in naturally fractured rock. In *All Days*. SPE.

Jeffrey, R. G. and Bunger, A. (2009). A detailed comparison of experimental and numerical data on hydraulic fracture height growth through stress contrasts. *SPE Journal*, 14(03):413–422.

K., P., F.J., U., and A.T., A. (2017). Rate-independent fracture toughness of gray and black kerogen-rich shales. *Acta Geotechnica*, 12(6):1207–1227.

Keating, R. and Sinclair, G. (1996). On the fundamental energy argument of elastic fracture mechanics. *International journal of fracture*, 74(1):43–61.

Kemp, L. (1990). Study of Nordgren's equation of hydraulic fracturing. *SPE Production Engineering*.

Kovalyshen, Y. and Detournay, E. (2009). A reexamination of the classical PKN model of hydraulic fracture. *Transport in Porous Media*, 81(2):317–339.

Leblond, J. B., Patinet, S., Frelat, J., and Lazarus, V. (2012). Second-order coplanar perturbation of a semi-infinite crack in an infinite body. *Engineering Fracture Mechanics*, 90:129–142.

Lecampion, B., Bunger, A., and Zhang, X. (2018). Numerical methods for hydraulic fracture propagation: A review of recent trends. *Journal of Natural Gas Science and Engineering*, 49:66–83.

Lecampion, B. and Detournay, E. (2007). An implicit algorithm for the propagation of a hydraulic fracture with a fluid lag. *Computer Methods in Applied Mechanics and Engineering*, 196(49):4863–4880.

Lecampion, B. and Zia, H. (2019). Slickwater hydraulic fracture propagation: near-tip and radial geometry solutions. *Journal of Fluid Mechanics*, 880:514–550. Selected as Focus On Fluids (January 2020), Slickwater hydraulic fracturing of shales, comment by E. Detournay (doi.org/10.1017/jfm.2019.1023).

Li, X. and Keer, L. (1992). The growth of pressurized planar cracks between barriers. *International Journal of Solids and Structures*, 29(1):27–39.

Lister, J. and Kerr, R. (1991). Fluid-mechanical models of crack propagation and their application to magma transport in dykes. *Journal of Geophysical Research: Solid Earth*, 96(B6):10049–10077.

Liu, D., Lecampion, B., and Garagash, D. (2019). Propagation of a fluid-driven fracture with fracture length dependent apparent toughness. *Engineering Fracture Mechanics*, 220.

Bibliography

Madyarova, M. (2003). Fluid-driven penny-shaped fracture in elastic medium. Master's thesis, University of Minnesota.

Mendelsohn, D. A. (1984). A review of hydraulic fracture modeling—II: 3d modeling and vertical growth in layered rock. *Journal of Energy Resources Technology*, 106(4):543–553.

Montgomery, C. T. and Smith, M. B. (2010). Hydraulic fracturing: History of an enduring technology. *Journal of Petroleum Technology*, 62(12):26–40.

Moska, R., Labus, K., and Kasza, P. (2021). Hydraulic fracturing in enhanced geothermal systems—field, tectonic and rock mechanics conditions—a review. *Energies*, 14(18):5725.

Moukhtari, F. and Lecampion, B. (2018). A semi-infinite hydraulic fracture driven by a shear-thinning fluid. *Journal of Fluid Mechanics*, 838:573–605.

Murdoch, L. (2002). Mechanical analysis of idealized shallow hydraulic fracture. *Journal of Geotechnical and Geoenvironmental Engineering*, 128(6):488–495.

Nordgren, R. (1972). Propagation of a vertical hydraulic fracture. *Society of Petroleum Engineers Journal*, 12(04):306–314.

O'Keeffe, N. J. (2019). *Fluid-Driven Fractures in Elastic Hydrogels: Propagation and Coalescence*. PhD thesis, Department of Applied Mathematics and Theoretical Physics University of Cambridge.

O'Keeffe, N. J., Huppert, H. E., and Linden, P. F. (2018a). Experimental exploration of fluid-driven cracks in brittle hydrogels. *Journal of Fluid Mechanics*, 844:435–458.

O'Keeffe, N. J., Zheng, Z., Huppert, H. E., and Linden, P. F. (2018b). Symmetric coalescence of two hydraulic fractures. *PNAS; Proceedings of the National Academy of Sciences*, 115(41):10228–10232.

Peirce, A. (2006). Localized jacobian ILU preconditioners for hydraulic fractures. *International Journal for Numerical Methods in Engineering*, 65(12):1935–1946.

Peirce, A. (2015). Modeling multi-scale processes in hydraulic fracture propagation using the implicit level set algorithm. *Computer Methods in Applied Mechanics and Engineering*, 283:881–908.

Peirce, A. and Detournay, E. (2008). An implicit level set method for modeling hydraulically driven fractures. *Computer Methods in Applied Mechanics and Engineering*, 197(33):2858–2885.

Perkins, T. and Kern, L. (1961). Widths of hydraulic fractures. *Journal of Petroleum Technology*, 13(09):937–949.

Peruzzo, C. and Lecampion, B. (2023). Conditions for the local arrest of a hydraulic fracture by a region of larger toughness. *in preparation*.

Phillips, W. J. (1972). Hydraulic fracturing and mineralization. *Journal of the Geological Society*, 128(4):337–359.

Rice, J. (1968). *Mathematical analysis in the mechanics of fracture*, volume 2, pages 191–311. Academic Press, N. Y.

Rice, J. (1988). Crack front trapped by arrays of obstacles, solutions based on linear perturbation theory, in analytical, numerical and experimental aspects of three dimensional fracture processes. *AMD-91, ASME*, pages 175–184.

Rice, J. R. (1985). First-Order Variation in Elastic Fields Due to Variation in Location of a Planar Crack Front. *Journal of Applied Mechanics*, 52(3):571–579.

Rivalta, E., Taisne, B., Bunger, A., and Katz, R. (2015). A review of mechanical models of dike propagation: Schools of thought, results and future directions. *Tectonophysics*, 638:1–42.

Saad, Y. (1994). ILUT: A dual threshold incomplete LU factorization. *Numerical Linear Algebra with Applications*, 1(4):387–402.

Sarvaramini, E. and Garagash, D. (2015). Breakdown of a pressurized fingerlike crack in a permeable solid. *Journal of Applied Mechanics*, 82(6).

Savitski, A. and Detournay, E. (2002). Propagation of a penny-shaped fluid-driven fracture in an impermeable rock: asymptotic solutions. *International Journal of Solids and Structures*, 39(26):6311–6337.

Schmidt, H. (2010). Us patent: Hydraulic geofracture energy storage system. US 2011/0030362 A1, https://patents.google.com/patent/US20110030362.

Schmidt, H., Wright, S., Mauroner, C., Lau, H., Hill, B., Zhou, J., and Bunger, A. (2023). Geomechanical Pumped Storage in Hydraulic Fractures. *SPE Hydraulic Fracturing Technology Conference and Exhibition*, Day 3 Thu, February 02, 2023. D031S008R004.

Schmoker, J. and Oscarson, S. (1995). Descriptions of continuous-type (unconventional) plays of the u.s. geological survey 1995 national assessment of united states oil and gas resources.

Schultz, R., Skoumal, R. J., Brudzinski, M. R., Eaton, D., Baptie, B., and Ellsworth, W. (2020). Hydraulic fracturing-induced seismicity. *Reviews of Geophysics*, 58(3):e2019RG000695.

Schultz, R., Stern, V., Novakovic, M., Atkinson, G., and Gu, Y. J. (2015). Hydraulic fracturing and the crooked lake sequences: Insights gleaned from regional seismic networks. *Geophysical Research Letters*, 42(8):2750–2758.

Senseny, P. and Pfeifle, T. (1984). Fracture toughness of sandstones and shales. In *The 25th US Symposium on Rock Mechanics (USRMS)*. OnePetro.

Sethian, J. A. (1999). Fast marching methods. *SIAM review*, 41(2):199–235.

Bibliography

Simonson, E., Abou-Sayed, A., and Clifton, R. (1978). Containment of massive hydraulic fractures. *Society of Petroleum Engineers Journal*, 18(01):27–32.

Sone, H. and Zoback, M. D. (2013). Mechanical properties of shale-gas reservoir rocks—part 1: Static and dynamic elastic properties and anisotropy. *Geophysics*, 78(5):D381–D392.

Spence, D., Sharp, P., and Turcotte, D. (1987). Buoyancy-driven crack propagation: a mechanism for magma migration. *Journal of Fluid Mechanics*, 174:135–153.

Szeri, A. Z. (2010). *Fluid film lubrication*. Cambridge university press.

Tada, H., Paris, P., and Irwin, G. (2000). *The Stress Analysis of Cracks Handbook*. Wiley.

Thiercelin, M. and Desroches, J. (1993). Improving the performance of open hole stress tools. *International Journal of Rock Mechanics and Mining Sciences I& Geomechanics Abstracts*, 30(7):1249–1252.

Thiercelin, M., Jeffrey, R., and Naceur, K. B. (1989). Influence of fracture toughness on the geometry of hydraulic fractures. *SPE Production Engineering*, 4(04):435–442.

Thiercelin, M., Plumb, R. A., Desroches, J., Bixenman, P., Jonas, J., and Davie, W. (1996). A New Wireline Tool for In-Situ Stress Measurements. *SPE Formation Evaluation*, 11(01):19–25.

Tsai, V. C. and Rice, J. R. (2010). A model for turbulent hydraulic fracture and application to crack propagation at glacier beds. *Journal of Geophysical Research: Earth Surface*, 115(F3).

Tsai, V. C. and Rice, J. R. (2012). Modeling turbulent hydraulic fracture near a free surface. *Journal of Applied Mechanics*, 79(3).

Van As, A. and Jeffrey, R. (2000). Caving induced by hydraulic fracturing at northparkes mines. In *4th North American Rock Mechanics Symposium*. OnePetro.

van der Vorst, H. A. (1992). Bi-CGSTAB: A fast and smoothly converging variant of bi-CG for the solution of nonsymmetric linear systems. *SIAM Journal on Scientific and Statistical Computing*, 13(2):631–644.

van Eekelen, H. (1982). Hydraulic fracture geometry: Fracture containment in layered formations. *Society of Petroleum Engineers Journal*, 22(03):341–349.

Vasoya, M., Leblond, J. B., and Ponson, L. (2013). A geometrically nonlinear analysis of coplanar crack propagation in some heterogeneous medium. *International Journal of Solids and Structures*, 50(2):371–378.

Walker, H. F. and Ni, P. (2011). Anderson acceleration for fixed-point iterations. *SIAM Journal on Numerical Analysis*, 49(4):1715–1735.

Warpinski, N., Schmidt, R., and Northrop, D. (1982). In-situ stresses: The predominant influence on hydraulic fracture containment. *Journal of Petroleum Technology*, 34(03):653–664.

Watwood, V. (1970). The finite element method for prediction of crack behavior. *Nuclear Engineering and Design*, 11(2):323–332.

Wu, R., Bunger, A. P., Jeffrey, R. G., and Siebrits, E. (2008). A comparison of numerical and experimental results of hydraulic fracture growth into a zone of lower confining stress.

Xing, P. (2018). *Hydraulic fracture containment in layered reservoirs*. PhD thesis, University of Pittsburgh.

Zehnder, A. (2012). *Fracture mechanics*, volume 62. Springer Science & Business Media.

Zia, H. and Lecampion, B. (2019). Explicit versus implicit front advancing schemes for the simulation of hydraulic fracture growth. *International Journal for Numerical and Analytical Methods in Geomechanics*, 43(6):1300–1315.

Zia, H. and Lecampion, B. (2020). PyFrac: A planar 3d hydraulic fracture simulator. *Computer Physics Communications*, 255:107368.

Zia, H., Lecampion, B., and Zhang, W. (2018). Impact of the anisotropy of fracture toughness on the propagation of planar 3d hydraulic fracture. *International Journal of Fracture*, 211:103–123.

Zou, C. (2013). *Unconventional Petroleum Geology*. Geology Press, Beijing, second edition.

Carlo Peruzzo

Phone: +39 348 2543865 | Email: mailcarloperuzzo@gmail.com
Date & place of birth: March, 1992 – Italy, Treviso
Nationality: Italian

2018-2023	doctoral studies at the Geo Energy Lab EPFL (CH) to obtain a PhD in Mechanics from 01/12/2018 to the present.
2017-2018	early stage researcher at CISM-Lab (from 04/2017 to 10/2018). Seconded to the Institute of Continuum Mechanics, Leibniz University, from 01/11/2017 to 31/10/2018.
2014-2016	Studies to obtain the master of science in civil engineering, from 01/10/2014 to 01/10/2016.
2011-2014	Studies to obtain the bachelor of science in civil engineering, from 01/10/2011 to 01/10/2014.

Education:

Master of Science – Civil and Environmental Engineering

Institution	University of Padua, Italy
Grading	110/110 with honours
Supervisor	Prof. ing. Francesco Pesavento
Specialization	Structural Engineering
Title of thesis	Implementation of mixed type finite elements in a FEM code for the analysis of multiphase porous media on parallel architectures.

Bachelor of Science – Civil Engineering

Institution	University of Padua, Italy
Grading	110/110 with honours
Title of thesis	Numerical analysis for coupled simulation of fire in tunnels.

Publications:

- Peruzzo, C., Cao, D. T., Milanese, E., Favia, P., Pesavento, F., Hussain, F., & Schrefler, B. A. (2019). *Dynamics of fracturing saturated porous media and self-organization of rupture.* European Journal of Mechanics-A/Solids, 74, 471-484.

- Peruzzo, C., Simoni, L., & Schrefler, B. A. (2019). *On stepwise advancement of fractures and pressure oscillations in saturated porous media.* Engineering Fracture Mechanics, 215, 246-250.

- Milanese, E., Ni, T., Peruzzo, C., Zaccariotto, M., Galvanetto, U., Mishuris, G. S., & Schrefler, B. A. (2022). *Forerunning and bridging in dry and saturated fracturing solids.* In Current Trends and Open Problems in Computational Mechanics (pp. 343-353). Cham: Springer International Publishing.

- Peruzzo, C., & Lecampion, B. (2023). *Elongated hydraulic fracture emerging from layers of alternating fracture toughness.* Submitted for presentation at the 57th US Rock Mechanics/Geomechanics Symposium held in Atlanta, Georgia, USA, 25–28 June 2023.

- Möri, A., Peruzzo, C., Lecampion, B., & Garagash D.I. (2023). *Arrest Mechanisms of Buoyant Hydraulic Fractures.* Submitted for presentation at the 57th US Rock Mechanics/Geomechanics Symposium held in Atlanta, Georgia, USA, 25–28 June 2023.

Participation in conferences:

- *Interaction and Coalescence of Fluid-driven Fractures: Numerical Predictions Versus Experiments.* Peruzzo, Carlo; Lecampion, Brice; O'Keeffe, N.; Linden, P.F.. APS physics March Meeting 2021, [Online], March 15-19, 2021.

- *The Breakthrough Time of a Hydraulic Fracture Contained Between Two Tough Layers.* Peruzzo, Carlo; Capron, Judith; Lecampion, Brice. 19th Swiss Geoscience Meeting, Geneva 2021, [Online], 19-20 November 2021.

- *Improved Fracture Front Reconstruction in Planar 3D Fluid Driven Fractures Simulation.* Peruzzo, Carlo; Lecampion, Brice; Zia, Haseeb. 14th World Congress on Computational Mechanics (WCCM XIV) and 8th European Congress on Computational Methods in Applied Sciences and Engineering (ECCOMAS 2020) (Eccomas Congress 2020 & 14th WCCM), Virtual Congress, January 11-15, 2021.

- *When, and For How Long, Two Tough Layers Can Contain the Propagation of a Fracture Driven by the Injection of a Viscous Fluid.* Peruzzo, Carlo; Capron, Judith; Lecampion, Brice. 8th European Congress on Computational Methods in Applied Sciences and Engineering (ECCOMAS Congress 2022), Oslo, Norway, 5-9 June 2022.

- *The Transient Phase of Planar, Three-Dimensional Buoyant Hydraulic Fractures Emerging from a Point Source.* Möri, Andreas; Peruzzo, Carlo; Lecampion, Brice. 8th European Congress on Computational Methods in Applied Sciences and Engineering (ECCOMAS Congress 2022), Oslo, Norway, 5-9 June 2022.

- *Comparison Between Laboratory Experiments and Numerical Simulations of a Hydraulic Fracture Propagating in an Anisotropic Rock.* Lu, Guanyi; Momeni, Seyyedmaalek; Peruzzo, Carlo; Lecampion, Brice. Fall Meeting 2022. AGU, 2022.

- *3D Quasidynamic Cycles Accelerated Using Hierarchical Matrices: Role of Complex Fault Geometry.* Jinhui, Cheng; Almakari, Michelle; Peruzzo, Carlo; Lecampion, Brice; Bhat, Harsha. No. EGU23-7807. Copernicus Meetings, 2023.

Students supervised at EPFL:

- Yazbeck Charbel, semester project, 2020
- Schütt Kilian, semester project, 2020
- Neypatraiky Yannick André, semester project, 2020
- Capron Judith, semester project, 2020
- Capron Judith, Master Thesis, 2021
- Schaufelberger Annik Julia, semester project, 2021
- Levkov Joana-Sophia, semester project, 2022

Last update: 10/04/2023